Microdynamics and Thermal Snap Response of Deployable Space Structures

by

Michel D. Ingham

B. Eng. Mechanical Engineering (Honours)
McGill University, 1995

Submitted to the Department of Aeronautics and Astronautics
in partial fulfillment of the requirements for the degree of

MASTER OF SCIENCE IN AERONAUTICS AND ASTRONAUTICS
AT THE
MASSACHUSETTS INSTITUTE OF TECHNOLOGY

May 1998

Signature of Author .....
Department of Aeronautics and Astronautics
May 15, 1998

Certified by .....
Professor Edward F. Crawley
Department of Aeronautics and Astronautics
Thesis Supervisor

Accepted by .....
Professor Jaime Peraire
Chairman, Department Graduate Committee

Microdynamics and Thermal Snap Response of Deployable Space Structures

by

Michel D. Ingham

Submitted to the Department of Aeronautics and Astronautics
on May 15, 1998 in Partial Fulfillment of the Requirements for
the Degree of Master of Science in Aeronautics and Astronautics

Abstract

Due to the size constraints imposed by the payload bays of carrier spacecraft, future precision space structures (e.g. interferometric telescopes) will undoubtedly require some form of on-orbit deployment mechanism, including joints or hinges which will introduce nonlinearity to the structure. Results are presented from a two-part experimental investigation of the microdynamic response of nonlinear structures, to both mechanical and thermal excitation sources.

In the first experiment, the dynamic response of a deployable truss at sub-microstrain levels of vibration is characterized in terms of modal parameters. The test article is subjected to stepped-sine sweeps through its fundamental flexible modes over a range of excitation amplitudes. High-sensitivity piezoceramic strain sensors are used in conjunction with a lock-in amplifier to measure the truss response from tens of microstrain down to one nanostrain. The natural frequency and damping ratio are computed from the frequency response functions, using a circle fit method. Results show that the values of the modal parameters are strain-dependent at high response amplitudes, and strain-independent at low amplitudes. It is inferred that, at microdynamic levels of excitation, the internal loads needed to overcome the joint friction are not attained. The nonlinear mechanisms in the structure are thus not activated, resulting in a linear truss response.

In the second experiment, the phenomenon of thermal snap, or creak, is investigated. Thermal snap is a disturbance which occurs when thermally-induced stress in a statically indeterminate structure is suddenly released via a slip internal to a joint or other frictional mechanism. A representative deployable truss is suspended in a thermal chamber, where its temperature is cycled between –30°C and 50°C, in order to determine whether thermal snap occurs in such a structure. High-bandwidth accelerometers distributed across the truss are used as the primary sensors for detecting structural events. Thermal snaps are found to occur during the thermal transients, before steady-state is achieved throughout the truss. The truss response to the impulsive and broadband disturbances is characterized in both the time and frequency domains. The transient response exhibits telltale signs of structural behavior, including multi-mode or dominant-mode excitation, and reasonable modal damping in the time decay.

Thesis Supervisor: Edward F. Crawley
Title: Professor of Aeronautics and Astronautics

Acknowledgements

I would like to express utmost appreciation to my advisor, Professor Edward Crawley, for his guidance and support, in matters academic and otherwise. I also owe a debt of gratitude to Professor David Miller, Director of the MIT Space Systems Lab, for his invaluable advice and faith in my abilities. A special thank-you goes to Yool Kim, with whom I worked on the thermal snap experiment, for the hours of enlightening discussion which filled the (sometimes lengthy) gaps between snap events. A hearty round of thanks is due to Marthinus van Schoor, Javier de Luis and the folks at Payload Systems Inc. and Midé Technology Corp., as well as Ed Mencow, Ron Efromson, Jon Howell and Al Mason from MIT Lincoln Laboratory, for their patience and generosity in allowing us to use their facilities for the thermal snap experiment. Their assistance was greatly appreciated.

This research was sponsored under Jet Propulsion Laboratory grant #960747, with Dr. Marie Levine-West as technical monitor. I would like to extend a personal note of appreciation to Marie for her helpful input and interest in my work. The National Sciences and Engineering Research Council of Canada and the Canadian Space Agency are acknowledged, for contributing to the support of my research in the form of an NSERC postgraduate scholarship and supplement.

I am also grateful for the help I received from members of the technical staff of the Department of Aeronautics and Astronautics. In particular, many thanks to Paul Bauer, for passing along some of his experimental know-how. I would certainly be remiss in forgetting to thank SharonLeah Brown for going above and beyond the call of duty in her efforts to make life happy for the graduate students in the Space Systems Lab and Active Materials and Structures Lab. To my labmates, I would like to say how fortunate I am to have worked or otherwise interacted with all of you.

And last but certainly not least, I would like to thank my family and friends for being an endless source of encouragement.

Table of Contents

List of Tables

List of Figures

Chapter 1 – Introduction

1.1 Importance of Microdynamics

The hunt for Earth-like planets orbiting other stars has come to the forefront of the space community's interest. This is one of the primary objectives of NASA's Origins Program, which will launch a number of space-based observatories, starting in the next decade. These missions will employ both connected interferometers and large aperture telescopes with adaptive mirrors. Due to the size constraints imposed by the payload bays of carrier spacecraft, these telescopes will undoubtedly require some form of on-orbit deployment mechanism, including joints or hinges which will introduce nonlinearity to the structure.

The success of the Origins missions will hinge on whether positioning of the optical elements can be maintained to within fractions of the viewing wavelength. Consequently, any minute disturbance will pose a serious threat to the stability of the precision optical systems. The response of structures with nonlinear elements to such small disturbances has yet to be researched in depth. In order to predict the structural response in this regime, and ultimately control the structure, accurate models of the disturbances and the low-amplitude dynamics of the structure must be developed. Such models can only result from thorough experimental characterizations of the disturbance sources and the structure itself.

The term "microdynamics" has been coined to describe the dynamics of materials and structures at levels of vibration smaller than those targeted by standard testing levels. A more quantitative definition of microdynamics is given by Wang and Hadaegh [1]: the regime in which the structural vibration amplitudes are in the micron or submicron range. It is often convenient to use a nondimensional metric such as strain to quantify and compare the vibration levels from different tests. Typical levels of strain achieved during standard dynamic tests are in the range between 10 and 1000 microstrain. Microdynamic levels of interest therefore cover the strains on the order of microstrain, or smaller. Depending on the size and requirements of the structural system, information on the dynamics down to nanostrain levels, or lower, may be sought.

One of the many microdynamic-level disturbances of interest is the phenomenon commonly referred to as thermal snap, or creak. Statically indeterminate structures with nonlinear friction interfaces are vulnerable to this disturbance source. As the thermal load on such a structure changes, perhaps due to the change in radiation environment as the spacecraft passes in or out of the Earth's shadow, the structure tries to contract or expand as dictated by the coefficients of thermal expansion (CTE) of its components (see simplified model in Figure 1.1). Due to a mismatch in CTE between components made of different materials, free thermal expansion is not allowed to occur, and stresses are created in the structure. This stress buildup can also occur due to non-uniform heating or cooling across a structure, even one composed of a single material, perhaps as a result of partial shadowing. If there are frictional interfaces in the load path between stressed elements, a level of internal load can be attained such that the static friction force is exceeded. The two elements then experience a sudden slip along the friction interface, which releases the built-up stress, until the slip is halted due to one of two reasons: either enough stress is relieved such that the internal load falls below the level of the dynamic friction, or the end of the frictional deadband is reached (i.e. the fixed boundary of the interface is contacted). This slip releases some of the thermally-induced elastic energy stored in the stressed elements, and translates an impulsive disturbance internal to the structure.

Thermal snap is a potentially serious problem in space structures, especially in deployable and flexible structures. The poor understanding of this type of disturbance is exacerbated because thermal creaks have rarely, if at all, been directly observed. Their nature must generally be inferred from the spacecraft sensors, and the control system response [2]. Nonlinear joints with deadbands, tensioning cables and pulleys, and other structural elements that depend on friction and allow relative motion are all examples of potential creak elements that are common in space structures. The ability to predict creak events and the resulting structural response, either deterministically or in a statistical sense, would benefit the design of dimensionally stable space structures.

The overall objective of this research, therefore, is to perform a microdynamic-level investigation of structures with nonlinear mechanisms, representative of future precision space structures. Specifically, the main goal is to experimentally characterize the dynamic response of a deployable truss at sub-microstrain levels of vibration, due to mechanically- and thermally-induced structural excitation.

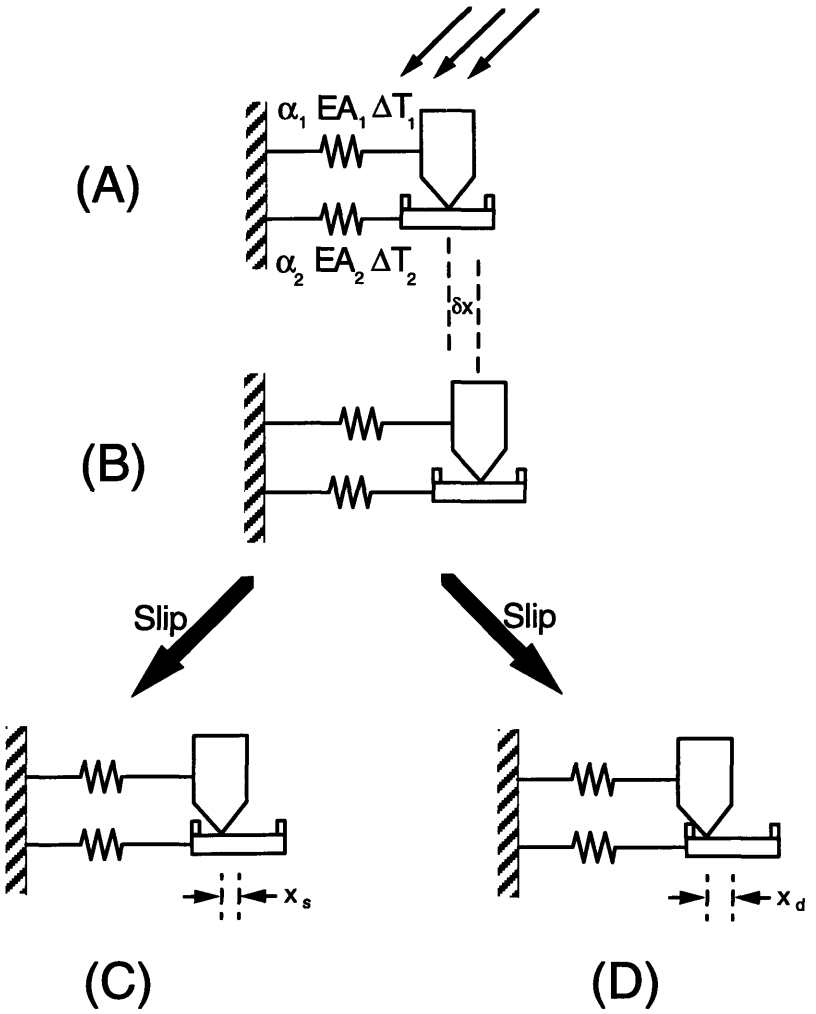

Figure 1.1 Simplified structural model illustrating thermal snap.

A potentially non-uniform temperature gradient is applied to a statically indeterminate structure with CTE-mismatched components (A). Constrained thermal deformation δx occurs, as internal stresses build up (B). Once a critical level of stress is reached, the frictional interface slips. The slip halts after a relative displacement x_s, if the internal load falls below the dynamic friction level (C), or x_d, if the end of the joint deadband is reached (D).

1.2 Background

In the middle of the last decade, the field of microdynamics was born from the need for high-precision structures in space: the standard structural testing methodologies of the time were incapable of evaluating whether the new breed of spacecraft would satisfy their stringent stability

requirements. Since then, researchers have devoted considerable resources to develop facilities and procedures which would allow them to design such spacecraft. In this section, past and ongoing research in the fields of microdynamics and general structural dynamics is discussed, as background for the study documented in this thesis.

The dynamics of structures with nonlinear mechanisms is a field which has matured considerably since the early 1980s. Considerable work has focused on the characterization of such structures at the mechanism- or component-level, as well as at the global structure-level. At the mechanism-level, several types of joints that display nonlinear behavior have been analyzed. Hertz and Crawley developed models of sleeve-stiffened and pinned joints, to investigate displacement-dependent friction damping and impact losses [3]. Further analytical work on nonlinear sleeve joints incorporated into flexible space structures was pursued by Ferri [4]. Tzou et al. modeled a 3-D spherical ball/socket joint, including friction and clearance effects [5]. The key problem with joint models such as these is the difficulty in accurately characterizing the friction mechanisms and other nonlinear joint behavior. Design-specific parameters such as the coefficient of friction and joint deadband are difficult to predict. In general, they must be determined experimentally, using methods such as force-state mapping [6, 7, 8]. An ongoing program at NASA Langley Research Center focuses on developing key structure and mechanism technologies for micron-accuracy, in-space deployment of future science intruments [9, 10]; one of the most recent results of their efforts is a new design for precision revolute joints, which exhibit high linearity and repeatability.

In addition to research on particular nonlinear mechanisms, a number of researchers have developed techniques for modeling the global dynamics of joint-dominated truss structures, both at "standard" and microdynamic levels. Wang and Hadaegh proposed a methodology for the mathematical modeling of preloaded truss-based space structures, in the microdynamic regime [1]. Their models incorporated monoball and butt joints, where the dynamic behavior was derived from Hertzian contact theory. Chapman et al. employed a residual force technique to perform transient analyses of trusses having joints with arbitrary force-state map characteristics [11]. The time response of trusses with nonlinear joints was also analyzed by Belvin, using a nonlinear finite element approach [12]. Sarver developed an analytic model for jointed space structures based on continuous damped beams and a piecewise linear joint [13]; his model correlated well with experimental results, which demonstrated dissipation and energy transfer between modes in a structure due to the presence of joints. Structural nonlinearities have also been modeled using

the describing function technique, in which a quasi-linearization of the force-state characteristics of the nonlinearity is performed [14, 15, 16].

Considerable experimental work has focused on the dynamics of jointed truss structures. Notably, MIT's Middeck 0-Gravity Dynamics Experiment (MODE) addressed the structural response of a deployable truss test article at relatively large strain levels [17]. Linear and nonlinear models were constructed, for both gravity and zero-gravity environments. Model accuracy was verified by comparing the modeling results with the ground and on-orbit data obtained. In particular, the effects of nonlinearities (due to the joint friction and slackening tension cables) on modal parameters (frequency, damping) were investigated. These millimeter-to-micron-level dynamics experiments also demonstrated that increased preload results in stiffening and decreased modal damping. Component-level characterization of the structural nonlinearities was performed by Masters, via the force-state mapping technique [18]. The results from the component characterization experiments were used to generate dynamic models of the global truss behavior [19].

Another space flight experiment, the Joint Damping Experiment (JDX), was developed by researchers at Utah State University to measure the influence of gravity on the structural damping of a truss with pinned joints [20]. The results from the ground and flight data indicated that friction and impacting in the joints were primary sources of damping. In the absence of gravity preload, increased damping was observed; greater freedom for impacting within the joint deadbands was identified as the likely source of this increase in damping, as energy is transferred to the higher-frequency modes excited by the impacting.

Damping within an erectable truss structure, subject to nanostrain levels of disturbance, was characterized by Ting and Crawley [21]. This work, done on a tetrahedral interferometer testbed, showed that structural damping is independent of strain below 1 microstrain, and increases with strain above that level. One of the objectives of the study documented in this thesis is to verify this conclusion for deployable trusses, where behavior may be significantly altered by the frictional joint mechanisms required for deployment.

Warren and Peterson [22] performed an experimental characterization of the microdynamics of a prototype deployable telescope support structure. They discovered that intentional application of impulses to the structure induced abrupt changes in structural shape at the microdynamic level

(dubbed "micro-lurches"). Furthermore, their study illustrated that successive impulses applied to the structure eventually brought the structure to a microdynamically stable position (the "equilibrium zone"). They developed a model for this behavior, which suggests that these effects were due to the dynamically-induced relaxation of strain energy stored by friction mechanisms within the structure.

In his text titled "Thermal Structures for Aerospace Applications" [2], Thornton provides a historical review of published work on the subject of thermally-induced structural disturbances. Most of the documented research focused on the excitation of low-frequency modes of long and slender structures, due to the application of sudden thermal gradients. This phenomenon has been observed during orbital day-night or night-day transitions on numerous spacecraft, including the OGOs spacecraft in the 1960s, and more recently, the Hubble Space Telescope [23]. This coupled thermal-structural response has been replicated in laboratory environments by a few different researchers, and has been alternately dubbed "thermal elastic shock" [24], or "thermal jitter" [25]. Another type of thermally-induced structural disturbance is thermal snap, or creak, which was described in section 1.1. Very little work on this phenomenon has been documented, despite on-orbit evidence of its occurrence: Foster et al. speculated that the Hubble Space Telescope experienced a thermal creak problem in the solar array drums and spreader bars [26]. As a first order approach to modeling the thermal creak problem, a simple generic model was developed by Kim and McManus [27]. In this model, a simple temperature distribution is assumed to determine the thermoelastic response of the structure, and a Coulombic friction joint introduces the nonlinearity which results in the creaking response. Their ongoing work includes a simple slipping joint experiment which should shed light on the friction mechanisms involved in thermal creak, and lead to more complex and accurate analytical models of the structural behavior.

Finally, a few words should be mentioned regarding a particularly relevant series of technology demonstration flight experiments designed by the Jet Propulsion Laboratory at Caltech. The goal of the Interferometry Program Experiments (IPEX I and II) was to investigate the microdynamic issues of concern to the Origins Program missions [28]. The nature of the experiments was threefold. IPEX-I (STS-80, December 1996) performed a microdynamic-level characterization of the disturbance environment on board a representative space telescope platform, the German DARA/DASA free-flying satellite pallet ASTRO-SPAS. For the second flight experiment, IPEX-II (STS-85, August 1997), a deployed truss boom was mounted to the ASTRO-SPAS; during the 10 days in orbit, microdynamic modal identification tests were performed on the truss, and a

thermal snap investigation was performed, during which the truss was monitored for the possible occurrence of thermally-induced transient events. While the data reduction process from the flights is still in progress, at the time of this writing, initial analysis has revealed that transient, microdynamic-level events, correlated with temperature transitions, were indeed detected on the boom. However, analysis has also shown that the overall disturbance environment experienced by the truss structure met the requirements for precision space optical systems.

1.3 Approach

Two different types of experiments were performed, with the common goal of characterizing the microdynamic response of a deployable truss structure to a specific excitation source. In the first experiment, modal identification of a truss (via stepped-sine sweep tests) was performed, in order to ascertain how the natural frequency f_n and damping ratio ζ_n vary as a function of decreasing levels of excitation. In the second experiment, the phenomenon of thermal snap was investigated; the same type of statically indeterminate truss characterized in the first experiment was subjected to a changing temperature environment, in order to determine whether thermal snap occurs in such structures. The truss response to any detected snap disturbances would be characterized in both the time and frequency domains.

Each of these two experiments is addressed in a separate chapter of this thesis. Chapter 2 describes in detail the different aspects of the modal parameter characterization experiment, while Chapter 3 covers the thermal snap investigation. Both of these chapters are organized in a consistent manner. In the opening section of each chapter, the experimental setup is described, including the test articles, actuators, and sensors used for each experiment. The second section outlines the test procedure followed for each experiment, including the data reduction techniques employed. In the third section, particular issues related to the microdynamic nature of each experiment are addressed. Finally, in the fourth section of the chapter, the experimental results are presented and discussed. The conclusions from both sets of experiments are summarized in Chapter 4; this final chapter also discusses the implications of this research for precision space structures, such as the Origins telescopes referred to in section 1.1, and suggests some areas for future work in the field of microdynamics.

Chapter 2 – Modal Parameter Characterization

The dynamics of a structure are often characterized in terms of its mode shapes and modal parameters, which represent the resonant natural frequencies of the structure, and the level of damping associated with each resonance. Accurate estimates of these parameters are required to build and verify dynamic models of structural systems, which may be used to predict the behavior of the structure in response to a given disturbance, or to represent the structural plant in the design of a control system. While much research has been done in the field of modal identification at "standard" levels of excitation, very little work has focused on the microdynamics regime. This regime is of critical importance to current and future precision space structures, for which the vibration environment must be known (and controlled) down to nanometer level.

This chapter presents an overview of the microdynamic modal parameter characterization experiment, performed on the two lowest-frequency global modes of a representative deployable space structure. The dynamics of the jointed truss are known to be nonlinear at high levels of excitation [17]. The goal here is to fully document the tests undertaken, and in the process, offer some general insight into the stringent requirements associated with experimentation in the microdynamic regime.

The opening section of the chapter describes the hardware, instrumentation and experimental setup used. The procedure followed during the stepped-sine sweep tests is outlined in the second section. The third section addresses the critical issues of precision and accuracy in the measurements from this microdynamic experiment. In the final section of this chapter, the results from the experiment are presented, discussed, and correlated with findings from relevant past experiments.

2.1 Hardware Description and Experimental Setup

The purpose of this section is to provide detail on the hardware used in the microdynamic experiment, and to describe the physical setup in the laboratory. In the first subsection, a description of the deployable truss testbed is given. The second subsection addresses the two actuators used to excite the structure over different ranges of applied load. The suite of sensors is the subject of the third subsection, including the specialized sensors used to measure strains down to nanostrain levels. The last subsection focuses on the other instrumentation required for making the microdynamic measurements.

2.1.1 MODE Truss Testbed

The testbed used for the modal parameter characterization experiment was the Middeck 0-gravity Dynamics Experiment Structural Test Article (MODE STA). Since the purpose of this work was to gain insight on the microdynamic mechanisms at work in a typical deployable structure, tests were only performed on the baseline configuration of the STA. The baseline configuration consists of two four-bay deployable truss modules connected by erectable truss members, forming a straight truss, 9 bays long (Figure 2.1). The MODE and MODE-Reflight programs studied the dynamics of these and other truss modules assembled in different configurations, including a straight truss with a rotary joint, an L-shaped truss with a rotary joint, and an L-shaped truss with both a rotary joint and a flexible appendage [29, 32]. In both of these programs, the modal behavior of these truss configurations was investigated at "standard" dynamic levels.

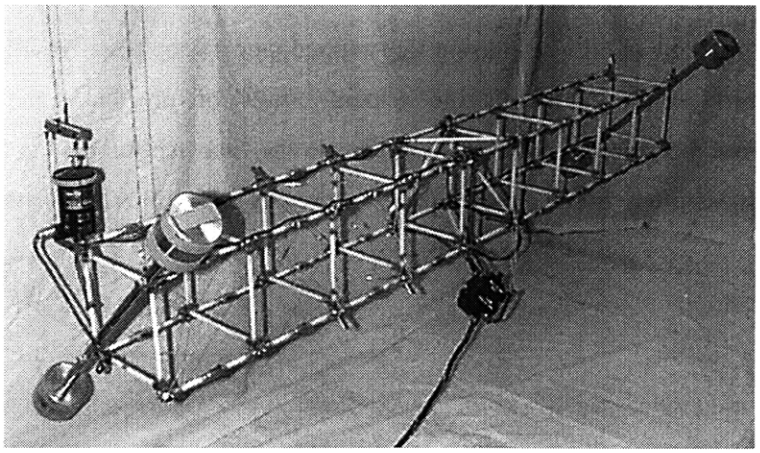

Figure 2.1 MODE STA baseline configuration

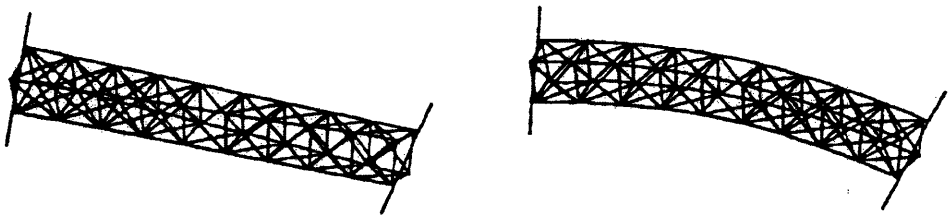

Figure 2.2 First torsion and bending modes for the MODE STA

For the purpose of limiting the test matrix size, microdynamic characterization was only performed on the two lowest-frequency global modes of the structure, namely the first torsion and bending modes. These two modes are illustrated in Figure 2.2. The natural frequency corresponding to the first torsion mode is approximately 7.7 Hz, while the first bending mode is in the vicinity of 20.7 Hz. The conclusions drawn from the tests on these modes are assumed to apply to the higher modes in which similar dynamic mechanisms are excited.

A brief description of the hardware follows, with emphasis placed on the joints and mechanisms relevant to this microdynamic study. Each component of the MODE STA baseline configuration is addressed: the deployable truss modules, the erectable bay, the suspension system and the rigid appendages. A more thorough description of the structure is available in various reports published on the MODE and MODE-Reflight experiments [30, 31, 32]. The most complete description is presented in the thesis by Barlow [29].

Deployable Modules

The two deployable truss modules were originally designed as hybrid scaled models of the Space Station Freedom solar array truss structure [29]. Each four-bay section weighs approximately 3 lbs (1.4 kg), and measures 32 inches (81.3 cm) long in its deployed state. Each bay is cubic, 8 inches on a side. The longerons hinge at their midpoints and at the attachment points to the batten frames. The truss folds up in accordion fashion, with the batten frames remaining rigid (Figure 2.3). No automated deployment mechanism is used (i.e. the truss must be collapsed and deployed "by hand").

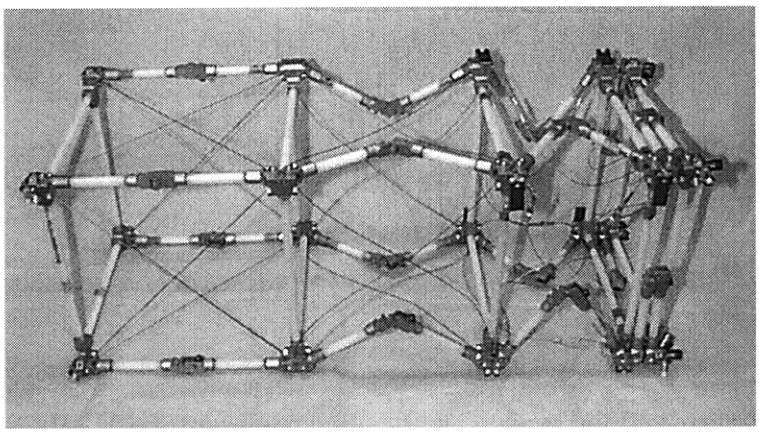

Figure 2.3 Partially collapsed deployable module

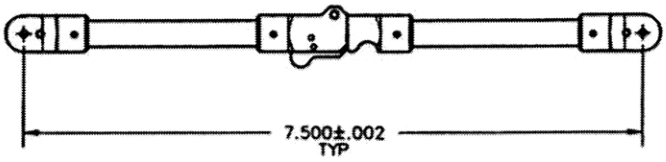

Figure 2.4 Deployable longeron

Figure 2.4 shows a drawing of a deployable longeron. The longerons are made of Series 500 Lexan rods with a 0.3125 inch (7.94 mm) diameter. The Lexan rods are epoxied to the knee joint assembly, made of aluminum Type 6061. Hysol EA 9394NA epoxy was used for all bonded interfaces on the structure. As the longeron unfolds during the deployment process, it locks approximately 2 degrees over center, and is held by a latch mechanism, as sketched in Figure 2.5. The end lugs of the longerons, also made of aluminum 6061, are hinged to the batten frame corner fittings. All aluminum parts on the STA are anodized for protection against corrosion.

The batten frames are made of four lengths of the same Lexan rods, connected with epoxy to four aluminum 6061 corner fittings (Figure 2.6, left photo). These fittings receive the pinned lugs of the longerons. The batten frames at either end of the deployable truss section have corner fittings with threaded holes (Figure 2.6, right photo), which allow connection with erectable truss members and attachment of the accelerometer sensors used for the MODE program (see subsection 2.1.3).

Each lateral face of each bay has a pair of crossing diagonal cables designed to preload the truss structure. These stranded Type 304 stainless steel cables have ball terminators, which sit in spherical receptacles in the batten frame corner fittings (Figure 2.7). Approximately 28 lbf (125 N) of pretension are applied to the longerons when they are locked in their fully deployed state, at room temperature. This corresponds to roughly 50% of their estimated buckling load. The tension level present in the diagonal cables is approximately 25 lbf (111 N) for the deployed section, corresponding to roughly 9% of the yield stress.

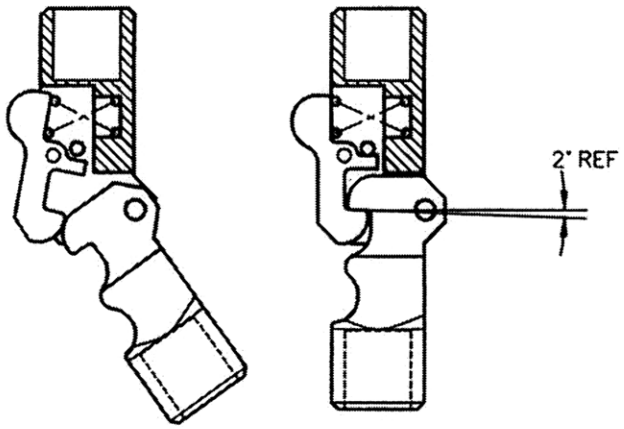

Figure 2.5 Knee joint and latch mechanism

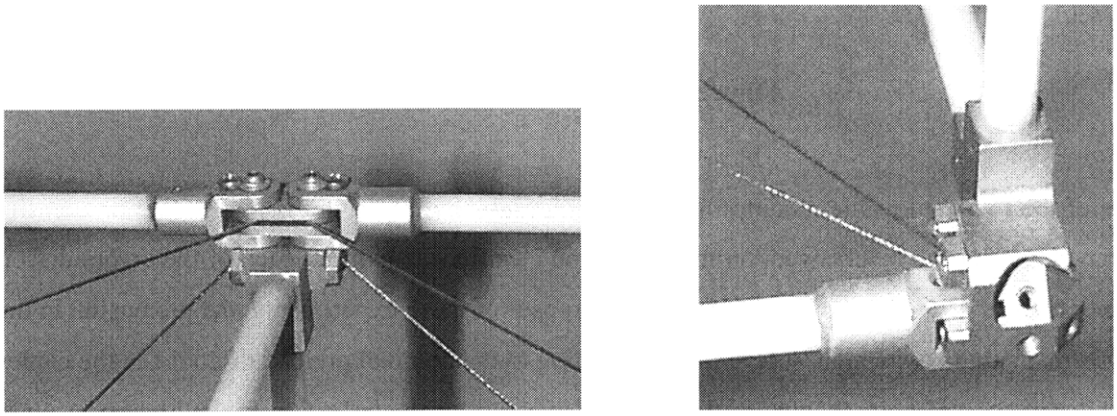

Figure 2.6 Batten frame corner fittings (intermediate and end bay)

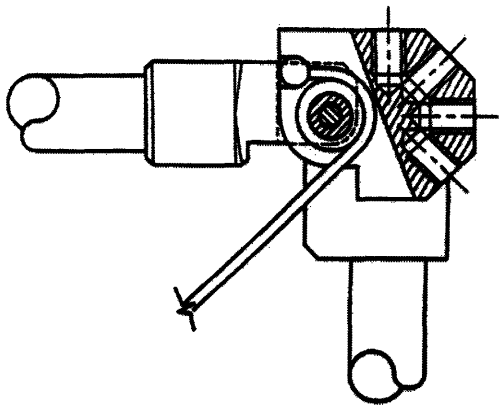

Figure 2.7 Cable termination detail

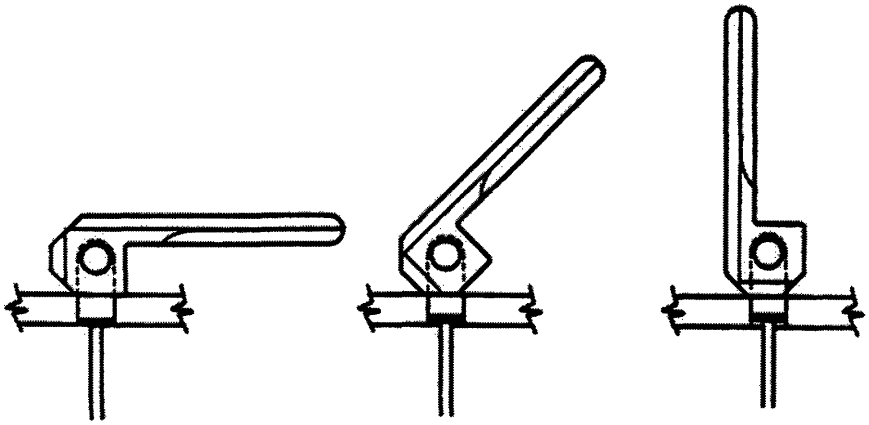

Figure 2.8 Tensioning lever detail

One of the two deployable modules has one bay for which the preload is adjustable. The tension in the diagonals can be changed via multi-position cleat mechanisms at each of the eight adjacent corner fittings (Figure 2.8). However, for the purposes of these experiments, the pretension in this bay is maintained at its highest level, corresponding to the nominal preload of 25 lbf in the cables. In this way, complete slackening of the cables is avoided for the tests at even the highest levels of excitation, and consistent preload is present across the structure. Both these conditions are reasonable for actual space truss designs.

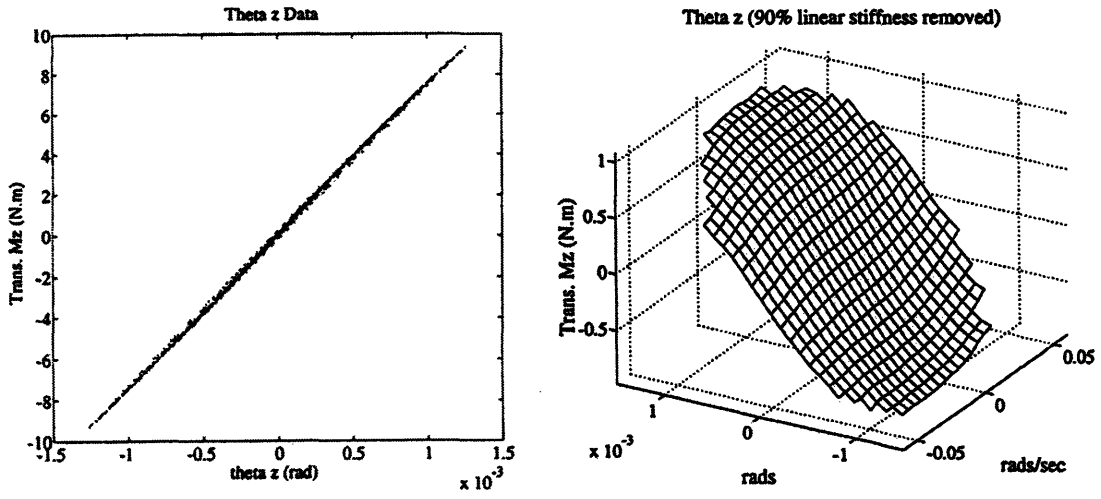

Figure 2.9 Force-state data for deployable bay [31]

Quasi-static force-state mapping was performed by Masters on a single deployable bay of the truss with the goal of identifying the nonlinear behavior, if not the actual mechanisms at work [31]. He observed that the bay exhibits low dissipation at low amplitudes, with increasing hysteretic softening with increasing amplitude after exceedance of a break amplitude. Performing his tests on an adjustable-preload bay, he also observed that nonlinearity increases as preload is decreased. Figure 2.9 presents results from Masters' experiment, in which the load on the deployable bay (high pretension setting) was a torsional moment applied at 7.6 Hz – roughly the frequency of the first torsion mode for the entire MODE STA. Data was sampled at 200 Hz for approximately 10 seconds. The first plot shows the torsional load-stroke relationship; while the data is predominantly linear, some hysteresis behavior is evident. The force-state map is shown in the second plot, with 90% of the linear stiffness removed. The increasing hysteretic softening behavior with increasing amplitude is observed, particularly with respect to the angular displacement.

Erectable Members

In the MODE baseline configuration, the two four-bay deployable sections are joined by a bay built from erectable truss members. There are four longerons and four diagonal truss members, all made from Series 500 Lexan with aluminum end lugs (see Figure 2.10). The end lugs fit into aluminum standoffs which screw into the threaded batten frame corner fittings. The struts are

fixed to the nodes by screwing threaded sleeves on the end lugs up against the standoffs. Finger tightening is adequate to secure the erectable members.

Masters [31] obtained force-state mapping data for the erectable bay, which led to two types of models. Tests on the bay with the joints tightly fastened resulted in essentially linear behavior. However, he discovered that vibration of the bay induced loosening of the erectable joints, which led to a second model, capturing the accumulated microfriction behavior of the loose joints. This model described one-way displacement dependent stiffness and dissipation in the bay, as well as one-way velocity dependent dissipation. Results from Masters' quasi-static tests on the erectable bay with loosened joints are shown in Figure 2.11. A torsional moment was applied to the bay at 7.5 Hz, and data was sampled at 200 Hz over 10 seconds, as for the deployable bay. The full stroke amplitude was around 1.5×10^{-4} radians. This amount of twist in the bay applies a strain of approximately 3.75×10^{-5} on the diagonal members. This strain level is on the same order of magnitude as the highest strains tested in the microdynamic modal parameter characterization experiment.

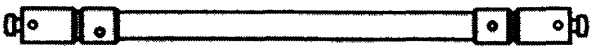

Figure 2.10 Erectable strut

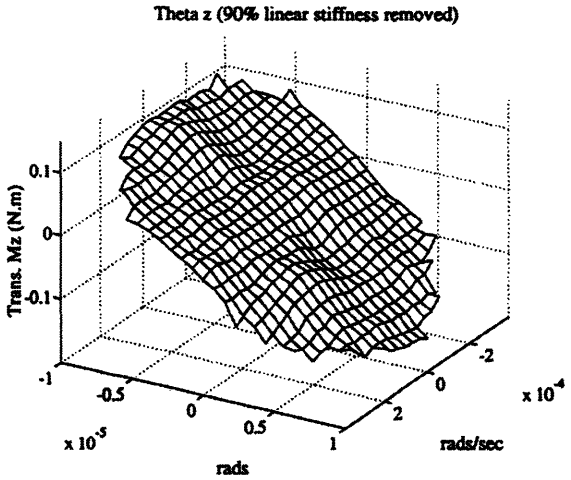

Figure 2.11 Force-state data for erectable bay with loosened joints [31]

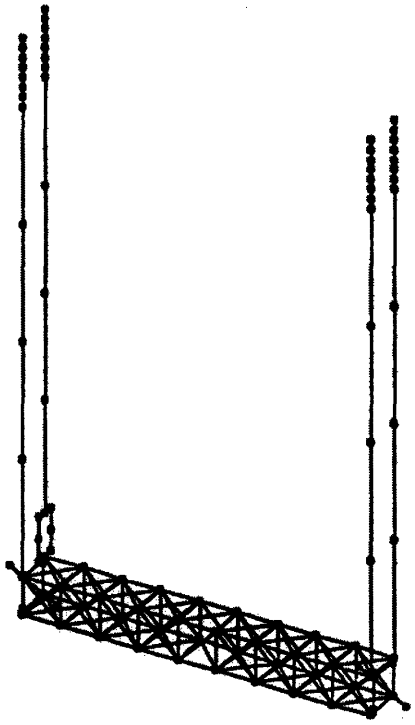

Figure 2.12 Suspended truss

Suspension system

One of the objectives of the MODE ground test program was to evaluate the influence of suspension stiffness on the identified modal parameters; suspension systems with fundamental bounce modes at 0.5, 1, 2, and 5 Hz were used and the results compared [29]. In theory, the suspension system should be designed to be as soft as possible. However, the softer 0.5 Hz springs used for MODE presented practical problems: as a result of their greater length and mass, various harmonics of the internal modes of the springs occurred at frequencies near the structural modes of interest.

For the purposes of the current study, only the "nominal" 1 Hz suspension system was used. This choice is based on conventional wisdom, which recommends an order of magnitude of separation between the fundamental frequencies of the suspension system and the structure. Of all the available suspension systems, the 1 Hz system provides the closest approximation to a free-free boundary condition, as would be encountered in space. The suspension system consists of four

coil springs attached to ceiling-mounted brackets, connected to lengths of piano wire which drop to the four end nodes at the top of the STA. The wires are made of high-strength steel, and have a 0.029 inch (0.74 mm) diameter. A sketch of the hanging truss is shown in Figure 2.12. About 8 inches above one of the corner attach points, the suspension wire branches into two wires, with the help of two 4-inch long horizontal spreader bars made of aluminum. This prevents the suspension wire from interfering with the actuator, which is attached to the truss at this corner. The overall length of the suspension system is 120 inches (3 m); at this length, the pendulum mode frequency is roughly 0.3 Hz.

Rigid Appendages

Rigid appendages, consisting of steel shafts with cylindrical steel masses at each end, are attached to the two end bays of the baseline truss (Figure 2.13). Their original purpose was to lower the fundamental mode of the truss to approximately the correct scaled frequency of the space station solar arrays that the MODE STA was modeled after. They also provide the mass required to decrease the bounce mode of the suspension system to 1 Hz.

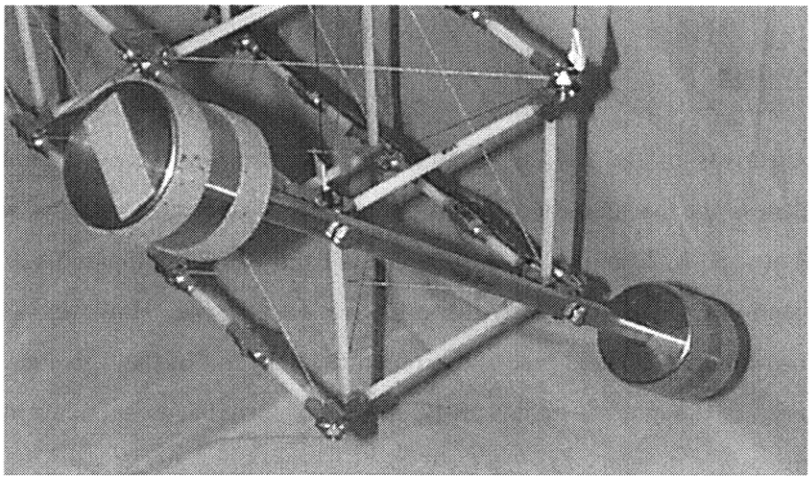

Figure 2.13 Rigid appendage

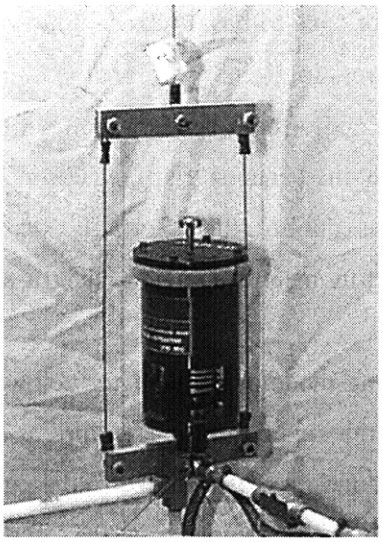

Figure 2.14 Electro-magnetic shaker

2.1.2 Actuators

In order to provide the harmonic excitation for the stepped-sine sweeps, an actuator must be used. In the MODE and MODE-Reflight experiments, the proof-mass actuator shown in Figure 2.14 was used to excite the STA. This electro-magnetic shaker uses a 1.0 lb throw mass and spring. Its total weight is approximately 1.8 lbs (0.82 kg), and its spring-mass resonance occurs at 2.3 Hz. The actuator was designed so that the resonance is heavily damped; the transfer function from the input voltage to the applied load is essentially constant from 3 to 50 Hz. Unfortunately, this electro-magnetic proof-mass shaker exhibits stiction at excitation levels below 0.04 lbf (0.18 N), the lowest level attained in the original MODE tests. This stiction prevented use of this shaker at the levels required for most of the microdynamic tests. It was only used as the actuator for the three highest-amplitude tests on the truss bending mode, where load levels greater than 0.04 lbf were required.

For the rest of the microdynamic tests, a second actuator was designed, which satisfied the following requirements: no stiction at low excitation, and dynamic range wide enough to excite the truss at levels ranging from 0.05 lbf down to $1x10^{-6}$ lbf. Previous microdynamic experiments successfully employed piezoceramic bending actuators [21]. This concept was chosen for the current tests because of its simplicity, effectiveness and relatively low cost. The actuator is shown in Figure 2.15. Its main components are two Active Control Experts, Inc. Model QP40W piezo

benders. These benders consist of back-to-back piezoceramic wafers, wired so that voltage across their terminals causes the top layers to extend while the bottom layers contract, inducing bending in the motors. By clamping one end of both benders between two aluminum plates, and exciting them with an AC voltage source, the benders "flap" synchronously, like the wings of a butterfly. For this reason, the actuator is dubbed the "Butterfly shaker". Because two symmetrically opposed benders are used, no net moment is applied to the truss during actuation.

In order to lower the first bending mode of the actuator below the fundamental flexible mode of the truss, and to increase the force applied to the structure as the benders flap, the length of the flapping "wings" was extended, and mass was added to the outboard tips. Thin aluminum plates were bonded to the ends of each bender, lengthening the "wings" to 6.2 inches (15.75 cm) from clamped end to free end. Equal masses of 0.056 lb (25.4 g), in the form of stainless steel nuts, were attached with wax to each tip. The entire Butterfly shaker assembly, including the load cell and mating parts, weighs 0.73 lb (331 g). The dynamics of the shaker are shown in Figure 2.16; the transfer function from the input voltage to the applied load is plotted for the shaker clamped to a fixed table surface. The applied load was measured by the load cell placed in the load path (the load cell is described in subsection 2.1.3). It is important to note that replacing the electro-magnetic shaker with this actuator had a significant effect on the truss dynamics, because their mass and inertia properties are quite different.

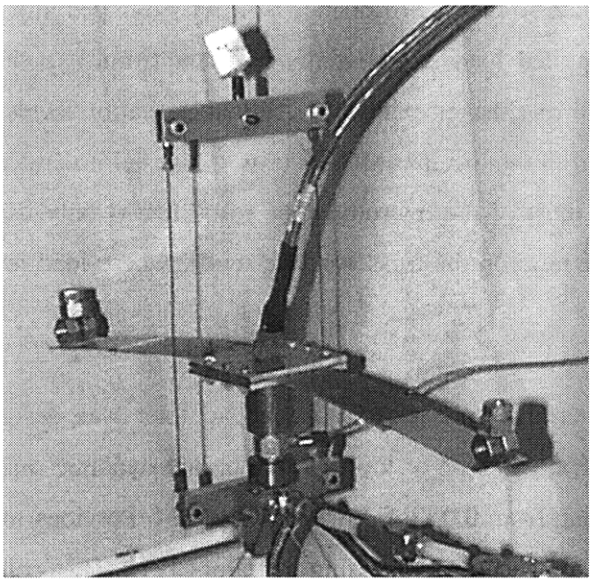

Figure 2.15 Butterfly shaker

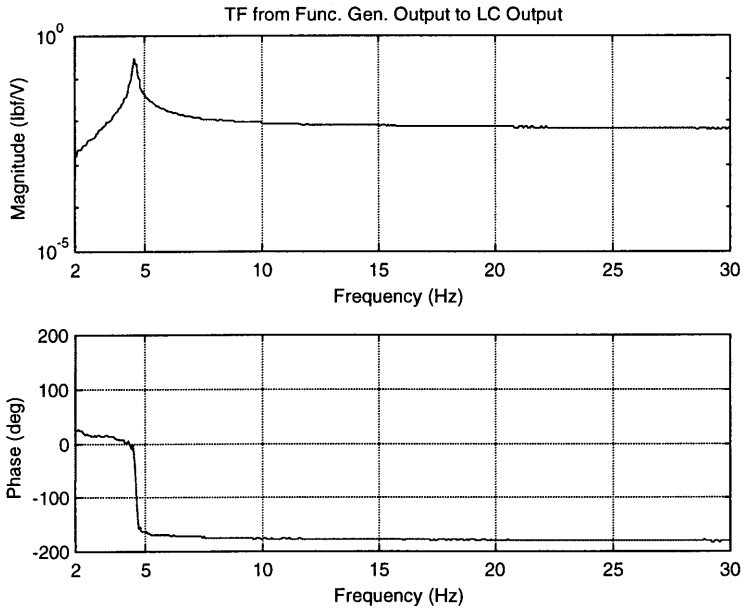

Figure 2.16 Dynamics of Butterfly shaker

The operating voltage range of the QP40W is given as 0 to ±200 V. In order to achieve the higher levels of load required in this experiment, a Crown Model DC-300A Series II power amplifier was used to amplify the voltage input to the Butterfly shaker.

2.1.3 Sensors

Just as critical as the selection of an actuator appropriate for microdynamic experiments is the selection of the sensors used to measure the structural response. In order to measure structural motion down to microdynamic levels, sensors must exhibit extremely good signal-to-noise characteristics and resolution. For his nanostrain-level experiments, Ting considered various types of sensors [21]. The list included laser interferometers, piezoelectric accelerometers, resistive strain gauges, piezopolymer film strain gauges and piezoceramic strain gauges, among others. The minimum resolution requirement for the sensors was that they had to provide measurements from which strains could be inferred down to 1 nanostrain. The piezoceramic strain gauges were chosen because they satisfied the resolution requirement, without being too bulky or prohibitively expensive to acquire. In fact, these sensors have been shown to have linear response down to a strain level of 10 picostrain [33]. For the same reasons mentioned by Ting,

piezoceramic gauges were selected as the main sensors for this microdynamic characterization experiment.

Piezoelectric materials produce electric field in response to physical strain [34]. A piezoceramic plate poled across its thickness will generate a voltage output proportional to the averaged strain at the surface of the structure it is bonded to. Since the truss members are assumed to strain uniformly in their axial direction only, the surface strain measurement can be taken at any location around the circumference of the member, anywhere along the length of the strut. Any transverse bending of the members due to warping or imperfections is assumed negligible, compared to the axial deflections.

The piezoceramic strain gauges used in these experiments were procured from Piezo Systems, Inc. They consist of flat pieces of lead zirconate titanate (PZT-5A) measuring 1.00"L x 0.08"W x 0.01"T. Since having a leadwire attached to the bottom electrode would interfere with the bonding of the gauge to the truss member, the gauges are custom fabricated to avoid the problem. A very thin stripe is etched off across the width of the top electrode, producing two separate top electrodes, each one covering half the length of the gauge. The piezoceramic is then poled across its thickness (in the "3" direction, by traditional piezo nomenclature) in the upwards direction over one half of its length, and downwards over the other half. The gauge can therefore be essentially viewed as two gauges of length 0.5", poled in opposite directions and acting in series. The two leads can then be attached to both top electrodes (Figure 2.17).

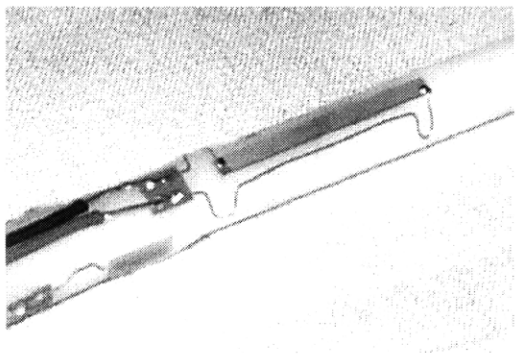

Figure 2.17 Instrumented strut

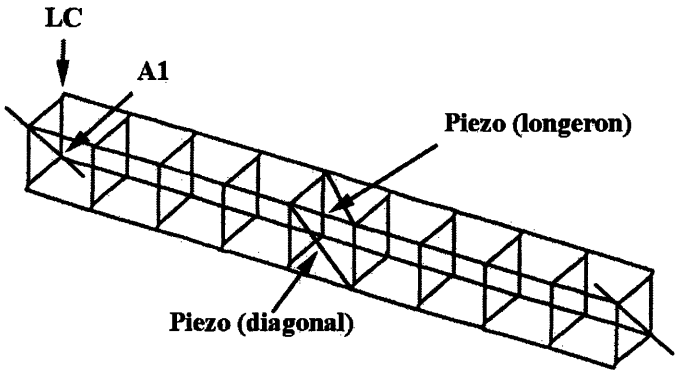

Figure 2.18 Sensor locations

A thin and stiff bond between the gauge and the truss member was desired to minimize losses in sensitivity induced by shear lag [35]. Due to the brittleness of the piezoceramic material, the bonding process was carefully undertaken. Adding to the difficulty was the fact that the flat gauges were bonded to truss members, which are cylindrical. Rather than machine a flat surface into the Lexan strut, which would have affected the local stiffness properties of the member, the gauges were bonded directly to the surface, using five-minute epoxy. Epoxy was selected over cyanoacrylate, despite its lower bond stiffness, because the very fluid cyanoacrylate could not bond to the cylindrical surface across the width of the gauge: the bond thickness had to increase from the center out to the edges. In order to minimize the average bond layer thickness, which increases as the ratio between gauge width and truss member radius increases, the gauges were designed to be narrow; their width of 0.08 inch (2 mm) is one quarter the diameter of the Lexan struts they are bonded to.

Two of the struts in the erectable center bay of the truss were chosen as locations for the piezo sensors, because they offer high observability of the first two global modes of the structure (Figure 2.2). The torsion mode puts the diagonal under significant strain, whereas the bending mode strains the instrumented longeron. The sensor locations are shown in Figure 2.18.

The main disadvantage in using piezoceramic strain gauges is that they must be calibrated against known strain measurements. Two resistive strain gauges wired in a 2-arm-active bridge were bonded to the truss member, each one at 90° around the strut circumference from the piezo gauge (Figure 2.17). The gauges used were Measurements Group EK-13-125BZ-10C type. The bridge output was amplified using a Measurements Group Model 2120A strain gauge

conditioner/amplifier. The bridge excitation level was limited to 4 Volts DC, to avoid overheating the gauges, as they were bonded to Lexan, a material with poor heat conduction properties. Calibration was performed for each mode of the structure tested, for strains between 0.1 με and 100 με. The voltage-to-strain relationship could then be extrapolated down to the nanostrain level. With the frequency of the input signal to the actuator held fixed, the structure was driven at different strain levels. The output of the piezo gauge at each strain level was plotted against the actual strain from the resistive half-bridge. Using a least-squares algorithm, a straight line was then fit to the data. The calibration process was repeated at least a half-dozen times for each mode tested, and the average slope of the best-fit lines was taken as the piezo gauge sensitivity. A typical value for the sensitivity is 1.5×10^5 V/ε (obtained for the torsion mode).

The MODE STA is also instrumented with eleven Endevco Model 7265A-HS accelerometers. These sensors were used during the original MODE and MODE-Reflight ground tests. For the purposes of the current experiment, only one of these piezoresistive accelerometers was used, in order to gauge traceability of the strain results to the previously-obtained acceleration transfer functions (see subsection 2.4.2). The location and line of action of the accelerometer used (MODE accelerometer A1) is shown in Figure 2.18.

The only other sensors used in this experiment were the load cells, which were placed in the load path between the actuators and the structure. The load cell built into the electro-magnetic shaker is an Entran Model ELF-82-TC1000I-2. A Measurements Group Model 2120A conditioner was again used to amplify the output of this sensor. The load cell used for the majority of the tests, in conjunction with the butterfly shaker, was a PCB Model 208B (which can be seen in Figure 2.15). Its output was amplified with a PCB Model 482A charge amplifier.

2.1.4 Other Instrumentation

The success of the microdynamic modal parameter characterization experiments was greatly dependent on the ability to achieve sufficient frequency resolution for the stepped-sine tests, as well as the ability to filter through the noise to extract the minute strain response signal. These two requirements were met with the help of two instruments: the Philips PM5191 programmable synthesizer/function generator and the EG&G Princeton Applied Research Corporation Model 5210 lock-in amplifier.

The PM5191 supplies up to 30 V (peak-to-peak), with a frequency resolution limit of 0.0001 Hz. Frequency steps as small as 0.0005 Hz were used for the stepped-sine sweeps on the structure. Using too large a frequency step would result in inaccurate estimates for the modal parameters.

The Model 5210 lock-in amplifier takes in the excitation signal from the function generator as a reference signal. The signal to be measured (output from the piezo strain gauge or load cell) is amplified and applied to a phase-sensitive detector operating at the frequency of the reference signal. In essence, the detector extracts the content of the measurement signal at the reference frequency. The detector output is a DC signal representing the magnitude of the signal of interest, as well as AC components due to noise and interference [36]. These AC components are reduced with the help of built-in low-pass filters with adjustable time constants. Selection of the time constant setting involves a trade between filter bandwidth (i.e. signal-to-noise ratio) and the response time. For all tests, the time constant was set to 3 seconds, resulting in a cutoff frequency of 0.33 Hz. In general, the lock-in amplifier acts like a very sharp bandpass filter (-40 dB or better at ±5 Hz), centered at the reference frequency. The RMS magnitude of the signal of interest and its phase with respect to the reference signal are read from the instrument.

It should also be noted that the Model 5210 only allows for a single input channel. This meant that the strain measurements from the piezo gauges and the load measurements from the load cell could not be taken simultaneously (see section 2.2, below). The input impedance of the lock-in amplifier is sufficiently high, such that the piezo gauge output required no charge amplification.

2.2 Test Procedure

In order to microdynamically characterize the MODE STA truss in the frequency domain, the stepped-sine sweep technique was employed. This technique is particularly suited for experiments like this one, in which the measurements have a significant time constant, due to the action of the lock-in amplifier. In this section, the test procedure is outlined, step by step.

Performing repeated stepped-sine sweeps is a tedious and time-consuming task. For obvious reasons, it was desirable to automate as much of the experiment as possible. Both the function generator and the lock-in amplifier are designed for remote operation via a personal computer

control platform. Experiment control software was written to perform all the data acquisition operations described in this section. The block diagram in Figure 2.19 summarizes the flow of commands and information through the experiment setup.

The microdynamic modal parameter characterization experiment procedure can be broken up into three main sub-tasks: course sweep for mode localization, stepped-sine sweeps about the mode of interest, and finally, data reduction. Each of these sub-tasks is described in detail below.

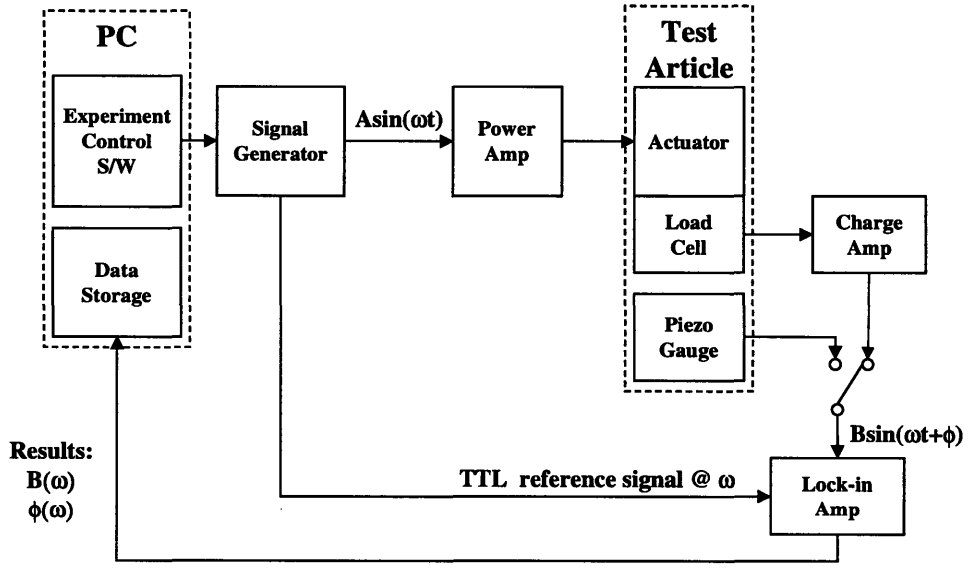

Figure 2.19 Flow of commands and information through the experiment setup

Course sweep for mode localization

For each mode and strain amplitude tested, a quick sweep of the piezoceramic gauge output was performed over a broad enough bandwidth to easily cover the modal peak & the half-power bandwidth, with the goal of more precisely locating the frequency of the mode. At this stage, the frequency resolution was not required to be particularly fine, since the results of this sweep were not used to obtain an estimate for the modal parameters. Typically, frequency steps of 0.005 Hz were adequate. Performing this course sweep was important because the nonlinear nature of the truss is manifested as a shifting of the modal frequencies from one strain amplitude to the next. Frequency shifts of as much as 0.3% were observed between tested amplitudes.

Stepped-sine sweeps about mode of interest

For each of the torsion and bending modes of the truss, sets of stepped-sine sweeps were performed at two different amplitude levels per decade of strain, down to nanostrain level (e.g. around 7 $\mu\varepsilon$, 2 $\mu\varepsilon$, 0.7 $\mu\varepsilon$, 0.2 $\mu\varepsilon$, etc...). The frequency increments were chosen small enough to accurately represent the peak in the frequency response function. Steps of 5×10^{-4} Hz were used for tests on the torsion mode, while larger steps of 4×10^{-3} Hz were allowed for the more highly damped bending mode.

Each set of sweeps was composed of 6 sweeps, alternating forward and backward, at a given excitation voltage amplitude. Each frequency change was followed by a twenty second wait, to allow the transients in the lock-in amplifier output to die out. Twenty seconds corresponds to just over six time constants, which was time enough for equilibrium to be reached. After the wait time, the magnitude of the sensor output and phase with respect to the reference signal (excitation voltage from the function generator) were read and stored on the controller PC.

For fixed excitation voltage amplitude, the actual load applied can vary somewhat over the bandwidth of the sweep, due to the Butterfly actuator dynamics. It turned out that the actuator dynamics were only significant for the tests at the first torsion mode, around 7.7 Hz. For the torsion mode tests, it was therefore necessary to perform sweeps with the load cell as the sensor. Since the lock-in amplifier accepts only a single input, each set of sweeps was first performed with the piezoceramic sensor connected, and was then repeated with the load cell. Of course, it would have been preferable to take both the strain and load measurements simultaneously;

nonetheless, the load cell output was reasonably repeatable from sweep to sweep, indicating that no appreciable error was introduced by taking the strain and load measurements in sequence. For the tests on the bending mode of the truss, the load cell measurements were essentially constant over the frequency range of the sweep, for both actuators used. Therefore, the piezo gauge output data was used directly to compute the modal parameters for the bending mode.

Data reduction

Once the magnitude and phase data was acquired for a set of sweeps, the next step was to use the frequency response functions to obtain estimates for the modal parameters, f_n and ζ_n. As mentioned above, the data for the torsion mode consisted of both piezo strain gauge and load cell measurements, while the bending mode data consisted only of the piezo strain gauge output. A description of the steps involved in reducing the data follows.

First, the frequency response data sets were converted from voltages to appropriate units (strain, lbf). For the torsion data, the six load cell sweeps were then averaged to obtain a single, mean load spectrum. Dividing each of the six piezo gauge output spectra by the mean load spectrum (and subtracting the respective phase angles) yielded the desired transfer functions (in strain/lbf). The modal parameters f_n and ζ_n could then be obtained from these six transfer functions.

For the three lowest strain amplitudes at which the torsion mode was tested (i.e. 2.4 nε, 7.5 nε and 20.9 nε), the load cell signal was swamped by the noise floor. Consequently, using the three corresponding transfer functions to get the modal parameters led to erroneous estimates of f_n and ζ_n. In order to get accurate results for the torsion mode, covering the complete range of interest from 0.1 mε down to 1 nε, the parameters were also estimated directly from the piezo gauge output. By comparing the parameters obtained from the transfer functions and the strain output alone, for all amplitudes greater than 20.9 nε, it was possible to gauge the error introduced by neglecting the dynamics of the actuator at the three lowest strain amplitudes.

Various methods can be used to obtain the natural frequency and damping ratio from the frequency response function of a single mode [37]. The quantitative measure of damping used in this research is the modal critical damping ratio ζ_n, defined as half the fractional decrease in energy of a system in one cycle [38]:

$$\zeta_n = \frac{\Delta U}{4\pi U}$$

The simplest method is the *peak-amplitude/half-power bandwidth approach.* The frequency of maximum response is taken as the natural frequency of the mode. The damping ratio is given by the following formula:

$$\zeta_n = \frac{\Delta f}{2 f_n}$$

where Δf is the difference between the frequencies of the two half-power points, and f_n is the natural frequency in Hz. This method can be used to obtain modal parameter estimates from sample microdynamic data, plotted in Figure 2.20. This transfer function data corresponds to a single sweep performed on the torsion mode, resulting in a peak strain amplitude of 7.4×10^{-7} ε. The values of f_n and ζ_n are found to be 7.745 Hz and 0.089%, respectively.

A second method, which uses more of the available information than the first, is the *single-degree-of-freedom resonance fit.* This approach uses a nonlinear least-squares algorithm to fit an analytical SDOF resonance to the frequency response function (FRF) magnitude data:

$$|FRF| = \frac{A}{\left\{\left[1-\left(\frac{f}{f_n}\right)^2\right]^2 + \left[2\zeta_n\left(\frac{f}{f_n}\right)\right]^2\right\}^{1/2}}$$

where A, f_n and ζ_n are the parameters to be solved for, in a least-squares sense. To illustrate this method, a fit to the sample microdynamic data is shown in Figure 2.20. Clearly, the experimental data is well represented by the SDOF model. Using this method, estimates of 7.746 Hz and 0.087% are computed for f_n and ζ_n, respectively.

A third procedure used to estimate the modal parameters is the *circle-fit method.* A complete explanation of the circle fit method is given by Ewins [37]. The magnitude and phase of the FRF

data can be plotted in the complex plane, roughly mapping out a modal circle, which is displaced from the origin by an amount determined by the contribution of all other modes. Using a least-squares algorithm, the circle which best fits the data is found. Figure 2.21 shows the polar plot of the same sample torsion data used to illustrate the SDOF resonance fit, overplotted with the best-fit circle. As might be expected, the data is easily fit to a modal circle.

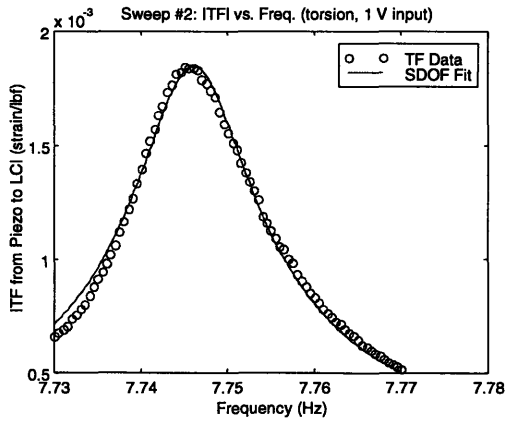

Figure 2.20 Torsion mode TF data with SDOF resonance fit

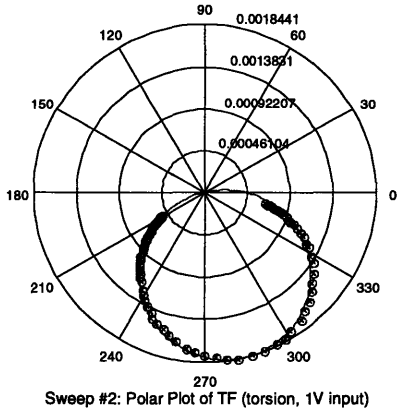

Figure 2.21 Polar plot of torsion mode TF data with circle fit

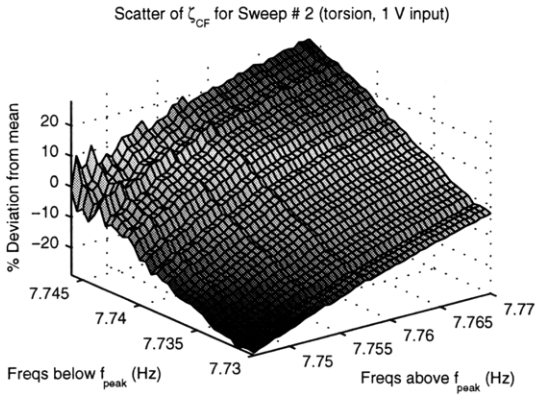

Figure 2.22 Scatter plot of damping estimates from circle fit

In theory, the natural frequency of the mode is determined by locating the point on the circle where the rate of radial sweep is a maximum (i.e. the point of maximum dθ/df, where θ is the angle subtended by a radial line of the circle, and f is the frequency corresponding to the point on the circle intersected by the radial line). In practice, however, the slightest deviation from the theoretical behavior results in significant error in the estimate for f_n. For the microdynamic MODE STA data, the rate of radial sweep had many local maxima, which were often larger than the rate corresponding to the expected natural frequency, resulting in erroneous natural frequency estimates. This is illustrated in Figure 2.21. Since equal frequency steps were used, the separation distance between adjacent data points along the modal circle gives a measure of the rate of radial sweep. The largest Δθ occurs at a phase angle of approximately 307 degrees, as evidenced by a gap in the polar plot data. This corresponds to a natural frequency of 7.743 Hz, which is lower than the frequency of the peak in Figure 2.20.

Next, damping ratio estimates are obtained from the polar plot by taking each pair of FRF data points comprised of one point with frequency below f_n and one point with frequency above f_n, and then using the formula:

$$\zeta = \frac{\left(f_{hi}^2 - f_{lo}^2\right)}{\left\{2 f_n \left[f_{hi} \tan\left(\theta_{hi}/2\right) + f_{lo} \tan\left(\theta_{lo}/2\right)\right]\right\}}$$

where f_n is the natural frequency, f_{hi} is the chosen frequency above f_n, f_{lo} is the chosen frequency below f_n, θ_{hi} is the radial angle corresponding to f_{hi}, and θ_{lo} is the radial angle corresponding to f_{lo}.

This yields as many damping estimates as there are (f_{lo}, f_{hi}) combinations. Ideally, they should all be identical; in reality, the mean value is taken as the actual damping ratio of the mode. For the sample data, the circle fit technique results in a damping ratio of 0.09%. By looking at the deviation from the mean for all the estimates, an indication of the quality of the circle fit analysis is obtained. The matrix of damping estimates can be plotted as a function of f_{lo} and f_{hi}. Figure 2.22 presents the scatter in damping for the sample microdynamic data. The resulting surface is almost a smooth plane, with damping values lying within ±30% of the mean ζ_n. Evidently there is a systematic variation in the damping estimates, which is likely due to some degree of nonlinearity in the modal data [37].

In order to obtain the modal parameter estimates for the microdynamic characterization experiment, combinations of the three methods were used for the different modes and amplitudes tested. As it turned out, the circle fit method provided reasonable estimates for ζ_n for all of the data sets taken. Therefore, this method was used exclusively to obtain the damping estimates. However, as demonstrated above, the natural frequency estimates obtained from the circle fit were inaccurate, due to the high sensitivity of the radial sweep rate to unavoidable deviations from theoretical behavior. For this reason, the circle fit estimate for f_n was never used. Rather, the natural frequency estimates were obtained using one of the peak-amplitude or SDOF resonance fit methods, depending on the quality of the data. For data taken at the higher strain levels (i.e. above 1 με for the torsion mode, and above 0.1 με for the bending mode), there is very little noise contamination (i.e. smooth FRF curves). Taking the frequency of the peak in these FRFs was a simple way to obtain f_n. Moreover, the FRFs tend to exhibit more nonlinear behavior at these higher levels, making the SDOF resonance fit procedure inaccurate. As the strain level drops, the FRF data becomes noisier, making it difficult to accurately identify the peak of the curve. In general, the SDOF resonance fits well to the lower amplitude data, so this method was used to obtain the estimates for f_n, for strain amplitudes below 1 με for the torsion mode and 0.1 με for the bending mode.

2.3 Precision and Accuracy of Measurements

In any experiment, there are limitations on the precision and accuracy of measured data. For microdynamic experiments, it is particularly important to identify and quantify these limitations, due to the high sensitivity of these types of tests to the disturbance environment. In order to

evaluate the level of precision attained in this experiment, it was necessary to look at the scatter in the results, both within each set of six sweeps and between different sets at the same nominal excitation level. The amount of scatter in the results from one set of six sweeps was determined by comparing the maximum, minimum and mean values of peak strain ε_{peak}, natural frequency f_n and damping ratio ζ_n. As another indication of the scatter, the standard deviation of each of these values was computed. A measure of precision was also obtained by comparing results from the repeatability tests (different sets of sweeps at the same excitation level, performed on different days – see section 2.4).

For modal parameter characterization in the microdynamics regime, several potential sources of error can be identified: aerodynamic effects, transmission of mechanical vibration through the suspension system and wiring, acoustic effects, electrical noise, actuator and sensor dynamics, and finally, temperature and humidity effects. Error can also be associated with the data reduction procedure, because it relies heavily on accurate least-square fits to the data. Each of these error sources is addressed below; steps taken to mitigate these errors are described, and quantitative measures of their effects on accuracy and precision are presented whenever possible.

Aerodynamic effects

Since the tests were performed in the laboratory environment, the effects of the aerodynamics on the modal parameters must be considered. It has been shown that testing in the presence of air can yield lower natural frequencies than testing in near-vacuum, a small effect attributed to the effective mass of air. Modal damping increases because the air acts as a viscous fluid which dissipates energy [39]. This aerodynamic damping adds to the structural and material damping in the truss. Obviously, this loss mechanism is not relevant to space structures, so the contribution of air damping can be considered a source of inaccuracy.

Many different models exist for aerodynamic damping. In a model postulated by Blevins [40], the viscous damping is linearly related to vibration amplitude, for high Reynolds number. For low Reynolds number, viscous damping is essentially independent of the vibration amplitude. In another simple model, presented by Batchelor [41], a cylinder oscillating in a fluid experiences damping due to the viscous friction in its boundary layer. The damping is independent of the amplitude of vibration, based on this second model.

Because of the low mass ratio associated with the truss structure, the mass of air displaced is negligible, thus the presence of air is assumed to have little effect on the natural frequencies of the MODE STA. The complex geometry of the truss structure prevents correlation with a simple aerodynamic damping model; however, experience from past microdynamic experiments performed on tube-shaped material specimens [21] showed that amplitude-independent air damping never accounted for more than 20% of the total damping ratio, in the worst case. In general, the contribution to the damping ratio due to air was found to be at least an order of magnitude lower than the total damping ratio.

Transmission of mechanical vibration

Another important source of error is the transmission of vibration disturbances through the suspension system and the electric wires leading from the various sensors. It is impossible to completely isolate the structure from the laboratory wall and ceiling vibrations. If the suspension system is modeled as a simple mass-spring-damper, the transmissibility transfer function from base displacement (vibration of lab ceiling) to truss displacement (vibration felt on truss) is given by [42]:

$$\left|H\left(\frac{f}{f_b}\right)\right| = \sqrt{\frac{1+\left(2\zeta\frac{f}{f_b}\right)^2}{\left(1-\left(\frac{f}{f_b}\right)^2\right)^2+\left(2\zeta\frac{f}{f_b}\right)^2}}$$

where f_b is the fundamental bounce frequency of the suspension system, and ζ is the material damping in the stainless steel springs and wires. Values of 1 Hz and 0.05% are used as estimates for f_b and ζ, respectively. The resulting transmissibility transfer function is plotted in Figure 2.23.

Since the lock-in amplifier filters out any signal which is not at the reference frequency, the only disturbances which are of concern are those with content near the frequency of the mode being tested. Figure 2.23 shows that any disturbance around 7.7 Hz (torsion mode) is attenuated by almost 40 dB after passing through the suspension system. The isolation is even more effective near the bending mode (at 20.7 Hz), attenuating by more than 50 dB. Based on these isolation

characteristics, the levels of vibration transmitted through the suspension wires would be negligible for traditional modal parameter characterization tests; for microdynamic-level tests, however, these vibrations are not insignificant. The noise floor encountered in the piezo gauge output, after filtering by the lock-in amplifier, was on the order of 1 nε RMS. Transmission of mechanical vibration through the suspension is identified as a likely contributor to the baseline noise level in the microdynamic tests.

The suspension system also presents a path for energy to leave the system, which results in inaccuracy in the damping measurement. An estimate of this effect's contribution to the total damping ratio can be obtained by computing the ratio of energy lost in the springs during one vibration cycle to the total strain energy of the truss. The damping due to energy lost through the suspension is estimated to be at least an order of magnitude lower than the total measured damping.

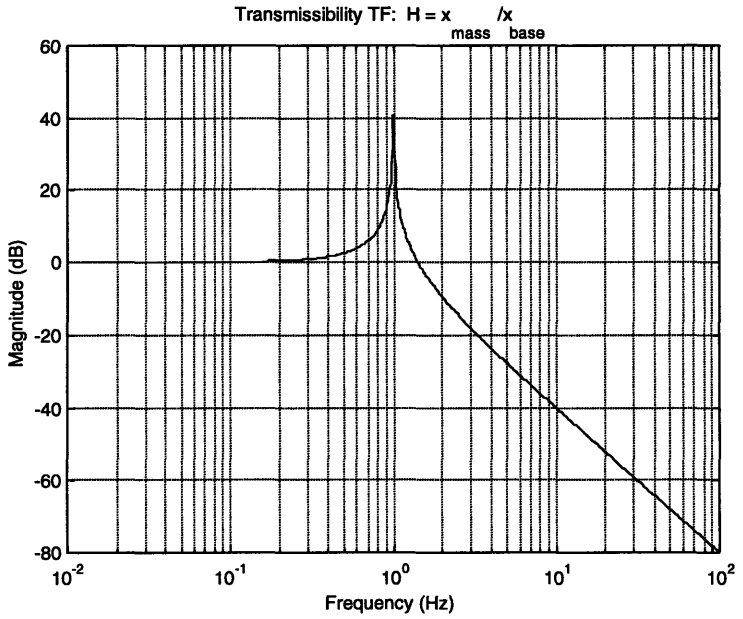

Figure 2.23 Transmissibility TF from ceiling to truss

Aside from the suspension system, the only other physical connection between the truss and the laboratory environment is provided by the wires running to the sensors and actuator. Much care was taken to minimize the effects of wires on the truss dynamics; this is of particular importance

given the small levels of vibration observed in this experiment. All the wires running to the butterfly shaker and from the piezo gauge sensors were secured away from the structure, slackened sufficiently so as to minimize their boundary condition effect at the points of attachment to the truss. The wires feeding the accelerometers and load cell on the MODE STA are bundled together to form a single umbilical cable, which runs off the baseline truss near its center and terminates in a heavy plastic connector. In order to take up the weight of this connector, an elastic cord was used to suspend it from the laboratory ceiling and offset it from the truss, as shown in Figure 2.24. Despite all these careful measures, variations in the modal parameters obtained between tests at the same excitation level may have been partially due to slight changes in boundary condition.

Another possible reason for day-to-day variations in modal parameters is small changes in the stress distribution as the truss settles on its suspension between tests. Under the action of gravity, the structure tends to sag over time, slightly increasing the compressive preload in the top members of the structure, and decreasing the preload in the bottom members. These small changes in the stress condition lead to changes in the loading of the joints, thus affecting the nonlinear frictional mechanisms.

Acoustic effects

Vibration can also be transmitted to the truss via acoustic excitation. The acoustic waves travel through the air, and excite modes of the structure with frequencies equal to the acoustic frequencies of the disturbance. However, for frequencies where the natural wave number of a beam-like structure is larger than the natural acoustic wave number (i.e. low frequencies), the structure does not respond well to the acoustic excitation [43]. Since the modes of interest in this experiment are at very low frequency compared to the acoustic frequencies, the effects of acoustic excitation on the MODE STA are considered negligible.

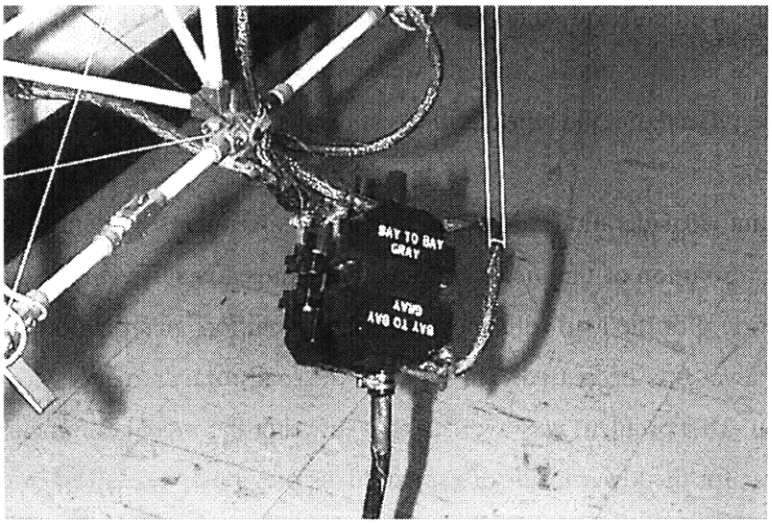

Figure 2.24 Elastic cord to offset weight of umbilical connector

Electrical noise

Given the low levels of signal involved in microdynamic experimentation, all signal-carrying wires must be properly insulated, and ground loops must be avoided. As shown in Figure 2.17, short lengths of thin, insulated strain gauge wire led from the electrodes of the piezo and resistive strain gauges to a terminal tab (also bonded to the strut). The gauges and leads were covered with an insulating layer of silicon rubber sealant, in order to reduce the effects of cross-talk between the closely-spaced sensors. Insulated wires led from the terminal tabs to a terminal strip located near the truss, and from the terminal strip to the respective amplifiers. To minimize signal loss along the transmission path, all wire lengths were kept as short as possible.

Despite the efforts made to minimize electrical noise, it is considered the other likely contributor to the noise floor in the output from the piezo gauge, along with transmission of mechanical vibration to the structure.

Actuator and sensor dynamics

Another source of error in the experiment is the imperfect transmission of sinusoidal voltage input to sinusoidal load output from the Butterfly shaker. Design imperfections caused the output of the shaker to have minor frequency content leakage away from the frequency of the sinusoidal input. This effect was only noticeable in the higher-amplitude tests at the bending mode of the

truss. Because the load cell and strain sensor outputs were filtered through the lock-in amplifier, the consequences of the signal leakage were alleviated. Nonetheless, imperfect sinusoidal actuation may be reflected in the repeatability test results for the bending mode.

A very important consideration for microdynamic experiments is sensor resolution. In this experiment, the resolution of the piezoceramic strain gauges is sufficiently small that it does not present a limitation. For the load cells, however, the resolution specification was exceeded as the truss excitation level was decreased. The noise in the load measurements was therefore due to a sensor limitation. This problem was avoided by extracting the modal parameters from the sensor output data alone, for the lower levels of excitation, as previously explained in section 2.2.

Temperature and humidity effects

Environmental variables such as temperature and humidity also affect the modal parameter characterization. For instance, a change in temperature results in a change in the internal stress level (preload) of the statically indeterminate truss, and varying humidity can affect the behavior of the friction mechanisms in the deployable joints. Because these variables were not strictly controlled during these experiments, fluctuations in these variables could have occurred in the short term, i.e. over the course of a single set of sweeps, and in the long term, i.e. from one day of testing to the next. The laboratory temperature was found to fluctuate little over each set of sweeps (by no more than ±0.5°F). No measurements of humidity level were made. The effect on the data within each set of sweeps was assumed to be negligible. Over the entire duration of the experiment, the temperature in the lab varied between 73°F and 78°F. Any change in temperature and humidity environment between different days of testing would be reflected in the results from the repeatability tests.

Error due to data reduction

An essential step in obtaining the modal damping ratio from the sweep data is the use of least-square fitting. Significant error in the estimate can be introduced by a poor fit. An example of a poor circle fit to the microdynamic data is shown in Figure 2.25. Performance of the fitting routines degrades as the level of noise in the data increases. Such errors lead to both imprecision and inaccuracy in the modal parameter estimates. The worst case was encountered for the lowest

strain amplitude tests on the bending mode of the truss (2.8 nε amplitude); the scatter in the ζ_n data for this set of sweeps, expressed in terms of the standard deviation, was found to be 4.5×10^{-4}, or 21% of the computed mean ζ_n of 2.1×10^{-3}.

As previously explained in section 2.2, the natural frequency estimates were obtained by finding the peak amplitude frequency for the FRF, for tests above 1 με for the torsion mode, and above 0.1 με for the bending mode. At these amplitude levels, the FRF curves are not contaminated with noise. Even so, the true value of f_n likely does not coincide with the frequency of the peak data point, but rather lies somewhere between this point and one of its neighboring points. This implies a bound on the precision equal to half the frequency discretization, i.e. the f_n estimate is within $\pm 2.5 \times 10^{-4}$ Hz of the actual value for the torsion mode, or within $\pm 2 \times 10^{-3}$ Hz for bending.

For the data taken below 1 με and 0.1 με, for the torsion and bending modes, respectively, the SDOF resonance fits provided the estimates for modal frequency. The quality of these fits directly affects the accuracy of f_n. Any nonlinearity in the FRF data, or contributions from other modes of the structure (unaccounted-for in the SDOF resonance equation), would result in some degree of inaccuracy in the f_n values. However, the results for these tests show the SDOF resonance approximation to be valid, so errors of this nature are assumed negligible. The precision and accuracy of the modal frequency estimates are also affected by noise in the data. The effect of noise was most significant for the lowest-level tests (2.8 nε amplitude) on the bending mode of the truss: the standard deviation of the f_n estimates was found to be 0.0075 Hz, corresponding to roughly .036% of the 20.727 Hz mean frequency.

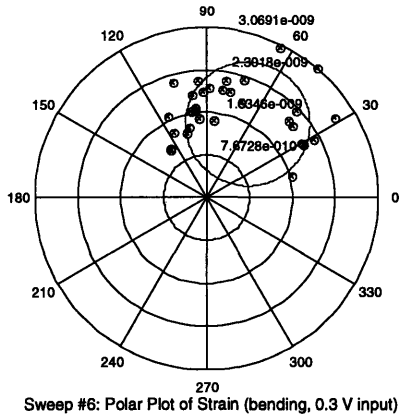

Figure 2.25 Circle fit to noisy data

Summary

In this section, the various possible sources of error in the microdynamic modal parameter characterization experiment have been addressed. The following list summarizes the effects of each on the precision and accuracy of the measurements:

- Inaccuracies in the f_n estimates due to aerodynamic effects are assumed to be negligible. Previous microdynamic experiments on material specimens have shown the contribution of air to the damping ratio to be at least an order of magnitude lower than the total damping ratio, in general.
- Transmission of mechanical vibration through the suspension and wiring is identified as a likely contributor to the baseline noise level of 1 nε RMS in the microdynamic tests. The damping due to energy lost through the suspension is estimated to be at least an order of magnitude lower than the total measured damping.
- Repeatability of the results between tests at the same excitation level may have been affected by slight changes in dynamic boundary conditions imposed by the electrical wires running to the sensors and actuator.
- Day-to-day variations in modal parameters may have been due to small changes in the stress distribution and joint loading as the truss settled on its suspension between tests.
- Acoustic effects are considered negligible.
- Electrical noise is considered the other likely contributor to the noise floor in the output from the piezo gauge, along with transmission of mechanical vibration to the structure.
- Imperfect sinusoidal actuation may be reflected in the bending mode repeatability results.
- The noise in the low-amplitude load measurements was due to the resolution limitation of the load cell.
- The effect of temperature and humidity variations over the course of each set of sweeps was assumed to be negligible. Any change in temperature and humidity environment between different days of testing would be reflected in the results from the repeatability tests.
- Noise in the data leads to inaccuracy and imprecision in the modal parameter estimates, due to poor fits at the data reduction stage. In the worst case tests, scatter in the ζ_n data from a single set of six sweeps was evaluated to be 21% standard deviation from the mean, while scatter in the f_n data was found to be .036% standard deviation from the mean.

2.4 Experimental Results

In this section, the results from the microdynamic modal parameter characterization experiment are presented and discussed. These results are then compared with those from two relevant past experiments: Ting's microdynamic tests on an erectable truss structure, and the MODE and MODE-Reflight dynamic characterizations of the same deployable truss investigated here.

2.4.1 Discussion of Results

For each of the two modes of interest in the experiment, frequency response functions were measured at various strain amplitudes between 0.1 mε and 1 nε. A considerable amount of data was collected from the stepped-sine sweep tests. The results from all tests are compiled in Tables A1 through A3, in Appendix A. In addition, the appendix contains FRF plots from each set of six sweeps, corresponding to each mode and strain amplitude tested. In this subsection, data and modal parameter estimates from the stepped-sine sweeps are presented and discussed. The torsion mode sweeps are addressed first, followed by the bending mode sweeps. Finally, the results from repeatability tests performed for both modes are given. For the sake of conciseness, data from only a few representative sweeps are presented in this subsection, for both modes of interest.

Sweep results – torsion

The results from the microdynamic stepped-sine sweeps of the first torsion mode will now be presented. In order to motivate the discussion of the results, plots corresponding to the analysis of a representative subset of the data will be shown here. The first set of representative plots corresponds to tests performed at the higher end of the microdynamic range, at a peak strain around 1.6×10^{-5} ε (Figures 2.26 through 2.34). Based on these typical plots, salient comments on the "high amplitude" microdynamic-level behavior of the structure will be made. Next, the relevant characteristics of the "low amplitude" microdynamic-level behavior will be highlighted, as illustrated by representative data in Figures 2.35 to 2.40 (for peak strain around 7.5×10^{-9} ε). Finally, the modal parameter estimates obtained from all the sweeps of the torsion mode will be plotted versus strain level, in Figures 2.41 and 2.42. The torsion mode results will also be presented in tabular form (Table 2.1). General discussion of the results will ensue.

In Figure 2.26, the transfer functions (TFs) for the six representative "high amplitude" sweeps are overlaid. Figures 2.27 and 2.28 show the overlaid piezo output FRFs and load cell output FRFs, respectively. These three figures describe the response of the truss to a sinusoidal excitation of amplitude around 0.014 lbf, which corresponds to a constant 30 V input to the Butterfly actuator. In the following discussion, the voltage input to the actuator will be frequently used to distinguish the different data sets. The average peak response of the truss was 1.58×10^{-5} ε, as measured with the piezoceramic gauge on the erectable diagonal member. This peak measurement was repeatable to within 4×10^{-7} ε, which amounts to 2.5% of the average peak strain. The deviation of the load cell output curves in Figure 2.28 from constant magnitude and phase lines implies that some degree of inaccuracy is incurred by using the piezo output FRFs to extract the modal parameters, instead of the TFs. A frequency difference of approximately 0.004 Hz is observed between the peaks in the TF (Figure 2.26) and the piezo output FRF (Figure 2.27). This inaccuracy will be further discussed once all the torsion mode data has been presented.

A qualitative measure of the repeatability within a set of sweeps can be inferred from how well the sweeps overlay each other. In this case, some spread is seen in the data on either side of the peak. It turned out that sweeps performed in opposite directions (i.e. increasing vs. decreasing frequency) tended to follow slightly different curves. This type of hysteretic behavior is attributed to nonlinearity in the torsion mode at high amplitudes.

The transfer function magnitude data from the first sweep in the set is plotted in Figure 2.29. The modal peak presents an obvious nonlinearity: it is shown to be skewed toward the low-frequency side, but not so much that it exhibits jump behavior in its frequency response. The dashed line corresponds to the single-degree-of-freedom resonance fit. Clearly, the nonlinearity in the first torsion mode prevents a good fit to the linear SDOF model. The estimate for natural frequency was therefore chosen as the frequency of the peak transfer function amplitude. Figure 2.30 shows a polar plot of the TF data from one sweep at 30 V excitation. The circle fit to the data points appears to be unaffected by the aforementioned nonlinearity. However, the damping estimates from the circle fit characterization technique are scattered by as much as ±40% about the mean (Figure 2.31), while the surface in the scatter plot remains relatively smooth. This systematic variation in the damping estimates is associated with the nonlinear behavior in the torsion mode [37]. Indeed, as the nonlinearity in the torsion mode decreases with decreasing excitation amplitude (from 100 V excitation down to 0.3 V excitation), a general trend of decreasing "steepness" in the scatter plots is observed.

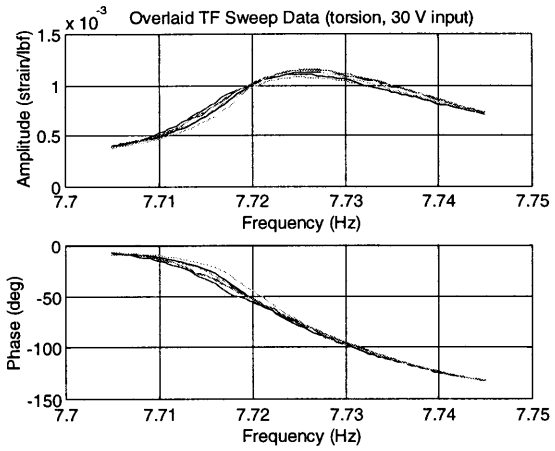

Figure 2.26 Typical transfer function data (torsion mode, high amplitude)

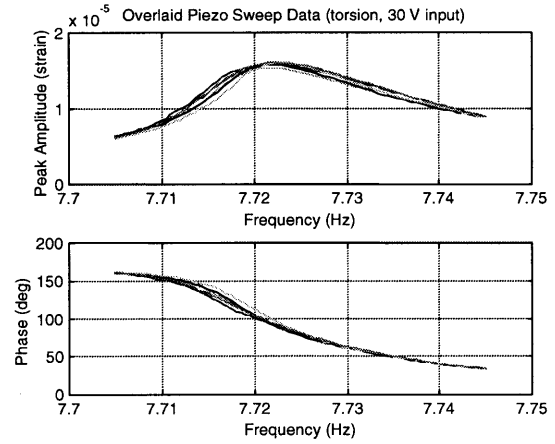

Figure 2.27 Typical piezo output data (torsion mode, high amplitude)

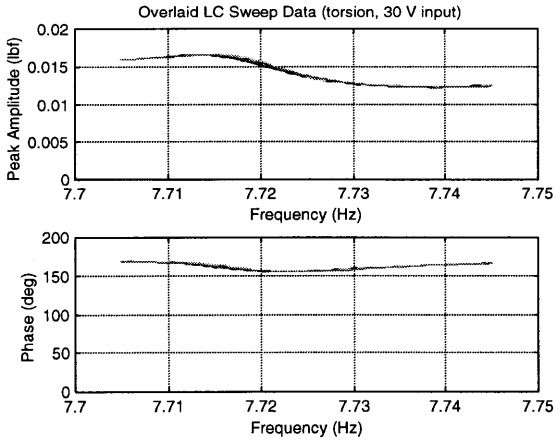

Figure 2.28 Typical load cell output data (torsion mode, high amplitude)

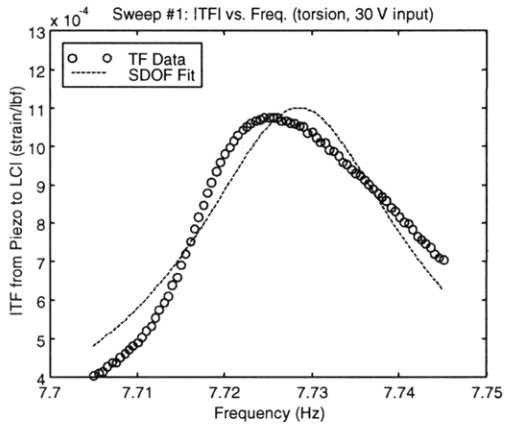

Figure 2.29 Typical transfer function sweep data (torsion mode, high amplitude)

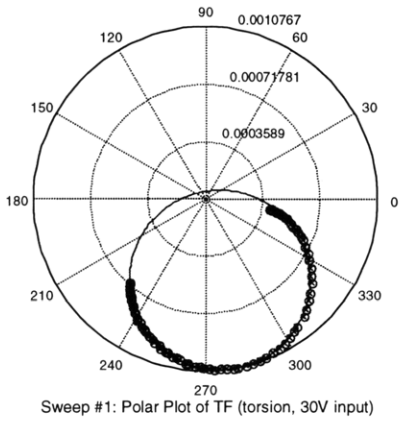

Figure 2.30 Typical circle fit to transfer function (torsion mode, high amplitude)

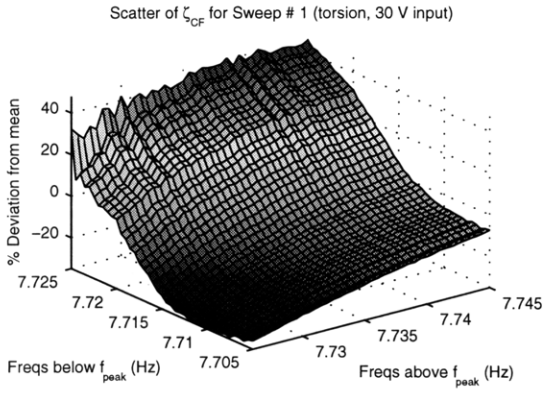

Figure 2.31 Typical scatter of damping from circle fit to transfer function (torsion mode, high amplitude)

Figures 2.32 through 2.34 show the corresponding analysis based on the piezo output FRF. The poor quality of the SDOF resonance fit and the systematic scatter in the damping ratios from the circle fit provide evidence of nonlinearity in the torsion mode at high amplitude, as was seen in the TF plots. However, as mentioned previously, the peak frequency is approximately 0.004 Hz lower in the strain output FRF than in the TF. In addition, the modal peak in the strain output FRF is clearly less damped than the peak in the TF. These differences in modal parameter estimates must be taken into consideration when using the strain output FRFs to determine f_n and ζ_n.

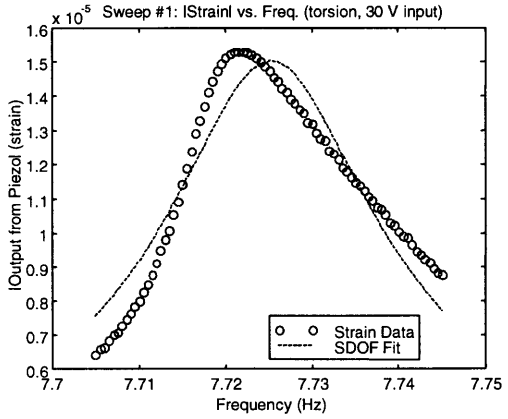

Figure 2.32 Typical piezo output sweep data (torsion mode, high amplitude)

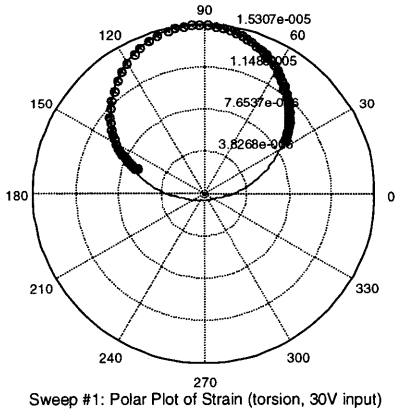

Figure 2.33 Typical circle fit to piezo output (torsion mode, high amplitude)

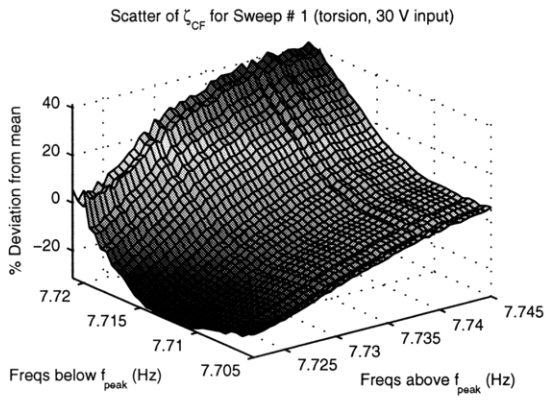

Figure 2.34 Typical scatter of damping from circle fit to piezo output (torsion mode, high amplitude)

In Figure 2.35, the representative "low amplitude" TF sweeps are overlaid. The input voltage to the Butterfly shaker was set to 0.01V, for this set of sweeps. The transfer functions are corrupted by noise, because the load cell noise floor has been reached (Figure 2.37), at a load level around 1.4×10^{-5} lbf. For this reason, the modal parameter characterization was performed based on the strain output FRFs alone (Figure 2.36). Although some noise is visible in the piezo output, the modal peak is still easily distinguishable. The average peak strain over this set of sweeps was 7.5 nε, repeatable to within 0.2 nε (or 2.5%).

The SDOF model fits well to this low amplitude FRF data (Figure 2.38). Evidently, the torsion mode becomes linear as excitation amplitude is decreased. Compared to the high amplitude data, the sharper peak in the low amplitude FRF indicates that the level of damping has decreased, while the natural frequency estimate has increased by more than 0.02 Hz. Despite the noise in the data, the circle fit procedure represents the FRF data quite well (Figure 2.39). The scatter in the damping ratios from the circle fit procedure lies predominantly within ±10% of the mean ζ_n (Figure 2.40); the random nature of the variations is consistent with the presence of noise in the data [37].

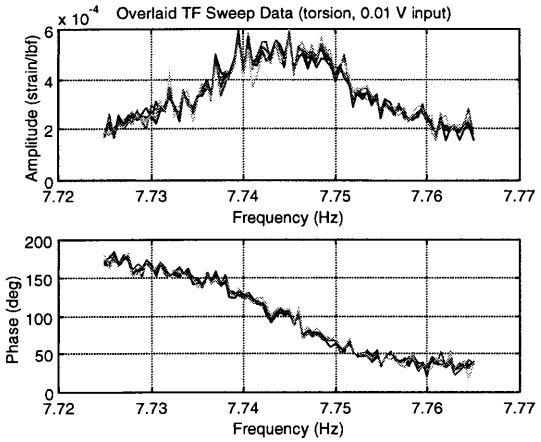

Figure 2.35 Typical transfer function data (torsion mode, low amplitude)

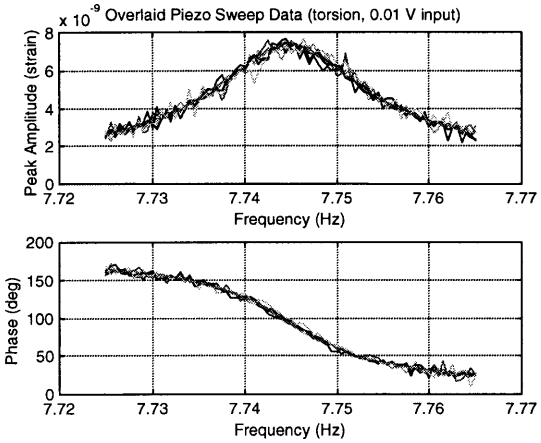

Figure 2.36 Typical piezo output data (torsion mode, low amplitude)

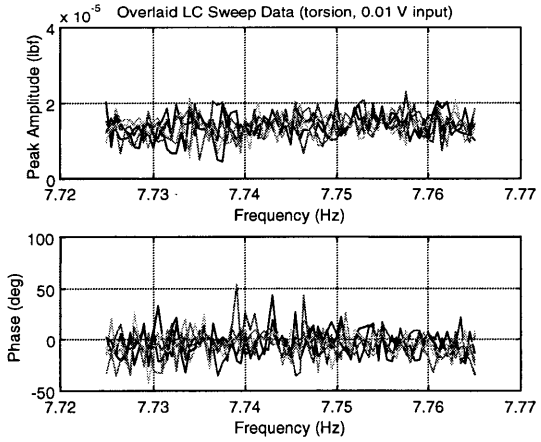

Figure 2.37 Typical load cell output data (torsion mode, low amplitude)

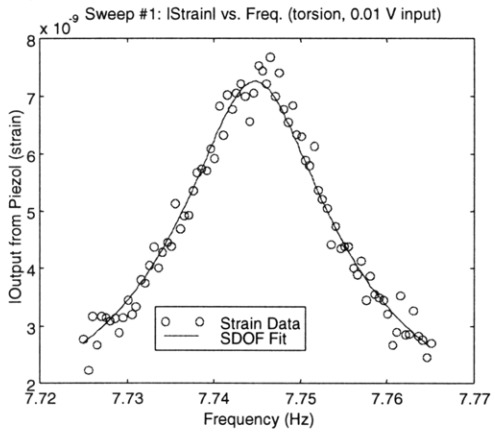

Figure 2.38 Typical piezo output sweep data (torsion mode, low amplitude)

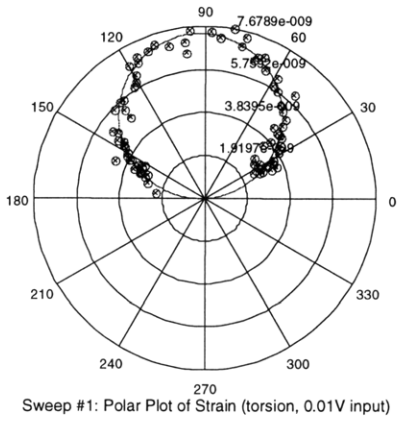

Figure 2.39 Typical circle fit to piezo output (torsion mode, low amplitude)

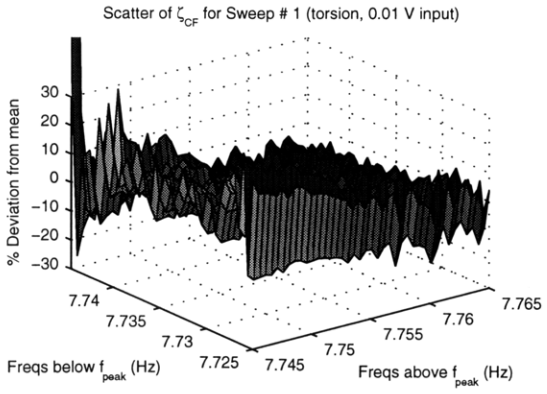

Figure 2.40 Typical scatter of damping from circle fit to piezo output (torsion mode, low amplitude)

Mode tested	Shaker used	Input voltage	FRF type	ε_{peak}				Ave. Load (lbf)	f_n (Hz)					ζ_{cfit}			
				ave	max	min	σ		source	ave	max	min	σ	ave	max	min	σ
torsion	B-fly	100	TF	4.04E-05	4.08E-05	3.98E-05	3.79E-07	5.12E-02	fpeak	7.7035	7.7055	7.7020	0.0013	2.56E-03	2.74E-03	2.30E-03	1.63E-04
torsion	B-fly	100	SO	4.04E-05	4.08E-05	3.98E-05	3.79E-07	5.12E-02	fpeak	7.6993	7.7000	7.6985	0.0005	2.35E-03	2.50E-03	2.11E-03	1.65E-04
torsion	B-fly	30	TF	1.58E-05	1.61E-05	1.53E-05	2.86E-07	1.42E-02	fpeak	7.7254	7.7260	7.7250	0.0004	1.50E-03	1.63E-03	1.32E-03	1.05E-04
torsion	B-fly	30	SO	1.58E-05	1.61E-05	1.53E-05	2.86E-07	1.42E-02	fpeak	7.7220	7.7225	7.7215	0.0003	1.40E-03	1.53E-03	1.27E-03	9.29E-05
torsion	B-fly	10	TF	6.26E-06	6.32E-06	6.11E-06	7.61E-08	4.34E-03	fpeak	7.7353	7.7360	7.7345	0.0006	1.14E-03	1.22E-03	1.09E-03	5.38E-05
torsion	B-fly	10	SO	6.26E-06	6.32E-06	6.11E-06	7.61E-08	4.34E-03	fpeak	7.7326	7.7335	7.7320	0.0006	1.25E-03	1.29E-03	1.19E-03	4.18E-05
torsion	B-fly	3	TF	2.00E-06	2.01E-06	2.00E-06	7.35E-09	1.32E-03	fpeak	7.7436	7.7440	7.7430	0.0004	1.05E-03	1.08E-03	1.02E-03	2.63E-05
torsion	B-fly	3	SO	2.00E-06	2.01E-06	2.00E-06	7.35E-09	1.32E-03	fpeak	7.7407	7.7410	7.7405	0.0003	1.10E-03	1.12E-03	1.08E-03	1.68E-05
torsion	B-fly	1	TF	7.42E-07	7.49E-07	7.29E-07	7.71E-09	4.22E-04	SDOF	7.7463	7.7466	7.7459	0.0002	8.62E-04	8.96E-04	8.11E-04	3.28E-05
torsion	B-fly	1	SO	7.42E-07	7.49E-07	7.29E-07	7.71E-09	4.22E-04	SDOF	7.7436	7.7441	7.7430	0.0004	1.00E-03	1.02E-03	9.63E-04	2.32E-05
torsion	B-fly	0.3	TF	2.03E-07	2.04E-07	2.03E-07	5.48E-10	1.24E-04	SDOF	7.7456	7.7459	7.7451	0.0003	9.25E-04	9.56E-04	8.82E-04	2.80E-05
torsion	B-fly	0.3	SO	2.03E-07	2.04E-07	2.03E-07	5.48E-10	1.24E-04	SDOF	7.7429	7.7433	7.7422	0.0004	1.06E-03	1.09E-03	1.02E-03	2.47E-05
torsion	B-fly	0.1	TF	7.84E-08	7.89E-08	7.80E-08	3.02E-10	2.80E-05	SDOF	7.7492	7.7493	7.7490	0.0001	7.81E-04	8.15E-04	7.44E-04	2.71E-05
torsion	B-fly	0.1	SO	7.84E-08	7.89E-08	7.80E-08	3.02E-10	2.80E-05	SDOF	7.7444	7.7448	7.7441	0.0002	9.22E-04	9.51E-04	9.04E-04	1.70E-05
torsion	B-fly	0.03	SO	2.09E-08	2.12E-08	2.05E-08	2.30E-10	-	SDOF	7.7450	7.7453	7.7447	0.0003	1.02E-03	1.04E-03	9.87E-04	2.37E-05
torsion	B-fly	0.01	SO	7.52E-09	7.68E-09	7.33E-09	1.51E-10	-	SDOF	7.7451	7.7458	7.7445	0.0004	1.00E-03	1.03E-03	9.83E-04	2.06E-05
torsion	B-fly	0.003	SO	2.40E-09	2.50E-09	2.26E-09	1.02E-10	-	SDOF	7.7446	7.7450	7.7443	0.0003	9.70E-04	1.03E-03	8.70E-04	6.26E-05

Table 2.1 Torsion mode results

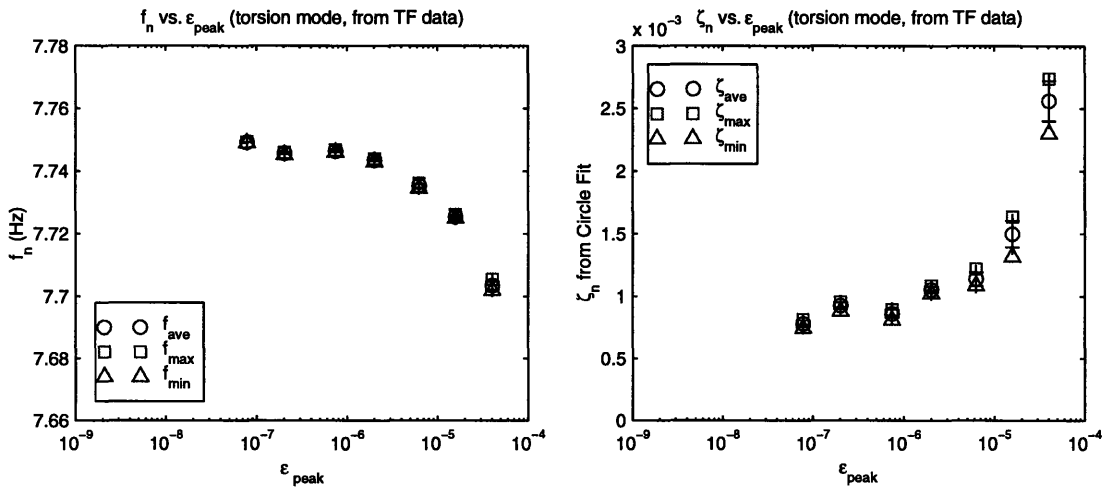

Figure 2.41 Modal parameters from TF data vs. strain amplitude (torsion mode)

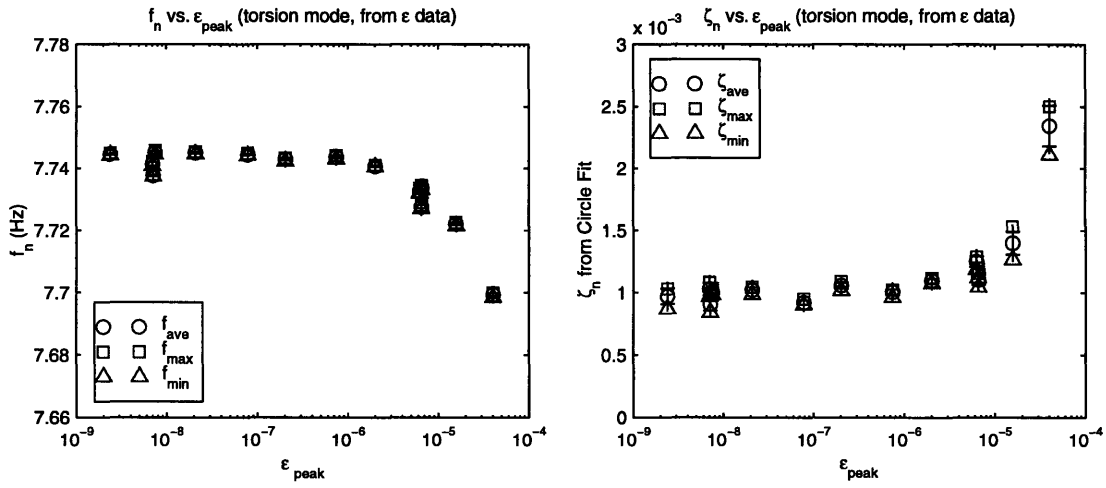

Figure 2.42 Modal parameters from piezo output data vs. strain amplitude (torsion mode)

The results from all the microdynamic tests on the torsion mode are tabulated in Table 2.1. Figures 2.41 and 2.42 present the results graphically, in the form of f_n vs. ε_{peak} and ζ_n vs. ε_{peak} plots. Figure 2.41 shows the modal parameters obtained from the TF data, while the parameters in Figure 2.42 were extracted from the piezo output data alone. In each of the four plots, the mean value of the modal parameter estimates from each set of six sweeps is plotted as a circle. The maximum and minimum values from each set of sweeps are represented as squares and triangles, respectively. The standard deviation of the six sweeps in each set was computed, as well. The

error bars on the plots correspond to one standard deviation above and below the mean value. As mentioned in section 2.3, the max and min values, and the standard deviations, give measures of the repeatability in the modal parameter estimates within each set of sweeps (i.e. the precision attained).

Below a strain level of one microstrain, the torsion mode of the structure behaves linearly: Figure 2.41 shows the natural frequency estimates flattening out at a value of approximately 7.747 Hz, and the damping ratio asymptoting to a value of roughly 0.0009. Above one microstrain, the torsion mode exhibits softening nonlinear behavior, with f_n decreasing to 7.704 Hz at the highest strain level tested. The corresponding ζ_n increases to a level of 0.0026 at this amplitude.

This behavioral trend (nonlinear softening at high amplitude, linear at low amplitude) is even more evident in the plots of modal parameters obtained from the piezo output FRFs, which present results down to nanostrain level (Figure 2.42). At low amplitudes, the natural frequency estimate reaches a constant value of around 7.745 Hz. In fact, the f_n estimates from the piezo output FRFs are slightly lower than those from the TFs, at all common strain levels tested, by approximately 0.004 Hz. The damping ratio does not exhibit such a consistent trend between the TF and strain output FRF estimates. A worst-case difference of 0.0002 is observed between TF-based and piezo output FRF-based ζ_n estimates, at the highest strain amplitude tested (40 $\mu\varepsilon$).

Good precision was achieved in all of the natural frequency estimates, judging by the close proximity of the max and min values to the mean, and the insignificant size of the error bars in left side plots of Figures 2.41 and 2.42. The standard deviation values are all smaller than 0.02% of their corresponding mean values. As far as the damping estimates are concerned, the best precision was achieved in the range of strains between 7.5nε and 6.26 $\mu\varepsilon$: the standard deviations in ζ_n for these sets of sweeps correspond to less than 5% of the mean values obtained. At the lowest strain level tested (2.4 nε), the standard deviation of the ζ_n estimates increased to roughly 7% of the mean ζ_n, due to significant noise in the data. At the two highest amplitude levels (15.8 $\mu\varepsilon$ and 40.4 $\mu\varepsilon$), the same hysteretic nonlinearity which caused the forward and backward sweeps to not overlay (Figure 2.26) results in decreased precision in the damping estimates, amounting to roughly 7% of the mean ζ_n.

In summary, the microdynamic modal parameter characterization of the torsion mode showed nonlinear softening behavior for strain levels above 1 με, and essentially linear behavior at lower strain amplitudes. It can be inferred from this behavioral trend that the nonlinear structural mechanisms, which dominate the damping at high excitation levels, do not get excited at the lower strain levels, and the underlying linear dissipation mechanisms become the main source of structural damping. In general, the modal parameter estimates from the strain output FRFs provided reasonably close approximations to the modal parameters obtained from the TFs. Good precision was obtained within each set of six sweeps in all natural frequency estimates and most damping ratio estimates. The precision of the ζ_n estimates was slightly decreased at the lowest strain amplitude tested (due to noise) and the two highest strain amplitudes (due to structural nonlinearity).

Sweep results – bending

Now the results from the microdynamic tests of the first bending mode will be presented. Again, only a representative subset of the data is included here. The full set of FRF data plots is presented in Appendix A. As discussed in section 2.2, the load cell output was essentially constant over the range of frequencies covered in the bending mode tests. Consequently, the modal parameters were extracted directly from the strain output FRFs. No load cell or TF data are presented.

Three different sets of representative plots will be presented here, the first two corresponding to "high amplitude" tests, and the third corresponding to a "low amplitude" set of sweeps. The first set, in Figures 2.43 through 2.46, corresponds to tests performed with the electro-magnetic shaker, at a peak strain of 1.07×10^{-6} ε. Next, the highest-amplitude set of sweeps performed using the Butterfly shaker will be discussed (Figures 2.47 through 2.50). A peak strain of 8.5×10^{-7} ε was reached in these tests, close enough for comparison with the first set of plots, which represents the lowest strain level excited with the electro-magnetic shaker. The third set of plots, in Figures 2.51 through 2.54, corresponds to a strain amplitude of 8.0×10^{-9} ε, also obtained using the Butterfly shaker. After the presentation of the representative plots, the f_n and ζ_n estimates from all of the bending mode sweep sets are plotted versus strain level, tabulated, and discussed.

In Figure 2.43, the six strain output FRFs from the set of representative "high amplitude" sweeps are overlaid. During these sweeps, the truss was actuated with the electro-magnetic shaker at a constant excitation amplitude of 3 V (peak-to-peak). Although load cell data was not collected for the full set of sweeps, the load applied at the peak frequency was found to be 0.039 lbf. The average peak strain of 1.07×10^{-6} ε was found to be repeatable to within 2×10^{-8} ε (2% of the average peak strain). The six sweeps overlay quite well, an indication that good precision was achieved in this set of sweeps.

The FRF magnitude data from the first sweep in the set is plotted in Figure 2.44, with the SDOF resonance fit curve (dashed line). The SDOF model is seen to fit the data reasonably well. Only slight nonlinearity is detected, barely tilting the peak toward the low frequencies. In Figure 2.45, the same data is presented in a polar plot. As expected, the points are easily fit to a modal circle. The damping estimates obtained from the circle fit characterization exhibit only slight systematic variation, staying within ±10% of the mean ζ_n (Figure 2.46). This is consistent with the predominantly linear behavior noted previously.

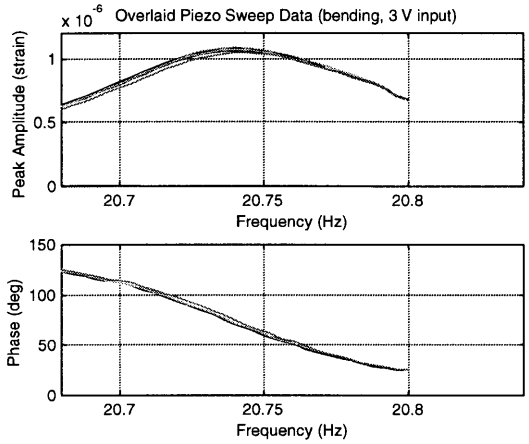

Figure 2.43 Typical piezo output data (bending mode, high amplitude, E-M shaker)

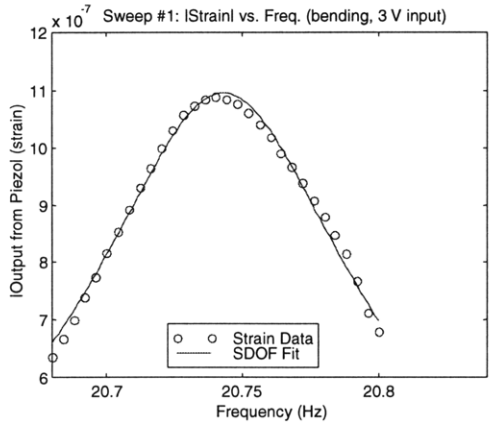

Figure 2.44 Typical piezo output sweep data (bending mode, high ampl, E-M shaker)

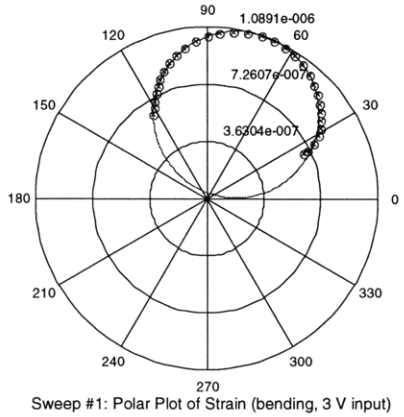

Figure 2.45 Typical circle fit to piezo output (bending mode, high ampl, E-M shaker)

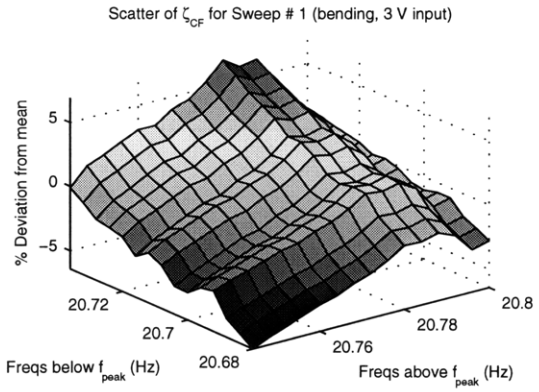

Figure 2.46 Typical scatter of damping from circle fit to piezo output (bending mode, high ampl, E-M shaker)

The next set of figures corresponds to the highest amplitude tested with the Butterfly shaker as actuator. Applying sinusoidal excitation voltage of 100 V resulted in an average load of approximately 0.032 lbf. Figure 2.47 overlays the strain output FRFs from the six sweeps. The average peak strain achieved over this set of sweeps was 8.5×10^{-7} ε, repeatable to within 2×10^{-9} ε (≈0.2% of the average peak strain). This level of peak strain is of the same order as the strain level reached using the electro-magnetic shaker with 3 V peak-to-peak excitation (Figure 2.43). By comparing these two sets of results, it is possible to gauge the effect on the modal parameters brought about by changing the shaker.

In Figures 2.48 and 2.49, the FRF data is shown to fit well with the SDOF resonance curve and the modal circle. The scatter in the circle fit damping estimates is again found to fall within ±10% of the mean ζ_n, with a slight systematic variation, as evidenced by the shallow-slanted planar surface in Figure 2.50. Comparing this set of sweeps to the previous set, corresponding to tests performed at roughly the same strain level with the electro-magnetic shaker as the actuator, it is found that both sets of data exhibit similar qualities. The FRF magnitude plots look alike, as far as their general shape is concerned, indicating that their damping ratios are similar. In fact, the mean damping ratio estimate from the FRFs obtained with the electro-magnetic shaker is 0.0023, while the mean ζ_n from the FRFs obtained with the Butterfly shaker is only slightly higher, at 0.0025. However, the difference in the natural frequency estimates obtained with the different shakers is significant: 20.741 Hz with the electro-magnetic actuator, versus 20.718 Hz with the Butterfly actuator. The different inertial properties of the shakers must account for this difference.

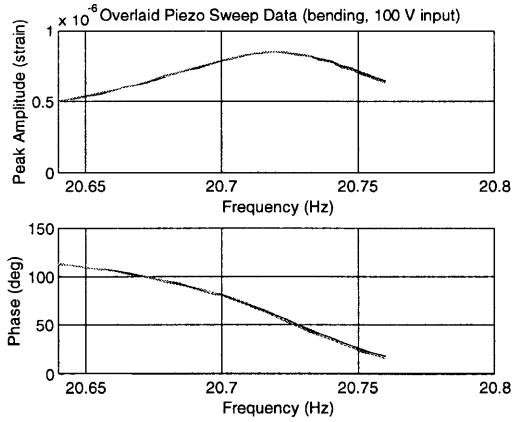

Figure 2.47 Typical piezo output data (bending mode, high amplitude, B-fly shaker)

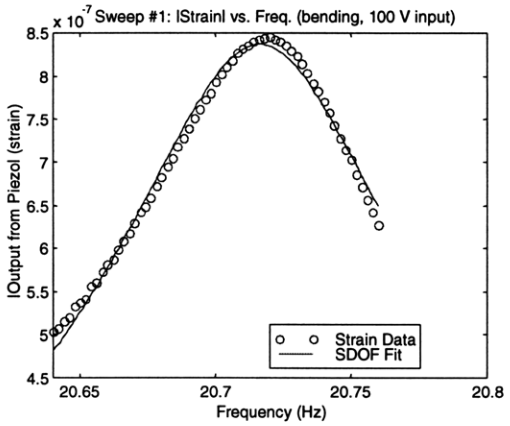

Figure 2.48 Typical piezo output sweep data (bending mode, high ampl, B-fly shaker)

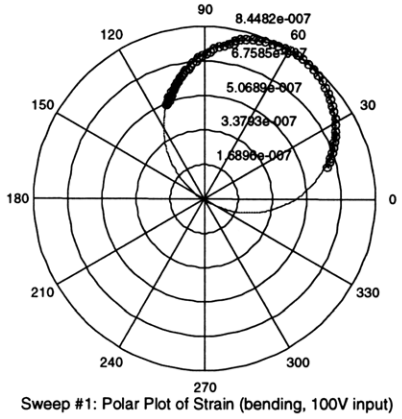

Figure 2.49 Typical circle fit to piezo output (bending mode, high ampl, B-fly shaker)

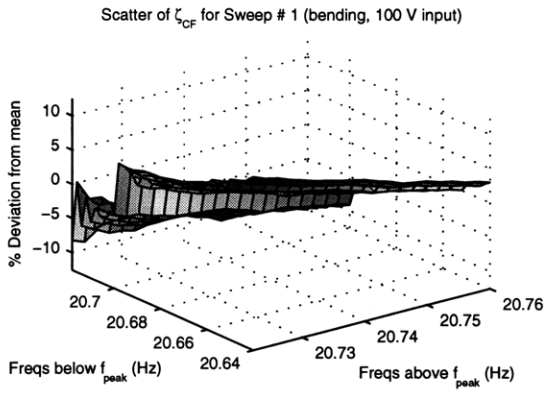

Figure 2.50 Typical scatter of damping from circle fit to piezo output (bending mode, high ampl, B-fly shaker)

Data from a typical "low amplitude" set of sweeps is shown in Figures 2.51 through 2.54. The average peak strain attained in these sweeps was 8.0×10^{-9} ε, repeatable to within 2×10^{-10} ε over the six sweeps. The average load applied was roughly 0.00023 lbf, corresponding to a sinusoidal excitation of 1 V to the Butterfly shaker. The overlaid FRFs in Figure 2.51 reflect the increased noise level at very low amplitude. Despite the noise, however, the modal peak is still distinct, and the six FRF curves appear to overlay quite well. Figure 2.52 presents the FRF magnitude data from one of the sweeps in the set. Due to the noise in the data, it is difficult to judge the quality of the SDOF resonance fit. Nonetheless, it would appear that the fit provides a decent estimate of the natural frequency. The mean f_n estimate from this set of sweeps was 20.721 Hz, not very different from the 20.718 Hz obtained in the tests using 100 V excitation to the same shaker. Indeed, the bending mode was found to be essentially linear over the entire range of strains actuated by the Butterfly shaker. The circle fit to the FRF data is quite good, despite the noise (Figure 2.53). The resulting damping estimates lie within ±20% of the mean ζ_n, aside from a single outlying point (Figure 2.54).

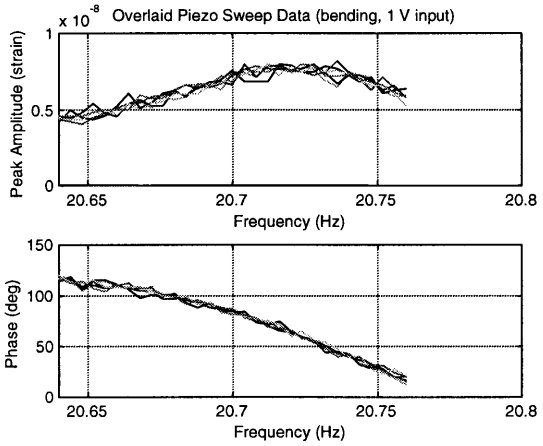

Figure 2.51 Typical piezo output data (bending mode, low amplitude, B-fly shaker)

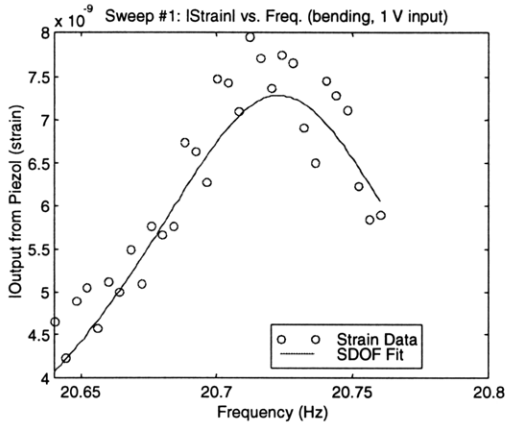

Figure 2.52 Typical piezo output sweep data (bending mode, low ampl, B-fly shaker)

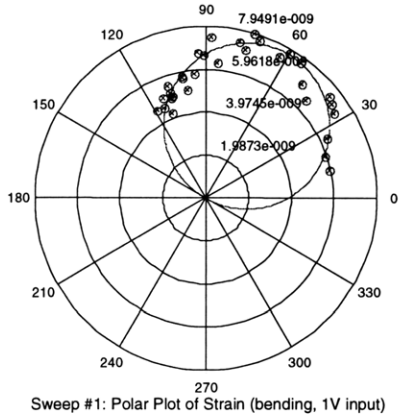

Figure 2.53 Typical circle fit to piezo output (bending mode, low ampl, B-fly shaker)

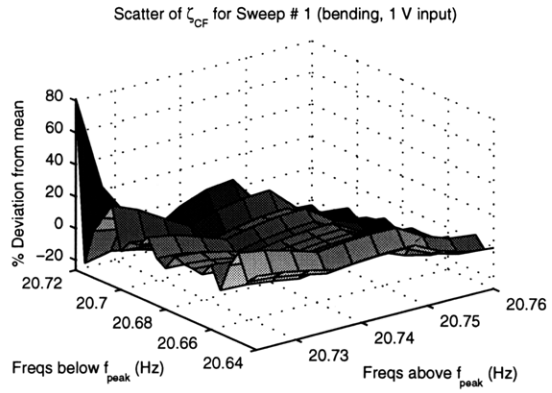

Figure 2.54 Typical scatter of damping from circle fit to piezo output (bending mode, low ampl, B-fly shaker)

Mode tested	Shaker used	Input voltage	FRF type	ε_{peak}				Ave. Load (lbf)	f_n (Hz)					ζ_{scfit}			
				ave	max	min	σ		source	ave	max	min	σ	ave	max	min	σ
bending	E-M	30 (pp)	SO	8.40E-06	8.51E-06	8.30E-06	8.81E-08	3.9E-01	fpeak	20.6793	20.6820	20.6760	0.0021	3.96E-03	4.16E-03	3.77E-03	1.84E-04
bending	E-M	10 (pp)	SO	3.64E-06	3.69E-06	3.58E-06	3.83E-08	1.3E-01	fpeak	20.7287	20.7320	20.7280	0.0016	2.66E-03	2.71E-03	2.61E-03	3.70E-05
bending	E-M	3 (pp)	SO	1.07E-06	1.09E-06	1.05E-06	1.52E-08	3.9E-02	fpeak	20.7407	20.7440	20.7400	0.0016	2.32E-03	2.37E-03	2.28E-03	3.19E-05
bending	B-fly	100	SO	8.46E-07	8.48E-07	8.44E-07	1.50E-09	3.2E-02	fpeak	20.7175	20.7200	20.7150	0.0018	2.52E-03	2.54E-03	2.47E-03	2.42E-05
bending	B-fly	30	SO	2.28E-07	2.30E-07	2.26E-07	1.45E-09	8.4E-03	fpeak	20.7227	20.7240	20.7200	0.0021	2.50E-03	2.58E-03	2.44E-03	5.07E-05
bending	B-fly	10	SO	7.97E-08	8.09E-08	7.86E-08	9.00E-10	2.7E-03	SDOF	20.7233	20.7251	20.7215	0.0012	2.53E-03	2.64E-03	2.43E-03	7.78E-05
bending	B-fly	3	SO	2.33E-08	2.36E-08	2.30E-08	1.89E-10	7.5E-04	SDOF	20.7205	20.7225	20.7189	0.0016	2.50E-03	2.55E-03	2.42E-03	4.95E-05
bending	B-fly	1	SO	8.00E-09	8.18E-09	7.89E-09	9.78E-11	2.3E-04	SDOF	20.7207	20.7231	20.7185	0.0017	2.50E-03	2.66E-03	2.35E-03	1.19E-04
bending	B-fly	0.3	SO	2.81E-09	3.07E-09	2.65E-09	1.56E-10	5.0E-05	SDOF	20.7270	20.7394	20.7186	0.0075	2.11E-03	2.72E-03	1.46E-03	4.54E-04

Table 2.2 Bending mode results

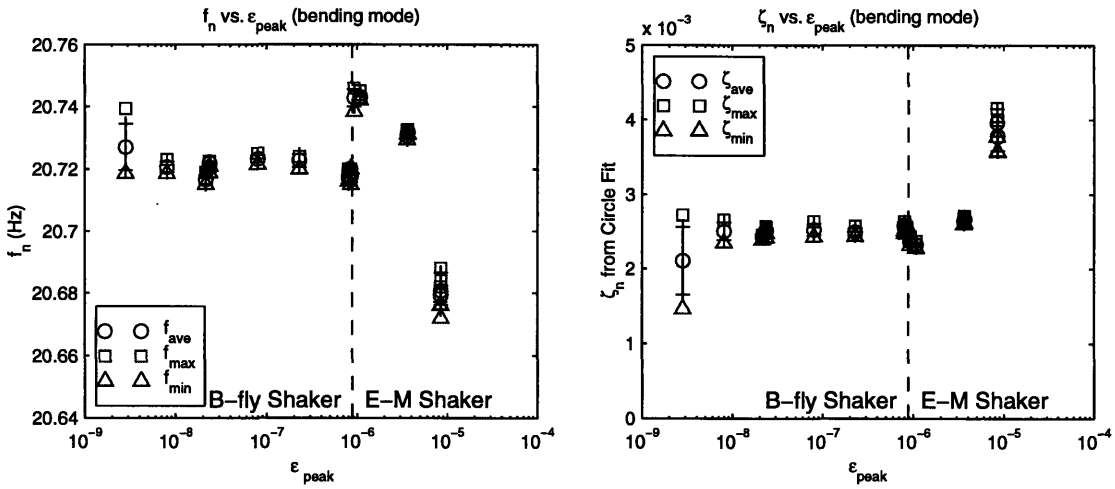

Figure 2.55 Modal parameters from piezo output data vs. strain amplitude (bending mode)

The results from all bending mode tests are tabulated in Table 2.2. These results are also presented in the form of f_n vs. ε_{peak} and ζ_n vs. ε_{peak} plots (Figure 2.55). As was done for the torsion mode results, the mean, max, and min values of each modal parameter estimate are plotted. The error bars extend one standard deviation above and below the mean value.

As previously noted, the transition between the two different actuators causes discontinuities in the plots of f_n vs. ε_{peak} and ζ_n vs. ε_{peak}, around the 1 $\mu\varepsilon$ mark. Despite these discontinuities, both plots exhibit the general trend of linearity at strain amplitudes below 1 $\mu\varepsilon$, and softening nonlinearity at higher amplitudes. Figure 2.55 shows that the natural frequency of the bending mode remains essentially constant at low amplitudes, at approximately 20.72 Hz based on the Butterfly shaker tests. The tests with the electro-magnetic shaker show the natural frequency asymptoting toward a frequency around 20.75 Hz. The damping ratio estimates decrease with amplitude, until a low-amplitude limit of roughly 0.0025 is reached.

Although the mean parameter estimates for the lowest strain amplitude (2.8 nε) seem to diverge slightly from the above-mentioned trends, is important to note that the accuracy of these estimates is suspect, because of systematic fitting errors induced by excessive noise in the data. Nonetheless, the low-amplitude parameter values predicted by the trends lie within the scatter of the lowest-amplitude results.

In general, reasonable precision was achieved in the bending mode tests, as judged by looking at the scatter in the parameter estimates within each set of sweeps. For all strain amplitudes tested other than the lowest, the standard deviation in the frequency estimates was 0.0021 Hz or better. The worst-case precision achieved in the f_n estimates was for the lowest amplitude tested (2.8 nε), where the data was corrupted by noise. The standard deviation of these six estimates rose to 0.0075 Hz. As for the damping ratio estimates, the standard deviations for all but the lowest amplitude tests are less than $2x10^{-4}$ (5% of the mean ζ_n values). The standard deviation of the damping ratio estimate from the lowest amplitude tests was found to be $4.5x10^{-4}$, or 22% of the mean ζ_n.

In summary, the microdynamic modal parameter characterization of the bending mode showed behavior similar to that seen in the torsion mode: nonlinear softening behavior for strain levels above 1 με, and essentially linear behavior at lower strain amplitudes. The same conclusion can therefore be drawn regarding the structural mechanisms of deployable truss: the nonlinear mechanisms dominate the damping at high excitation levels, but do not get excited at lower strain levels, so the underlying linear dissipation mechanisms become the main source of structural damping. Results from all modal parameter estimates, other than those from the lowest strain amplitude tested, showed acceptable precision. At the lowest strain amplitude, accuracy and precision suffered due to excessive noise in the data.

Repeatability

In addition to the measures of repeatability available within each set of sweeps, a measure of the precision between sets of sweeps performed on different days was sought. To this end, tests were repeated at various strain amplitudes, for both modes of interest. The modal parameter estimates from these repeatability tests were plotted with the original results in Figure 2.42 for the torsion mode (only strain output measurements were repeated), and in Figure 2.55 for the bending mode. The mean values of ε_{peak}, f_n, and ζ_n from the repeated tests are tabulated along with the corresponding original test results, in Table 2.3.

For the torsion mode, one "high amplitude" and one "low amplitude" set of sweeps were repeated, on two occasions. The high amplitude repeatability tests were performed with a constant excitation of 10 V to the Butterfly shaker. The resulting peak strain was repeatable to within 5.1%. The natural frequency estimates proved repeatable to within 0.0051 Hz (0.066%),

while the repeated damping ratio estimates fell within 1.4×10^{-4} of the original estimate (12%). The low amplitude repeated tests were performed with 0.01 V excitation to the shaker. Less than 6.5% difference was obtained between the repeated peak strain values and the original mean value. The f_n and ζ_n estimates were found to be repeatable within 0.0075 Hz (0.1%) and 9×10^{-5} (10%) of the original mean values, respectively.

Due to the use of two different shakers to excite the bending mode, more repeatability tests were performed than for the torsion mode. One set of "low amplitude" sweeps and one set of "high amplitude" sweeps were repeated with the Butterfly shaker as actuator. In addition, tests were repeated at all three amplitudes excited by the electro-magnetic actuator. First of all, three sets of sweeps were performed with the electro-magnetic shaker at 30 V (peak-to-peak) excitation. The peak strain values were repeatable to within 1.8% of the original mean value. Differences of less than 0.0014 Hz (0.006%) and 1.8×10^{-4} (5%) were obtained between the original and repeated values of the natural frequency and damping ratio estimates, respectively. Tests at the other two amplitudes excited by the electro-magnetic actuator were repeated only once, resulting in comparable margins of precision, with one notable point of exception: the 3 V (peak-to-peak) tests repeated with the electro-magnetic shaker resulted in a 13% drop in peak strain achieved. This drop may be due to the onset of stiction in the proof-mass actuator, as described in subsection 2.1.2. For all the repeatability tests performed with the Butterfly shaker, ε_{peak}, f_n, and ζ_n results were found to be reasonably close to the original mean values. The worst case occurred for the lowest amplitude test repeated (3 V excitation to the Butterfly shaker), for which an 8% difference in ε_{peak}, a 0.019% difference in f_n, and a 3% difference in ζ_n were obtained. Noisy data is identified as the source of this slight decrease in precision.

In summary, the repeatability test results generally followed the trends from the original sets of sweeps, thus reaffirming the conclusions drawn, for both the torsion and bending modes.

Mode tested	Shaker used	Input voltage	FRF type	ε_{peak}		Ave. Load (lbf)	f_n (Hz)			ζ_{cfit}	
				ave	% diff		source	ave	% diff	ave	% diff
torsion	B-fly	10	SO	6.26E-06		4.3E-03	fpeak	7.7326		1.25E-03	
torsion	B-fly	10	SO	6.58E-06	5.1%	4.6E-03	fpeak	7.7337	0.014%	1.11E-03	-11.5%
torsion	B-fly	10	SO	6.57E-06	4.8%	4.4E-03	fpeak	7.7275	-0.066%	1.16E-03	-6.8%
torsion	B-fly	0.01	SO	7.52E-09		-	SDOF	7.7451		1.00E-03	
torsion	B-fly	0.01	SO	7.03E-09	-6.5%	-	SDOF	7.7414	-0.048%	1.03E-03	2.8%
torsion	B-fly	0.01	SO	7.15E-09	-4.9%	-	SDOF	7.7376	-0.096%	9.06E-04	-9.5%
bending	E-M	30(pp)	SO	8.40E-06		3.9E-01	fpeak	20.6793		3.96E-03	
bending	E-M	30(pp)	SO	8.47E-06	0.9%	3.9E-01	fpeak	20.6807	0.006%	3.78E-03	-4.7%
bending	E-M	30(pp)	SO	8.55E-06	1.8%	3.9E-01	fpeak	20.6793	0.000%	3.78E-03	-4.6%
bending	E-M	10(pp)	SO	3.64E-06		1.3E-01	fpeak	20.7287		2.66E-03	
bending	E-M	10(pp)	SO	3.60E-06	-1.2%	1.3E-01	fpeak	20.7273	-0.006%	2.64E-03	-1.0%
bending	E-M	3(pp)	SO	1.07E-06		3.9E-02	fpeak	20.7407		2.32E-03	
bending	E-M	3(pp)	SO	9.26E-07	-13.4%	3.9E-02	fpeak	20.7373	-0.016%	2.37E-03	1.8%
bending	B-fly	100	SO	8.46E-07		3.2E-02	fpeak	20.7175		2.52E-03	
bending	B-fly	100	SO	7.99E-07	-5.5%	3.2E-02	fpeak	20.7173	-0.001%	2.58E-03	2.5%
bending	B-fly	100	SO	8.10E-07	-4.3%	3.2E-02	fpeak	20.7180	0.002%	2.53E-03	0.6%
bending	B-fly	100	SO	8.44E-07	-0.2%	3.2E-02	fpeak	20.7200	0.012%	2.51E-03	-0.2%
bending	B-fly	3	SO	2.33E-08		7.5E-04	SDOF	20.7205		2.50E-03	
bending	B-fly	3	SO	2.34E-08	0.5%	7.5E-04	SDOF	20.7218	0.006%	2.51E-03	0.4%
bending	B-fly	3	SO	2.14E-08	-8.4%	7.5E-04	SDOF	20.7166	-0.019%	2.43E-03	-2.8%

Table 2.3 Repeatability test results

2.4.2 Correlation with Previous Results

In this subsection, the results obtained during the microdynamic modal parameter characterization experiment are compared with those from two relevant past experiments. First, correlation is made between the microdynamic-level tests on the MODE STA truss and the "standard"-level dynamic characterizations of the same structure performed for the MODE and MODE-Reflight experiments [29, 32]. Next, the microdynamic behavior of the deployable truss structure is compared with that of an erectable (i.e. fixed-joint) truss structure, as investigated by Ting [21].

MODE and MODE-Reflight

In the MODE and MODE-Reflight programs, ground tests were performed on the MODE STA baseline truss, at "standard" dynamic load levels between 0.04 lbf and 0.4 lbf. Selected results from these modal parameter characterization experiments are presented in Table 2.4. The tabulated results are those which correspond to the same test configuration used for the microdynamic characterization: the baseline truss hanging on the 1 Hz suspension system, with the adjustable pretension bay set at high preload. The modal parameter estimates for the two series of MODE experiments were computed using different methods; the MODE program used a SDOF circle fit technique, while the MODE-Reflight employed a multiple-degree-of-freedom algorithm to fit all channels of data simultaneously.

For the microdynamic tests of the torsion and bending modes, the highest amplitude was selected so that at least one set of sweeps was performed at excitation levels overlapping the MODE and MODE-Reflight excitation levels. For the torsion mode, the highest excitation reached was around 0.05 lbf, which overlaps with the lowest levels tested in the past experiments. As for the bending mode, the three amplitudes actuated with the electro-magnetic shaker (0.39 lbf, 0.13 lbf, and 0.039 lbf) can all be compared with the old MODE data.

Experiment	Torsion			Bending		
	Ave. Load (lbf)	Ave. f_n (Hz)	Ave. ζ_n (%)	Ave. Load (lbf)	Ave. f_n (Hz)	Ave. ζ_n (%)
MODE	0.046	7.74	0.24	0.044	20.43	0.41
	0.224	7.70	0.40	0.208	20.37	0.39
	0.396	7.67	0.54	0.368	20.33	0.62
MODE-R	0.052	7.71	0.19	0.050	20.62	0.37
	0.213	7.68	0.29	0.198	20.67	0.61
	0.379	7.66	0.39	0.352	20.66	0.42
Microdyn.	0.0512	7.704	0.26	0.039	20.741	0.23
				0.13	20.729	0.27
				0.39	20.679	0.40

Table 2.4 Comparison of results for MODE STA truss

One difference between the microdynamic-level tests and the MODE tests was the type of sensor used. In order to confirm the traceability of the strain results to the previously-obtained acceleration transfer functions, one set of sweeps was performed with the accelerometer at A1 (located as shown in Figure 2.18). The highest-amplitude torsion tests were chosen for this set of sweeps. The results, tabulated in Table 2.5, show that the modal parameters computed from the strain-to-load TFs are directly traceable to those from the acceleration-to-load TFs. The FRF plots from the sweeps made with the accelerometer as sensor are included at the end of Appendix A.

Mode tested	Shaker used	Input voltage	FRF type	Ave. Load (lbf)	f_n (Hz)					ζ_{cfit}			
					source	ave	max	min	σ	ave	max	min	σ
torsion	B-fly	100	TF (accel.)	5.12E-02	fpeak	7.7028	7.7035	7.7005	0.0012	2.54E-03	2.71E-03	2.40E-03	1.25E-04
torsion	B-fly	100	TF (piezo)	5.12E-02	fpeak	7.7035	7.7055	7.7020	0.0013	2.56E-03	2.74E-03	2.30E-03	1.63E-04

Table 2.5 Comparison of accelerometer and piezo strain gauge data

The torsion mode results from the microdynamic characterization can be compared with the lowest-load results from MODE and MODE-Reflight (Table 2.4): the natural frequency estimate of 7.704 Hz is close to the value from MODE-Reflight (7.71 Hz), which had dropped from 7.74 Hz, obtained during the original MODE tests. The damping ratio estimate of 0.26% is higher than the 0.24% and 0.19% obtained from the MODE and MODE-Reflight data, respectively, and does not follow their trend of decreased damping with passage of time. However, an increase in the damping of the truss over time is not necessarily surprising – settling of the truss on its suspension, under the effect of gravity preload, could conceivably result in increased joint deadband, which would amplify the damping via increased friction and impacting in the joints. Slackening of the preloaded diagonal wires over time would also result in increased torsional damping, as was demonstrated during the MODE experiments [17]. These explanations would also justify the higher level of nonlinearity observed in the torsion mode, as compared to the older MODE and MODE-Reflight results at the same excitation.

As far as the bending mode is concerned, the three highest amplitude tests roughly overlap with the three load levels tested in the MODE experiments. While the modal parameters obtained in the microdynamic characterization experiment exhibit consistent trends of softening and increased damping with increasing applied load, those from the MODE experiments generally do

not. The softening behavior in the bending mode is evident in the original MODE results, however. Overall, the bending mode appears to have stiffened with time, as the f_n estimates have increased from the MODE to the MODE-Reflight tests, and from the MODE-Reflight to the most recent microdynamic experiments. With regards to the damping ratio, the general trend observed is increased ζ_n with time, contrary to the trend seen in the torsion mode. Based on the lack of consistency in the damping estimates for the bending mode between the older tests and the most recent, it is concluded that this parameter is particularly configuration-sensitive.

Microdynamic characterization of an erectable truss

A similar microdynamic investigation was performed by Ting, on an erectable truss structure [21]. His experiments focused on the characterization of damping within a tetrahedral truss structure, for strain levels from 10^{-9} up to 10^{-4}. The structure he tested, the SERC Interferometer Testbed, was composed of six identical 14-bay truss legs, which each measured 3.5 meters (11.5 ft) in length (see top view in Figure 2.56). The truss nodes and struts were all constructed of 6061-T6 aluminum, and were mated by screwing them together. The test procedure followed by Ting was similar to that described in section 2.2: stepped-sine sweeps were performed over the modes of interest, at different strain amplitudes, in order to obtain strain output FRFs, from which the damping ratio was estimated using the half-power bandwidth technique.

By comparing results from Ting's experiments and the microdynamic tests on the MODE STA, it was hoped that some conclusions could be drawn regarding the similarities and/or differences in the microdynamic behavior of erectable versus deployable truss structures. Selected results from Ting's experiments are presented in Figures 2.57 and 2.58. These plots show the damping ratio estimates versus strain amplitude for one mode of the structure, in the so-called "small strain range" and "large strain range", respectively. Different actuators were used to excite the structure in the two different ranges. Similar trends are observed in both experiments: the small strain range is evidently dominated by linear damping mechanisms (i.e. constant ζ_n), while the large strain range exhibits nonlinear damping behavior (increasing ζ_n with increasing ε_{peak}). The strain amplitude at which this transition occurs is around 1 $\mu\varepsilon$, the amplitude at which linear-to-nonlinear transition occurred in the microdynamic tests on the MODE STA. It should be noted that certain other modes tested by Ting did not exhibit any significant nonlinear behavior at all – their damping ratios were found to be essentially constant over the entire strain range tested.

The main conclusion drawn from the comparison of the two experiments is that, despite the presence of significantly more nonlinear mechanisms in a deployable structure, a lower limit in damping is reached nonetheless, once the vibration levels become small enough. For both the erectable and the deployable trusses tested, the mechanisms of this transition from nonlinear-to-linear are encountered as the strain amplitude falls below 1 με.

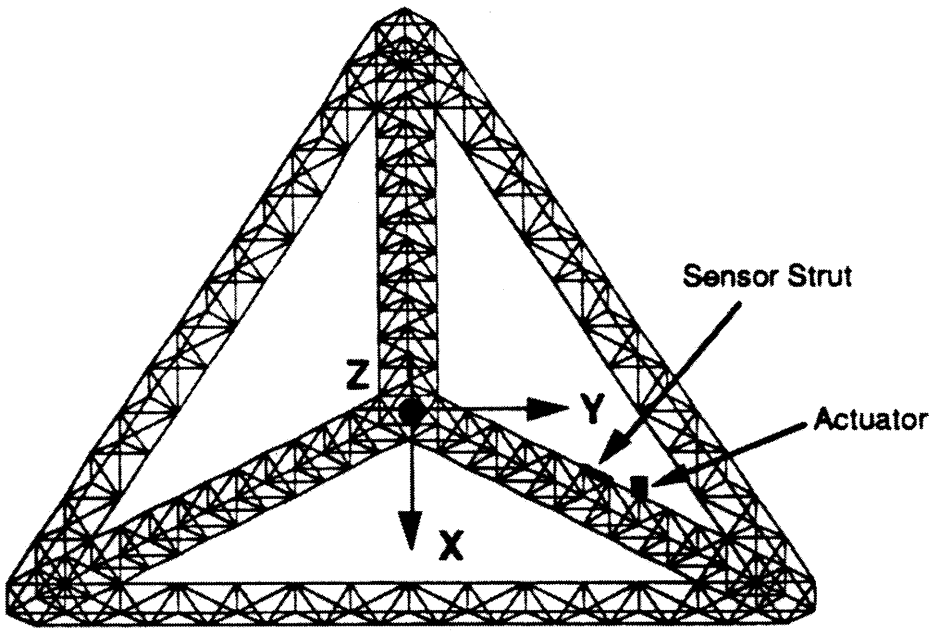

Figure 2.56 SERC Interferometer Testbed (top view)

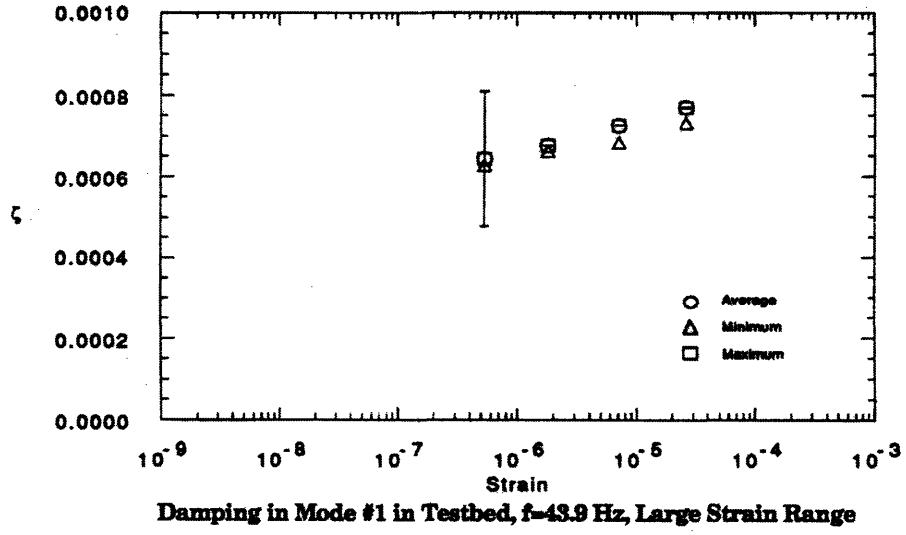

Figure 2.57 Microdynamic test results (erectable truss, high ampl) [21]

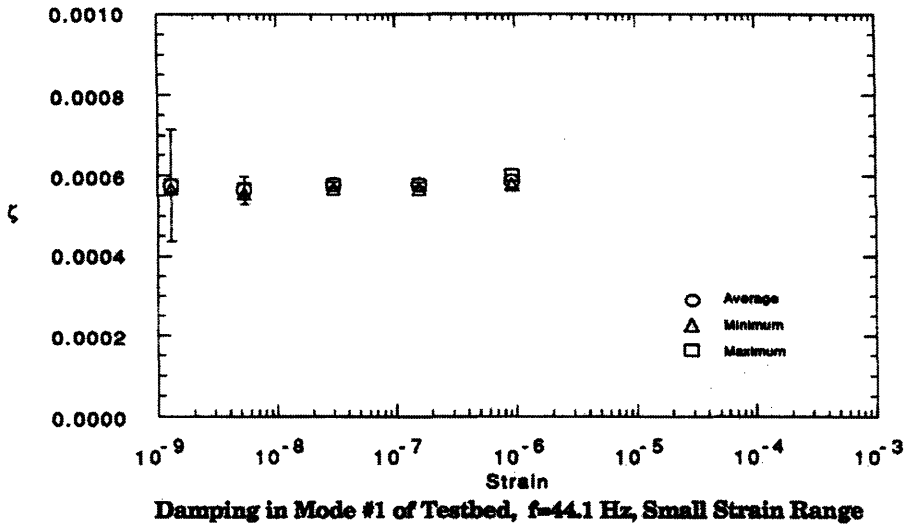

Figure 2.58 Microdynamic test results (erectable truss, low ampl) [21]

Chapter 3 – Thermal Snap Characterization

Due to stringent size limitations imposed by launch rocket shrouds or space shuttle payload bays, most spacecraft require deployment mechanisms for their extended appendages. For instance, solar arrays are typically unfolded once a satellite is released from the shroud or payload bay. Such deployment mechanisms are but one example of the numerous potential sources of nonlinear structural behavior on a typical spacecraft. As explained in section 1.1, any statically indeterminate structure with nonlinear friction interfaces is vulnerable to the disturbance phenomenon of thermal snap.

To date, very little work has been done to characterize thermal snap disturbances. Considering their potentially serious repercussions on the success of future precision space structures, such as the Origins Program telescopes, on-ground and on-orbit experiments must be conducted to better understand the nature of the disturbance. This chapter documents one such on-ground experiment, conducted on a deployable truss structure with a number of potential snap mechanisms. The first objective of this investigation is to determine whether thermal creak occurs in a preloaded deployable truss structure, when subjected to a thermal environment traceable to that encountered by a realistic spacecraft. If creak events are identified, the next goal is to characterize the ensuing structural response by traditional techniques, in both the time and frequency domains.

In the opening section of this chapter, the experiment setup is described. The test procedure for the thermal snap investigation is outlined in the next section, followed by a discussion of the measures taken to identify the observed structural events as due to thermal creak. The results of the tests and analysis are presented in the final section of the chapter.

3.1 Hardware Description and Experimental Setup

This section addresses the hardware, test facilities and instrumentation involved in this investigation of thermal snap. Subsection 3.1.1 deals with the deployable truss testbed, with focus on the particular mechanisms by which stored strain energy can be released. Also described is a "dummy" erectable truss bay used in some tests to confirm that the events observed were due to the deployable truss' nonlinear friction elements. The first subsection ends with a short discussion of the suspension system. The physical and thermal environments provided by the two test facilities are the subject of subsection 3.1.2. The various sensors and the data acquisition systems used in the tests are specified in subsection 3.1.3.

3.1.1 Structural hardware

The testbed used for this investigation of the phenomenon of thermal snap is the MODE STA deployable module with an adjustable pretension bay. The four-bay module was described in subsection 2.1.1, and in reference [29]. The chosen structure possesses several attributes which allowed it to meet the experimental objectives:

- Its compact size allowed tests to be performed in readily available thermal chambers.
- The different materials composing the module have significant mismatch in their coefficients of thermal expansion (CTE). As a member of the polycarbonate family of materials, Lexan has a relatively high CTE ($\approx 62.5 \times 10^{-6}$ ε/°C or 34.7×10^{-6} ε/°F). The CTE of the aluminum joints ($\approx 23.6 \times 10^{-6}$ ε/°C or 13.1×10^{-6} ε/°F) is less than half that of Lexan, while the steel diagonals have the lowest CTE on the structure ($\approx 14.5 \times 10^{-6}$ ε/°C or 8.06×10^{-6} ε/°F). An increase in the temperature environment results in a proportional increase in the preload.
- The design of the structure includes a number of nonlinear frictional mechanisms, which present the potential for thermal snap.

In order to understand the phenomenon of thermal creak, it is important to look at the different nonlinear mechanisms by which stored strain energy can be suddenly released. All the potential stick/slip interfaces in the design of the MODE STA deployable module are identified below. Subsequently, the dummy erectable bay used as a linear reference structure in some of the tests will be described. Finally, the suspension system used for the thermal snap tests will be discussed.

Details of nonlinear mechanisms

A number of possible mechanisms for snap are found within the longeron knee joint (see Figure 2.5). A frictional interface is found at the steel hinge pin, which was designed to snugly fit (to within some tolerance) through the holes in the mating aluminum joint pieces. The design clearance between the pin and the hole constitutes a very small frictional deadband, which provides a mechanism for stick/slip (and whose size will change with temperature due to the CTE mismatch between the steel pin and the mated aluminum parts). Other frictional interfaces are identifiable from the joint design, including those found at the contact surfaces between the plastic latch and mating aluminum joint part.

The batten frame corner fittings also offer a few potential creak mechanisms (see Figure 2.6). The contact surfaces between the longeron end lugs and the corner fittings provide frictional interfaces, which allow slip within the deadbands of the hinge pins. Also, every ball/receptacle interface (internal to the corner fittings) where the diagonal cables terminate is another possible source of stick/slip behavior (Figure 2.7). In the case of the adjustable pretension bay, the tensioning levers (Figure 2.8) present an obvious frictional contact surface where slip may occur.

Finally, two more nonlinear mechanisms can be attributed to the diagonal cables. At the center of each bay's outer faces two diagonal cables cross at a single contact point; any asymmetric deformation of the bay causes the cables to rub against each other. Also, the individual twisted strands which make up the cables can unwind as preload decreases due to decreasing temperature, although this mechanism is unlikely to transmit measurable disturbances to the truss.

Other nonlinear friction mechanisms are introduced at the connection points of the suspension system, and between the truss and the attached electronic wiring. Stick/slip events due to these mechanisms "external" to the truss are not of interest because they are dependent on the experimental setup, and are not traceable to realistic space structure thermal snap problems. The various measures taken to confirm that events detected on the deployable truss were truly due to slip in the internal nonlinear mechanisms, and not due to other sources, will be addressed in section 3.3.

Erectable truss bay

One of these measures employed was the simultaneous testing of a "dummy" structure without any nonlinear slip elements: during some of the tests, a nominally linear structure was suspended next to the deployable module and was subjected to the same thermal environment. The dummy structure used was the calibration bay that Masters used for his MDOF force-state component identification experiment [31]. This erectable bay is shown in Figure 3.1. The longerons, diagonals and battens are all 0.375 inch (9.5 mm) diameter Lexan rods. They are epoxied into cube-shaped aluminum nodes, 1.25 inches (31.75 mm) on a side, with Hysol EA 9394NA structural adhesive. The erected bay is the same size as each bay in the deployable module, 8"x8"x8" as measured from the centers of the nodes.

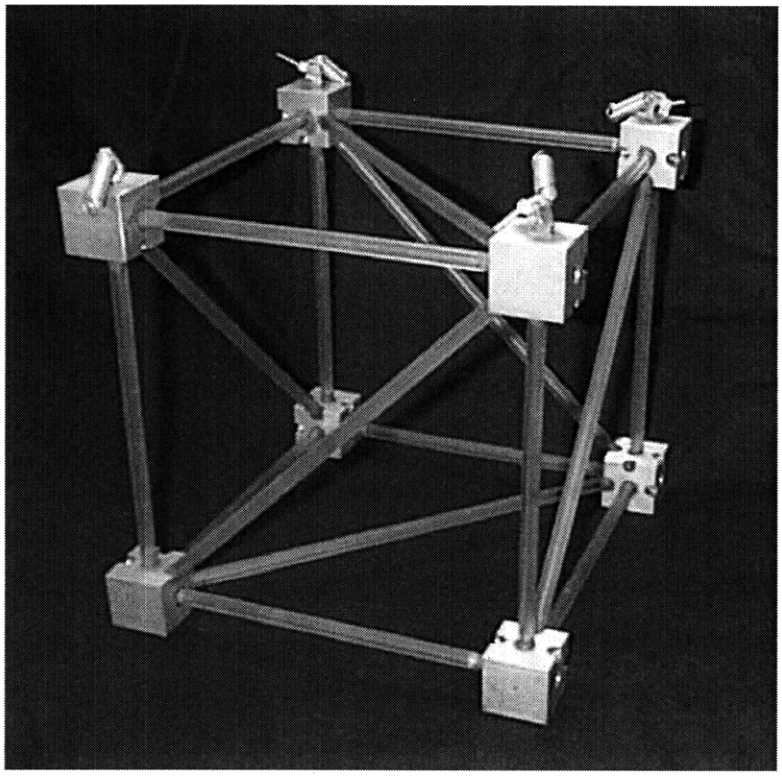

Figure 3.1 Dummy erectable truss bay

Suspension

For such an experiment, where the objective is to measure the structural response to an internal disturbance like thermal snap, it is critical to properly isolate the system from external disturbances, particularly those which are impulsive in nature and risk being mistaken for events of interest. The suspension/isolation system takes on an even more important role, considering that thermal test facilities can produce significant vibration environments. For the purposes of this investigation, a simple suspension system was chosen: four steel springs were attached to the four upper corners of the truss module with the help of plastic locking ties, as shown in Figure 3.2. These springs provided a fundamental bounce mode just under 2 Hz. As will be discussed in subsection 3.1.3, evidence of the impulsive snap events was to be detected at relatively high frequency levels, on the order of 1 kHz or greater; consequently, the transmission roll-off of the chosen springs was more than adequate. In the tests where it was used, the erectable bay was suspended with similar springs.

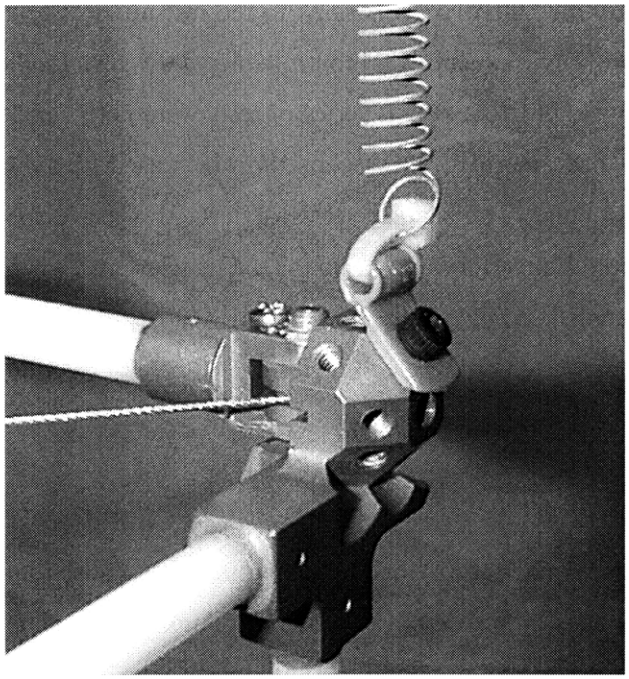

Figure 3.2 Detail of spring connection

3.1.2 Thermal Source

In order to induce slipping of frictional interfaces in the preloaded deployable truss structure, a significant enough change in the temperature environment had to be applied, such that the CTE mismatch between the different elements of the structure produced a large enough change in the internal stresses of these elements. Due to insufficient knowledge of the friction properties of the truss joints, the amplitude of the change in temperature required to induce snap could not be accurately predicted. Instead, the temperature range was set as wide as possible, bounded by physical limitations of the truss structure. Since the longerons were nominally preloaded to 50% of their buckling load, it was decided to concentrate most of the temperature range for the tests below room temperature, rather than risk damage to the truss. The upper temperature limit was therefore set conservatively at 50°C, while the lower limit was set at –30°C, the point at which the diagonal cables are expected to slacken completely (i.e. preload reduced to zero). Decreasing the temperature any further would impose no change in the internal stress state of the truss, thus precluding the occurrence of slip at the frictional interfaces.

The best way to apply this "thermal excitation" to the test article was to place it in a chamber where the temperature environment was controllable. Two test facilities with different heat transfer mechanisms were utilized. A first series of tests were performed in a thermal chamber at Payload Systems Inc., of Cambridge, Massachusetts, which used forced convection to change the temperature of the structure. The second series of tests was performed in a thermal vacuum chamber at MIT Lincoln Laboratory, in Lexington, Massachusetts, where heating and cooling of the truss was accomplished via radiation. In this subsection, the physical and thermal environments provided by each of these two facilities will be described in more detail.

Convection

A convection thermal chamber at Payload Systems, Inc. was chosen as the facility for the first series of thermal snap tests on the deployable truss module. The chamber measures roughly 4' x 4' x 4' (1.2m x 1.2m x 1.2m), large enough to accommodate the 2.7-foot-long truss. Feed-through holes in the chamber walls provide access to the interior during operation. The temperature inside the chamber is regulated via a controlled system, in which air is heated or cooled and circulated through the chamber with fans. The desired target temperature is set on the control panel of the chamber, and the temperature control system activates the heater or refrigerator cycles, as

required for the ambient temperature to attain the target temperature. Once the air blowing through the chamber reaches the set temperature, the control system regulates the chamber to maintain that temperature.

The refrigeration and heating cycles employ pumps and valves, which cause significant background vibration during operation of the chamber. Additionally, the turbulent air blowing through the chamber caused the structure to noticeably sway and bounce on its suspension. The nature of these low frequency vibrations transmitted to the structure is evident in measurements made of the background noise level on the truss. The bottom plot in Figure 3.3 shows acceleration time signals measured on the truss, with the chamber machinery turned on and off. The top plot presents the autospectra of the acceleration response on the truss due to background noise, for both "blower on" and "blower off" cases. The peak visible just under 3 Hz corresponds to one of the fundamental suspension modes. During chamber operation, the blowing air excites the truss at this frequency, and the resulting oscillations can be seen in the acceleration time trace. The next big peak seen in the "blower on" spectrum occurs at roughly 43 Hz, which corresponds to the first flexible mode of the deployable module. Clearly, it would be impossible to distinguish the low-frequency truss response to a thermal snap from the rest of the background noise. However, the isolating effect of the suspension system is seen in the roll-off of the spectra, particularly the "blower on" spectrum. By focusing the hunt for thermal snap at frequencies two to four orders of magnitude higher than those shown in Figure 3.3, vibrations due to the chamber operation are effectively filtered, resulting in a noise floor low enough to detect the structural events of interest.

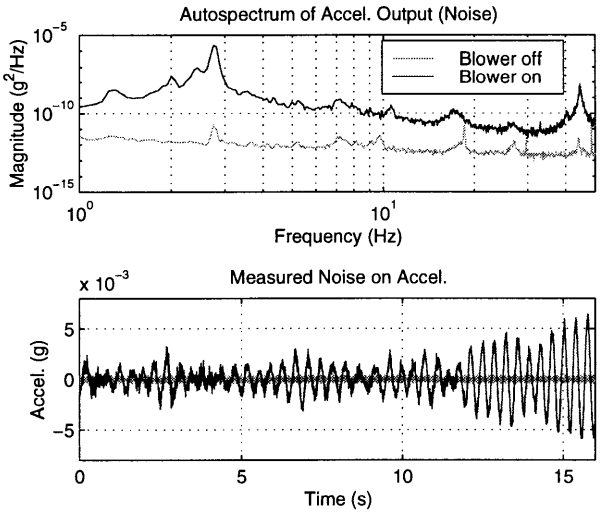

Figure 3.3 Noise due to convection chamber

Radiation

The other series of thermal creak tests were performed in a thermal vacuum chamber at MIT Lincoln Laboratory. The cylindrical chamber has a diameter of roughly 5 feet (1.5 m), and is approximately 6 feet (1.8 m) long. Two stages of pumps are used to evacuate the chamber to less than 10^{-4} torr (on the order of 10^{-7} atmosphere). A cylindrical aluminum shroud lines the chamber walls. By circulating cold liquid nitrogen through distributed tubing on the outside of the shroud, the black-painted inner surface of the shroud becomes a heat sink; the structure placed inside the shroud is cooled as heat is radiated away. The surface of the shroud rapidly attains temperatures close to that of the liquid nitrogen (around –200°C), so the amount of heat transferred is high. In order to heat the structure, the reverse process is followed. Hot nitrogen gas is pumped through the tubes on the shroud, heat conducts through the thin shroud to the inner surface, where it is radiated to the structure placed inside the shroud.

Figure 3.4 shows a photo of the deployable truss suspended in the chamber. The black surface behind the truss is one end of the cylindrical shroud. Also visible in the photo are cables leading to various sensors on the structure and on the shroud. Electrical connections between the data acquisition systems outside the chamber and the instrumentation inside the chamber are made via special sockets built into the walls.

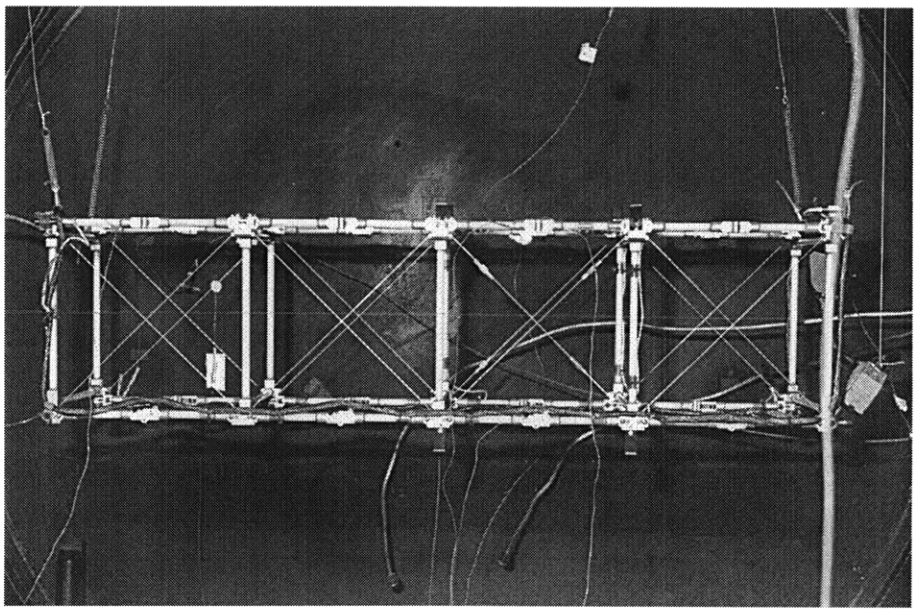

Figure 3.4 Deployable truss suspended in thermal vacuum chamber

Performing the tests in an evacuated chamber eliminates a number of the potential sources of non-thermally-induced structural events, as will be discussed in section 3.3. In addition, the amplitude of the noise floor at low frequencies is dramatically decreased, in the absence of blowing air. The background noise for the radiation test measurements consists of the suspension-attenuated chamber vibrations, and electrical noise. Moreover, the heat transfer by radiation was more traceable to the thermal environments encountered by orbiting space structures.

3.1.3 Sensors and data acquisition

Because of the impulsive nature of thermal snap disturbances, it is suspected that they can provide a reasonably broadband excitation to a structure. Very little work has been done in the past to characterize this type of disturbance, so a firm prediction of the frequency range and bandwidth of the excitation could not be made. The heretofore poor understanding of the phenomenon also made it difficult to predict which modes of the deployable truss would be excited strongly enough to be observed. Based on the location and line of action of the nonlinear mechanisms in the structure, it is quite possible that the most significantly excited modes would be high-frequency local modes (e.g. axial modes of the truss longerons). Furthermore, low-frequency response due to snap would be difficult to identify through the low-frequency noise induced by the convection thermal chamber. It was therefore decided that this experiment would focus on relatively high-frequency dynamics (on the order of 1 kHz to 100 kHz). The criterion for selecting appropriate sensors for detection of thermal snap events was thus established: the bandwidth and sensitivity specifications of the sensors should allow them to detect the potentially small vibrations resulting from slip in a nonlinear mechanism.

Various combinations of accelerometers, strain gauges, and thermocouples were used throughout the series of tests, in order to acquire information on the events (if/when they occurred), as well as on the temperature and stress state of the truss. Sensors were also used to measure the vibration and temperature levels of the surrounding environment in the thermal chambers. In this subsection, each of the types of sensors is addressed, with focus on their specifications relevant to this experiment. The combinations of sensors used for the different tests, as well as their distribution across the structure, varied from test to test; this information will be presented along with the results from each test, in section 3.4. The data acquisition systems used to read and store the data from the sensors are discussed at the end of this subsection.

Accelerometers

The amplitude of acceleration for an oscillating harmonic system is related to the amplitude of displacement by a factor of frequency squared:

$$\left|d^2x/dt^2\right| = \omega^2|x|$$

Due to this "amplification" factor at high frequency, accelerometers provide a good means of detecting high-frequency structural events, such as would be caused by thermal creak.

Two different types of accelerometers were used in the thermal creak investigations. Six Endevco Model 7265A-HS piezoresistive accelerometers originally used in the MODE and MODE-Reflight experiments were previously mounted to the deployable module, and were available for measuring the structural response to snap events. The operating temperature range and bandwidth specifications for these sensors are given as 0°F to +150°F (-18°C to +66°C) and 0 to 500 Hz, respectively. In this experiment, the Model 7265A-HS accelerometers were used beyond these temperature and frequency ranges. In addition, up to six Endevco Model 2222C piezoelectric accelerometers were used in the tests, both for detecting events on the structure, and for characterizing the vibration environment in the thermal chamber. These small, lightweight accelerometers have a much higher bandwidth than the Model 7265-HS: their frequency response is specified in the range from 5 Hz to 8000Hz. Their operating temperature range is from -100°F to +350°F (-73°C to +177°C). It should be noted that no correction was made to the sensitivities of either type of accelerometer to account for temperature effects, but the amount of acceleration amplitude error introduced by these effects should be less than 5% over the temperature range of interest, based on the manufacturer's specifications.

Strain gauges

For the original MODE experiment, one face of the adjustable pretension bay on the deployable module was instrumented with four resistive strain gauge bridges. Gauges wired in full bridge configurations provided temperature-compensated measurements of axial strain in the two longerons and two diagonals on the instrumented bay face. In the few tests during which they were used for snap detection, it was found that the strain gauges were not as effective as the accelerometers. This was due to their inherent noisiness, coupled with the fact that they do not

benefit from the accelerometers' frequency-squared amplification, as discussed previously. It turned out that thermal snap vibrations detected with the gauges were barely above the noise floor. However, they were used more effectively to measure the change in truss preload over the course of a temperature cycle.

Thermocouples

In order to keep track of the temperature of the truss structure, as well as its surrounding environment, Type K thermocouples were used. The precision of the temperature measurements made with the thermocouples was highly dependent on the data acquisition system used to take the readings (see below). Any errors in accuracy due to the calibration of the thermocouples were assumed negligible.

Data acquisition

For this experiment, important decisions had to be made regarding how the snaps would be detected and recorded, should they occur. One important consideration was that significant periods of time would pass, during which stress would be building up as a result of temperature loading, but no events would be observed on the structure. If/when an impulsive thermal creak event did occur, a high sampling rate would be required (on the order of tens of kHz), in order to characterize the high-frequency response of the truss. Rather than continuously recording the output signal from each accelerometer or strain gauge, which would have generated an unreasonably large quantity of (mostly uninteresting) data, it was decided that the sensor outputs should only be recorded upon detection of a potential snap event. This required a high-bandwidth data acquisition system, which could somehow be triggered by the occurrence of the event.

The data acquisition system chosen was the Tektronix Personal Fourier Analyzer unit. Two versions of this system were used over the course of the experiment. The Model 2630 has four input channels with adjustable bandwidth up to 20 kHz, each of which can be AC- or DC-coupled. The sampling rate is 2.56 times the bandwidth setting. For instance, if the 20 kHz bandwidth setting is selected, the data is sampled at 51200 samples per second. The Nyquist frequency is therefore 25.6 kHz. The top 22% (5.6 kHz, in this example) of the Nyquist band is potentially affected by the rolloff of the anti-aliasing filter, and is not guaranteed to be alias-protected [44]. An essential feature of the Tektronix unit is its triggering capabilities: it can be

configured to record the four channels of data, when a user-defined threshold signal level is exceeded on one predetermined channel. The other version of the Tektronix unit, Model 2640, is similar to the 2630, but it allows bandwidth settings up to 100 kHz. Both models are connected to PCs for user interface and data storage purposes.

One or two of these data acquisition units were used during each thermal snap test. For the convection tests at Payload Systems, Inc., two Model 2630 units were available, whereas for the radiation tests at Lincoln Laboratory, one of each version was employed. It should be noted that the Model 2640 unit used in these tests only had three input channels available. An improvement to the data acquisition system was added for some of the later tests at Lincoln Laboratory: a circuit was wired which enabled both Tektronix units to be triggered simultaneously if any of the sensors detected an event. This added feature reduced the chances of missing a thermal snap if the response happened to be unobservable from the sensors connected to each unit's chosen trigger channel.

In addition to the data acquisition systems required for thermal creak detection, an independent system was needed to keep track of the temperature measurements from the thermocouples. For the tests at Payload Systems, Inc., the thermocouple wires were connected to an Omega Model DP25-K-A-DSS thermometer box with a digital readout. The temperatures were recorded manually, with a precision of 0.1°F (0.06°C). For the radiation tests at Lincoln Laboratory, temperature data acquisition was automated via a Hewlett-Packard 3852A control unit. This unit was connected to a PC running National Instruments LabView experimental control software, for the display and storage of the various temperature measurements.

3.2 Test Procedure

The approach taken in this investigation of the thermal snap phenomenon was straightforward: thermal load was applied to the deployable truss, and the data acquisition system recorded any snap-like events when they occurred. In this section, this general approach is detailed, for the two types of thermal source used. It should be noted that the procedure evolved from test to test, as various measures were successively taken to distinguish thermally-induced structural events from other events. Any relevant deviations from the general test procedure described here will be addressed in section 3.4, with the results from the particular test in question. After presenting the

procedure for both the convection and radiation tests, the data reduction process will be discussed.

Convection

The first step taken was to suspend the truss in the convection chamber. The four springs were directly attached to the ceiling, screwed into thick foam insulation lining the inside of the chamber. For the tests where the dummy truss was being used, it was suspended next to the deployable truss from the ceiling in similar fashion, with reasonable distance between the two structures to allow for contact-free swaying, once the blower was turned on.

The next step was to instrument the truss with the various sensors. While the Endevco 7265A-HS accelerometers and the strain gauge were pre-mounted on the structure, the Endevco 2222C accelerometers had to be attached, at predetermined locations which varied from test to test. The forced convection heat transfer resulted in a very uniform temperature distribution across the truss; consequently, only one thermocouple was required to keep track of the temperature at the surface of the structure. Another thermocouple was hung from the ceiling, providing a measurement of the ambient temperature in the chamber. The accelerometer and thermocouple wires hanging off the truss were taped to the chamber walls, with enough slack to minimize possible transmission of vibrations to and from the structure.

Before starting the thermal cycle, the bandwidth settings on the Model 2630 Tektronix data acquisition unit(s) were set to the appropriate levels. For most tests, the bandwidth was set to the maximum possible level of 20 kHz. The amplitude at which the data acquisition units triggered the recording of an event was set just above the background noise level, so as to minimize the number of events missed due to overly high threshold amplitude.

The number of thermal cycles performed on each day of testing varied, as did the temperature amplitudes reached – not all tests covered the full allowable temperature range from –30°C to 50°C; particular details of the individual tests will be presented with the results. It is not known how the rate of temperature change affects the likelihood or nature of thermal snap behavior. A complete investigation of the effects of temperature rate was beyond the scope of this preliminary characterization experiment. For the present purposes, it was decided to attempt to simulate the worst-case on-orbit thermal load, seen when a spacecraft passes in or out of planetary shadow. To

this end, the chamber temperature was decreased or increased as rapidly as possible, until the target temperature was reached. At this point, the ambient temperature was maintained until the temperature of the structure reached approximately steady-state.

The temperature data presented in Figure 3.5 shows a sequence of representative thermal cycles from a convection test. Temperatures measured with four different thermocouples are plotted in the figure: sensors T5, T7 and T8 were attached to a Lexan batten member, an aluminum corner joint, and a steel diagonal cable, respectively, while T9 was hung from the ceiling to measure the ambient temperature. Very little difference is observed between the four curves, which indicates that the temperature of the structure varies quite uniformly, and follows closely the temperature of the air in the chamber. The figure shows that, for this particular test, the temperatures begin at room temperature at time zero, and drop to roughly –18°C in an hour. Once thermal equilibrium was attained on the truss, the heaters were turned on, and the temperature climbed to just under 45°C. It is evident from the figure that the heating rate was noticeably higher than the cooling rate: the temperature increased from –18°C to 40°C in only ten minutes. The 120-minute point marks the start of the second thermal cycle. As mentioned in subsection 3.1.2, the upper temperature limit was set conservatively, so as to avoid overstressing the longerons. It was therefore reasoned that thermal snap would be more likely to occur during the cooling process, when the change in stress with respect to the nominal (room temperature) stress would be greater. Consequently, the temperature was only brought back up to room temperature during the second heating phase, so that a third cooling phase could be undertaken.

When the data acquisition systems were triggered by signals on the trigger channels which exceeded the threshold settings, the resulting time traces were stored on the control PCs. For the tests where two Tektronix data acquisition units were used, no common triggering electronics were employed: each unit was triggered individually, by one of the sensors connected to it.

At the end of the test, the chamber was returned to room temperature, and the test article was removed from its suspension. The deployable truss was then folded up, to be re-deployed prior to the next thermal snap test. This practice ensured a consistent initial condition for the frictional joints. It is suspected that the likelihood of thermal snap occurrence would be adversely affected by letting the deployed truss remain suspended over an extended period of time, as gravity preload effects may cause the joints to "lock", in a microdynamic sense.

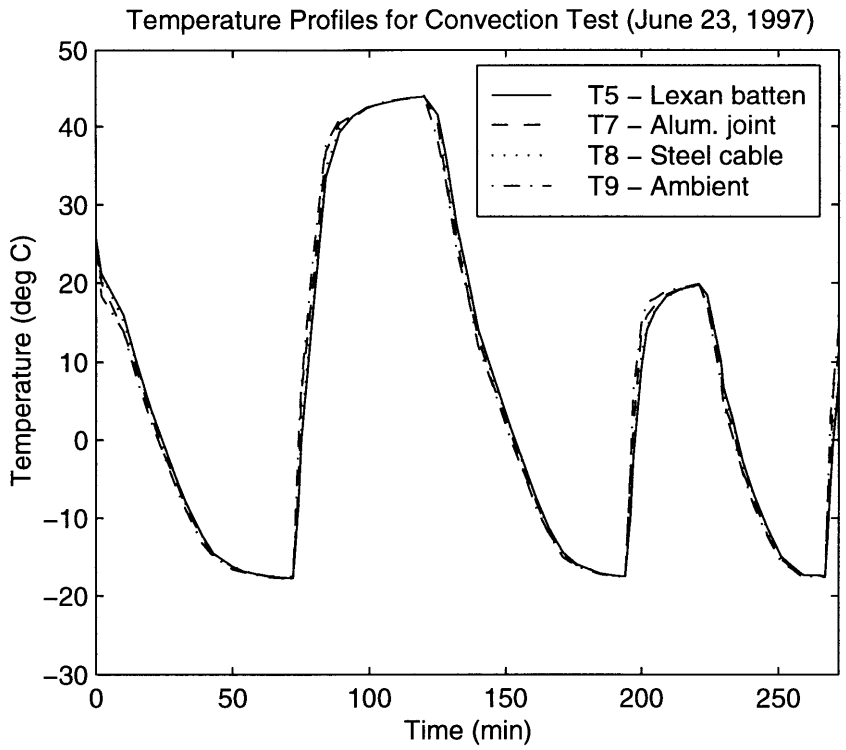

Figure 3.5 Typical convection thermal cycles

Radiation

A space environment simulation chamber was used to provide the radiation cooling and heating for the second series of thermal creak tests. The first step was to suspend the deployable module, with aluminum wire running from attachments at the top of the shroud down to the top of the springs (see Figure 3.4). It should be noted that the dummy truss was not used during any tests in the thermal vacuum chamber. The deployable truss and surrounding shroud were then instrumented with the various sensors to be used for snap event detection and temperature state measurement. The sockets in the walls of the vacuum chamber only allowed for the connection of up to six 2222C accelerometers and one strain gauge. No 7265A-HS accelerometers were used during the tests at Lincoln Laboratory. The thermocouple sensor connections, however, were made through separate sockets; the number of thermocouples available for the tests was not subject to the same stringent limit as the other sensors. As many as 9 thermocouple channels were employed to keep track of the temperature at different locations on the structure and chamber.

Unlike the case of forced convection, heat was transferred to and from the truss very non-uniformly. Several factors contributed to the non-uniform temperature distribution across the deployable module:

- the difference in the radiation absorptivity and emissivity properties of Lexan and aluminum;
- the lower thermal mass of Lexan compared to aluminum, which implies a lower thermal time constant (thermal mass is defined as mass multiplied by specific heat c_p);
- the non-uniform temperature distribution across the radiation source (the temperature at the bottom of the shroud changes much more rapidly than does the temperature at the top, so the bottom members of the truss, with an unobscured view of the bottom of the shroud, are subject to greater radiation heat transfer – see discussion below).

After all the sensors were connected, the data acquisition units were adjusted to the appropriate bandwidth and trigger amplitude settings. The chamber was then shut and the evacuation pumps were turned on. Once the chamber was evacuated to a pressure on the order of 10^{-4} torr, the thermal cycling could begin. Figure 3.6 presents a representative plot of the truss and shroud temperatures, as measured during one of the thermal snap tests at Lincoln Laboratory. All temperatures start around room temperature; at the 20-minute mark, a valve was opened, allowing liquid nitrogen to flow into the shroud. As the liquid N_2 entered the tubing at the bottom of the shroud, it began to boil, slowing its progress around the outside of the shroud. This resulted in a significant lag in the temperature drop between the bottom of the shroud and the top. The temperature at the bottom of the shroud dropped rapidly, decreasing to –170°C within 7 minutes, while the top did not quite reach –100°C. In this time, the worst-case temperature on the truss dropped below 0°C. The liquid nitrogen valve was then immediately shut, and another valve was opened, causing the shroud to begin filling with hot nitrogen gas. The temperature of the gas could be varied, but was generally set between 30°C and 75°C. While the temperature at the bottom of the shroud began rising instantly, lags in the other temperature response measurements were observed. The worst-case surface temperature of the truss (measured on a Lexan batten member located on the bottom face of the structure) would ultimately drop to between –25°C and –30°C, before starting to increase again. The procedure of applying this type of uncontrolled "thermal impulse" to the structure had to be carefully followed: a delay of one minute in the closing of the liquid N_2 valve would result in overshoot of the established lower temperature limit for the truss, by as much as ten or more degrees centigrade.

An alternative procedure was followed for two of the tests in the thermal vacuum chamber, which avoided the risk of temperature limit overshoot on the truss. Instead of using the entire shroud as the heat sink/source, a 4' long x 1' wide x 1" thick copper plate with distributed tubing on its underside was placed 6" beneath the suspended truss. A control valve was used to feed liquid or gaseous N_2 through the plate's tubing, in order to maintain a fixed temperature on the plate. A thermocouple attached to the black-painted plate provided the control measurement. By keeping the plate temperature fixed at the established lower temperature limit for the truss, the possibility of overshooting the limit was eliminated, at the expense of a decreased rate of temperature change. In order to minimize radiation losses to the surrounding shroud during these controlled radiation tests, a three-layer reflective foil thermal blanket was placed over the truss and plate.

As for the tests in the convection chamber, time traces of the sensor output signals were only recorded when a signal was detected on the trigger channel exceeding the threshold setting on a Tektronix data acquisition unit. For a few of the later radiation tests, two Tektronix data acquisition units were used in conjunction with the common triggering circuit described in subsection 3.1.3, thereby reducing the likelihood of "missed" events.

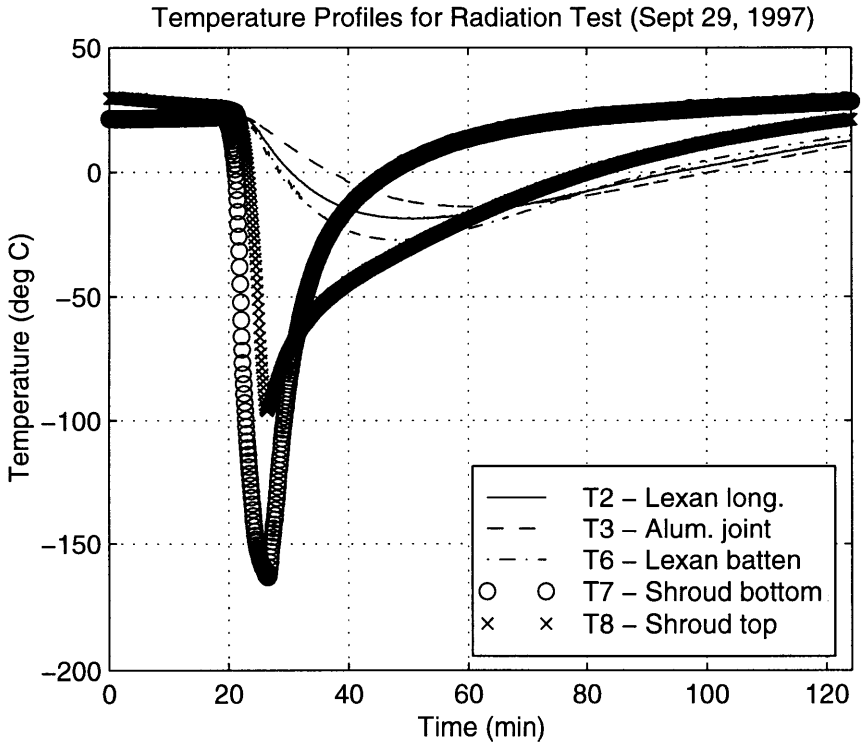

Figure 3.6 Typical uncontrolled radiation thermal cycle

Data reduction

The data taken from each event consists of time traces from all channels of the triggered data acquisition units, corresponding to readings from all accelerometer or strain gauge sensor locations. Each time trace contains 4096 points; the duration of the trace depends on the bandwidth setting of the corresponding data acquisition unit. In addition, the temperature data taken for each test is available, and is used to correlate the events with the ambient and structural temperature state.

In order to characterize the events recorded, traditional time- and frequency-domain techniques are employed. First of all, the time traces themselves can provide information on the nature of the event: the amplitude of the response, the dominant mode or modes observed in the trace, and the amount of damping in the ring-down response of a dominant mode. Furthermore, by computing Fourier transforms of each signal over short time intervals, the frequency spectra can be obtained. These spectra can be represented in spectrogram plots, which provide estimates of the short-term, time-localized frequency content of the signals. Alternatively, the power spectral densities (PSDs) of the time traces can be computed, to give a general idea of the frequency content of the truss response. While the PSD is traditionally considered in the context of characterizing stationary random processes, this mathematical tool can also provide a rough frequency characterization of deterministic response signals, such as the impulsive transients from thermal snap events.

To illustrate the various time- and frequency-domain characterization techniques employed, a sample event is considered. Figure 3.7 shows sample data from an event detected during a radiation test at Lincoln Laboratory. The response at a single accelerometer location is plotted here versus time; clearly, the structural ring-down transient is evident, starting around zero seconds. The time-varying frequency content of the signal can be effectively visualized using a spectrogram, as plotted beneath the time trace in Figure 3.7. The spectrogram was generated by dividing the signal into overlapping 128-point segments, windowing each segment with a 128-point Hanning window, and computing the Fourier transform of each windowed segment. An overlap of half the window size (i.e. 64 points) was chosen. Each vertical "slice" through the spectrogram represents the spectrum computed from a time interval corresponding to one 128-point segment. Darker shaded areas represent more significant content at a given frequency. Looking at the portion of the spectrogram near time zero, the broadband nature of the disturbance is evident, as the dark stripe extends across the entire frequency range. Immediately after the

initial broadband event, the response becomes concentrated at a few particular frequencies: 9 kHz, 14.5 kHz and 18kHz. Presumably, these frequencies correspond to modes of the structure, which are being excited by the thermal creak disturbance.

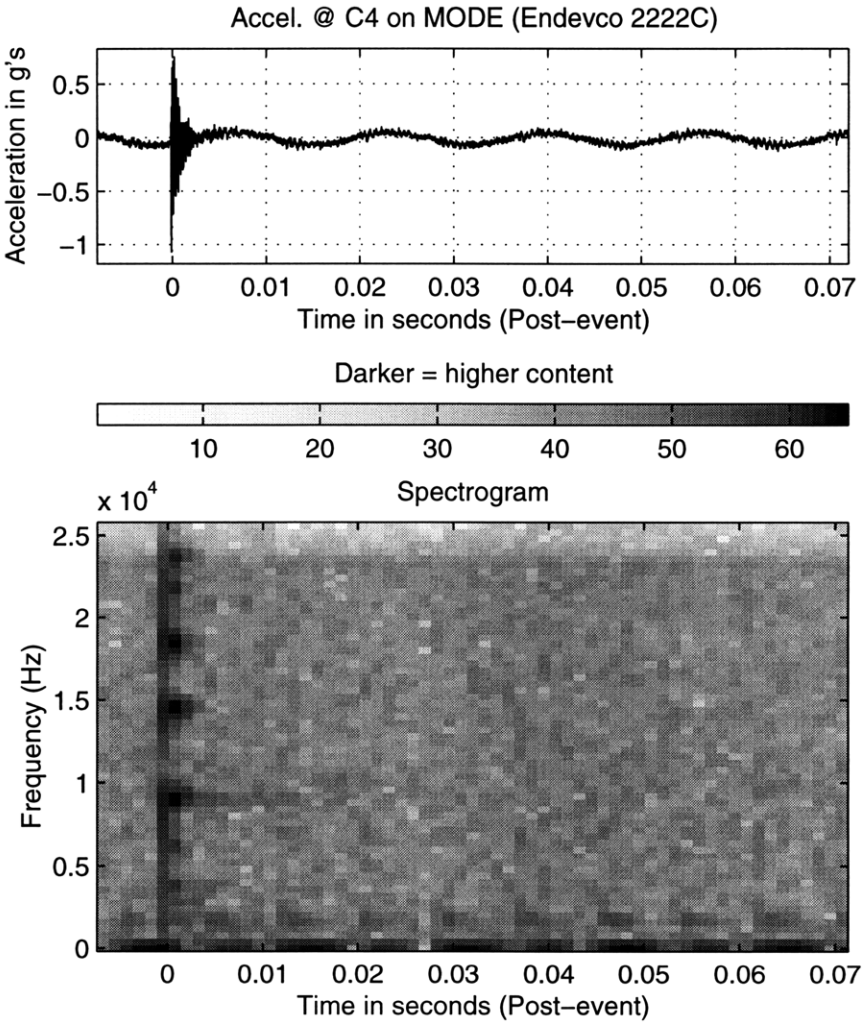

Figure 3.7 Time trace and spectrogram of sample snap event

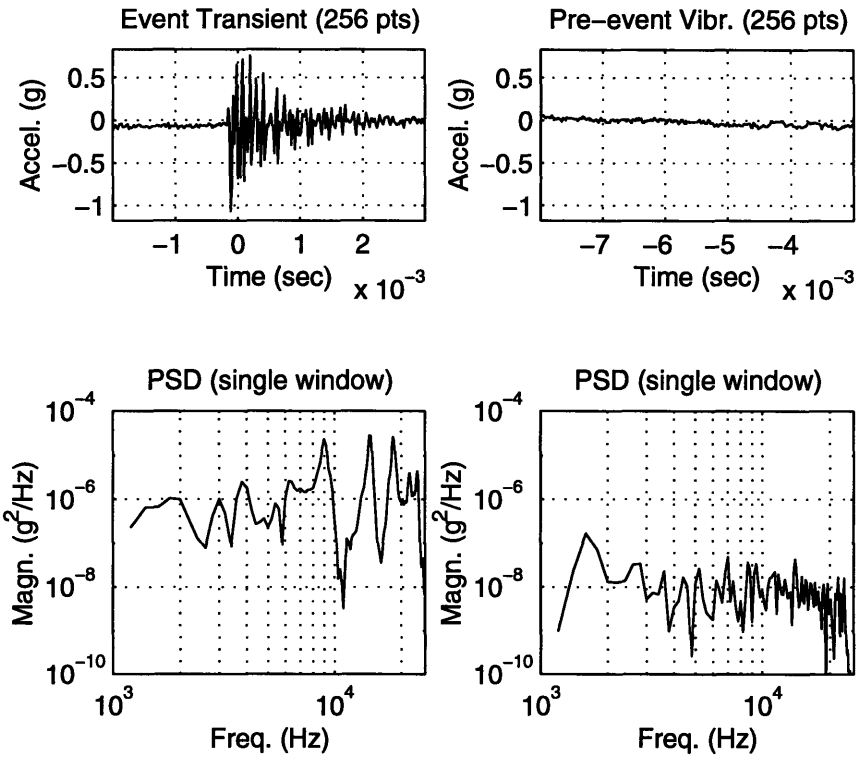

Figure 3.8 Truncated sample data (256-point windows)

An alternative way to perform the frequency-domain characterization would be to compute the PSD of the event transient. Rather than computing the PSD based on the full time trace, of which the event may only represent a small fraction, the data can be truncated to focus on the snap event. Proper selection of the window is important, as the Fourier analysis via PSD is rather sensitive to the windowing process: choosing too large a window, or not centering it around the event transient results in inaccurate representation of the modal content of the signal. The two plots on the left-hand side of Figure 3.8 show the truncated data and the corresponding PSD; a single 256-point Hanning window was convolved with the time trace shown, prior to computing the spectrum. For comparison purposes, a 256-point time trace of the pre-event vibration is presented on the right-hand side of Figure 3.8, along with the corresponding PSD. The differences between the two PSDs represent the frequency content of the response to the thermal snap disturbance. The PSD of the event transient is generally higher than that of the pre-event response; this is an indication of the broadband nature of the disturbance. The peaks in the left-hand side PSD represent the particular frequencies at which truss response was excited. The same structural modes are evident as in the spectrogram, located around 9 kHz, 14.5 kHz and 18kHz. In general, however, frequency-domain characterization via PSD analysis does not provide

information on time-varying frequency content as effectively as the spectrogram, so the latter technique will be used to analyze the results from the bulk of the thermal snap tests.

A time-domain characterization of the event can also provide valuable information on the frequency content and damping of the transient vibration. Figure 3.9 shows a zoomed-in view of the sample event transient. The multi-mode nature of the transient vibration, which was shown in the frequency-domain analysis, is also evident in this time trace. In order to extract the portion of the response due to a particular mode of the truss, a narrow bandpass filter can be used. The middle plot of Figure 3.9 shows the transfer function characteristics of an eighth-order bandpass Butterworth filter, with pass-band between 8800 Hz and 9200 Hz. Since the filtering is being performed on the data during post-processing (i.e. the full data trace is available), a non-causal filtering technique can be used to eliminate phase distortions in the filtered response. The resulting filtered signal corresponds to the truss response at the 9 kHz mode, and is shown in the bottom plot of Figure 3.9. While some signal amplitude may be lost due to the filtering process, and some startup transients may be present, this filtered signal should nonetheless be a fairly good approximation to the true 9 kHz mode response, particularly once the startup transients have died out.

The modal damping can be estimated, by fitting an expression for an exponentially-decaying sinusoidal function to a truncated portion of the filtered trace. This simple SDOF time-domain technique is based on the assumption that the free decay response of a single-mode system is given by:

$$y = Ae^{-\zeta\omega t}\sin(\omega t + \phi)$$

where ζ is the modal damping ratio (a viscous damping model is assumed), ω is the frequency of the mode, ϕ is the initial phase angle, and A is a scaling amplitude factor. Figure 3.10 shows a truncated portion of the filtered signal, overlaid with the exponentially-decaying sinusoid fit. Clearly, the fit does a reasonably good job of representing the filtered signal; however, after the 1.5 millisecond point, the filtered signal becomes more heavily damped than the fit. This may indicate that another damping mechanism takes over once the amplitude of oscillation gets small enough, which cannot be accurately modeled using a single-mode decay. The value of the ζ obtained from this fit is roughly 2%. It should be noted that this damping estimate would include the effect of any apparent damping which might be occurring, due to energy transfer to other

modes [13]. Nonetheless, such a ζ value is consistent with the level of damping expected in a high-frequency local mode of a jointed structure made of Lexan and aluminum.

In summary, various time- and frequency-domain characterization techniques have been demonstrated here on the sample data trace. These are the methods which will be used to analyze the results from the thermal snap experiment, to be presented in section 3.4.

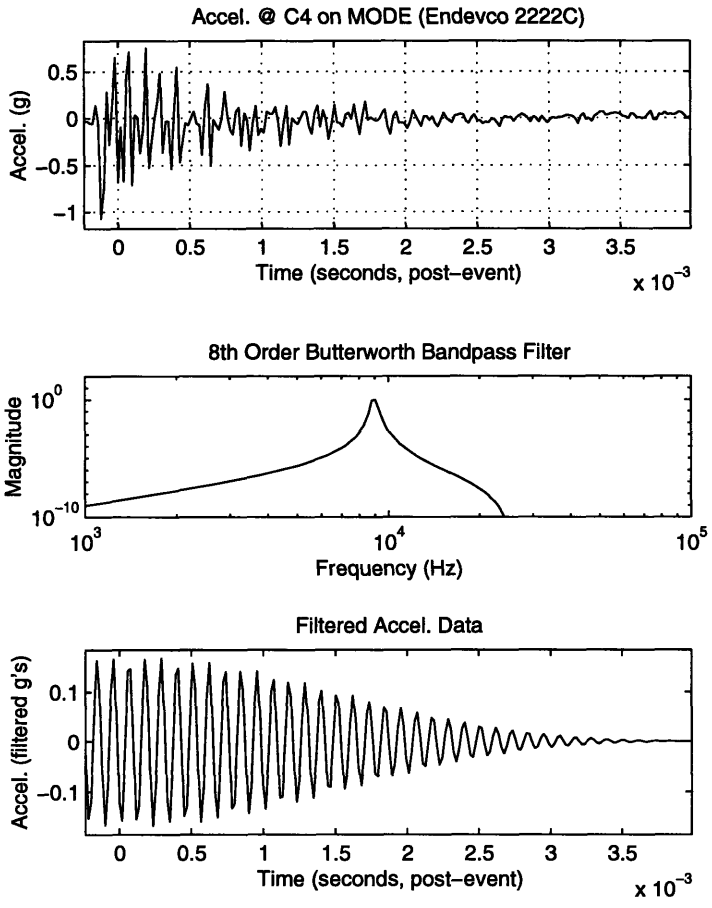

Figure 3.9 Truncated and filtered transient event data

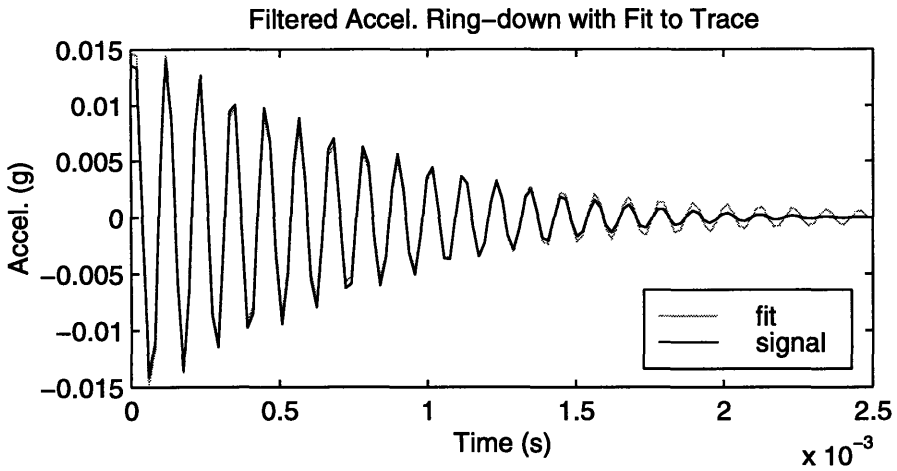

Figure 3.10 Exponentially-decaying sinusoid fit to filtered event

3.3 Measures Taken to Identify Thermal Snap

In an investigation of this kind, great care must be taken to ensure that vibration events due to the phenomenon of interest – thermal snap, in this case – can be identified as such. This section highlights the recognizable characteristics of thermal snap events, and documents the different measures taken to distinguish events due to thermally-induced structural vibrations from events due to other sources.

Although a review of the existing literature has turned up very few actual observations of the phenomenon, certain expected characteristics of thermal creak can be identified, through knowledge of a structure and its frictional mechanisms, combined with simple models of the disturbance, such as those developed by Kim [27]. Thermal creak only occurs once a critical level of internal stress is reached in an indeterminate structure; the creak event is therefore expected to occur sometime during a temperature transient, after stress has built up over some time, but before steady-state has been attained. It should be noted, however, that temperature measurements taken on the surface of the structure do not necessarily reflect the mean temperature distribution internal to the structure: some amount of temperature lag between the internal temperature of the structure and the surface temperature is unavoidable. The extent of this lag is dependent on the thermal mass and conductivity of the material. For instance, even though the temperature may have reached steady-state on the surface of a Lexan batten member in the deployable module, internal stress may still be building up inside the member, because the

internal temperature of the strut may still be changing. Correlating the time of occurrence of an event and the temperature state of the structure at that instant should provide a first indication of the likelihood that an observed event is due to thermal snap. Another indication is provided by the time- and frequency-domain analyses of the event signal. Since thermal snap is an impulsive (i.e. broadband) structural disturbance, the time trace and frequency spectrum should reflect the telltale signs of structural response: multi-modal, lightly-damped harmonic vibration.

With the "expected" characteristics of the phenomenon of interest identified, the next step is to identify all of the non-thermally-induced disturbance sources in the tests. If these sources can be eliminated, or if the signals caused by these sources can be distinguished from those caused by thermal creak, then it ensures that the objectives of this investigation (demonstration and characterization of thermal snap) can be met. The different possible non-thermally-induced disturbances can be listed as follows, based on the test conditions encountered:

- aerodynamic buffeting of the suspended truss;
- vibrations transmitted through the suspension system, or sensor wires;
- incidental contact with the structure (by wires, umbilical connector, debris);
- acoustic excitation of the structure (from noisy pumps, compressors, fans);
- electrical events picked up by the sensors or wiring;
- excitation of accelerometer resonances.

These disturbance sources are described below, along with the various measures taken to mitigate, or at least identify, each of them.

Aerodynamic buffeting

During the tests performed in the convection thermal chamber, the deployable module experienced noticeable aerodynamic buffeting, as a result of the turbulent air being circulated through the chamber by the fans. The bouncing of the truss on its suspension springs was visible through a window on the chamber door. The roll-off of the suspension system caused this disturbance to only affect low-frequency vibration, as evidenced in the autospectrum of the background noise in Figure 3.3. Since the hunt for thermal snaps focused on frequencies above 1 kHz, this disturbance could not be confused with potential snap events. However, the constant motion of the structure may have significantly affected the observed snap behavior. It is conceivable that by constantly dithering the frictional joints in the structure, the amplitude and

frequency of occurrence of thermal snaps may be different than would be for a completely stationary truss. This dithering effect is identified as a likely reason why snap events were much more globally observable in the convection tests, compared to the radiation tests (see section 3.4).

Transmission of mechanical vibrations

The thermal chambers provide a significant background vibration environment, due to the various heaters, pumps and compressors they employ. During the tests, transmission of these vibrations to the truss could only occur through the suspension springs, or the various sensor wires running from the truss to the chamber walls. A number of measures were in place to eliminate as much of the transmitted disturbance as possible. First of all, the roll-off of the suspension system would greatly attenuate any chamber vibration, particularly in the high-frequency range of interest. Also, care was taken to keep enough slack in the accelerometer cables and thermocouple wires leading off the structure to avoid an accidental load path. In addition to these two attenuating effects, extra precautions were put in place to identify any chamber-induced vibration, should it somehow be detectable on the truss. Accelerometers were always mounted at either end of one suspension spring (on the chamber ceiling and the truss corner fitting), in order to correlate any structural vibrations with chamber vibrations. In addition, for a number of the convection tests, the dummy truss bay described in subsection 3.1.1 was suspended next to the deployable truss and instrumented with accelerometers; a true thermal snap would only be detected on the deployable truss, and not on the dummy.

Incidental contact

For tests performed in the convection chamber, there was concern that the blowing air might cause debris, or perhaps a wire or the umbilical connector to impact the truss, causing a response which might be difficult to discern from a thermal snap event. For this reason, a few measures were implemented to eliminate this possibility. The chamber was thoroughly cleaned before each test, so that all debris large enough to cause a significant impact was removed. The sensor wires were taped off the structure in such a way that they would not be able to contact it (yet still remained slack enough to prevent a load path to the structure). As for the heavy umbilical connector, an elastic cord was used to "isolate" it and keep it separated from the truss, in much the same way as in the microdynamic modal parameter characterization experiment (see

discussion in section 2.3 and photo in Figure 2.24). In addition, the umbilical was completely removed for the final tests performed at Lincoln Laboratory.

Acoustic excitation

Unlike the microdynamic modal parameter characterization experiment discussed in Chapter 2, the frequency range of interest for the thermal snap tests was high enough that acoustic transmission of disturbances through the air became a concern. By performing tests in an evacuated chamber at Lincoln Laboratory, this disturbance source was eliminated. For the tests performed in the convection chamber, the instrumented dummy structure provided a means of distinguishing between acoustic and thermal creak disturbances: acoustic excitation should affect the dummy and deployable trusses similarly.

Electrical events

Another type of disturbance, which was of concern in both the radiation and convection tests, was the pick-up of electrical signals by the sensors or their wiring. Electrical disturbances were unavoidable in an experiment of this type; the data acquisition system was susceptible to "false" triggering, due to electrical events, such as those associated with activation of valves or pumps from the chamber. The accelerometer signals were even sensitive to the cross-talk generated by switching the thermocouple being read on the Omega digital thermometer.

Although electrical disturbances could not be eliminated, they were fairly easy to identify, fortunately. They were evident as very sharp spikes in the data, which exhibited very little of the exponentially-decaying ringing one would expect from a structural disturbance. Figure 3.11 shows an example of an event identified as electrical in origin. On the time trace, the event appears as a very sharp impulse; this translates to a short-duration broadband frequency response visible on the spectrogram. However, no structural ringing or multi-mode behavior is excited, distinguishing this type of event from a thermal creak.

Accelerometer resonance excitation

Another possible, although unlikely, source of disturbance is the excitation of an Endevco 7265A-HS accelerometer resonance, perhaps due to internal stiction within the sensor, at

temperatures exceeding its operating range (which could be thought of as "thermal snap" inside the accelerometer). However, should this type of excitation occur, it would be easily identifiable as a single-mode, highly-damped resonance (the f_n and ζ specifications for these accelerometers are ~1400 Hz and 70%, respectively). Furthermore, all of the 7265A-HS accelerometers were removed with the umbilical cable, for several tests performed in the radiation chamber. The 2222C accelerometers were then exclusively used as the sensors for snap detection.

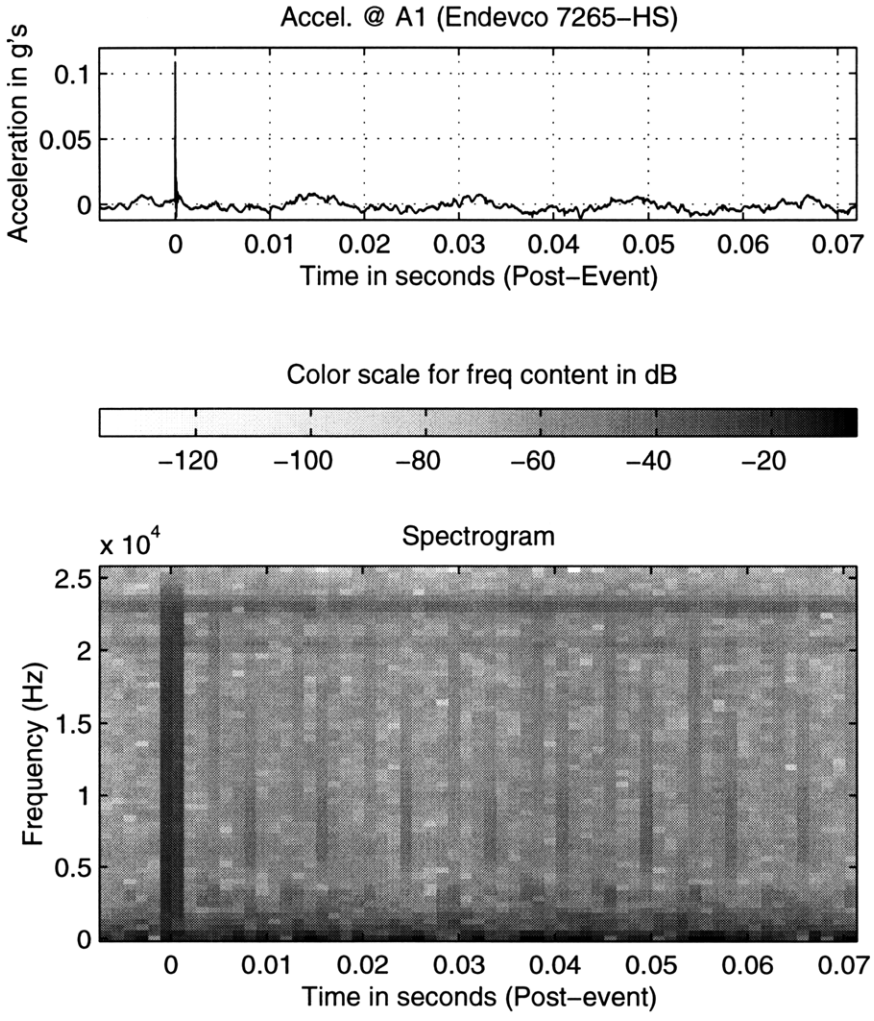

Figure 3.11 Sample electrical event

3.4 Experimental Results

In this section, the results from the thermal creak investigation are presented. Aside from the thermal tests performed at Payload Systems, Inc. and MIT Lincoln Laboratory, a simple series of tap tests was performed, in order to spatially characterize the truss response to an impulsive disturbance. The results from this preliminary tap test are discussed in subsection 3.4.1, followed by the results from the convection and radiation tests, in subsections 3.4.2 and 3.4.3, respectively. Finally, in subsection 3.4.4, the findings of the investigation will be summarized, based on the ensemble of test results.

3.4.1 Tap Test Results

When an impulsive disturbance like thermal snap occurs, its effects are felt differently across the structure, depending on various factors, such as materials, size and shape of the structural elements, mechanisms in the disturbance transmission path, etc... For instance, the magnitude and frequency content of the transient response may be different, from measurements taken at different locations on the structure. Time lags in the onset of the event may be evident between different sensor locations, illustrating the speed of propagation of the disturbance through the structure. Some disturbances may be impeded strongly enough as they progress through the structure, such that they are unobservable from certain locations.

The wave propagation of disturbances through periodic lattice structures, like the deployable truss considered here, has been studied by numerous researchers [45, 46]; a full wave propagation analysis of the thermal snap response is outside the scope of this work. However, a simple experimental investigation can provide considerable insight into the spatial response to an impulsive disturbance. In order to simulate thermal snap disturbances, the suspended structure was tapped at different joint locations with a steel instrument. Even though the nature of the disturbance thus applied to the truss is not internal to a joint, like the slip of a frictional interface would be, it nonetheless results in a broadband, impulsive excitation, traceable to thermal creak. Using the same sensors and data acquisition system as the thermal tests, the response to the taps can be observed at selected locations on the truss. In this subsection, typical results from this series of tests are discussed, followed by a summary of the relevant response characteristics.

Representative tap test data is presented in Figures 3.13 and 3.14. Each of these two figures shows the truss response at two different locations, in response to a given tap location. The sensors used for these tests were Endevco 2222C accelerometers; their locations and sensing directions are illustrated in Figure 3.12. These sensor locations correspond to a subset of those used in the thermal tests performed at Lincoln Laboratory, on November 25th, 1997 (see subsection 3.4.3). Figure 3.12 also shows the locations and directions of the two tap disturbances. The sensor and tap locations were limited to a single bay, in order to focus the investigation on local phenomena, which were the most likely to be observed during the thermal snap tests, as explained in subsection 3.1.3.

Tap #1 was applied transversely to a knee joint, on a neighboring longeron to the one instrumented with sensors C1 and C2. Figure 3.13 shows the response time traces at both accelerometer locations, as well as spectrograms highlighting the time-varying frequency content of each signal. Both traces show somewhat similar behavior: initial high-frequency vibration which dies out rapidly, superposed with lower-frequency oscillations which persist through to the end of the trace. By zooming in on the two traces, no discernable difference is evident between the event start times, indicating that the disturbance from the tap propagates to both accelerometers in roughly the same amount of time. The broadband nature of the impulsive disturbance is evident in the spectrogram plots – dark horizontal streaks represent the multi-modal response of the structure. The streaks at low frequencies are longer than those at higher frequencies, evidence of the shorter time constants associated with higher structural modes. Though the maximum amplitudes of vibration attained are comparable for C1 and C2, the initial high-frequency transient is stronger at C2; this may be evidence of local modes within the batten frame corner fitting, which would occur at higher frequencies than the dominant local modes of the longeron. It may also indicate that the axially-oriented accelerometer at C2 is picking up axial modes of vibration of the longeron struts, which would not be observable from the transverse-sensing accelerometer at C1.

The second tap location was collocated with accelerometer C2. Figure 3.14 shows the response to this disturbance, again in the form of a time trace and spectrogram, as observed from C1 and C2. Three impulsive events are visible in the time traces, due to "rebound" of the tapping instrument during the tap process. Again, the broadband nature of the disturbance is seen in both spectrograms. However, this time the modal response is much stronger at high frequencies; unlike the response to Tap #1, no low-frequency oscillations are evident in the time traces. The

exponential decay of the high-frequency transient is particularly clear in the response at C2: it would appear that the response measurement collocated with the impulsive disturbance is dominated by the high-frequency local dynamics directly excited by the impulse. Not surprisingly, the magnitude of vibration is much higher at the tap-collocated sensor. In addition, the event is picked up approximately 0.1 millisecond earlier at C2 than at C1, representing the wave propagation time required for the disturbance to travel halfway down the Lexan longeron.

The observations drawn from the series of tap tests can be summarized as follows:

- the event start times and the amplitudes of vibration depend on the distance from the disturbance source, and the sensing direction of the accelerometers (as expected, the event occurs sooner, and the response amplitude is higher, for a sensor collocated and aligned with the disturbance);
- the vibration response near the disturbance source is dominated by high-frequency, "local" transients;
- for sensors far enough away from the source (along the load path), the only evidence of the event is low-frequency response, as energy leaks into more "globally-acting" modes of the structure.

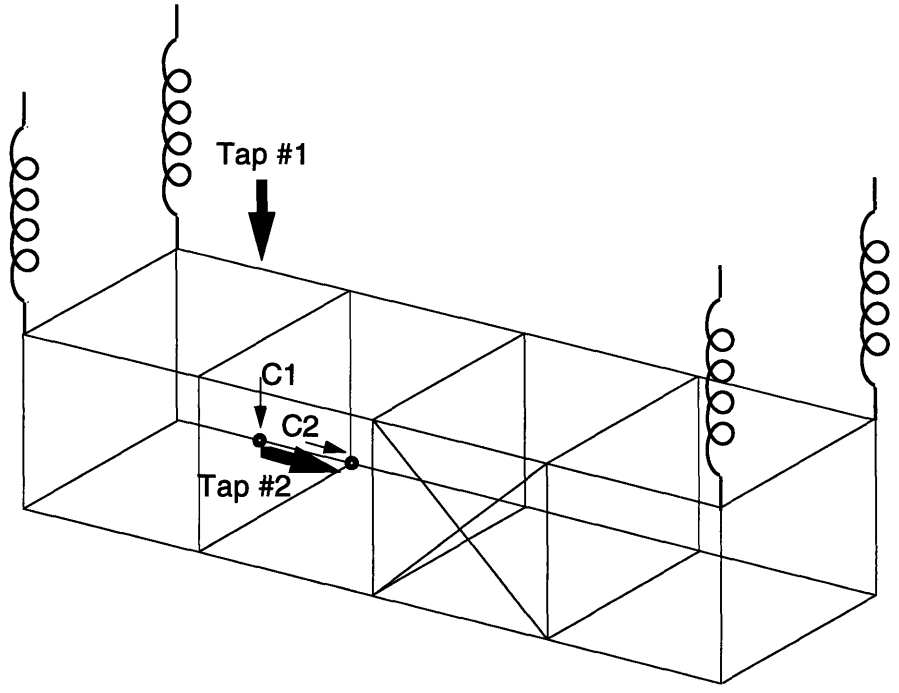

Figure 3.12 Sensor and tap locations for tap tests

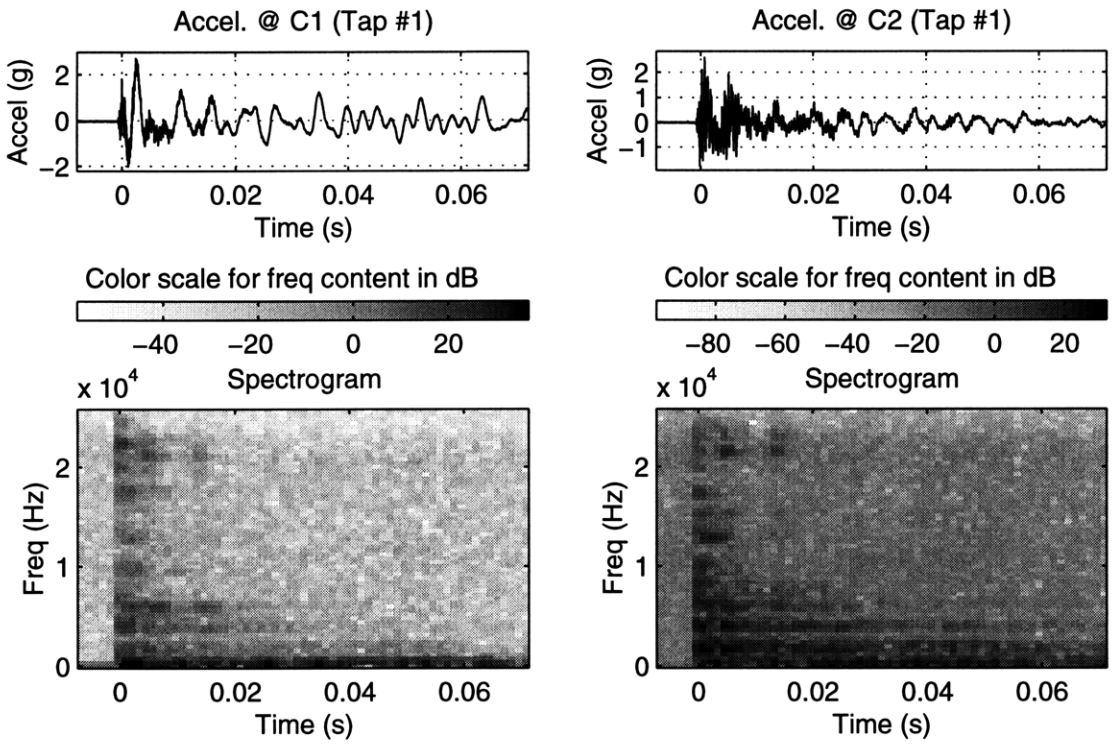

Figure 3.13 Response to Tap #1

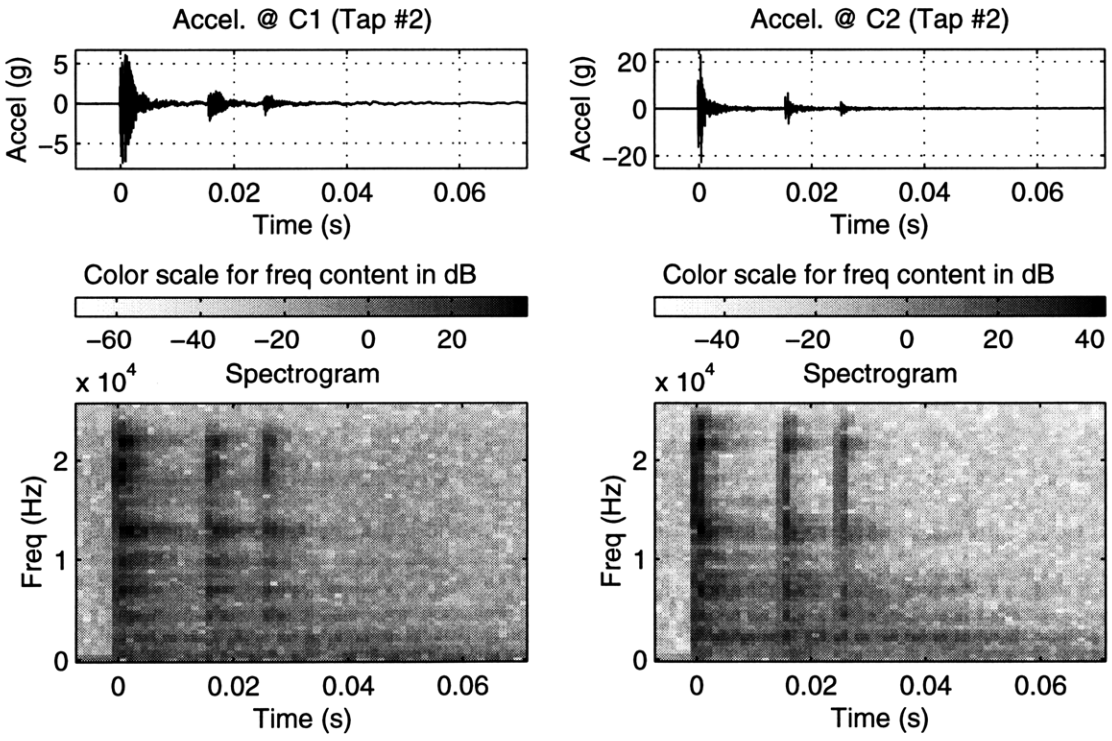

Figure 3.14 Response to Tap #2

3.4.2 Convection Test Results

Between May 22nd and September 2nd, 1997, thermal tests were performed on the MODE deployable module in the convection chamber at Payload Systems, Inc. These tests yielded a number of events which were identified as thermal creak, based on arguments presented in section 3.3. In this subsection, discussion will focus on two representative events in particular, which exhibit characteristics typical of the events observed during the convection tests. One typical event is chosen from among those recorded during the test performed on June 23rd, while the other is chosen from the results of the September 2nd thermal test. For both of these events, the results from the time- and frequency-domain analyses are presented and discussed.

Figure 3.15 shows the temperature profiles from the June 23rd test; the temperature data was obtained from the thermocouples, placed at various locations on the deployable truss and in the chamber. The locations of these thermocouples are indicated by triangles on the sensor map of Figure 3.16. Three of these thermocouples, labeled T5, T7 and T8, were attached to different parts of the truss structure: a Lexan batten, an aluminum batten frame corner fitting and a steel diagonal cable. A fourth thermocouple (T9) was attached off the chamber ceiling, to measure the ambient temperature in the chamber. As evident in Figure 3.15, the three truss temperature profiles follow the ambient temperature profile quite closely, indicating that the convection heat transfer process results in rapid equilibration of the surface temperatures across the test article with the ambient temperature.

For the June 23rd test, only the deployable truss was suspended in the thermal chamber; the dummy truss bay was not used. The sensor location diagram in Figure 3.16 shows the placement and orientation of the accelerometers used to detect thermal snap events, for this set of tests. Throughout this chapter, a consistent labeling code is used to discriminate between the various types of sensors: each sensor is identified by a letter and number, corresponding to the sensor type and location, respectively. The labels for the 7265A-HS accelerometers all begin with the letter "A"; the 2222C accelerometers are identified with the letter "C"; the strain gauges, with the letter "S"; and finally, the thermocouples, with the letter "T". For instance, the Model 2222C accelerometer placed on the ceiling of the thermal chamber, near the attachment point of one of the suspension springs, is labeled C1. Another 2222C sensor, labeled C2, is located on the deployable truss, at the base of the same suspension spring. Two Model 7265A-HS

accelerometers are given the tags A2 and A4. As mentioned above, the four thermocouples on the diagram are identified as T5, T7, T8 and T9.

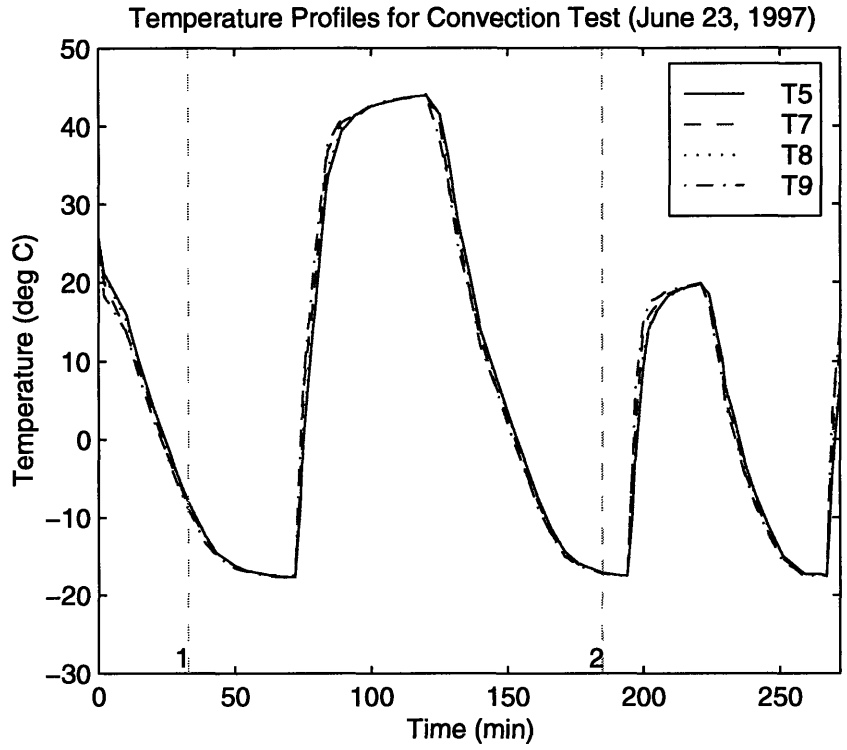

Figure 3.15 Temperature profile for typical convection test (June 23, 1997)

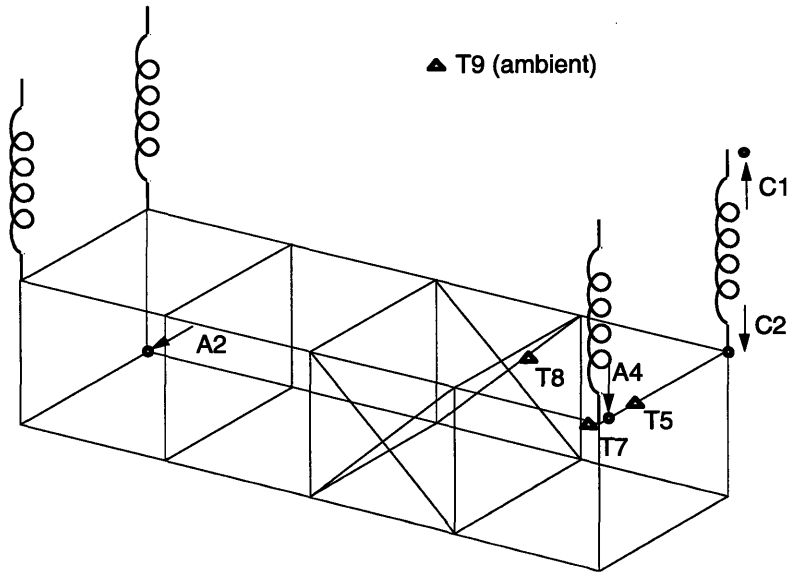

Figure 3.16 Sensor distribution for typical convection test (June 23, 1997)

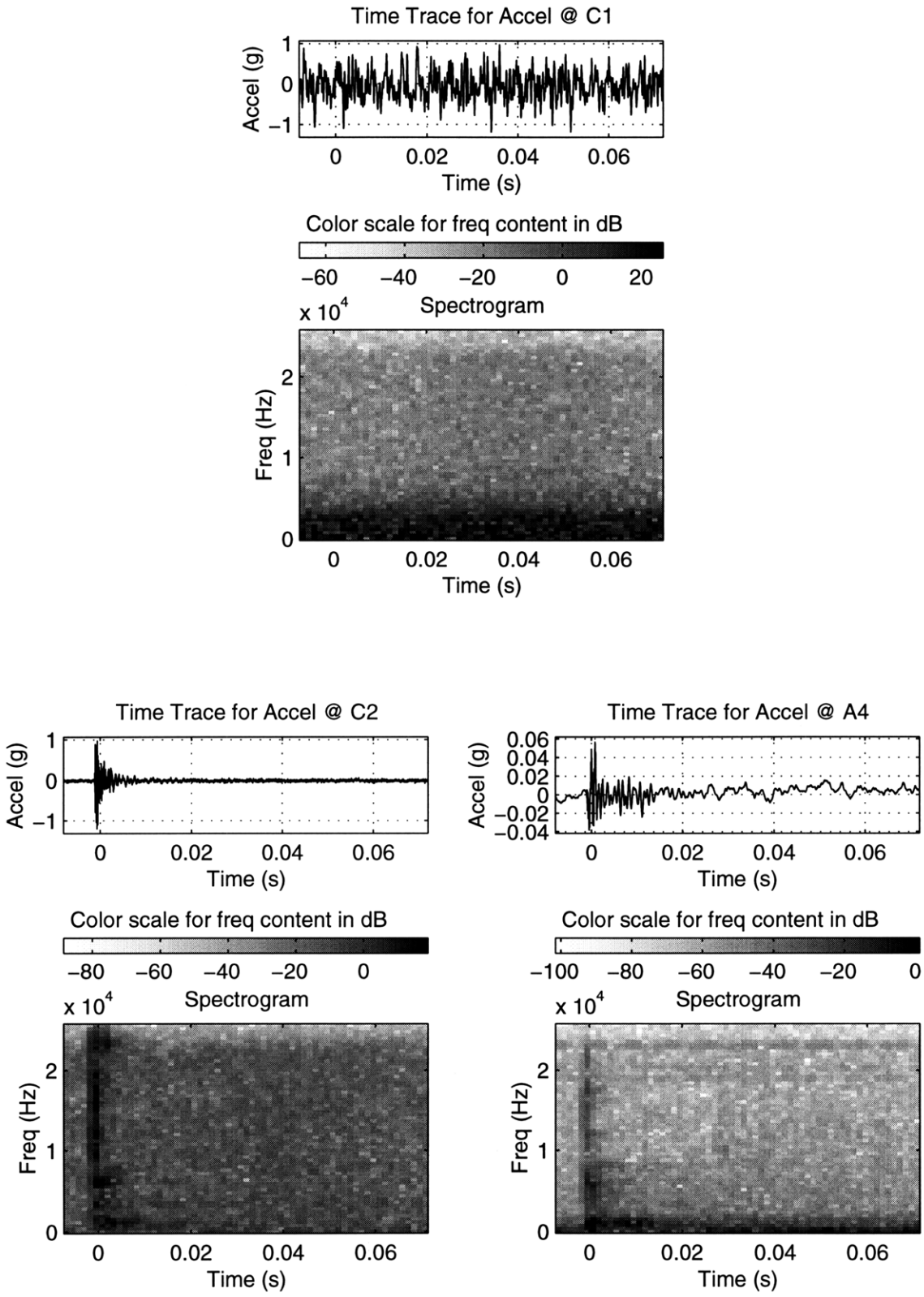

Figure 3.17 Thermal snap data from typical convection test (June 23, 1997)

The first typical event to be discussed here was detected during the cooling phase of the second thermal cycle, after approximately 185 minutes had elapsed since the start of the June 23rd test. This event is identified by the vertical dashed line labeled "2", in the temperature profile diagram (Figure 3.15). One Tektronix Model 2630 data acquisition unit was used to record the typical event as observed from three accelerometer sensors (C1, C2, and A4). Accelerometer A2 was not connected to the fourth channel of the data acquisition unit at the time the event occurred. The nominal bandwidth setting of 20 kHz was chosen, resulting in a sampling frequency of 51200 Hz and time traces of 0.08 second duration, of which 0.008 second corresponds to pre-event data.

The time traces and spectrograms of the event as measured on the three accelerometers are presented in Figure 3.17. Looking at the three time traces, it is evident that the impulsive event picked up by the two accelerometers on the test article (C2 and A4) is not visible in the trace from the accelerometer attached to the chamber ceiling (C1). Furthermore, the broadband frequency content seen at time zero in the spectrograms for signals C2 and A4 is not present in the plot for signal C1, confirming that the impulsive event was felt on the deployable truss, but not on the chamber ceiling. One of the conclusions drawn from the tap tests (see subsection 3.4.1) was that high-frequency transients dominate the vibration response in close proximity of the disturbance source. Judging by the dominance of the high-frequency transient behavior in both signals C2 and A4, it is reasonable to deduce that the snap occurred near those accelerometer locations.

Both accelerometers on the truss show frequency content in the disturbance up to greater than 20 kHz. However, the spectrogram plot reveals that significant content of the A4 signal is found in frequencies below 2 kHz. This is most likely due to the roll-off of the Model 7265A-HS accelerometer (as mentioned in section 3.3, these sensors have a heavily-damped resonance around 1400 Hz). The darker spots in the content band around time zero correspond to modal content in the response transients. In particular, strong modal content around 6 kHz is evident in both the C2 and A4 data. Because these two sensors are located reasonably close to one another and share the same line of action, it is not surprising to see common modal content in the event transient signals. The different frequency response characteristics of the 2222C and 7265A-HS accelerometers make comparison between the magnitudes of the C2 and A4 acceleration traces difficult. Accelerometer A4 has a much lower bandwidth, and consequently, the higher-frequency (and thus higher-amplitude) content is being significantly attenuated. This effect is certainly the main reason why the maximum acceleration level of 1 g attained in the C2 trace is more than an order of magnitude greater than that reached in the A4 trace. Hence, looking at the response

amplitude provides no clue as to which of the two accelerometers is nearest to the source of the disturbance. Zooming in on the time traces, however, it is observed that the event starts 0.2 ms sooner at C2 than at A4, suggesting that C2 is "closest" to the source, along the wave propagation path provided by the structure.

By filtering both traces as described in section 3.2, the exponential ring-down of the 6 kHz mode can be obtained; fits to both filtered signals yield a damping ratio of 0.5%, a realistic value for structural damping. This provides further evidence that the disturbance is structural in nature, and is not due to electrical cross-talk. The source of this disturbance is deduced to be thermal snap, as opposed to an acoustic disturbance: an acoustic event capable of generating such significant response on the truss would have been unlikely to go unnoticed (i.e. unheard, or undetected by accelerometer C1) during the test. In order to confirm this deduction, other thermal tests were performed with the dummy truss bay suspended next to the deployable module; the second typical snap event to be discussed was recorded during one such test.

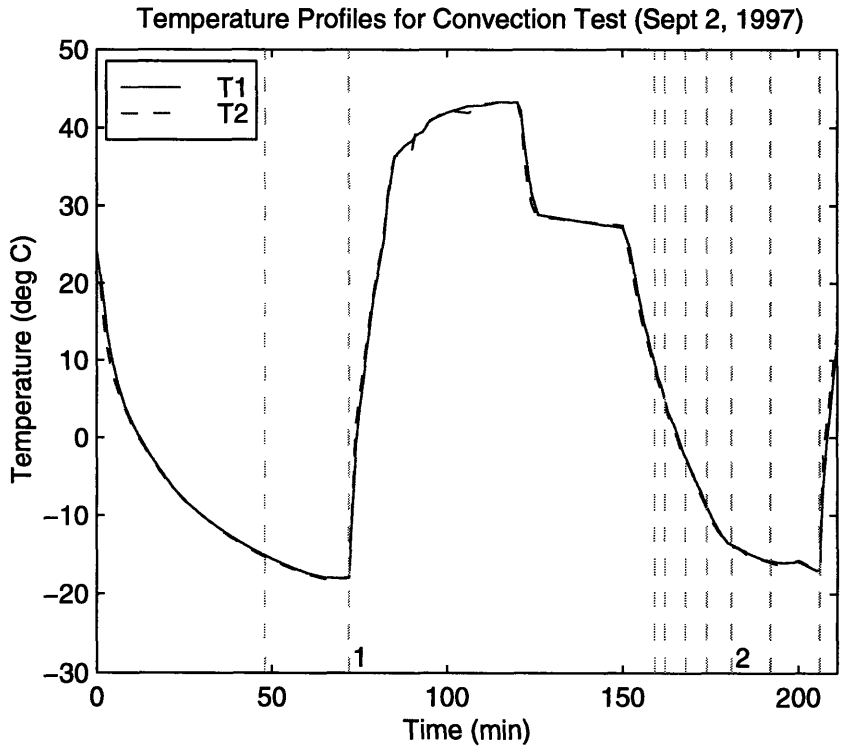

Figure 3.18 Temperature profile for typical convection test (September 2, 1997)

For the test performed on September 2nd, the temperature profiles are plotted in Figure 3.18. This time, only two thermocouples were used: one to keep track of the surface temperature on the test article (T1), and another to measure the ambient temperature in the convection chamber (T2). As expected, no significant difference is noted between the two measured temperatures, at any time during the test. Figure 3.19 shows the sensor distribution across the deployable truss and dummy truss bay. Five accelerometers were used to detect thermal snaps on the deployable module (C2, C3, C4, A1 and A6). As for the June 23rd test, one accelerometer (C1) was placed on the chamber ceiling, at the base of one of the springs. Finally, the dummy bay was instrumented with two more accelerometers (C5 and C6).

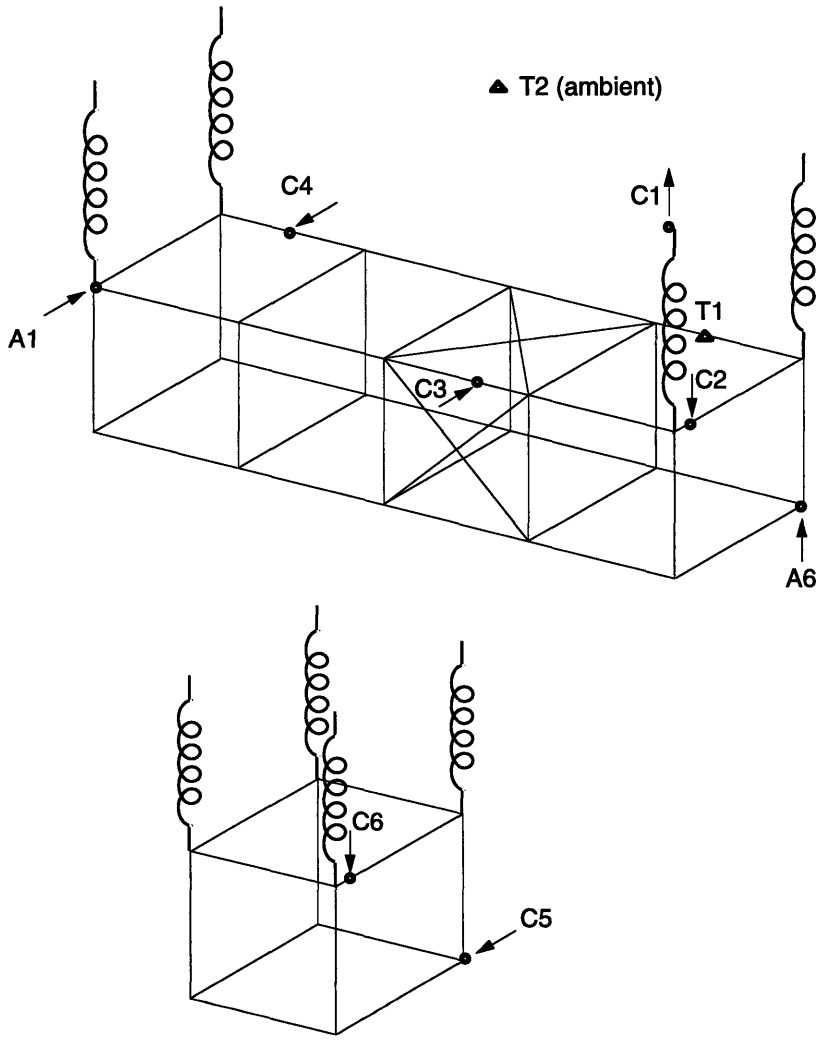

Figure 3.19 Sensor distribution for typical convection test (September 2, 1997)

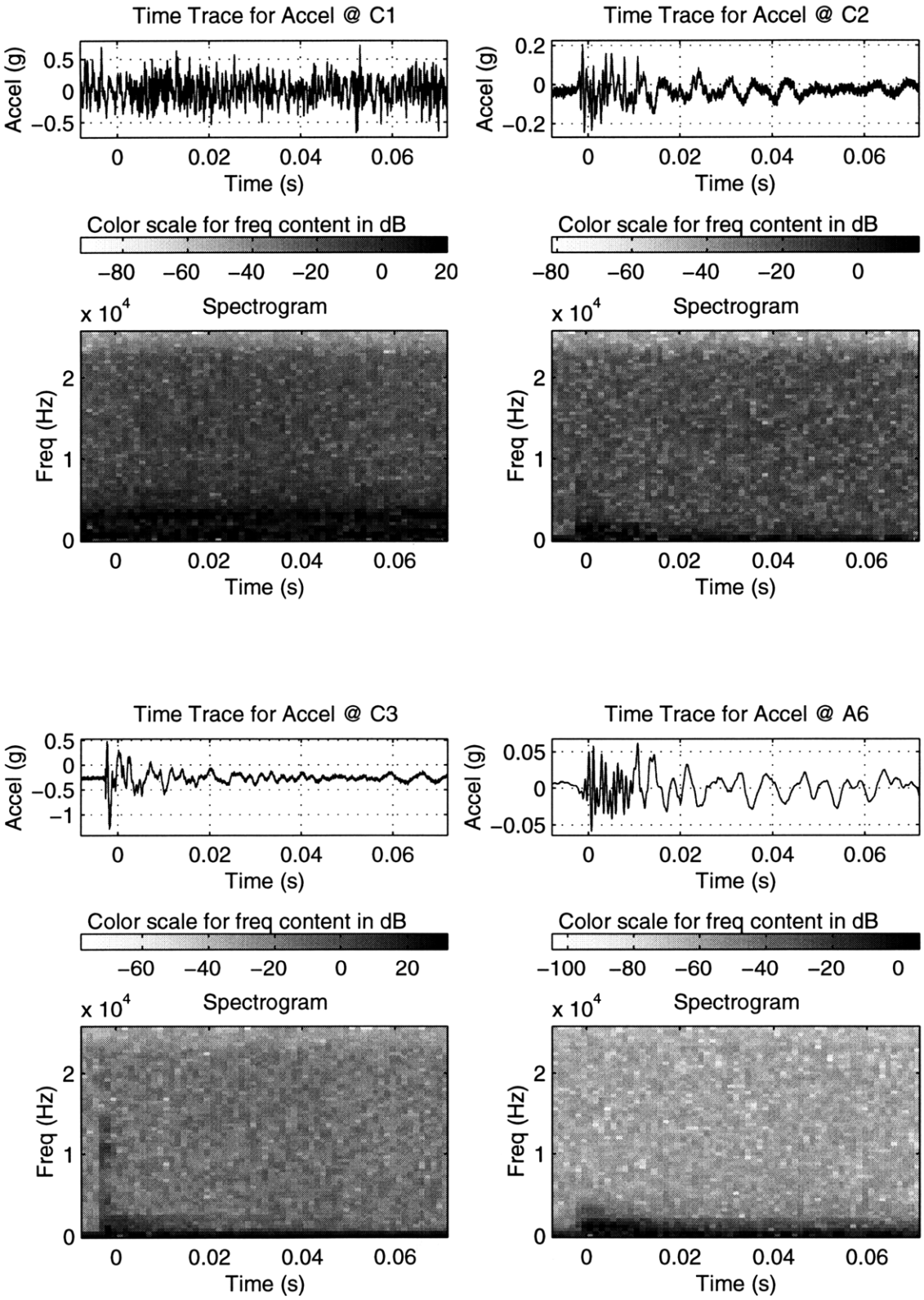

Figure 3.20a Thermal snap data from typical convection test (September 2, 1997)

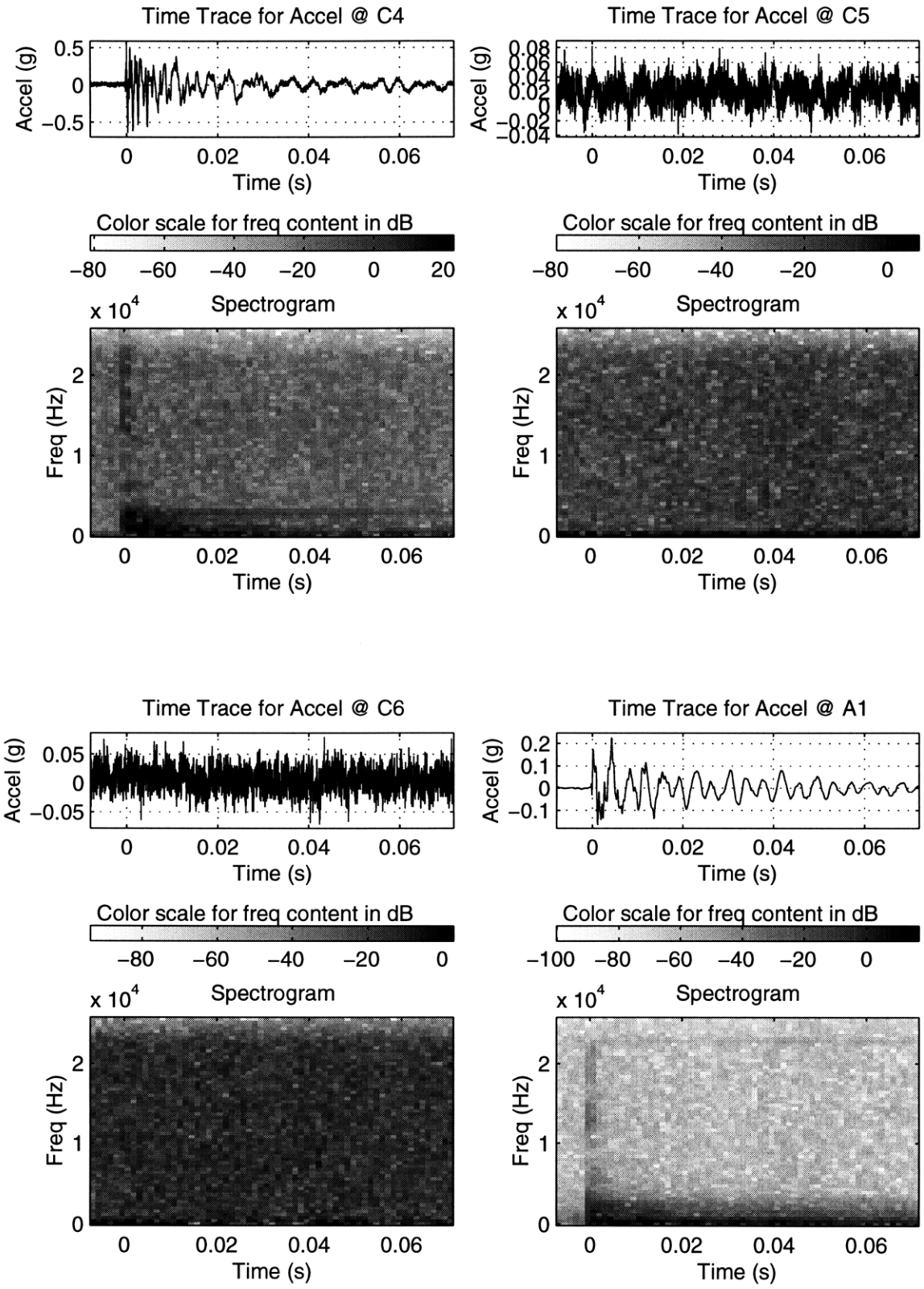

Figure 3.20b Thermal snap data from typical convection test (September 2, 1997)

During the September 2nd test, a number of events identified as thermal snaps were recorded, as indicated by the vertical dashed lines on the temperature profile plot. Of these, one is presented here as the second typical snap event for the convection tests. The chosen event occurred approximately 180 minutes into the test, and is identified as event "2" in Figure 3.18. In order to record the snap, two Model 2630 data acquisition units were used. Both were set to 20 kHz bandwidth. Accelerometers C1, C2, C3 and A6 were connected to the channels on one unit, while C4, C5, C6 and A1 were hooked up to the second unit. It should be noted that these two units were triggered independently from each other, so the time scales for channels on different units do not overlay exactly (i.e. comparison cannot be made between the event start times for signals captured on different data acquisition units).

Figures 3.20a and 3.20b present the time traces and spectrograms corresponding to the typical event. No sign of the event was seen in the signals from the accelerometers on the chamber ceiling and the dummy truss (C1, C5 and C6), even though evidence of an impulsive disturbance was clearly observed by all the sensors on the deployable truss (C2, C3, C4, A1 and A6). Based on the time traces from the accelerometers on the deployable truss, and the insight acquired from the tap tests, it appears that the thermal snap occurred roughly midway along the length of the truss, in the vicinity of C3 and C4 (see Figure 3.19). These two traces exhibit the highest-amplitude transients (maximum amplitudes greater than 0.5 g), and are the signals most dominated by high-frequency response, as expected in proximity of the disturbance source (although neither signal shows the same level of high-frequency dominance as the C2 signal from the June 23rd typical event). A comparison between the start times of the event as measured by sensors C2, C3 and A6 (all connected to the first Tektronix data acquisition unit) supports the deduction that the event occurred near C3: zooming in on the traces reveals that the event began 0.7 millisecond later at C2 and A6 than at C3. However, no discernable time lag is seen between the event start times on C4 and A1, which were hooked up to the second Tektronix unit. Accelerometer A1 shows more high-frequency content than C2 and A6, suggesting that the snap acted predominantly in the horizontal, transverse direction with respect to the deployable truss (in the sensing direction of A1, C3 and C4, perpendicular to the sensing directions of C2 and A6).

As far as frequency content of the response is concerned, the C3, C4, and A1 spectrograms show that various modes between 10 kHz and 23 kHz were excited by the snap; in general, the dark spots occur at different frequencies for different sensors, indicating that these high-frequency modes are predominantly local. In particular, the C3 trace shows strong modal response around

10.5 kHz in the initial transient. The filtering and fitting process described in section 3.2 results in a damping ratio of approximately 1% for this mode, a reasonable value for structural damping. Although the poor resolution of the spectrograms makes it difficult to accurately characterize the low-frequency content, it is evident that all the accelerometers on the deployable truss picked up significant response below 2 kHz or so.

It should be noted that this typical event was fifth in the sequence of events picked up during the second cooling phase of the September 2nd thermal test (see Figure 3.18). All of these sequential events looked very much alike, in terms of the "shape" and frequency content of the response time traces, except that the overall magnitude of response seemed to decrease with each successive event. Additionally, each pair of successive snaps exhibited the trend of increasing separation in time. This type of behavior points to the possibility of repeated creaking of one slip interface over the temperature transient, with increasing time intervals between slips as the structure approached steady-state temperature. Thus, even in a nominally symmetric and repeated structure like the deployable module, some joints are more "at risk" than others for experiencing thermal creak, perhaps due to differences in the friction parameters at the interface, or slight asymmetries in the internal stress distribution. Similar successive impulsive disturbances, exhibiting the general trends of decreasing amplitude and increasing time separation, were observed on the Hubble Space Telescope during its initial on-orbit checkout; these impulsive events, which occurred during the orbital "day", were attributed to thermal creak in the solar array spreader bars [26].

In summary, results from the time- and frequency-domain analyses performed on two typical thermal snap events from the thermal convection tests have been presented and discussed. The accelerometer response data from these two sample snaps exhibited certain characteristics which were representative of the ensemble of convection test results:

- the events were all seen as impulsive, broadband disturbances;
- the response to every event was observed across the entire deployable structure;
- the response was multi-modal in nature;
- the response exhibited significant modal content at frequencies below 2 kHz;
- the varying magnitude and frequency content of the response across the truss permitted some degree of spatial localization of the event.

3.4.3 Radiation Test Results

In order to eliminate the aerodynamic buffeting and acoustic disturbance sources present in the convection tests, a series of thermal snap investigations was performed in a vacuum chamber, using radiation as the mechanism for heat transfer to the deployable truss. This also allowed for a more realistic simulation of the orbital environment which would be encountered by a space structure. As described in subsection 3.1.2, a thermal vacuum chamber at MIT Lincoln Laboratory was the site of the radiation tests, between September 29th and November 26th, 1997. During these tests, several events were identified as thermal snaps. In this subsection, two representative events are selected to illustrate the typical characteristics of the snaps from the radiation tests. The first thermal creak to be discussed here occurred on September 29th, during the first radiation test; the second was observed on November 25th. As was done for the typical convection results, the time- and frequency-domain analyses of these two representative snaps are discussed below.

Figure 3.21 shows the temperature profiles for the September 29th test. Although eight thermocouples were placed on the structure and shroud during the test, only five of the temperature traces are plotted in the profile, for clarity. As shown in the sensor map of Figure 3.22, thermocouples T2 and T3 were bonded to one of the longerons, on a Lexan strut and an aluminum joint, respectively, while thermocouple T6 was attached to a Lexan batten member. Sensors T7 and T8 were used to measure the temperatures on the radiation shroud, at the bottom and top, respectively. In order to simulate a sudden, significant thermal load, such as would be encountered by a spacecraft entering or exiting planetary eclipse, an "impulsive" thermal load was applied to the test article. The lowest truss temperature was measured on the Lexan batten (T6), which dropped to just under –25°C after approximately 50 minutes.

For this test, four Model 2222C accelerometers were used to detect structural events (see Figure 3.22). Sensor C1 was placed on the top of the shroud, at the attachment point for one suspension wire and spring. Accelerometer C2 was bonded to the aluminum corner fitting on the deployable module, at the other end of the same spring. The other two accelerometers, C3 and C4, were attached to aluminum joints on two different longerons.

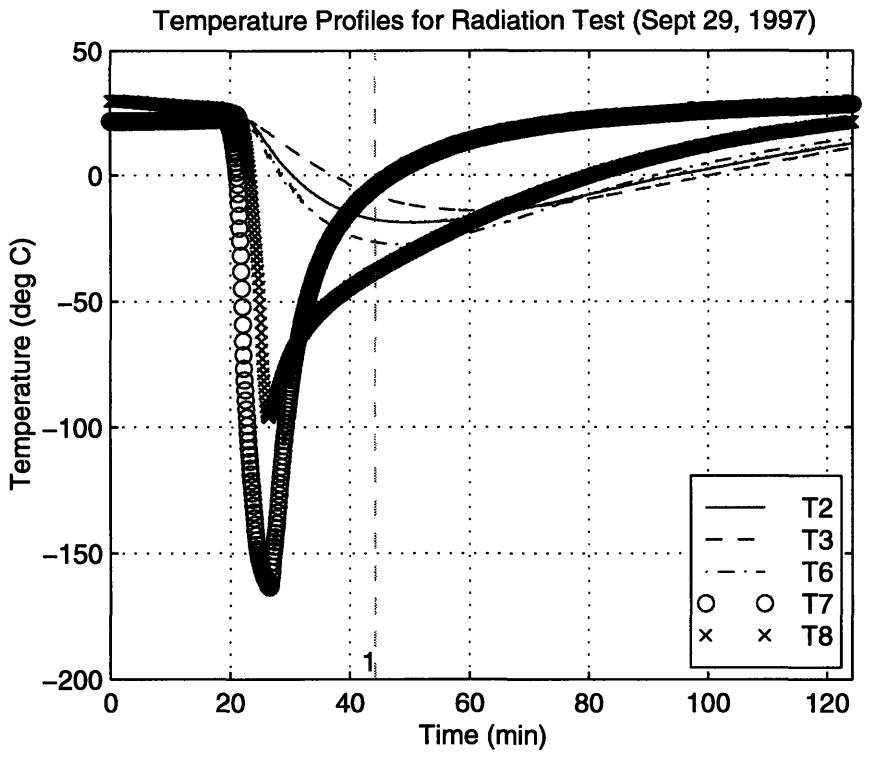

Figure 3.21 Temperature profiles from typical radiation test (September 29,1997)

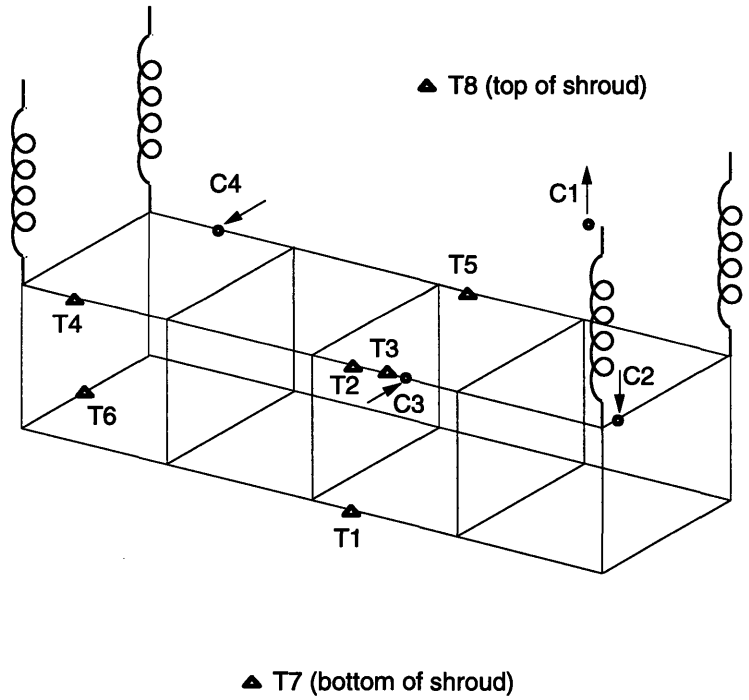

Figure 3.22 Sensor distribution for typical radiation test (September 29, 1997)

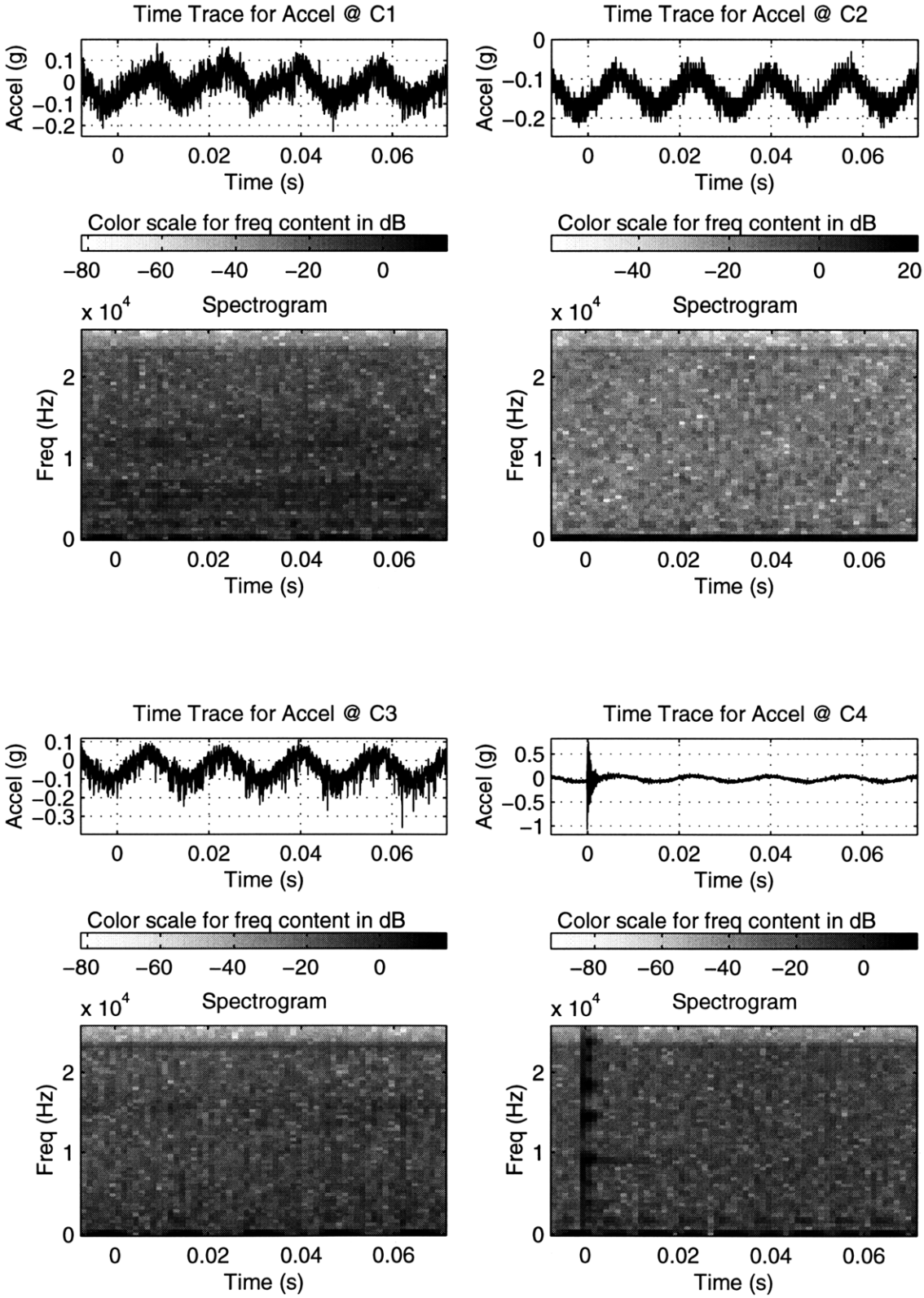

Figure 3.23 Thermal snap data from typical radiation test (September 29, 1997)

During the September 29th test, one event was identified as thermal creak. It occurred approximately 43 minutes into the test, as indicated by the vertical dashed line in Figure 3.21. One Tektronix Model 2630 unit (set to a bandwidth of 20 kHz) was used to record the accelerometer data resulting from the event. Figure 3.23 contains the time traces and spectrograms from the four channels. The oscillatory signal evident in all four traces is actually electrical line noise at 60 Hz, which was picked up by the sensor wires. As expected for a thermal creak occurring on the test article, the trace from the accelerometer placed on the shroud (C1) shows no sign of the event. Unlike the events recorded during the convection tests, only one accelerometer on the truss detected the broadband snap: the impulsive event with peak amplitude around 1 g is clearly evident in the trace from accelerometer C4. Another important difference between this event and those from the convection tests is that the post-event frequency content is not concentrated at frequencies below 2 kHz; rather, the energy in the response is focused at higher frequencies. Evidently, the response to the snap was only felt in high-frequency modes, localized in the vicinity of accelerometer C4.

The time- and frequency-domain analysis of the event in the C4 trace has already been performed in section 3.2, in order to illustrate the data reduction procedure. This analysis identified the broadband nature of the disturbance, and the three dominant modes of response at 9 kHz, 14.5 kHz and 18kHz. Truncating and bandpass filtering the trace around the 9000 Hz mode allowed the modal damping ratio to be estimated at around 2%, a reasonable level of damping for a local mode in a jointed structure predominantly made of Lexan. The damping estimates for the other two dominant modes yield values between 1% and 2%, as well.

The second typical snap event to be discussed here was observed during the November 25th thermal test. The temperature profiles are plotted in Figure 3.24, and the sensor distribution is given in Figure 3.25. For this test, the sensors on the deployable truss were clustered in two groups, with the goal of providing a better spatial characterization of the response to highly localized snaps. The first cluster comprised sensors C2, C3 and C6: accelerometers C3 and C6 were placed on the same batten frame corner fitting, while C2 was bonded to the tab on a neighboring diagonal cable. Strain gauge S1 was located on a longeron connected to the fitting instrumented with C3 and C6. Two other accelerometers, C4 and C5, were placed on the opposite side of the truss, attached to a mid-longeron joint and one of its adjacent batten frame corner fittings, respectively. As usual, C1 was placed on the top of the shroud, at a suspension attachment point. Two data acquisition units (one Model 2630 set to 20 kHz bandwidth, and one

Model 2640 set to 100 kHz bandwidth) were used to record the time traces of the accelerometer signals. This time, the common triggering circuit described in subsection 3.1.3 was used, in order to ensure that both units triggered simultaneously, when a preset trigger level was exceeded in the output of any sensor.

The typical event occurred roughly 30 minutes after the start of the test, as indicated in Figure 3.24. Figures 3.26a and 3.26b show the time traces and spectrograms from the seven sensors. Accelerometers C2, C3 and C6 were connected to the higher-bandwidth data acquisition unit, therefore their time traces are shorter in duration. The horizontal lines in the spectrograms for these three channels at 30 kHz (and integer multiples thereof) are due to the resonances of the Model 2222C accelerometers. Looking at all the accelerometer traces, a 60 Hz electrical line noise waveform is evident. As it turned out, the broadband snap event was again only detected on one sensor (C4), with content between 6 kHz and 25 kHz, and peak amplitude around 0.5 g. None of the other channels picked up the impulsive disturbance, not even accelerometer C5, which was located reasonably close to C4, albeit with a different sensing axis. This indicates that, as for the September 29th event, the response was extremely spatially localized. Not surprisingly, the spectrogram shows significant response at only one mode, around 22.5 kHz, which likely corresponds to a very local resonance, perhaps even internal to the aluminum knee joint. The modal damping ratio of this mode was computed to be around 0.8%.

In summary, analysis of these two typical thermal snap events revealed certain characteristics traceable to all of the snaps detected during the radiation tests:

- as was the case in the convection tests, the events were impulsive and broadband;
- the response to each snap was only observed by one accelerometer (i.e. very localized disturbance);
- the snap response exhibited content at higher frequencies than in the convection tests, in general;
- the response was generally multi-modal in nature, although some of the events were dominated by a single high-frequency mode;
- the snaps occurred less frequently than in the convection tests.

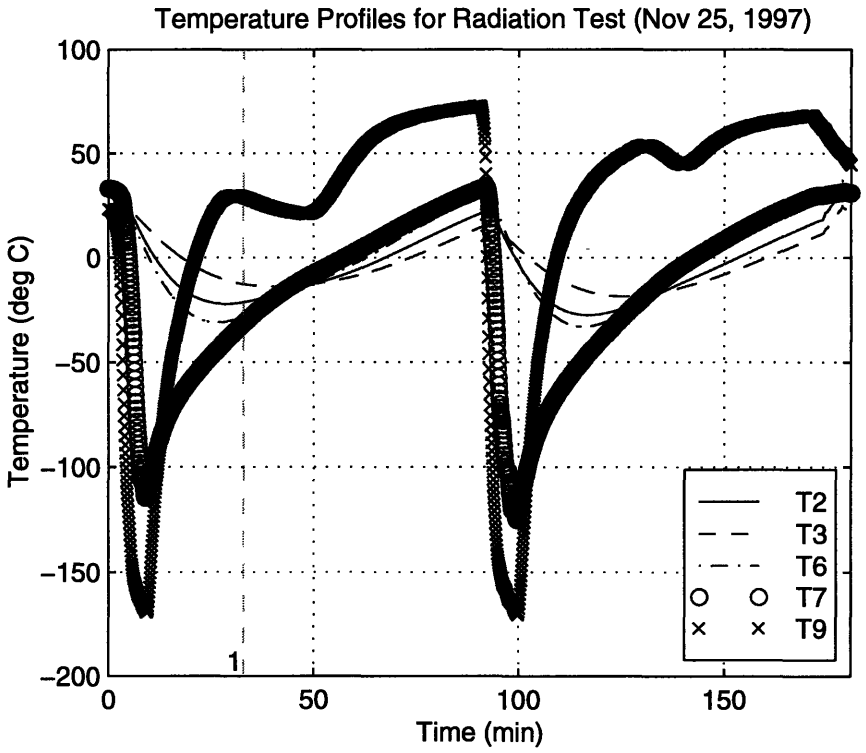

Figure 3.24 Temperature profiles from typical radiation test (November 25, 1997)

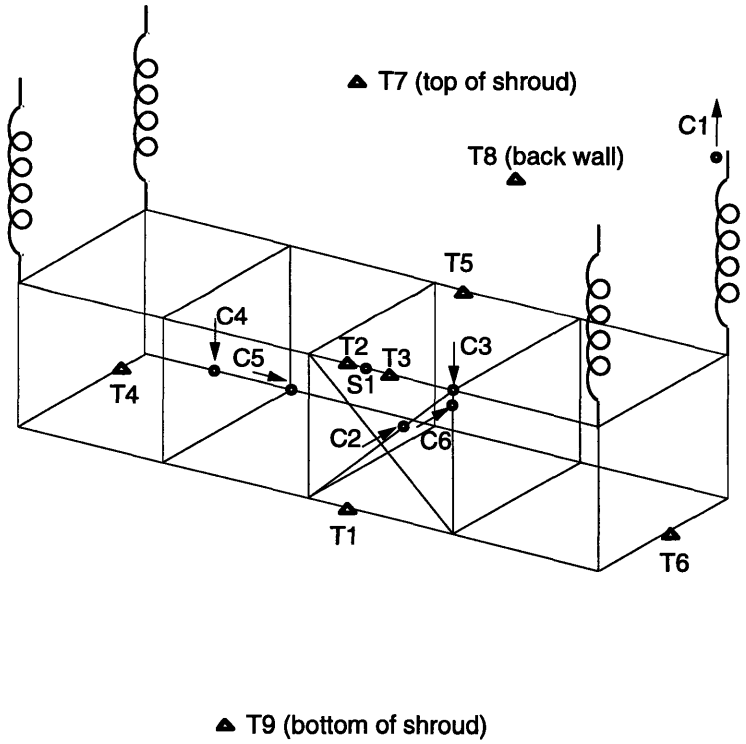

Figure 3.25 Sensor distribution for typical radiation test (November 25, 1997)

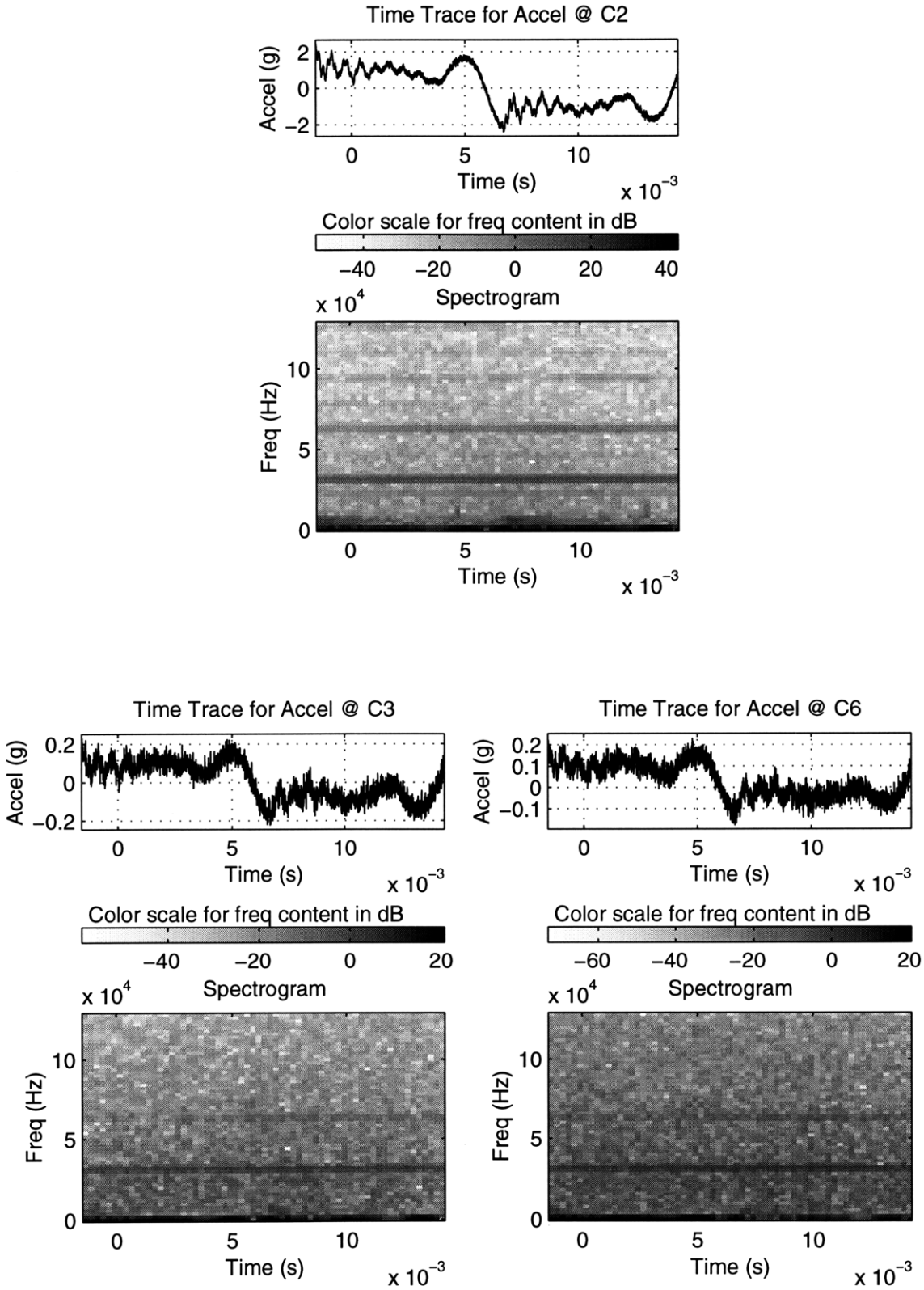

Figure 3.26a Thermal snap data from typical radiation test (November 25, 1997)

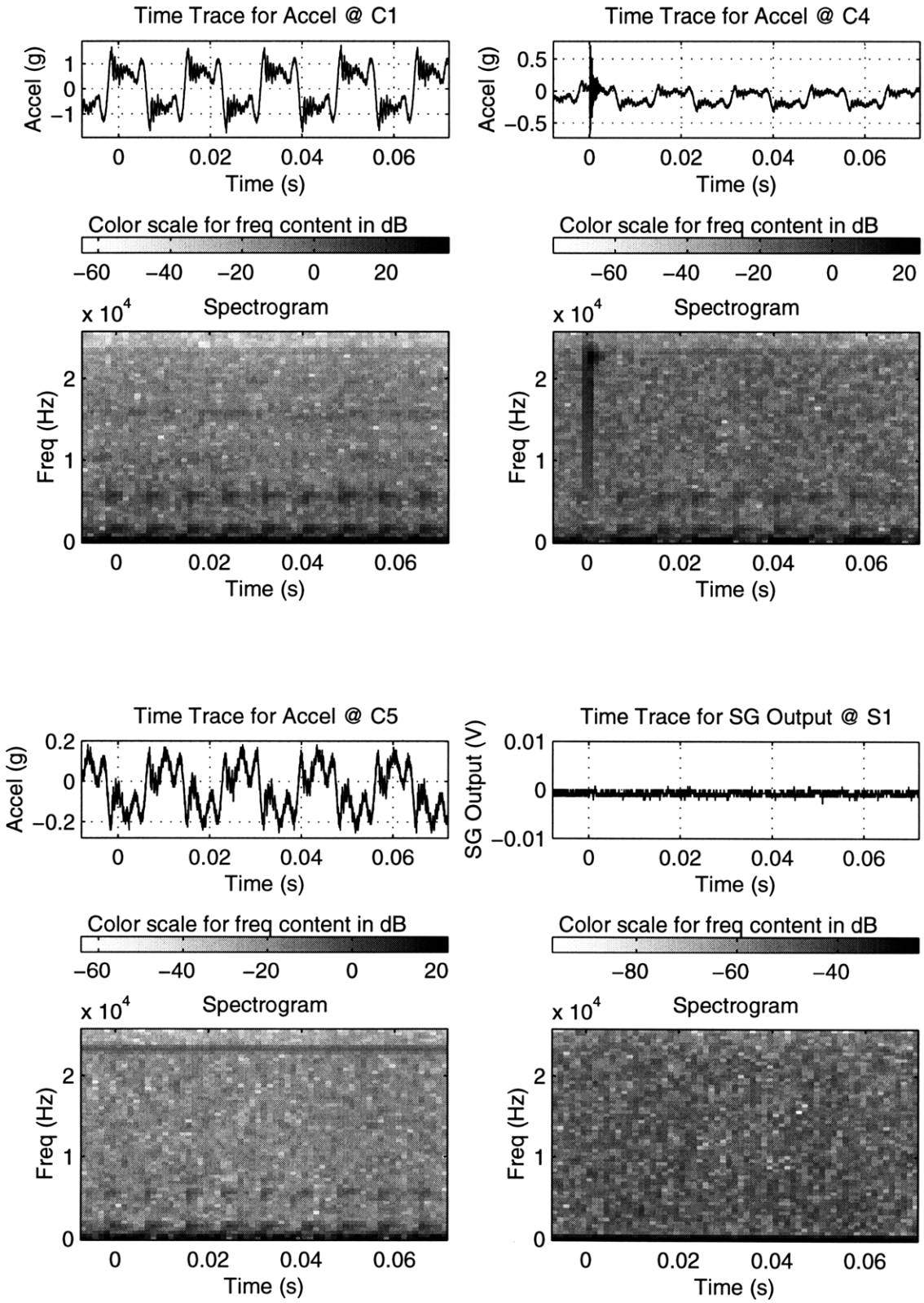

Figure 3.26b Thermal snap data from typical radiation test (November 25, 1997)

3.4.4 Summary of Findings

In this subsection, the results from the analyses on the typical creak events in subsections 3.4.2 and 3.4.3 are summarized. The opportunity is also taken to address a few other findings from the thermal tests, which were not covered in these two previous subsections. Based on the results from the full suite of thermal tests, conclusions can be drawn regarding the test procedures and environments which increase the likelihood of thermal creak in a structure.

In total, over 14 days of thermal testing, about 30 events were identified as thermal snaps. A representative selection of snaps from both the convection and radiation tests are included in Appendix B. The results are presented in the same format as the typical events described previously in this chapter: the temperature profiles and sensor distribution diagram are given for a particular test, followed by the time traces and spectrograms for each event. The selected events are identified on the appropriate temperature profile plots as the vertical dashed lines labeled with event numbers. Unless otherwise noted in the appendix, the nominal test procedure described in section 3.2 was followed during each test.

From the test results discussed in subsections 3.4.2 and 3.4.3, certain common characteristics of thermal snap were identified, independent of the heat transfer mechanism. First of all, the snaps were generally detected at propitious times: during thermal transients, after a significant change in temperature had occurred, but before steady-state was attained throughout the structure. The disturbances themselves were impulsive and broadband in nature. The transient response measurements exhibited telltale signs of structural behavior, including multi-mode or dominant-mode excitation, and reasonable amounts of modal damping in the decay of the response. The frequency content of the truss response was found to vary significantly from event to event: the response to some snaps could only be seen at the lower end of the bandwidth of interest, below 2 kHz or so, while other snaps excited modes in the tens of kHz range. Generally, the peak acceleration amplitudes were found to be on the order of 0.1 to 1 g, although certain high-frequency events were observed which caused accelerations up to 20 g in magnitude (e.g. Event #2 from the October 3rd radiation test, in Appendix B). These acceleration levels correspond to displacement vibration amplitudes estimated to be on the order of nanometers or greater. Furthermore, for each of the events, a rough idea of the location of the snap source could be obtained by comparing the transient start times in the traces from each sensor. Finally, the magnitude and frequency content of the response varied across the truss, thus providing another

clue as to the location of the disturbance source. It should be noted that these insights into the spatial localization of the creak sources were based on qualitative similarities to the tap tests outlined in subsection 3.4.1.

Beyond these common characteristics, however, several important differences were noted between snaps observed in the convection chamber, and those observed in the thermal vacuum chamber. Overall, fewer thermal snaps were recorded during the radiation tests than during the convection tests. Furthermore, each event was only detected by one accelerometer on the truss, during the radiation tests; the snap response was therefore far more localized than for the convection tests, where evidence of each event was generally detected across the entire truss. The highly localized nature of the disturbance was also reflected in the fact that snap response generally had content at significantly higher frequency in the radiation tests. These differences in the snap response must somehow be related to the different environments the truss was subjected to in the two types of test. The first, and perhaps most significant difference in the test environments is the nature of the two heat transfer processes. The blowing air in the convection chamber induced constant, low-frequency and relatively large-amplitude motion of the truss, whereas in the evacuated radiation chamber, the test article remained comparatively still, feeling only the vibrations transmitted through the suspension system. It is reasonable to deduce that the constant dithering of the truss joints during the convection tests could have resulted in more frequent slips of the frictional interfaces, and could also have affected the extent to which the disturbance is felt across the structure. Other important differences between the two types of test were the rate of temperature change and the temperature distribution across the truss. Further study would be required in order to gauge the effects of the faster cooling rate and non-uniform temperature distribution achieved in the radiation tests.

While most of the discussion in this chapter focused on the thermal tests during which thermal snaps were recorded, it is important to note that structural events were not detected during every test. While it is simply possible that no thermal snaps occurred on the truss during certain tests, it is very likely that numerous creak events were missed, due to various reasons. It is possible that the trigger signal threshold level was set too high to detect smaller amplitude snaps, or that the snap response level was on the same order as the background noise. For tests in which the common triggering circuit was not used, the accelerometer connected to the channel chosen for triggering may have been positioned such that snaps occurring at certain locations were

undetectable. Even when the common triggering circuit was used, in the later radiation tests, the highly localized nature of the snaps may have resulted in a large number of missed events.

Chapter 4 – Conclusions

4.1 Microdynamic Results

Based on the results from the two microdynamics experiments presented in Chapters 2 and 3, a number of conclusions can be drawn. In the first experiment, modal parameter characterization was performed on the first torsion and bending modes of a representative deployable truss, at strain response levels between 1 nε and 100 με. These tests showed nonlinear softening behavior for strain response levels above 1 με, but essentially linear behavior below 1 με (i.e. constant values for natural frequency and damping ratio are approached, below this critical response level). From this result, it is inferred that the nonlinear structural mechanisms, which dominate the damping at high excitation levels, are not activated at low excitation levels; the underlying linear dissipation mechanisms become the main source of structural damping. While the actual source of the linear damping limit was not identified, it is assumed to be dictated by material damping, and perhaps also linear dissipation mechanisms within the joints.

The second experiment performed was an investigation of the type of thermally-induced structural disturbances known as thermal snap. When subjected to varying thermal environments, the deployable truss test article exhibited occasional transient vibrations, which were attributed to thermal snap, based on various measures implemented to identify the disturbance source. In general, these impulsive events induced accelerations with magnitudes on the order of 0.1 to 1 g, over frequencies ranging from hundreds of Hz up to tens of kHz. The highest-frequency snaps showed peak amplitudes as high as 20 g in the response transients. The snap-induced displacements were estimated to be on the order of nanometers, or greater. Time traces from the sensors on the truss showed characteristics common to all the detected events: they occurred during thermal transients, before steady-state was attained; the events induced broadband response, often multi-mode in nature, typical of a structural response to an impulsive disturbance. Based on insight gleaned from tap tests performed on the test article, indications as to the approximate location of the disturbance source (i.e. the slipping interface) were found. In certain respects, the nature of the snap events was dependent on the heat transfer mechanism employed:

the events recorded during the radiation tests were much more localized than those detected during the convection tests; as such, they generally exhibited higher frequency content, as well.

The experience gained from performing these two experiments also leads to a few general conclusions regarding microdynamic-level test methodology. Due to the highly sensitive nature of such experiments, great care must be taken to establish test procedures designed to isolate the measurements of interest from the extraneous disturbances and noise sources, which may be of comparable magnitude. For example, use of appropriate suspension systems and careful electrical isolation were required in both of the microdynamic experiments described in this thesis. Selection of appropriate actuators and sensors is crucial: they must cover the full dynamic range of the test with sufficient resolution, while contributing as little noise as possible to the measurements. This point was illustrated in the microdynamic modal parameter characterization experiment, with the stiction-free design of the Butterfly actuator, and the use of piezoelectric strain gauges which can resolve strains below one nanostrain. In addition to the actuators and sensors, specialized instrumentation may be required to obtain the data of interest. A good example of this is the combined use of the lock-in amplifier and high-resolution function generator, described in section 2.1. Often, specific data reduction procedures are required to extract the correct information from the microdynamic data, e.g. use of the spectrogram to visualize the time-varying frequency content of the structural response to thermal snaps. Finally, emphasis should always be placed on establishing the limitations on precision and accuracy for microdynamic experiments, and understanding the sources of these limitations.

4.2 Implications for Future Precision Space Structures

The structural requirements for future space telescopes (from NASA's Origins Program) will present a challenging "packaging" problem. For example, plans for the Space Interferometry Mission (SIM) call for an Earth-orbiting interferometer with baseline length on the order of 10 m. One of the possible designs, depicted in Figure 4.1, has two box-beam arms which fold out to the full baseline, and a deployable truss housing the metrology systems [47]. Another possible design involves two half-cylinder shell booms which fold out on hinges and latch into place, as shown in Figure 4.2 [48]. Despite the absence of a deployed metrology boom, these hinges and latches undoubtedly form a statically indeterminate mechanism with frictional interfaces. In addition, either design for SIM would have other mission-critical mechanisms with potentially nonlinear

dynamics, e.g. optical delay lines. Depending on their positions (Earth orbit, Lagrangian point, or other), the Origins telescopes will encounter potentially unfamiliar thermal environments. They will certainly be subjected to sudden changes in the thermal load due to planetary eclipse or changes in spacecraft orientation. Such increases or decreases in the thermal load may induce dynamic structural response at frictional interfaces, as discussed in section 1.1. Clearly, the results from the microdynamic experiments, as summarized in the previous section, may have important implications on the design of these precision space structures.

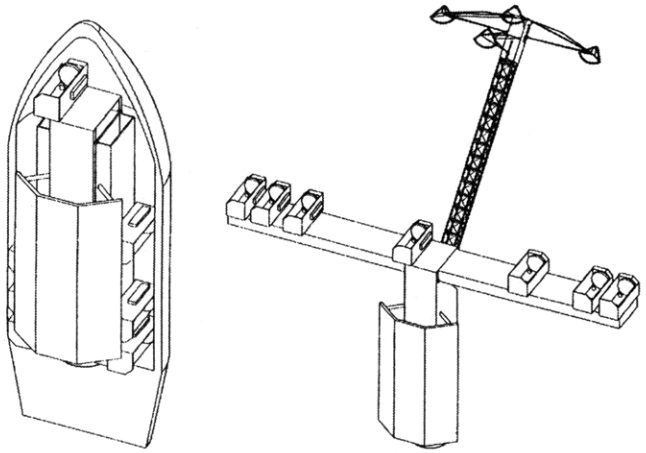

Figure 4.1 "SIM Classic" concept [47]

Figure 4.2 "Son of SIM" concept [48]

The capabilities of the SIM interferometer as currently envisioned will push back existing barriers in astronomy by orders of magnitude [49]. This instrument will perform high precision astrometric measurements (resolving absolute parallaxes to within microarcseconds, and proper motions accurate to within microarcseconds/year), as well as high dynamic range imaging at milliarcsecond resolution. In addition, the instrument may also be able to demonstrate deep central fringe nulling, a capability essential for the detection of faint light sources (planets) in proximity of much brighter ones (stars). To accomplish its lofty astrometry and imaging goals, the distance between the telescopes on the deployed beam-like SIM structure must be kept stable to within 10 nm. The stability requirement for nulling is even more stringent: a 99.99% null of the central fringe needs $\lambda/1000$, i.e. sub-nanometer, stability (λ represents the electromagnetic wavelength of interest, ~ 0.5 μm for the optical regime). This corresponds to vibration levels on the order of nanostrain, or smaller.

The results from the microdynamic modal parameter investigation can be seen as "good news" for precision space structures such as SIM: this work indicates that linearity of a structure is approached at low levels of vibration, a fact which will greatly simplify the microdynamic modeling task. Along with Ting's work on an erectable structure, these findings represent two data points confirming linear behavior in the modal parameters at low strain. Despite the fact that both experiments pointed to a linear/nonlinear transition occurring around 1 με, the actual response level for which transition occurs is certainly mechanism-dependent, in general. For structures featuring different types of joints and made from other materials, the critical strain response level may well change. It is difficult, if not impossible, to predict the nonlinear dynamics of a particular structure without testing it, either at the mechanism-level, component-level, or system-level.

Although the microdynamic behavior of a representative nonlinear structure has been characterized on the ground, it remains to extend these results to a zero-gravity environment. Without the loading applied to the joints due to the action of gravity, the modal damping vs. strain amplitude relationship would certainly be different, due to the change in the joint friction. The MODE program demonstrated that nonlinear effects are more strongly manifested in zero-gravity, with increased participation of the nonlinear mechanisms in the absence of gravity preload. It is therefore expected that frictional damping would cause an increase in the overall damping values; the strain level at which the constant lower limit for damping would be reached would likely decrease. However, since it was inferred that the lower damping limits for each

mode are most likely due to inherent material damping properties, it is expected that the limits found during the ground tests would constitute lower bounds for the zero-gravity situation. These limits may not be attainable in 0-g, if frictional damping continues to be manifested down to nanostrain levels or below.

The thermal snap investigation confirmed that thermally-induced transient events can indeed be observed on statically indeterminate structures with frictional interfaces. During the suite of tests, the high-frequency response of a deployable truss structure to thermal snap disturbances was characterized. As mentioned in the previous section, the snap events induced accelerations up to 20 g in magnitude on the structure, over frequencies ranging from hundreds of Hz up to tens of kHz; the corresponding displacements were estimated to be at least on the order of nanometers. These levels of transient response are of concern in the design of precision space structures: at such high frequencies (which lie beyond the bandwidth of the structural and optical control systems), vibrations of this amplitude could cause the precision optics to lose lock. This would foul up the measurement in progress, and require valuable time to be spent on optical re-capture.

On the other hand, there are preliminary indications that certain actions can be taken to mitigate the thermal snap problem. If snaps primarily excite local dynamics, as observed in the tests performed in the thermal vacuum chamber, it may be possible to design the structure such that its sensitive instruments are isolated from the propagation path of the transient disturbance. As an alternative to designing "around" the snap problem, it may be preferable to make efforts to avoid it. One way would be to design the structure such that differential thermal expansion is minimized (by balancing the CTEs across the structure and making the thermal environment as uniform as possible, or by using a statically determinate structure). Also, it may be possible to eliminate from the spacecraft design many of the potential nonlinear energy release mechanisms.

Although this section has focused on the implications of this research for precision space structures, like those planned for NASA's Origins Program, it should be noted that the results from this work are also relevant to many types of space structures, other than space telescopes. It is easy to envision, for instance, clusters of LEO-orbiting communication satellites with laser communication crosslinks which must be maintained between the different spacecraft. It is likely that these satellites would depend on deployable solar arrays for their power. The nonlinear mechanisms traditionally associated with these arrays pose an obvious risk for thermal creak, as the satellites pass in and out of Earth's shadow. There are very precise pointing requirements

associated with laser communication systems: a significant snap event occurring near the optical components might cause the laser beam link to be broken, disrupting the flow of information.

4.3 Recommendations for Future Work

The field of microdynamics has not yet reached maturity; research in this area over the last decade or so has posed many more questions than it has answered, as pertaining to the behavior of materials and structures at low levels of vibration. Much work remains to be done before sufficient understanding of the field can be claimed, such that the microdynamic response of a precision space structure can be predicted or modeled with confidence. Based on the results from the two types of microdynamic experiments discussed here, a number of research topics have been identified as prime areas for further investigation:

(a) Microdynamic characterization of representative nonlinear structures in zero-gravity, to isolate the effect of gravity preload on the response level at which linear/nonlinear transition occurs.

(b) Microdynamic-level characterization of various types of materials, mechanisms and structure designs, with the ultimate objective of creating a broad microdynamics database, for reference by designers of future precision space structures.

(c) Improved thermal snap experiment:
- use a structure composed of materials and mechanisms which are more traceable to realistic spacecraft;
- extend the bandwidth of observation, to characterize snap response at lower frequencies, at which the structure may be more easily modeled;
- instrument the structure with the goal of identifying the actual nonlinear mechanisms which experience thermal creak;
- investigate the effect of heating/cooling rate on the likelihood and nature of thermal snap.

(d) Use of wave propagation theory to model the structural response to thermal snap, and correlation with experimental data from (c).

(e) Use of alternative modeling techniques to address the stochastic nature of thermal snap (e.g. statistical energy analysis).

References

[1] Wang, P.K.C. and Hadaegh, F.Y., "Microdynamic modelling of joint-dominated truss-based structures", 28th AIAA Aerospace Sciences Meeting, Reno, Nevada, Jan. 8-11, 1990. AIAA Paper 90-0661.

[2] Thornton, E.A., *Thermal Structures for Aerospace Applications*, AIAA Education Series, Reston, Virginia, 1996.

[3] Hertz, T.J. and Crawley, E.F., "Damping in space structure joints", AIAA Dynamics Specialists Conference, Palm Springs, California, May 17-18, 1984. AIAA Paper 84-1039.

[4] Ferri, A.A., "Modeling and analysis of nonlinear sleeve joints of large space structures", *Journal of Spacecraft and Rockets*, Vol. 25, No. 5, 1988, pp.354-360.

[5] Tzou, H.S., Rong, Y., and Sadler, J.P., "Nonlinear dynamics of a spherical joint and a jointed truss-cell unit structure – Theory and ARMA analysis", 31st AIAA/ASME/ASCE/AHS/ASC Structures, Structural Dynamics, and Materials Conference, Long Beach, California, Apr. 2-4, 1990. AIAA Paper 90-0939.

[6] Crawley, E.F. and Aubert, A.C., "Identification of nonlinear structural elements by force-state mapping", *AIAA Journal*, Vol. 24, No. 1, 1986, pp.155-162.

[7] Crawley, E.F. and O'Donnell, K.J., "Force-state mapping identification of nonlinear joints", *AIAA Journal*, Vol. 25, No. 7, 1987, pp.1003-1010.

[8] Ikegami, R., Church, S.M., et al., "Experimental characterization of deployable trusses and joints", Workshop on Structural Dynamics and Control Interaction of Flexible Structures, Marshall Space Flight Center, Huntsville, Alabama, Apr. 22-24, 1986.

[9] Rhodes, M.D., "Design considerations for joints in deployable space truss structures", 1st NASA/DOD Control/Structures Interaction Technology Conference, Norfolk, Virginia, Nov. 18-21, 1986.

[10] Lake, M.S., Fung, J., et al.,"Experimental characterization of hysteresis in a revolute joint for precision deployable structures", 38th AIAA/ASME/ASCE/AHS/ASC Structures, Structural Dynamics, and Materials Conference, Kissimmee, Florida, Apr. 7-10, 1997. AIAA Paper 97-1379.

[11] Chapman, J.M., Shaw, F.H., and Russell, W.C., "Nonlinear transient analysis of joint dominated structures", 28th AIAA/ASME/ASCE/AHS/ASC Structures, Structural Dynamics, and Materials Conference, Monterey, California, Apr. 6-8, 1987. AIAA Paper 87-0892.

[12] Belvin, W.K., "Modeling of joints for the dynamic analysis of truss structures", Report NASA-TP-2661, 1987.

[13] Sarver, G.L., "Energy transfer and dissipation in structures with discrete nonlinearities", PhD Thesis, Dept. of Aeronautics and Astronautics, MIT, Cambridge, Massachusetts, Feb. 1988.

[14] Mercadal, M., "Joint nonlinearity effects in the design of a flexible truss structure control system", Report NASA-CR-180633, 1986.

[15] Bowden, M. and Dugundji, J., "Joint damping and nonlinearity in dynamics of space structures", *AIAA Journal*, Vol. 28, No. 4, 1990, pp.740-749.

[16] Webster, M. and Vander Velde, W., "Modelling beam-like space trusses with nonlinear joints", 32nd AIAA/ASME/ASCE/AHS/ASC Structures, Structural Dynamics, and Materials Conference, Baltimore, Maryland, Apr. 8-10, 1991. AIAA Paper 91-1225.

[17] Crawley, E.F., Barlow, M.S., et al., "Measurement of the modal parameters of a space structure in zero gravity", *Journal of Guidance, Control, and Dynamics*, Vol. 18, No. 3, 1995, pp.385-394.

[18] Masters, B.P. and Crawley, E.F., "Multiple degree-of-freedom force-state component identification", *AIAA Journal*, Vol. 32, No. 11, 1994, pp.2276-2285.

[19] Masters, B.P., Crawley, E.F., and van Schoor, M.C., "Global structure modeling using force-state component identification", *Journal of Guidance, Control, and Dynamics*, Vol. 19, No. 1, 1996, pp.198-206.

[20] Bingham, J.G. and Folkman, S.L., "Measured influence of gravity on the dynamic behavior of a truss using pinned joints", 37th AIAA/ASME/ASCE/AHS/ASC Structures, Structural Dynamics, and Materials Conference, Salt Lake City, Utah, Apr. 15-17, 1996. AIAA Paper 96-1437.

[21] Ting, J.M. and Crawley, E.F., "Characterization of damping of materials and structures from nanostrain levels to one thousand microstrain", *AIAA Journal*, Vol. 30, No. 7, 1992, pp.1856-1863.

[22] Warren, P.A. and Peterson, L.D., "Sub-micron mechanical stability of a prototype deployable space telescope support structure", 38th AIAA/ASME/ASCE/AHS/ASC Structures, Structural Dynamics, and Materials Conference, Kissimmee, Florida, Apr. 7-10, 1997. AIAA Paper 97-1375.

[23] Thornton, E.A. and Kim, Y.A., "Thermally induced bending vibrations of a flexible rolled-up solar array", *Journal of Spacecraft and Rockets*, Vol. 30, No. 4, 1993, pp.438-448.

[24] Zimbelman, D.F. and Zimbelman, H.F., "Self-induced thermal elastic shock disturbance for a dual-array spinning spacecraft", AAS/AIAA Spaceflight Mechanics Meeting, Houston, Texas, Feb. 11-13, 1991. AAS Paper 91-147.

[25] Foster, R.S. and Thornton, E.A., "An experimental investigation of thermally induced vibrations of spacecraft structures", 35th AIAA/ASME/ASCE/AHS/ASC Structures, Structural Dynamics, and Materials Conference, Hilton Head, South Carolina, Apr. 18-21, 1994. AIAA Paper 94-1380.

[26] Foster, C.L., Tinker, M.L., et al., "The solar array-induced disturbance of the Hubble Space Telescope pointing system", Report NASA-TP-3556, 1995.

[27] Kim, Y.A. and McManus, H.L., "Thermally-induced vibrations of space structures", 2nd International Symposium on Thermal Stresses and Related Topics, Rochester, New York, June 8-11, 1997.

[28] Levine, M.B., "The Interferometry Program Flight Experiments: IPEX I & II", *Proc. SPIE Astronomical Telescopes and Instrumentation Conference*, Kona, Hawaii, Mar. 1998. Paper 3350-14.

[29] Barlow, M.S., "Modeling and ground modal identification of space structures", S.M. Thesis, Dept. of Aeronautics and Astronautics, MIT, Cambridge, Massachusetts, Jan. 1992.

[30] Crawley, E.F., van Schoor, M.C., and Bokhour, E.B., "The Middeck 0-gravity Dynamics Experiment – Summary report", Report NASA-CR-4500, 1993.

[31] Masters, B.P., "Multiple degree of freedom force-state component identification", S.M. Thesis, Dept. of Aeronautics and Astronautics, MIT, Cambridge, Massachusetts, Feb. 1994.

[32] Bobronnikov, S.V., "Modeling and modal identification of jointed space structures in one- and zero-gravity environments", S.M. Thesis, Dept. of Aeronautics and Astronautics, MIT, Cambridge, Massachusetts, Sep. 1994.

[33] Forward, R.L., "Picostrain measurements with piezoelectric transducers", *Journal of Applied Physics*, Vol. 51, No. 11, 1980, pp.5601-5603.

[34] Institute of Electrical and Electronics Engineers, Inc., *IEEE Standard on Piezoelectricity*, ANSI/IEEE Std. 176-1987, New York, 1988.

[35] Crawley, E.F. and Anderson, E.H., "Detailed models of piezoceramic actuation of beams", *Journal of Intelligent Material Systems and Structures*, Vol. 1, No. 1, 1990, pp.4-25.

[36] Princeton Applied Research Corporation, *Model 5210 Lock-in Amplifier Instruction Manual*, Princeton, New Jersey, 1987.

[37] Ewins, D.J., *Modal Testing: Theory and Practice*, John Wiley and Sons, Inc., New York, 1984.

[38] Meirovitch, L., *Elements of Vibration Analysis*, McGraw-Hill, Inc., New York, 1975.

[39] Belvin, W.K. and Edighoffer, H.H., "Dynamic analysis and experiment methods for a generic space station model", 27th AIAA/ASME/ASCE/AHS/ASC Structures, Structural Dynamics, and Materials Conference, San Antonio, Texas, May 19-21, 1986. AIAA Paper 86-0838.

[40] Blevins, R.D., *Flow-induced Vibration*, Van Nostrand Reinhold Company, New York, 1977.

[41] Batchelor, G.K., *An Introduction to Fluid Dynamics*, Cambridge University Press, Cambridge, England, 1967.

[42] Wirsching, P.H., Paez, T.L., and Ortiz, K., *Random Vibrations: Theory and Practice*, John Wiley and Sons, Inc., New York, 1995.

[43] Glaese, R.M., "Impedance matching for structural-acoustic control", PhD Thesis, Department of Aeronautics and Astronautics, MIT, Cambridge, Massachusetts, June 1997.

[44] Tektronix, Inc., *Instrument Program for the Tektronix 2600 Analyzer - User's Guide*, Campbell, California, 1991.

[45] Brillouin, L., *Wave Propagation in Periodic Structures*, Dover, Inc., New York, 1946.

[46] von Flotow, A.H., "Disturbance propagation in structural networks", *Journal of Sound and Vibration*, Vol. 106, May 1986, pp.433-450.

[47] Shao, M., Laskin, R., "SIM Overview", presentation to SIM Technical Advisory Committee, Jet Propulsion Laboratory, Pasadena, California, July 17, 1996.

[48] Aaron, K., "SIM SOS Configuration", presentation to SIM Technical Advisory Committee, Jet Propulsion Laboratory, Pasadena, California, Feb. 3, 1998.

[49] Peterson, D. et al., *Space Interferometry Mission: Taking Measure of the Universe*, Final Report of the Space Interferometry Science Working Group, NASA Office of Space Science, Astrophysics Division, Washington, D.C., April 5, 1996.

Appendix A

Modal Parameter Characterization Results

Mode tested	Shaker used	Input voltage	FRF type	ε_{peak}				Ave. Load (lbf)	f_n (Hz)					ζ_{cfit}			
				ave	max	min	σ		source	ave	max	min	σ	ave	max	min	σ
torsion	B-fly	100	TF	4.04E-05	4.08E-05	3.98E-05	3.79E-07	5.12E-02	fpeak	7.7035	7.7055	7.7020	0.0013	2.56E-03	2.74E-03	2.30E-03	1.63E-04
torsion	B-fly	100	SO	4.04E-05	4.08E-05	3.98E-05	3.79E-07	5.12E-02	fpeak	7.6993	7.7000	7.6985	0.0005	2.35E-03	2.50E-03	2.11E-03	1.65E-04
torsion	B-fly	30	TF	1.58E-05	1.61E-05	1.53E-05	2.86E-07	1.42E-02	fpeak	7.7254	7.7260	7.7250	0.0004	1.50E-03	1.63E-03	1.32E-03	1.05E-04
torsion	B-fly	30	SO	1.58E-05	1.61E-05	1.53E-05	2.86E-07	1.42E-02	fpeak	7.7220	7.7225	7.7215	0.0003	1.40E-03	1.53E-03	1.27E-03	9.29E-05
torsion	B-fly	10	TF	6.26E-06	6.32E-06	6.11E-06	7.61E-08	4.34E-03	fpeak	7.7353	7.7360	7.7345	0.0006	1.14E-03	1.22E-03	1.09E-03	5.38E-05
torsion	B-fly	10	SO	6.26E-06	6.32E-06	6.11E-06	7.61E-08	4.34E-03	fpeak	7.7326	7.7335	7.7320	0.0006	1.25E-03	1.29E-03	1.19E-03	4.18E-05
torsion	B-fly	10	SO	6.58E-06	6.69E-06	6.41E-06	1.05E-07	4.60E-03	fpeak	7.7337	7.7345	7.7330	0.0006	1.11E-03	1.15E-03	1.05E-03	4.09E-05
torsion	B-fly	10	SO	6.57E-06	6.63E-06	6.42E-06	7.86E-08	4.43E-03	fpeak	7.7275	7.7280	7.7270	0.0005	1.16E-03	1.20E-03	1.12E-03	2.85E-05
torsion	B-fly	3	TF	2.00E-06	2.01E-06	2.00E-06	7.35E-09	1.32E-03	fpeak	7.7436	7.7440	7.7430	0.0004	1.05E-03	1.08E-03	1.02E-03	2.63E-05
torsion	B-fly	3	SO	2.00E-06	2.01E-06	2.00E-06	7.35E-09	1.32E-03	fpeak	7.7407	7.7410	7.7405	0.0003	1.10E-03	1.12E-03	1.08E-03	1.68E-05
torsion	B-fly	1	TF	7.42E-07	7.49E-07	7.29E-07	7.71E-09	4.22E-04	SDOF	7.7463	7.7466	7.7459	0.0002	8.62E-04	8.96E-04	8.11E-04	3.28E-05
torsion	B-fly	1	SO	7.42E-07	7.49E-07	7.29E-07	7.71E-09	4.22E-04	SDOF	7.7436	7.7441	7.7430	0.0004	1.00E-03	1.02E-03	9.63E-04	2.32E-05
torsion	B-fly	0.3	TF	2.03E-07	2.04E-07	2.03E-07	5.48E-10	1.24E-04	SDOF	7.7456	7.7459	7.7451	0.0003	9.25E-04	9.56E-04	8.82E-04	2.80E-05
torsion	B-fly	0.3	SO	2.03E-07	2.04E-07	2.03E-07	5.48E-10	1.24E-04	SDOF	7.7429	7.7433	7.7422	0.0004	1.06E-03	1.09E-03	1.02E-03	2.47E-05
torsion	B-fly	0.1	TF	7.84E-08	7.89E-08	7.80E-08	3.02E-10	2.80E-05	SDOF	7.7492	7.7493	7.7490	0.0001	7.81E-04	8.15E-04	7.44E-04	2.71E-05
torsion	B-fly	0.1	SO	7.84E-08	7.89E-08	7.80E-08	3.02E-10	2.80E-05	SDOF	7.7444	7.7448	7.7441	0.0002	9.22E-04	9.51E-04	9.04E-04	1.70E-05
torsion	B-fly	0.03	SO	2.09E-08	2.12E-08	2.05E-08	2.30E-10	-	SDOF	7.7450	7.7453	7.7447	0.0003	1.02E-03	1.04E-03	9.87E-04	2.37E-05
torsion	B-fly	0.01	SO	7.52E-09	7.68E-09	7.33E-09	1.51E-10	-	SDOF	7.7451	7.7458	7.7445	0.0004	1.00E-03	1.03E-03	9.83E-04	2.06E-05
torsion	B-fly	0.01	SO	7.03E-09	7.24E-09	6.76E-09	1.83E-10	-	SDOF	7.7414	7.7422	7.7408	0.0006	1.03E-03	1.08E-03	9.69E-04	5.22E-05
torsion	B-fly	0.01	SO	7.15E-09	7.43E-09	7.03E-09	1.39E-10	-	SDOF	7.7376	7.7379	7.7374	0.0002	9.06E-04	9.83E-04	8.42E-04	5.14E-05
torsion	B-fly	0.003	SO	2.40E-09	2.50E-09	2.26E-09	1.02E-10	-	SDOF	7.7446	7.7450	7.7443	0.0003	9.70E-04	1.03E-03	8.70E-04	6.26E-05

Table A1 - Torsion Mode Results

Mode tested	Shaker used	Input voltage	FRF type	peak accel. (g)				Ave. Load (lbf)	f_n (Hz)					ζ_{cfit} (%)			
				ave	max	min	σ		source	ave	max	min	σ	ave	max	min	σ
torsion	B-fly	100	TF (accel.)	6.31E-02	6.36E-02	6.22E-02	5.05E-04	5.12E-02	fpeak	7.7028	7.7035	7.7005	0.0012	2.54E-03	2.71E-03	2.40E-03	1.25E-04

Table A2 - Accelerometer Sweep Results

Mode tested	Shaker used	Input voltage	FRF type	ε_{peak}				Ave. Load (lbf)	f_n (Hz)					ζ_{cfit} (%)			
				ave	max	min	σ		source	ave	max	min	σ	ave	max	min	σ
bending	E-M	30(pp)	SO	8.40E-06	8.51E-06	8.30E-06	8.81E-08	3.9E-01	fpeak	20.6793	20.6820	20.6760	0.0021	3.96E-03	4.16E-03	3.77E-03	1.84E-04
bending	E-M	30(pp)	SO	8.47E-06	8.60E-06	8.37E-06	9.66E-08	3.9E-01	fpeak	20.6807	20.6880	20.6720	0.0059	3.78E-03	4.00E-03	3.58E-03	1.93E-04
bending	E-M	30(pp)	SO	8.55E-06	8.67E-06	8.39E-06	1.14E-07	3.9E-01	fpeak	20.6793	20.6840	20.6760	0.0030	3.78E-03	4.00E-03	3.57E-03	1.96E-04
bending	E-M	10(pp)	SO	3.64E-06	3.69E-06	3.58E-06	3.83E-08	1.3E-01	fpeak	20.7287	20.7320	20.7280	0.0016	2.66E-03	2.71E-03	2.61E-03	3.70E-05
bending	E-M	10(pp)	SO	3.60E-06	3.61E-06	3.56E-06	1.91E-08	1.3E-01	fpeak	20.7273	20.7280	20.7240	0.0016	2.64E-03	2.68E-03	2.60E-03	3.09E-05
bending	E-M	3(pp)	SO	1.07E-06	1.09E-06	1.05E-06	1.52E-08	3.9E-02	fpeak	20.7407	20.7440	20.7400	0.0016	2.32E-03	2.37E-03	2.28E-03	3.19E-05
bending	E-M	3(pp)	SO	9.26E-07	9.52E-07	9.03E-07	2.11E-08	3.9E-02	fpeak	20.7373	20.7420	20.7340	0.0030	2.37E-03	2.44E-03	2.31E-03	4.57E-05
bending	B-fly	100	SO	8.46E-07	8.48E-07	8.44E-07	1.50E-09	3.2E-02	fpeak	20.7175	20.7200	20.7150	0.0018	2.52E-03	2.54E-03	2.47E-03	2.42E-05
bending	B-fly	100	SO	7.99E-07	8.01E-07	7.96E-07	2.20E-09	3.2E-02	fpeak	20.7173	20.7200	20.7160	0.0021	2.58E-03	2.64E-03	2.51E-03	5.63E-05
bending	B-fly	100	SO	8.10E-07	8.11E-07	8.08E-07	1.06E-09	3.2E-02	fpeak	20.7180	20.7200	20.7160	0.0022	2.53E-03	2.60E-03	2.48E-03	4.87E-05
bending	B-fly	100	SO	8.44E-07	8.46E-07	8.43E-07	1.02E-09	3.2E-02	fpeak	20.7200	20.7200	20.7200	0.0000	2.51E-03	2.57E-03	2.48E-03	3.33E-05
bending	B-fly	30	SO	2.28E-07	2.30E-07	2.26E-07	1.45E-09	8.4E-03	fpeak	20.7227	20.7240	20.7200	0.0021	2.50E-03	2.58E-03	2.44E-03	5.07E-05
bending	B-fly	10	SO	7.97E-08	8.09E-08	7.86E-08	9.00E-10	2.7E-03	SDOF	20.7233	20.7251	20.7215	0.0012	2.53E-03	2.64E-03	2.43E-03	7.78E-05
bending	B-fly	3	SO	2.33E-08	2.36E-08	2.30E-08	1.89E-10	7.5E-04	SDOF	20.7205	20.7225	20.7189	0.0016	2.50E-03	2.55E-03	2.42E-03	4.95E-05
bending	B-fly	3	SO	2.34E-08	2.38E-08	2.32E-08	2.41E-10	7.5E-04	SDOF	20.7218	20.7224	20.7209	0.0005	2.51E-03	2.57E-03	2.48E-03	3.27E-05
bending	B-fly	3	SO	2.14E-08	2.16E-08	2.11E-08	1.81E-10	7.5E-04	SDOF	20.7166	20.7188	20.7151	0.0014	2.43E-03	2.45E-03	2.39E-03	2.60E-05
bending	B-fly	1	SO	8.00E-09	8.18E-09	7.89E-09	9.78E-11	2.3E-04	SDOF	20.7207	20.7231	20.7185	0.0017	2.50E-03	2.66E-03	2.35E-03	1.19E-04
bending	B-fly	0.3	SO	2.81E-09	3.07E-09	2.65E-09	1.56E-10	5.0E-05	SDOF	20.7270	20.7394	20.7186	0.0075	2.11E-03	2.72E-03	1.46E-03	4.54E-04

Table A3 - Bending Mode Results

Torsion mode sweeps (B-fly shaker; 100 V input)

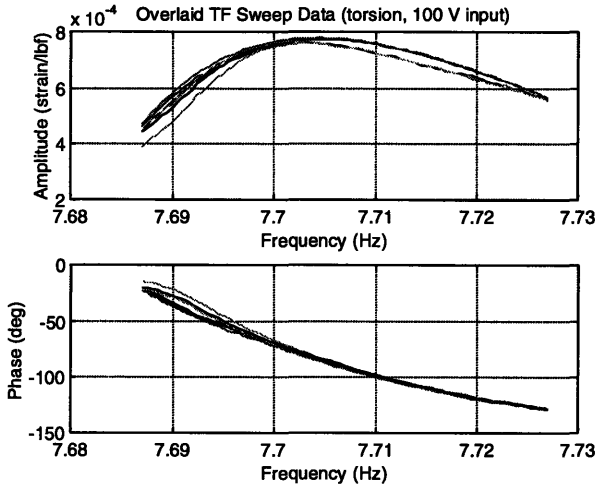

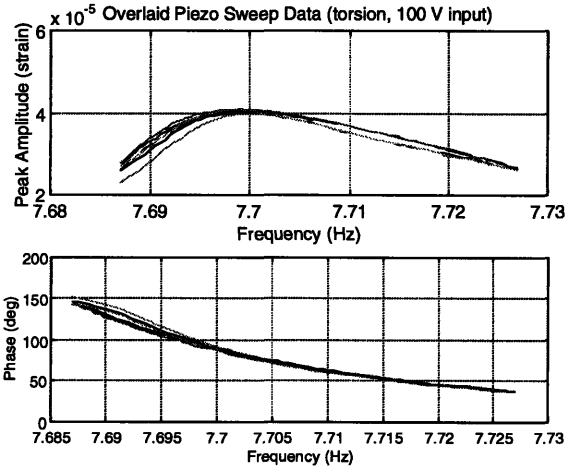

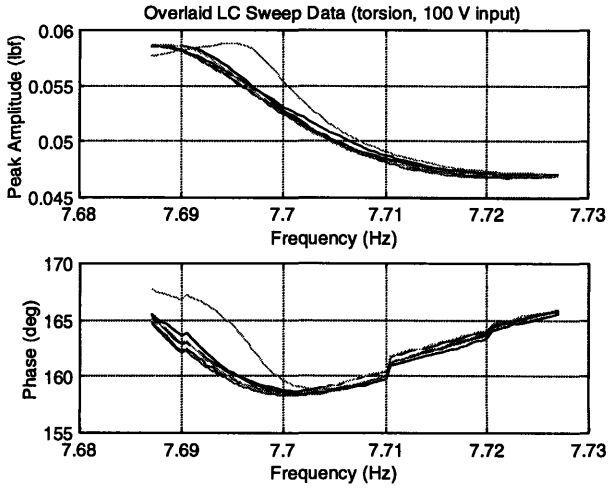

Torsion mode sweeps (B-fly shaker; 30 V input)

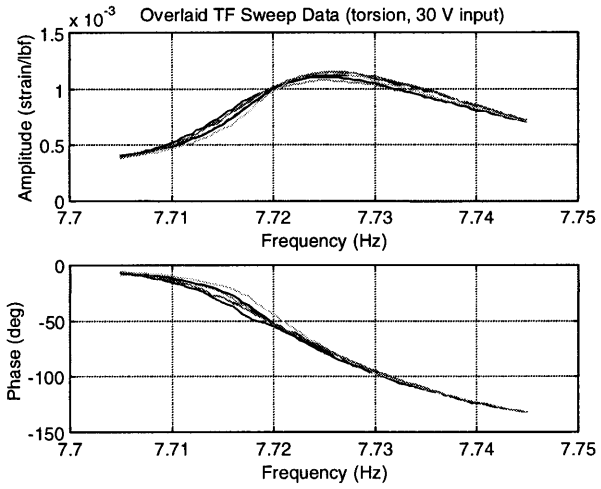

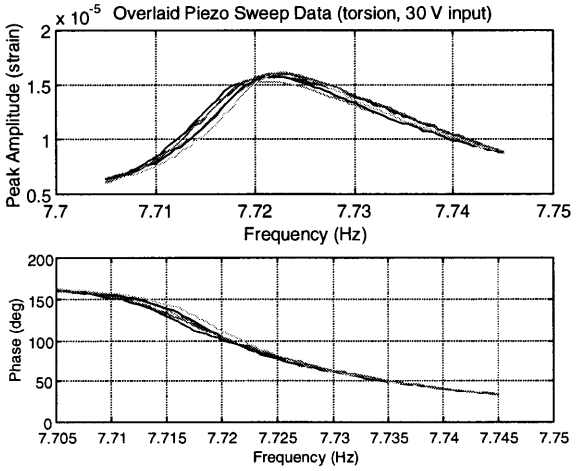

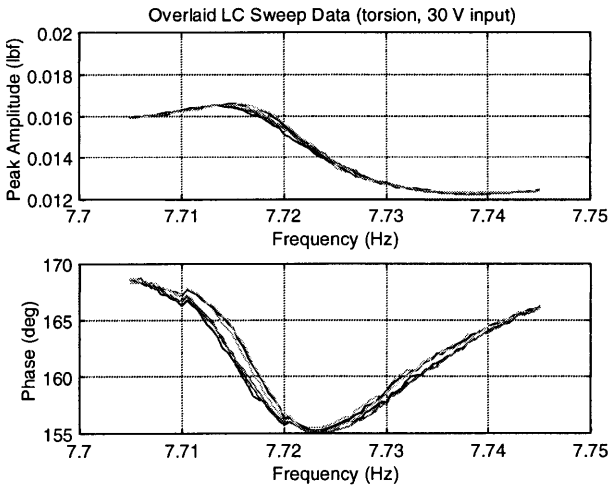

Torsion mode sweeps (B-fly shaker; 10 V input)

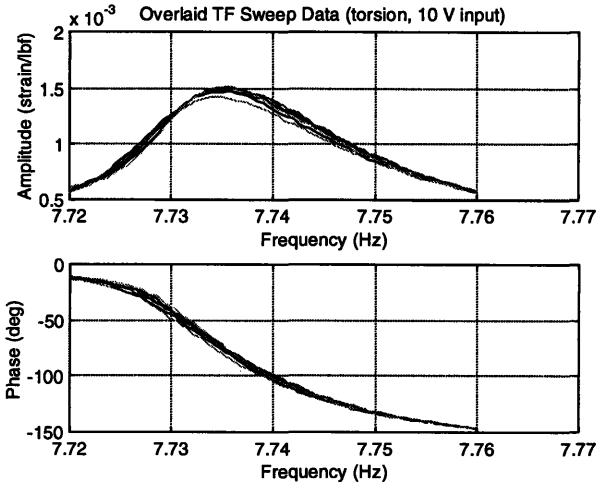

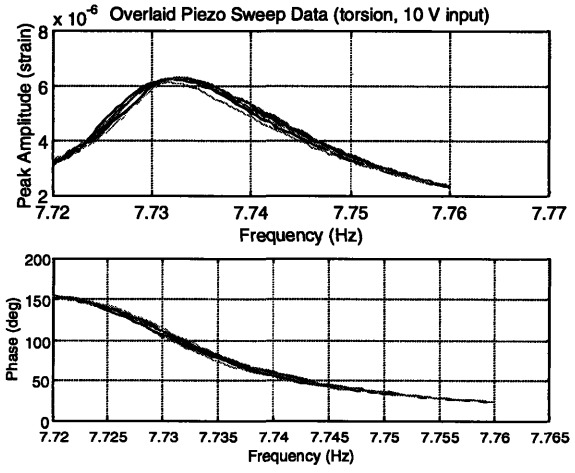

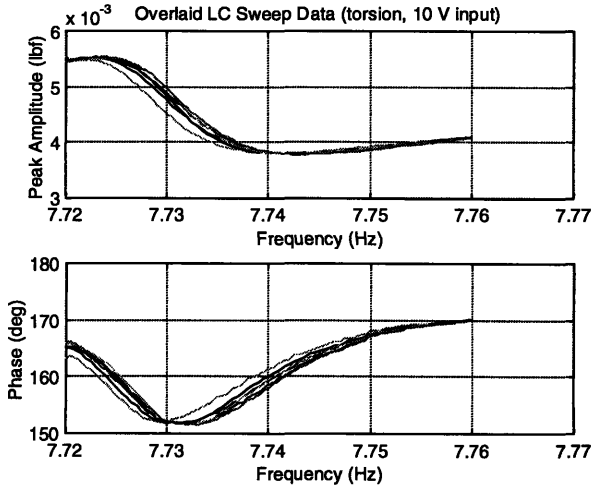

Torsion mode sweeps (B-fly shaker; 3 V input)

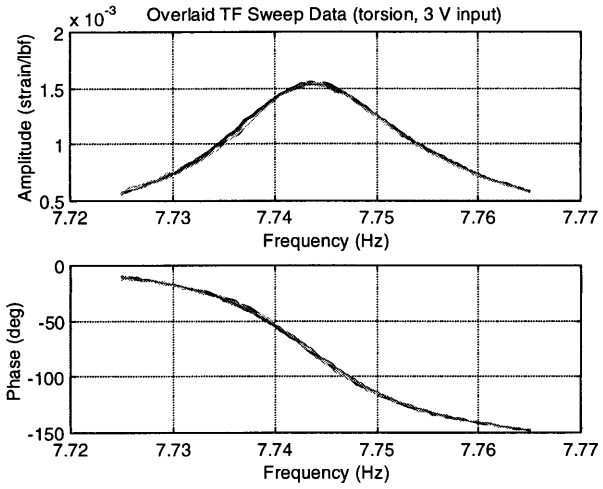

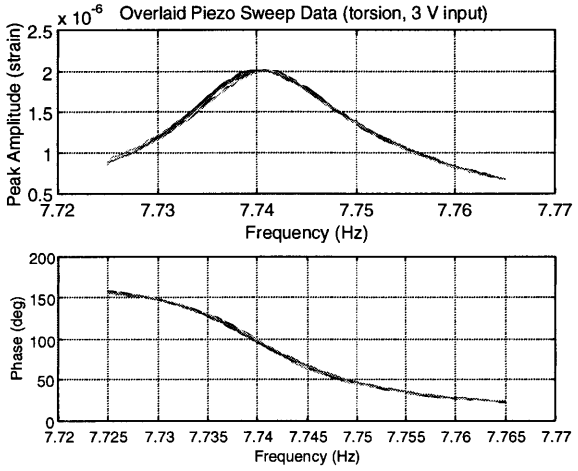

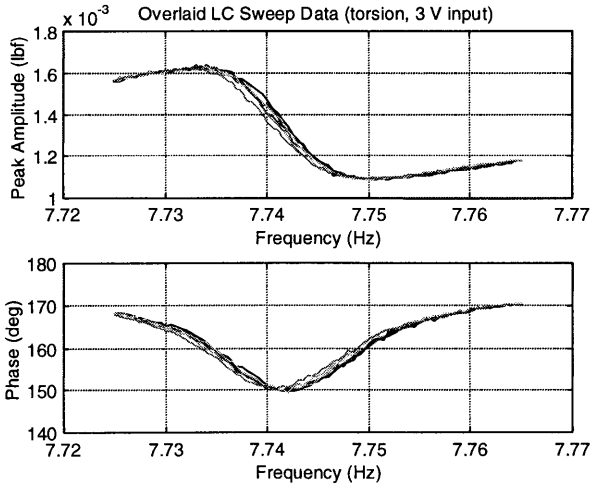

Torsion mode sweeps (B-fly shaker; 1 V input)

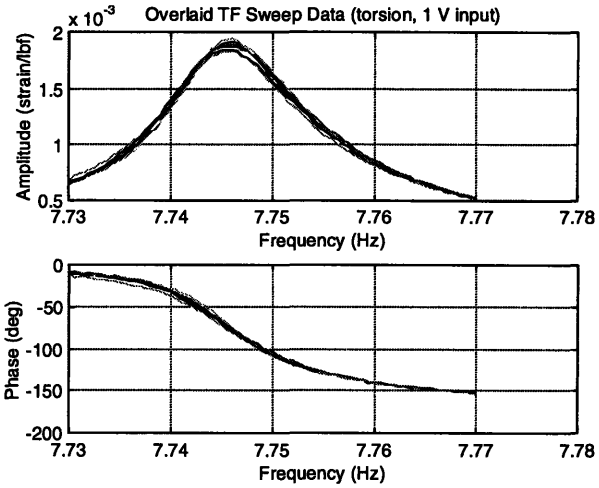

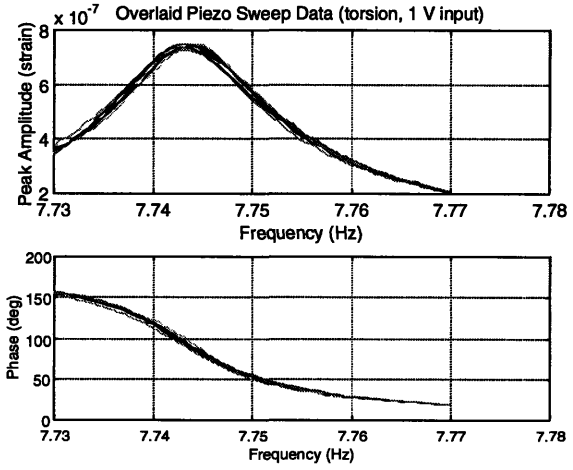

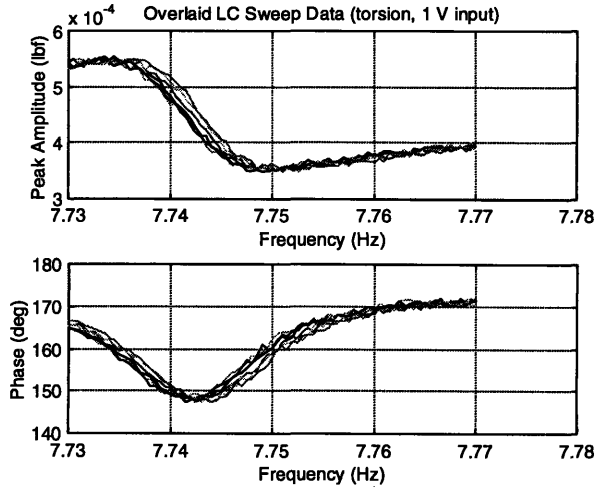

Torsion mode sweeps (B-fly shaker; 0.3 V input)

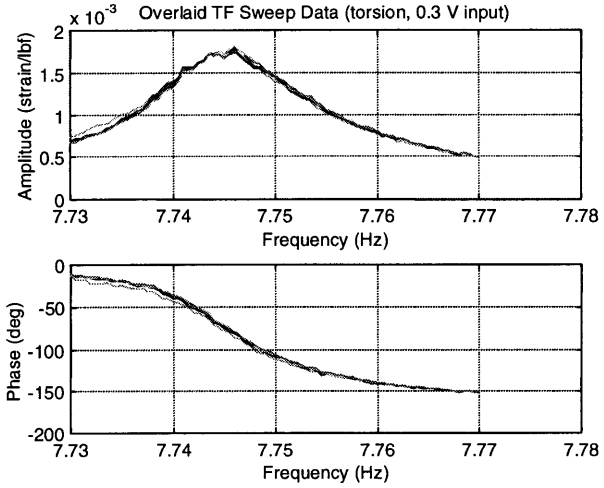

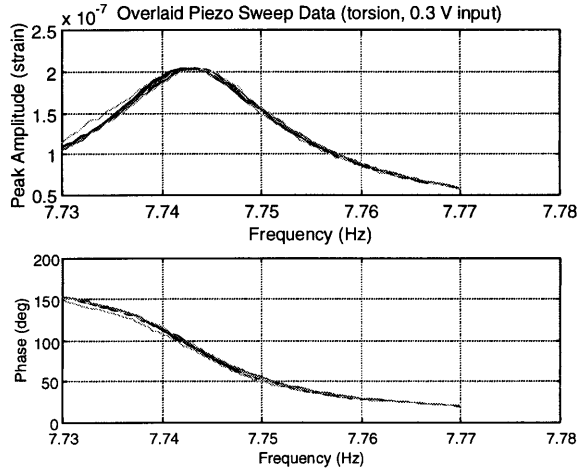

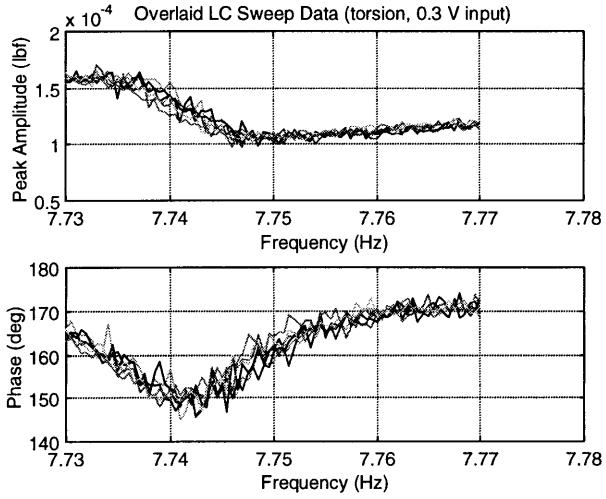

Torsion mode sweeps (B-fly shaker; 0.1 V input)

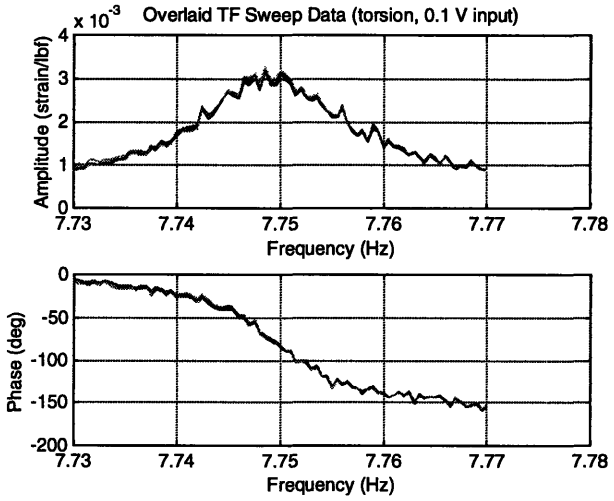

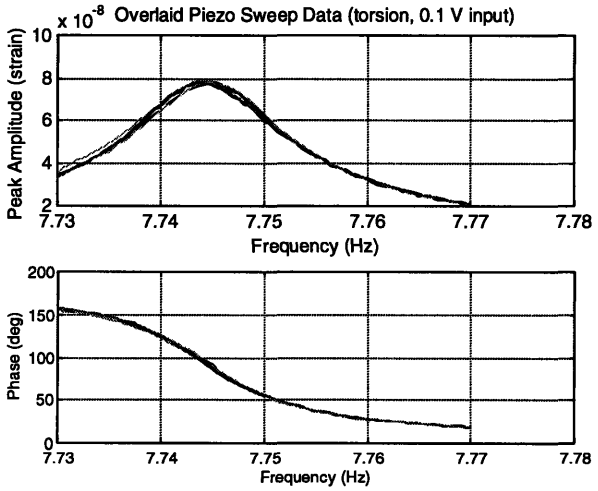

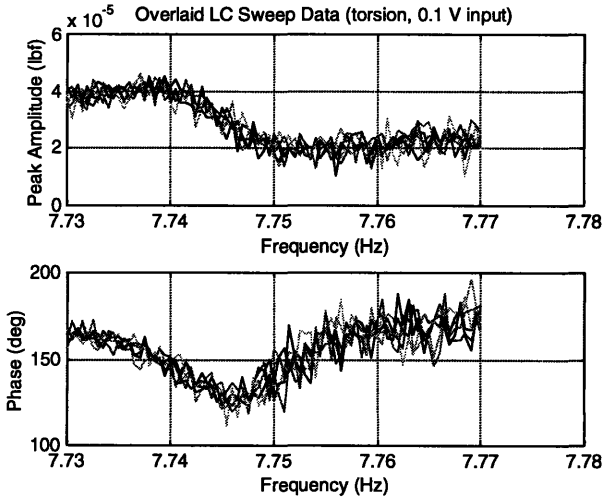

Torsion mode sweeps (B-fly shaker; 0.03 V input)

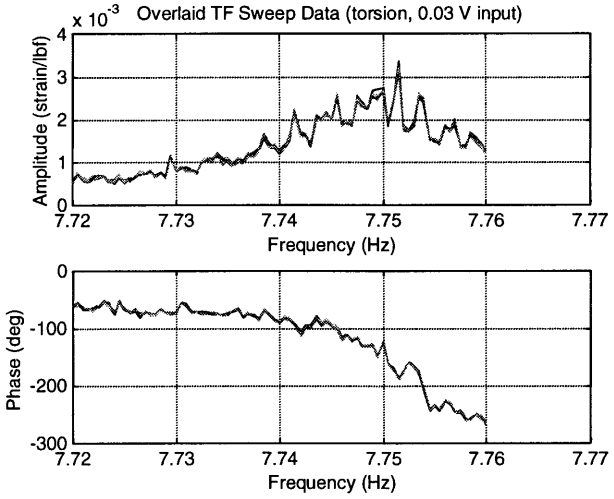

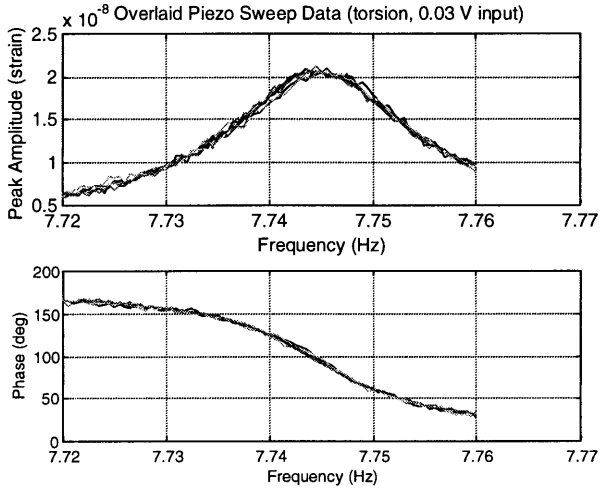

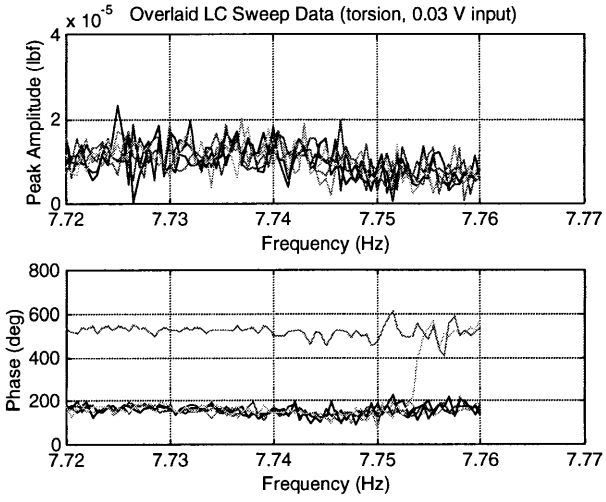

Torsion mode sweeps (B-fly shaker; 0.01 V input)

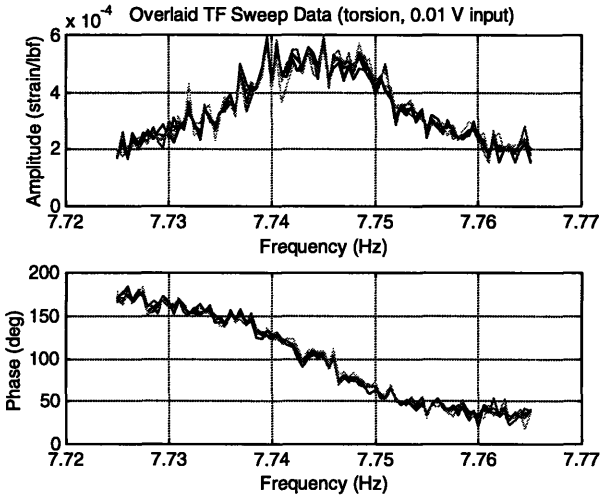

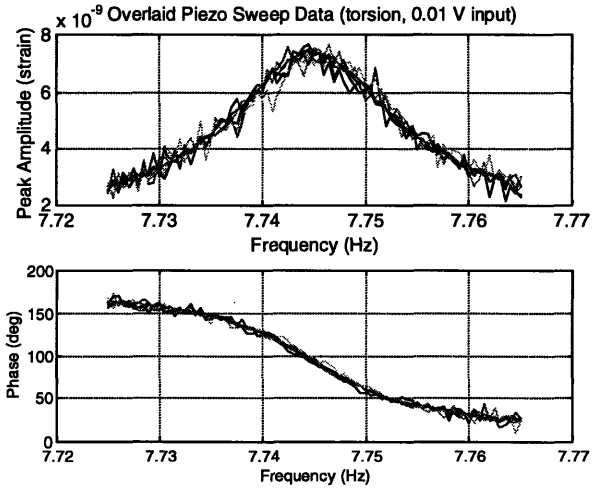

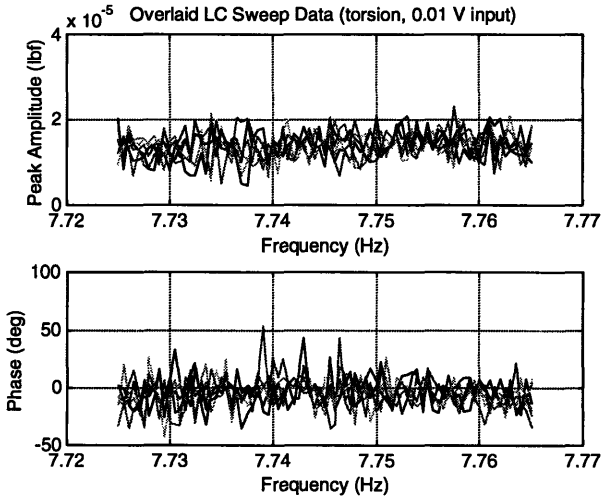

Torsion mode sweeps (B-fly shaker; 0.003 V input)

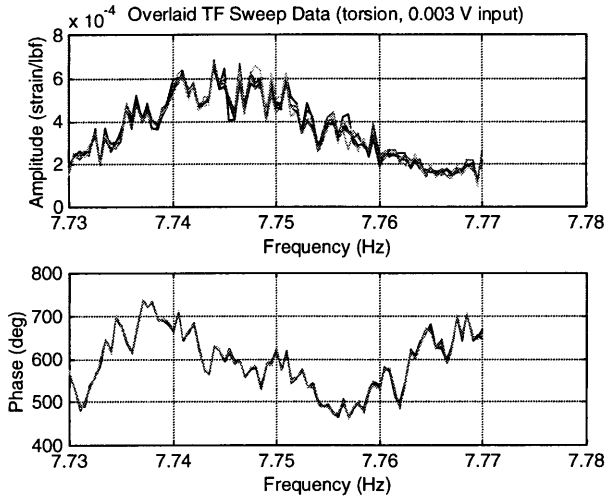

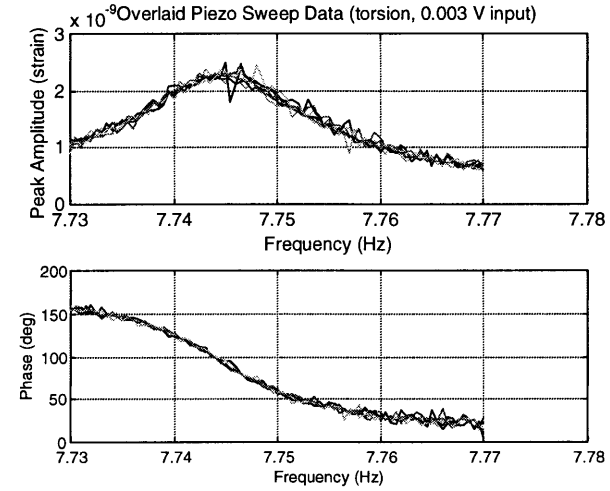

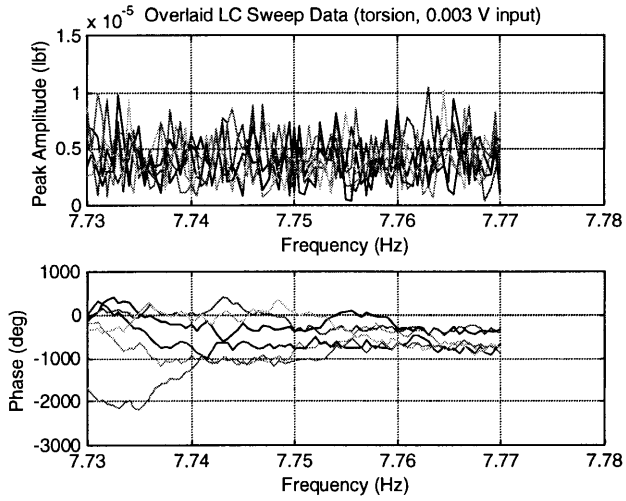

Bending mode sweeps (E-M shaker; 30, 10 & 3 V_{pp} input)

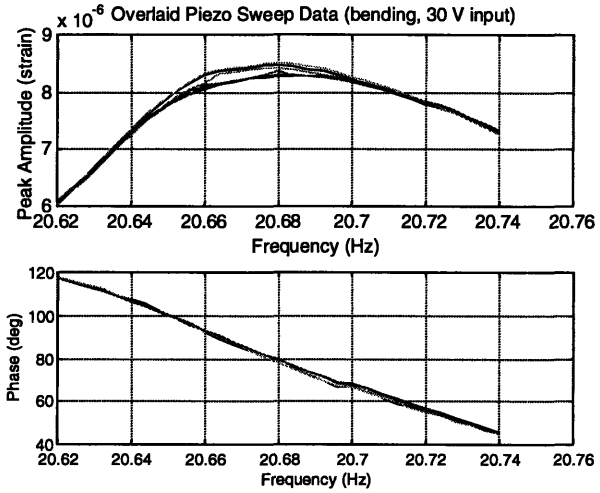

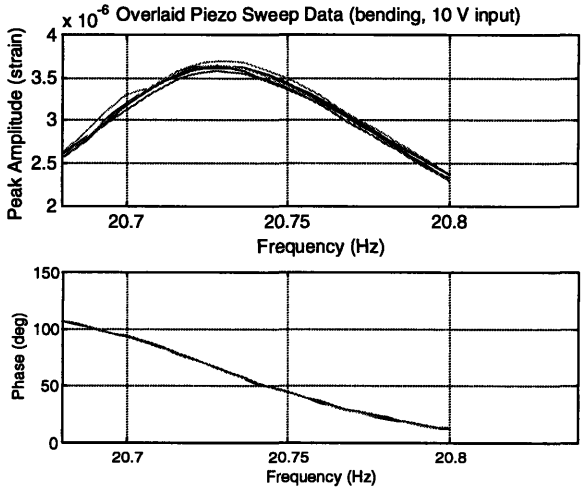

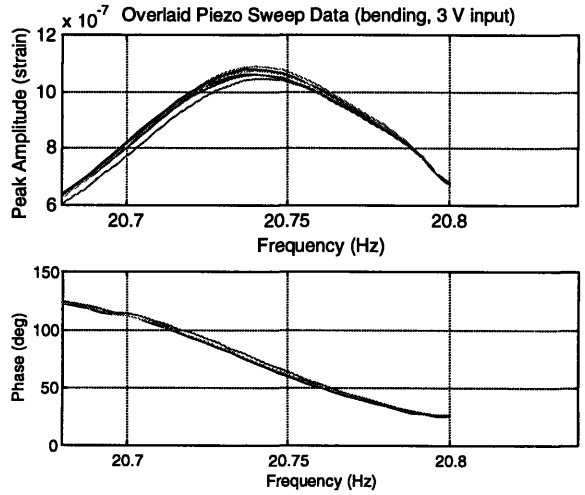

Bending mode sweeps (B-fly shaker; 100, 30 & 10 V input)

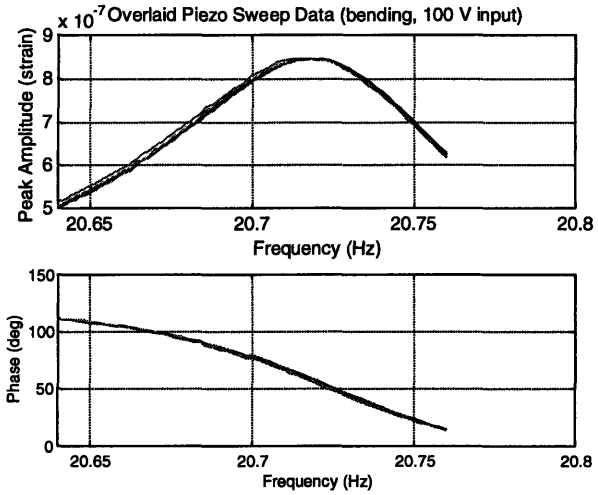

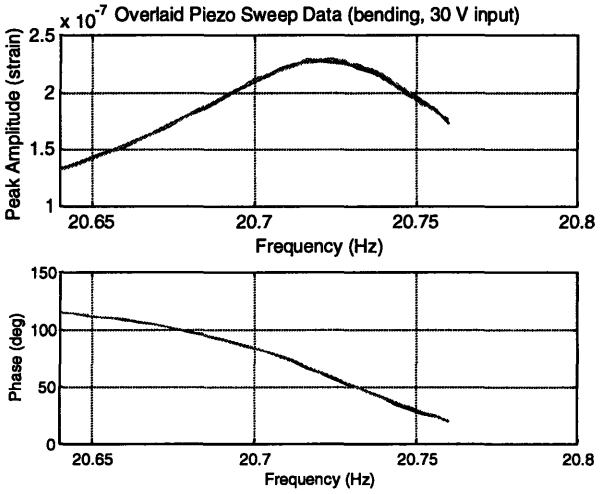

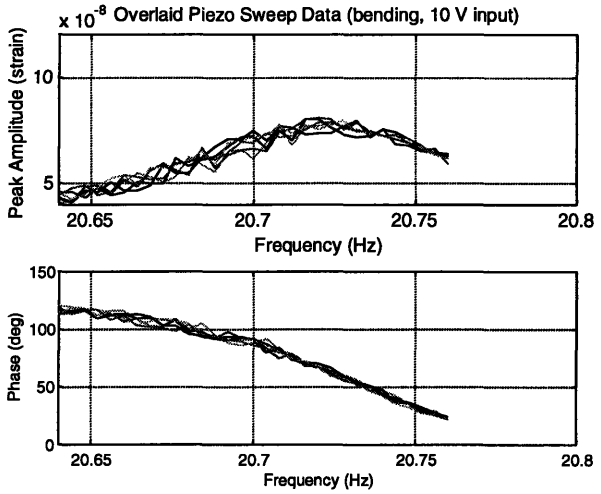

Bending mode sweeps (B-fly shaker; 3, 1 & 0.3 V input)

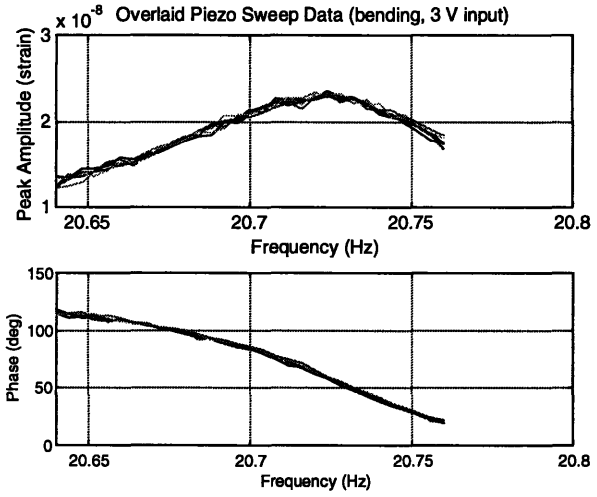

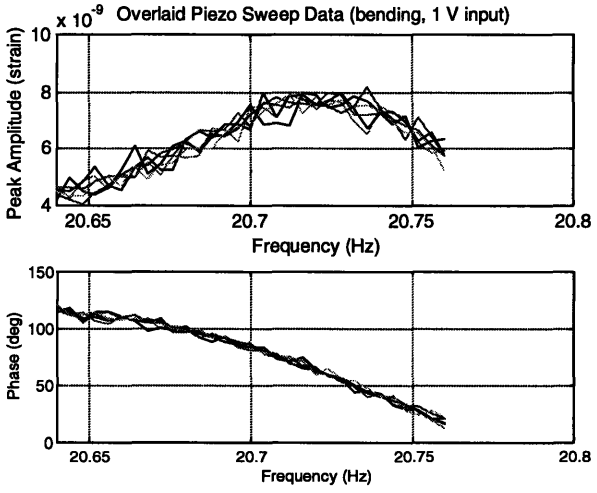

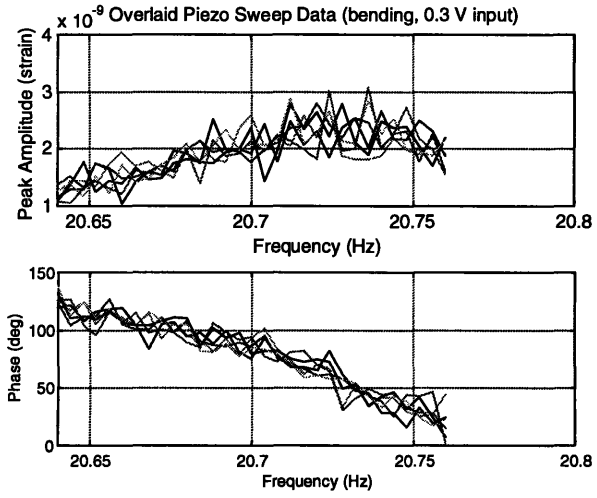

Torsion mode sweeps with accelerometer as sensor (B-fly shaker; 100 V input)

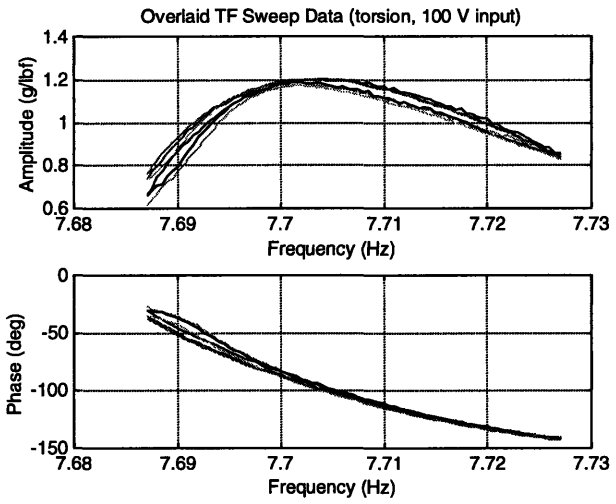

Appendix B

Thermal Snap Characterization Results

Convection Test – June 5th, 1997

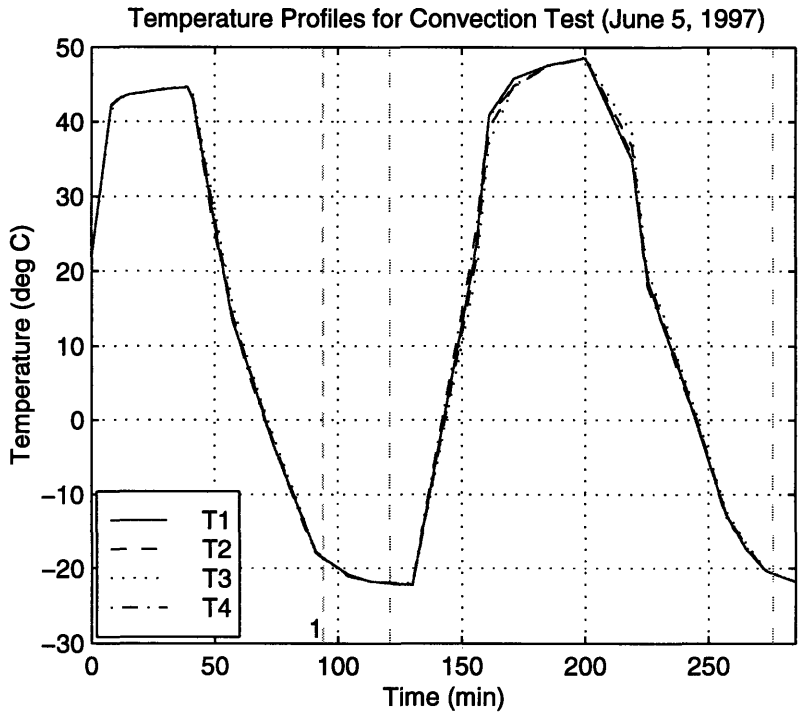

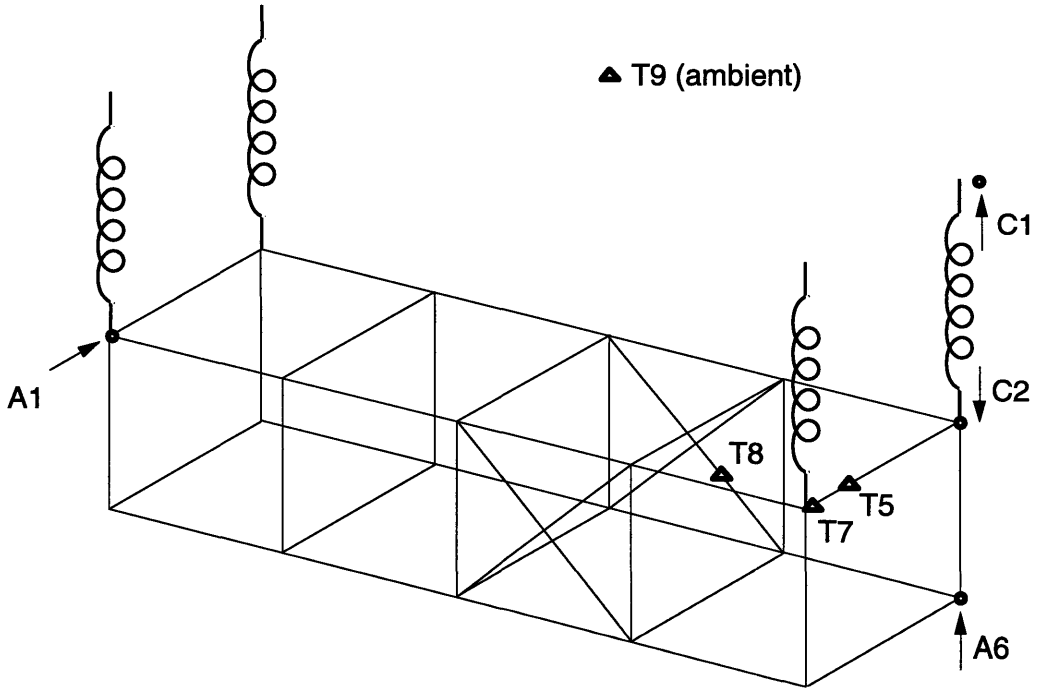

Test Procedure Notes: 5 kHz BW setting on data acquisition unit; medium preload setting on adjustable pretension bay

Convection Test – June 5th, 1997

Event #1

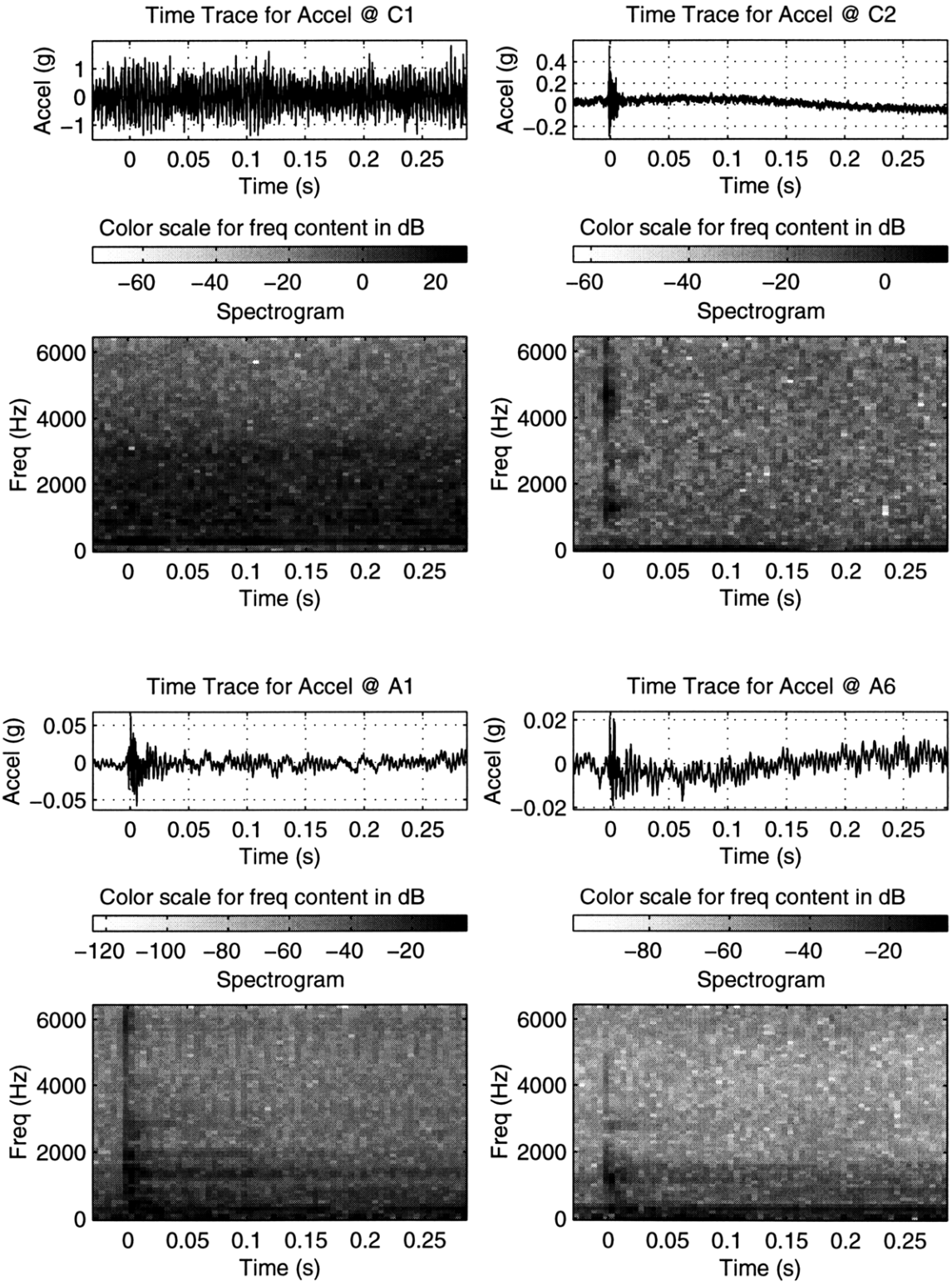

Convection Test – June 23rd, 1997

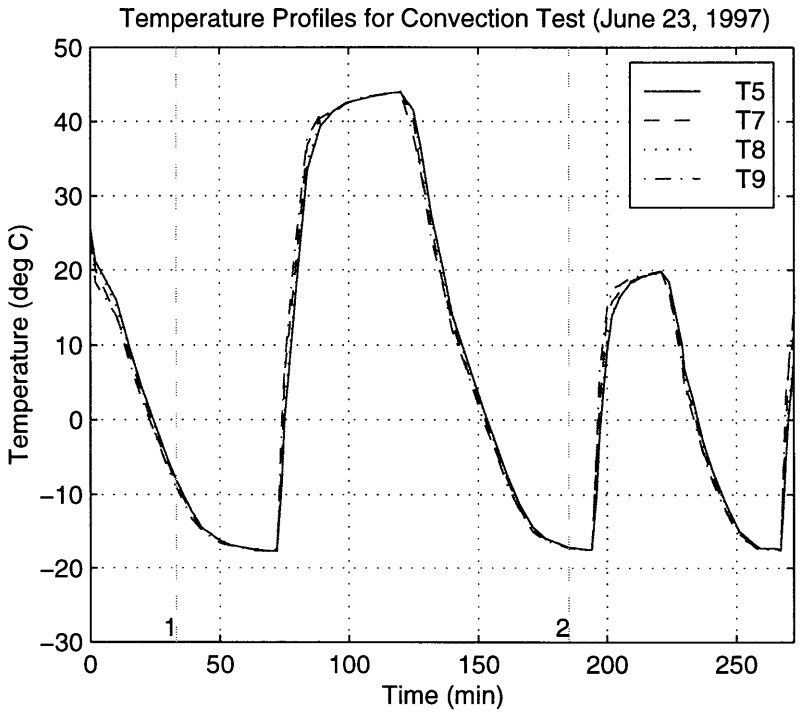

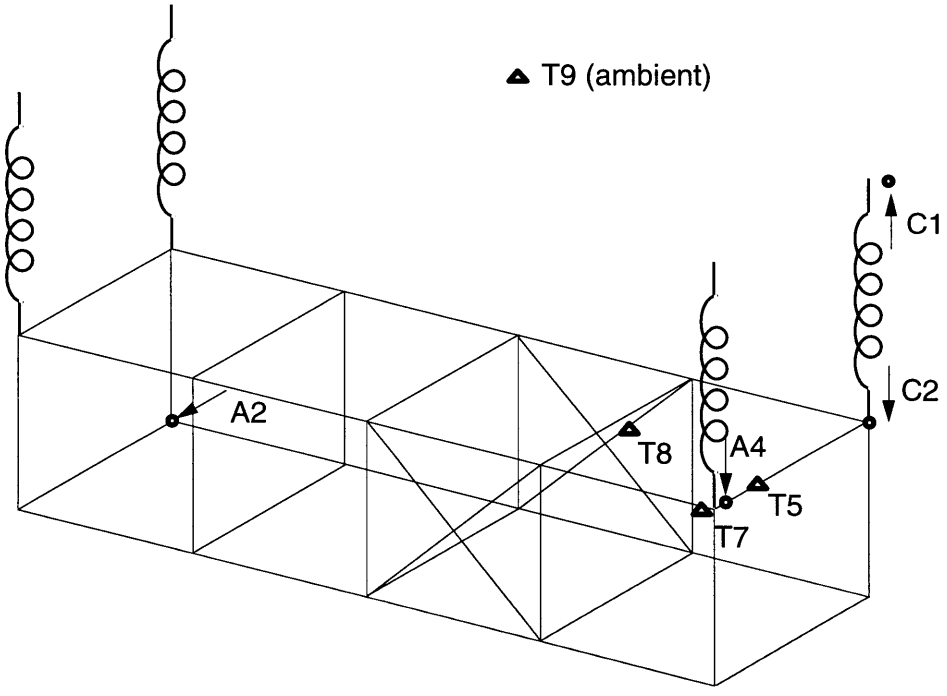

Convection Test – June 23rd, 1997

Event #1

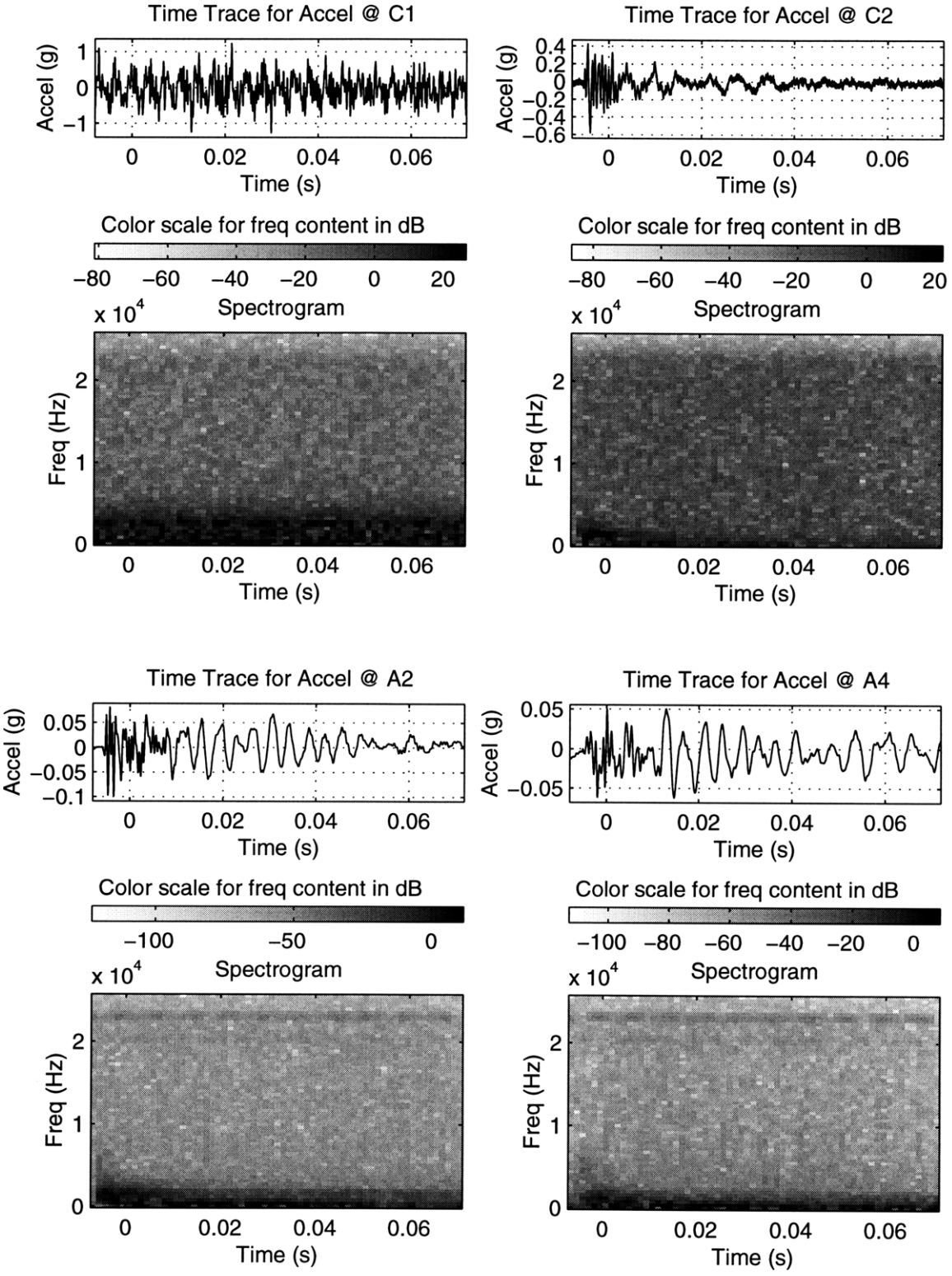

Convection Test – June 23rd, 1997

Event #2

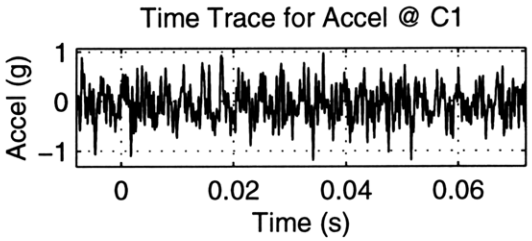

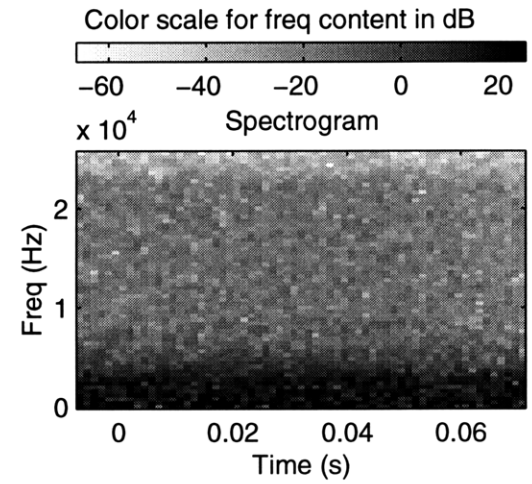

Accelerometer A2
not connected to
data acquisition unit

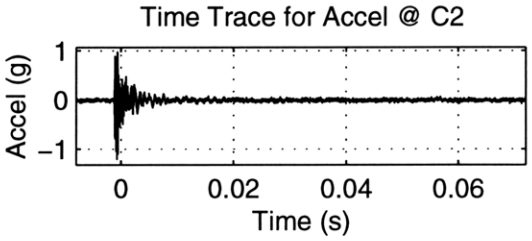

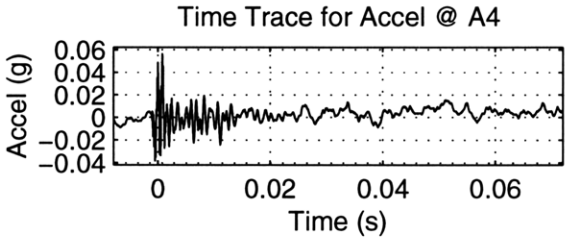

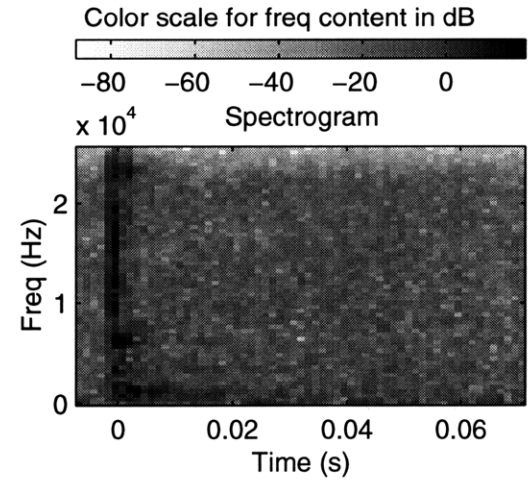

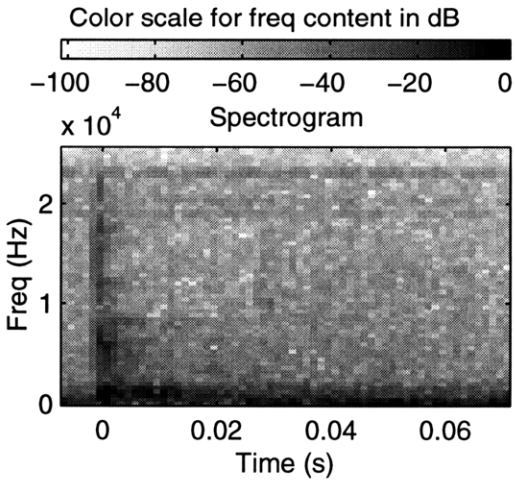

Convection Test – August 28th, 1997

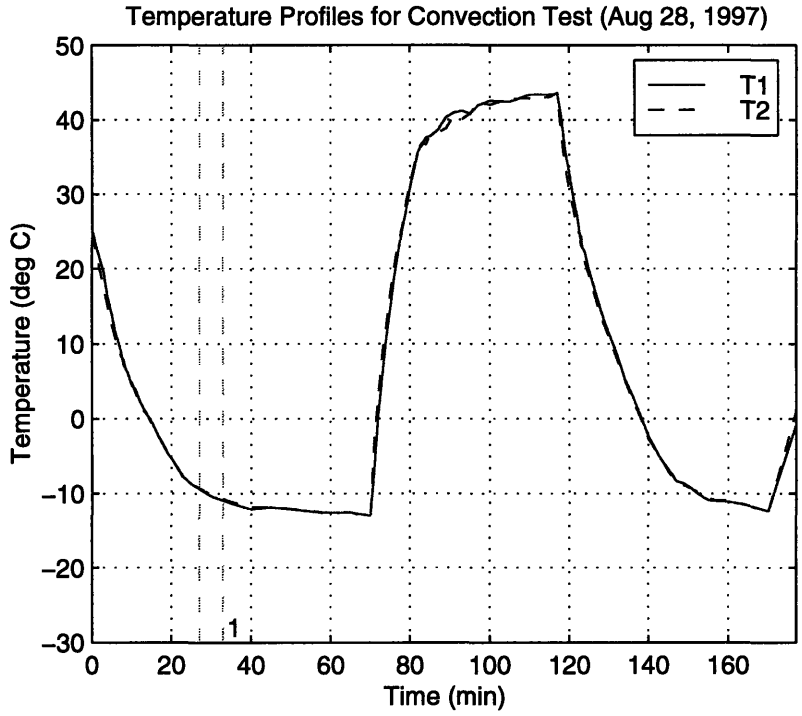

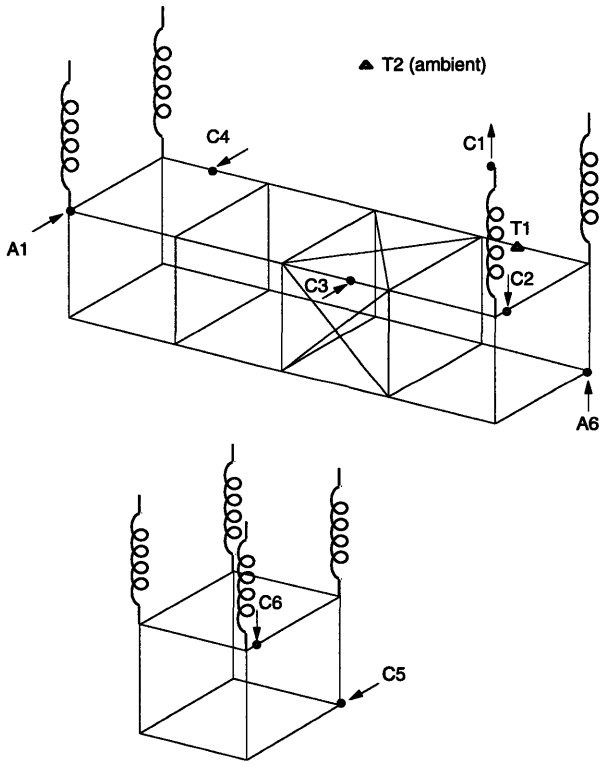

Test Procedure Notes: 1st data acquisition unit did not trigger on events (channels C1, C2, C3 & C4 not available)

Convection Test – August 28th, 1997

Event #1

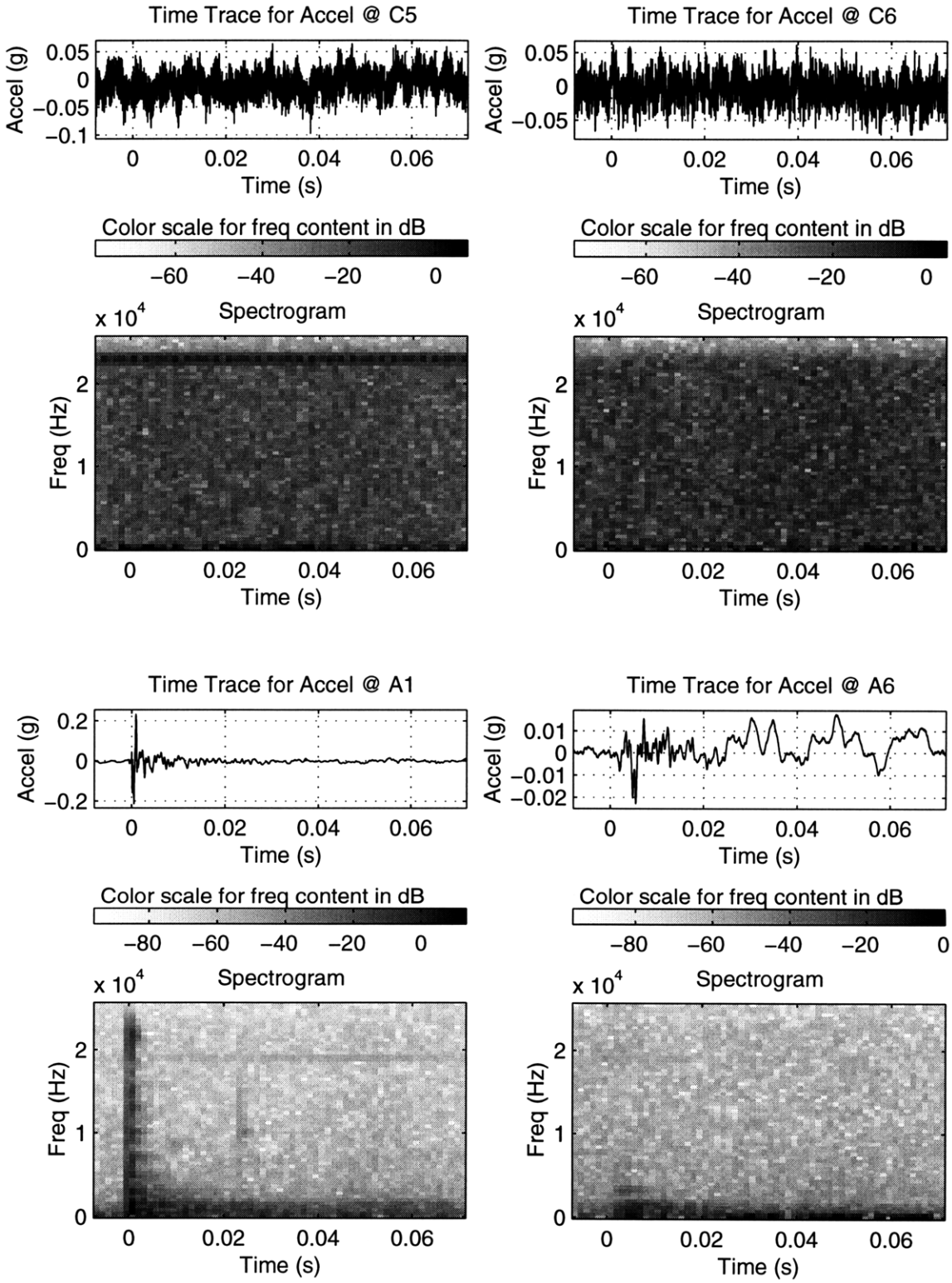

Convection Test – September 2nd, 1997

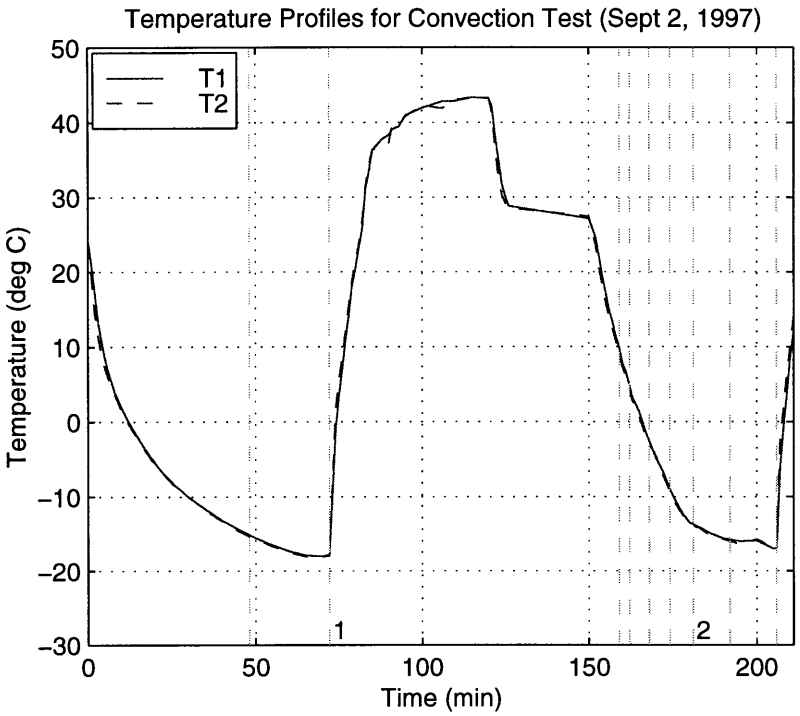

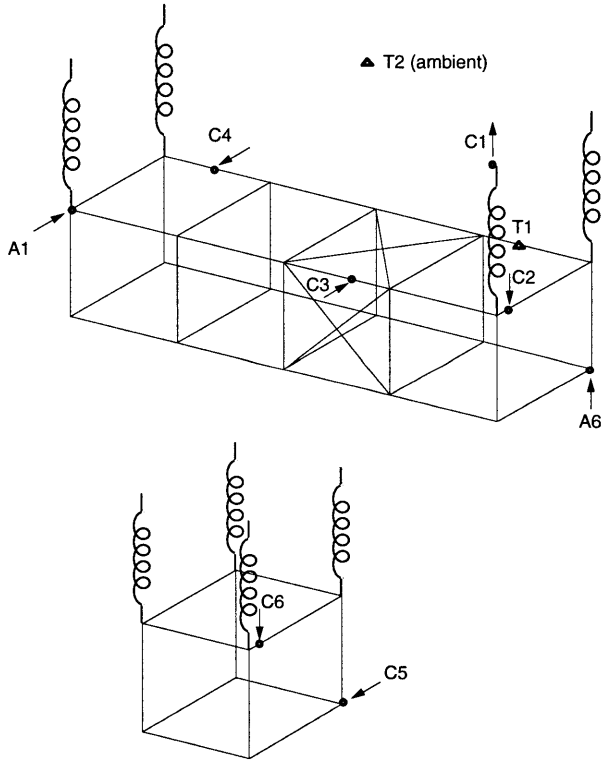

Convection Test – September 2nd, 1997

Event #1

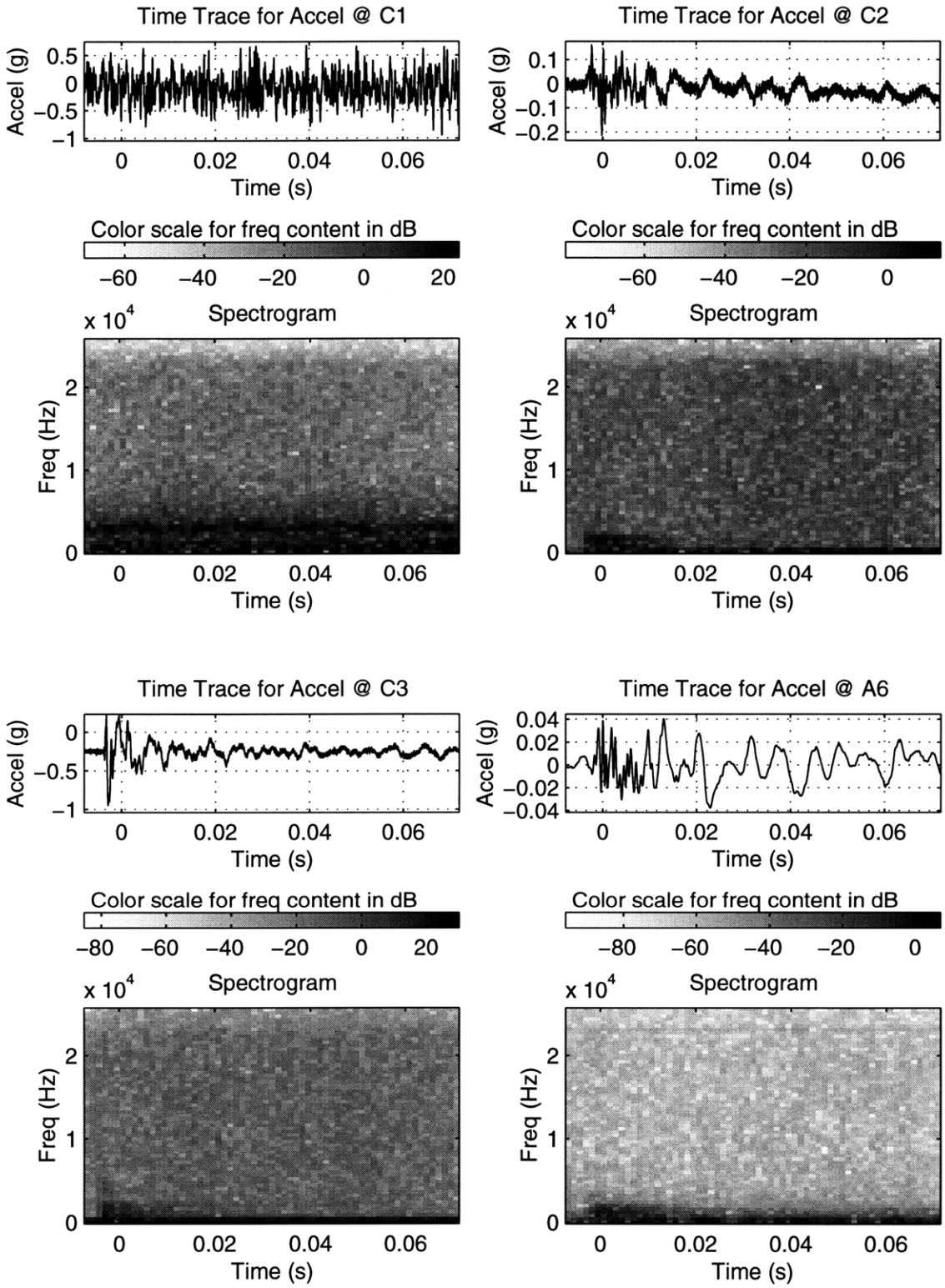

Convection Test – September 2nd, 1997

Event #1 (continued)

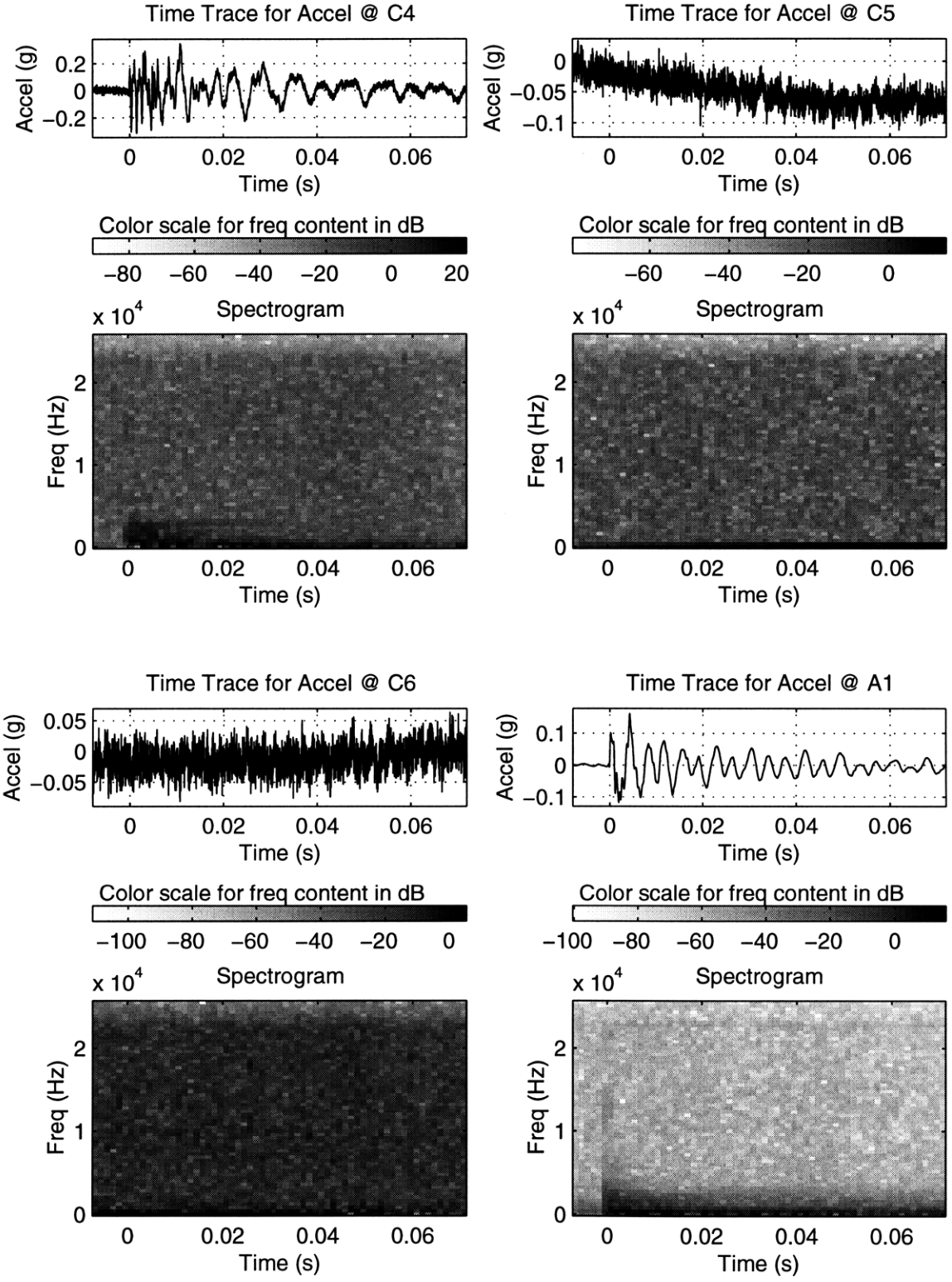

Convection Test – September 2nd, 1997

Event #2

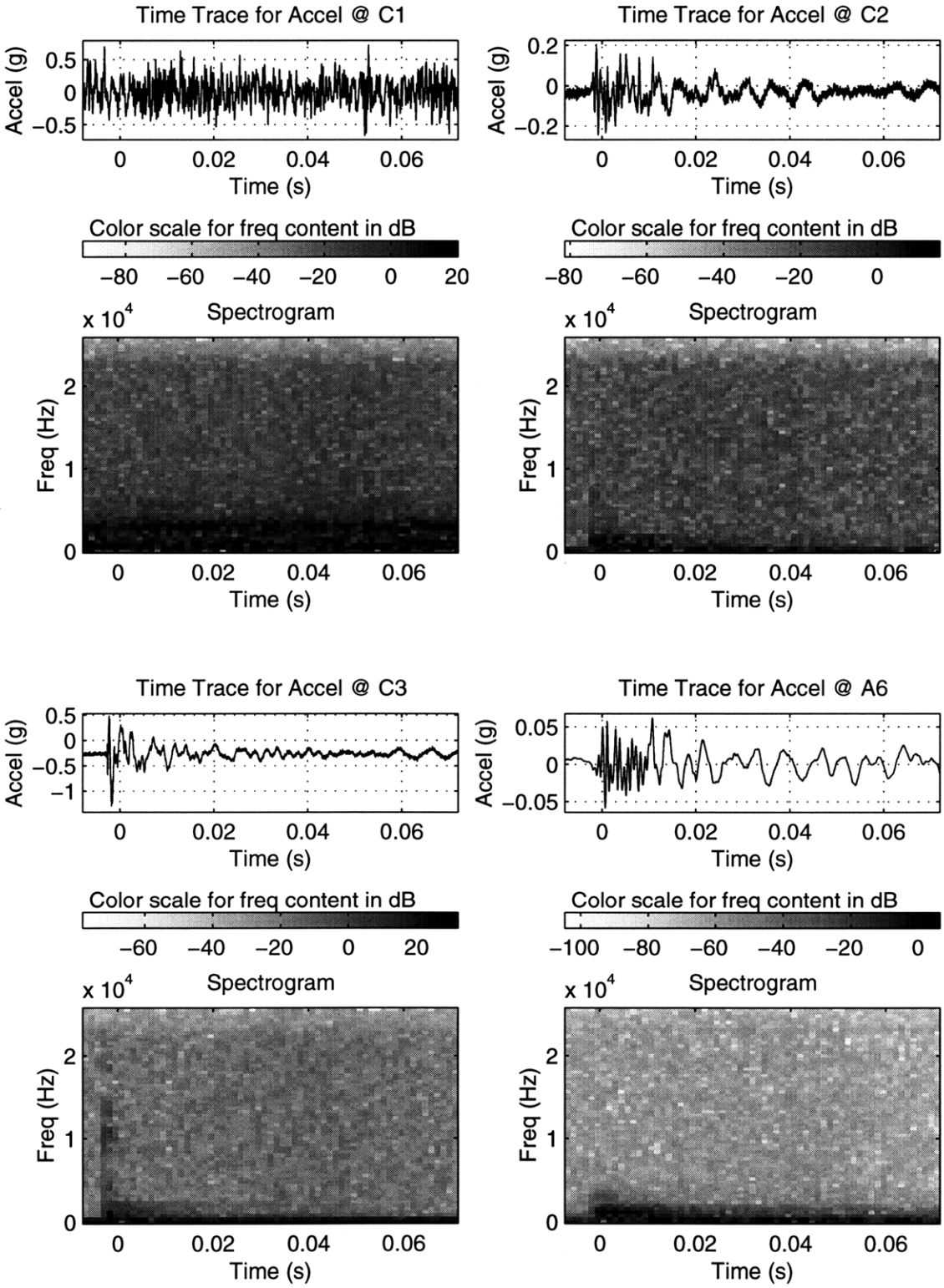

Convection Test – September 2nd, 1997

Event #2 (continued)

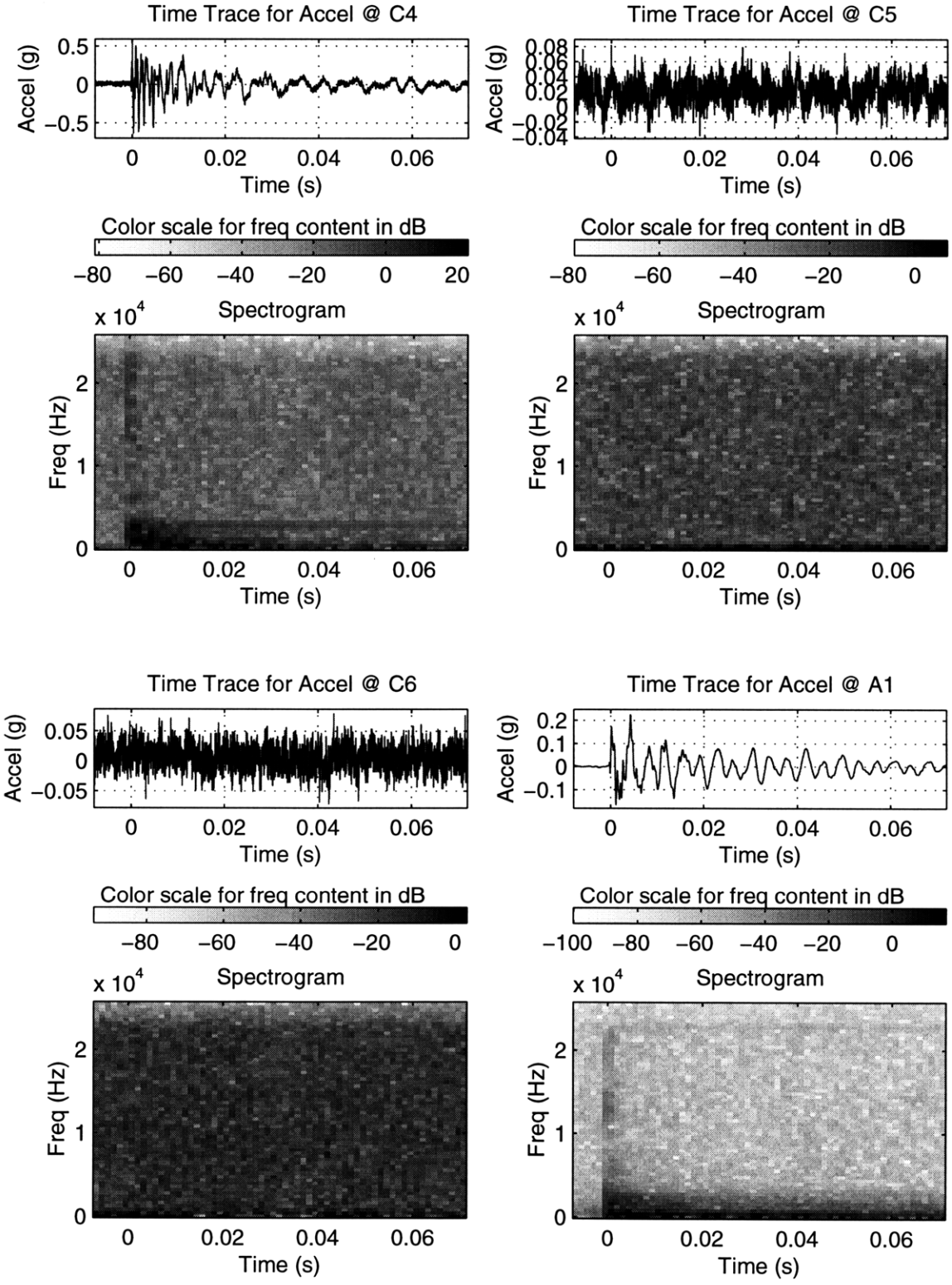

Radiation Test – September 29th, 1997

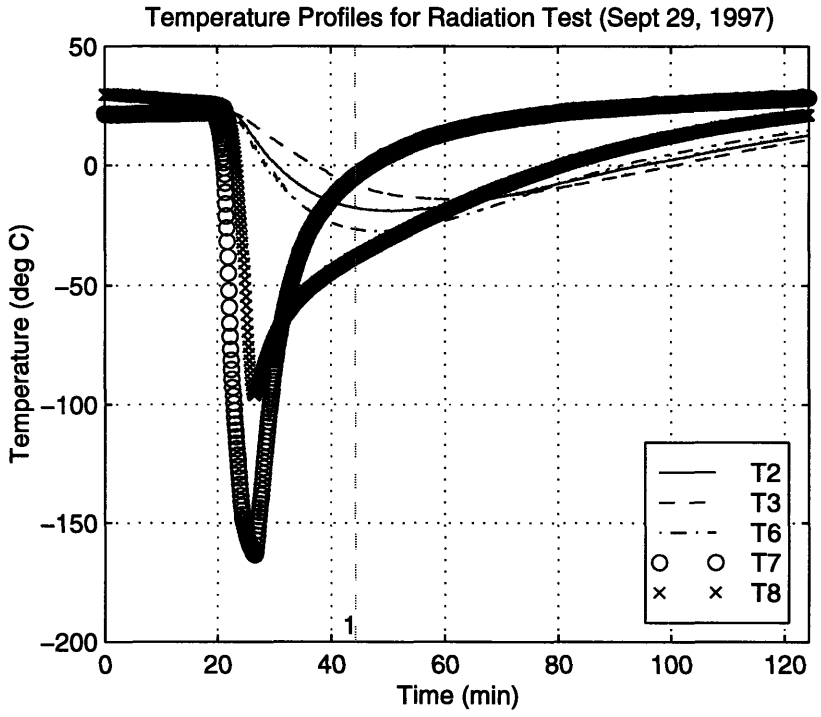

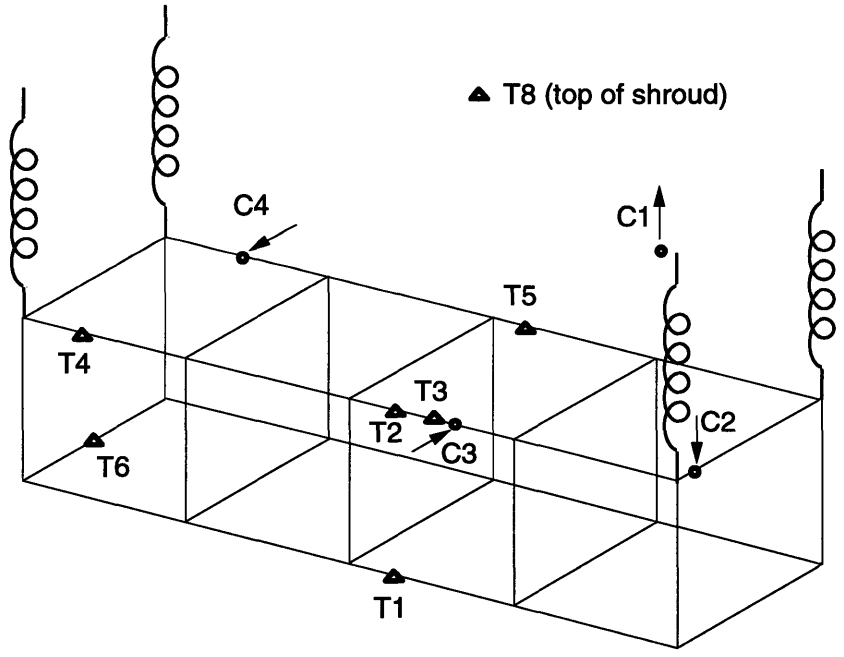

T7 (bottom of shroud)

Radiation Test – September 29th, 1997

Event #1

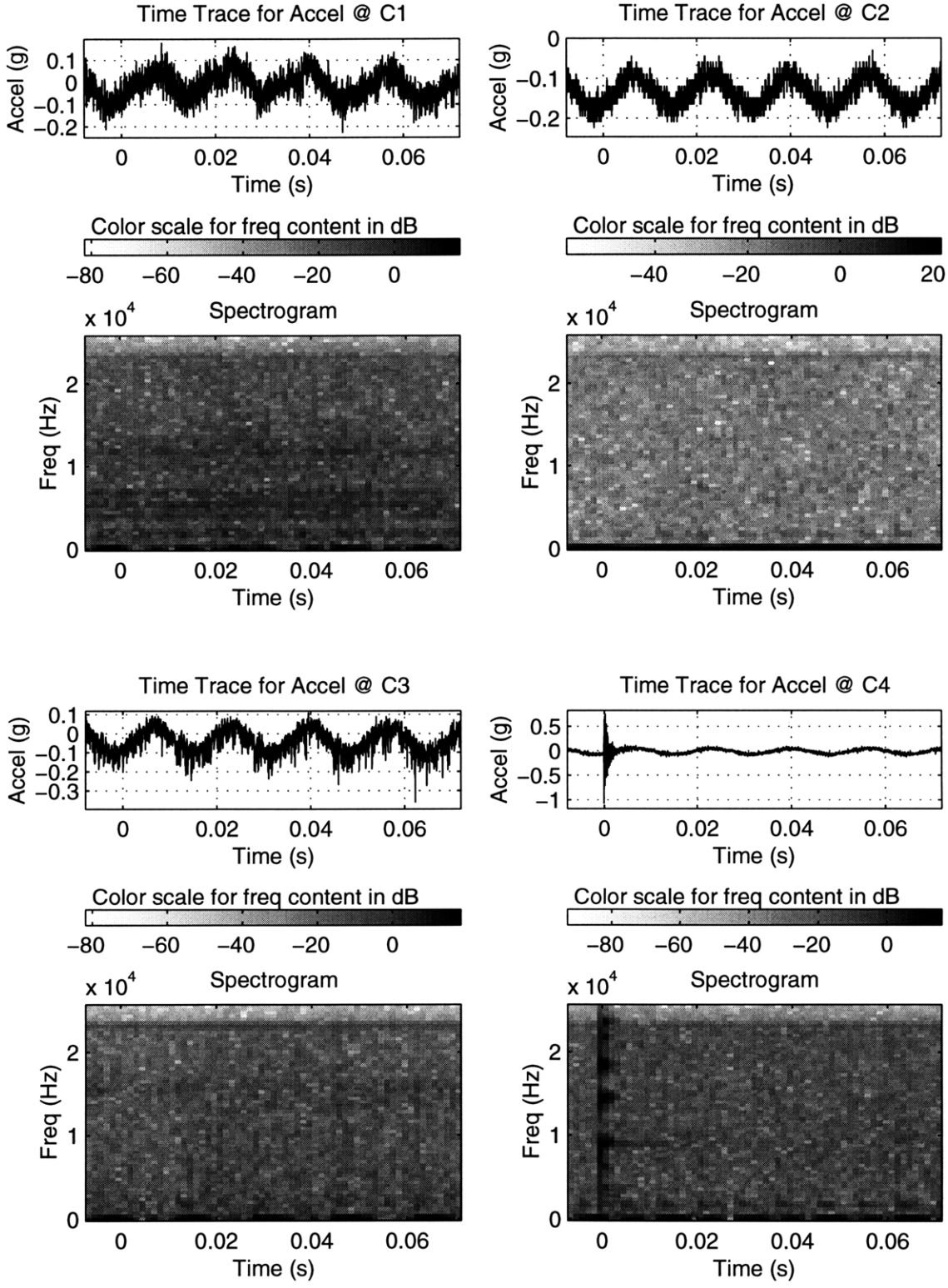

Radiation Test – October 3rd, 1997

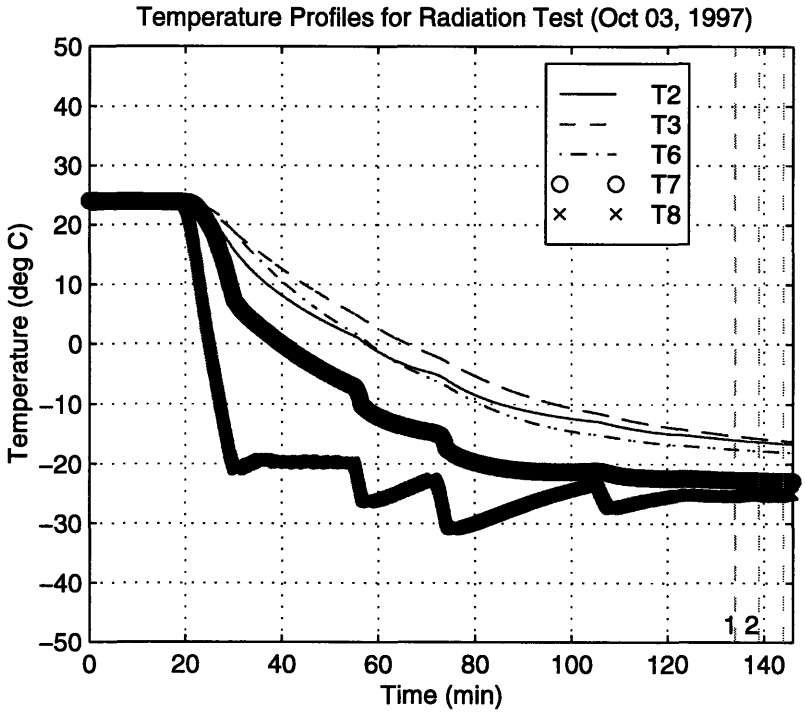

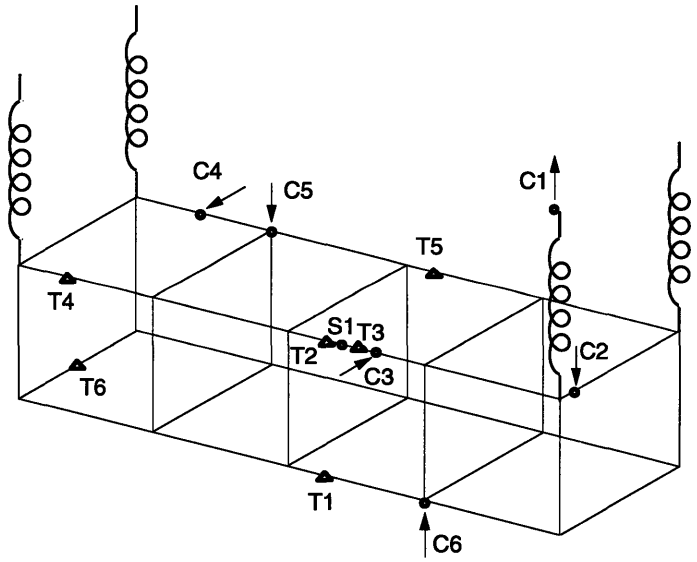

Test Procedure Notes: controlled radiation test using plate instead of shroud; 100kHz BW setting on 2nd data acquisition unit; DC coupling on strain gauge S1; 1st data acquisition unit did not trigger on events (channels C1, C2, C3 & C4 not available)

Radiation Test – October 3rd, 1997

Event #1

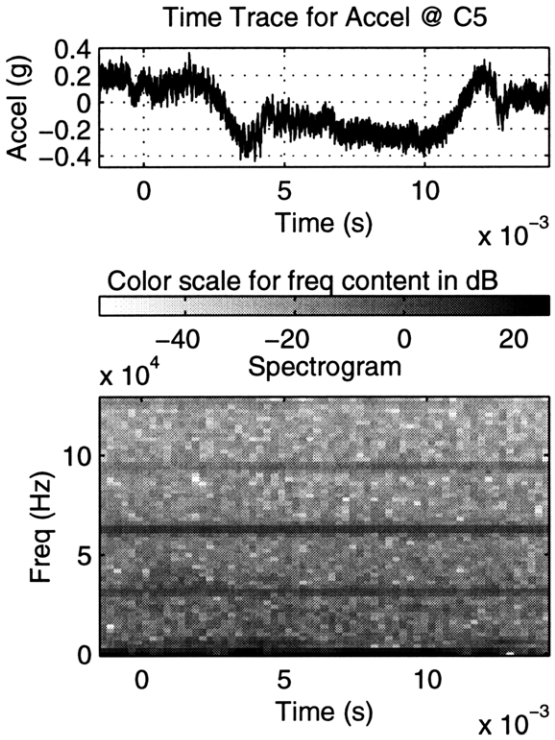

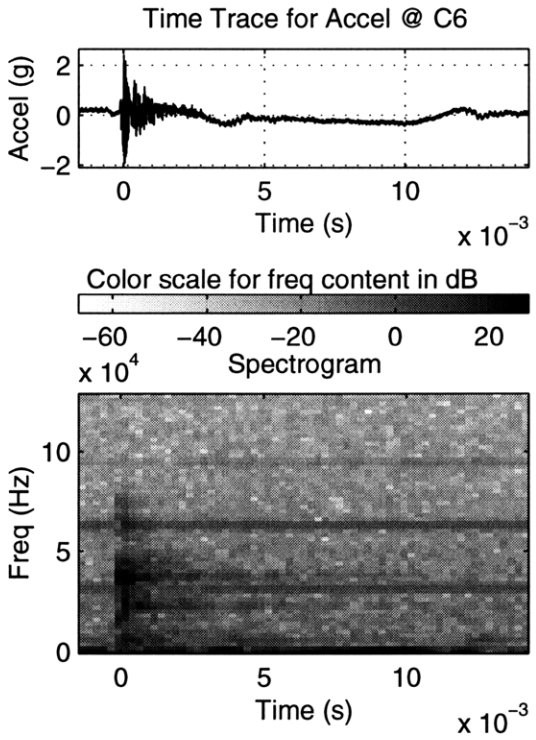

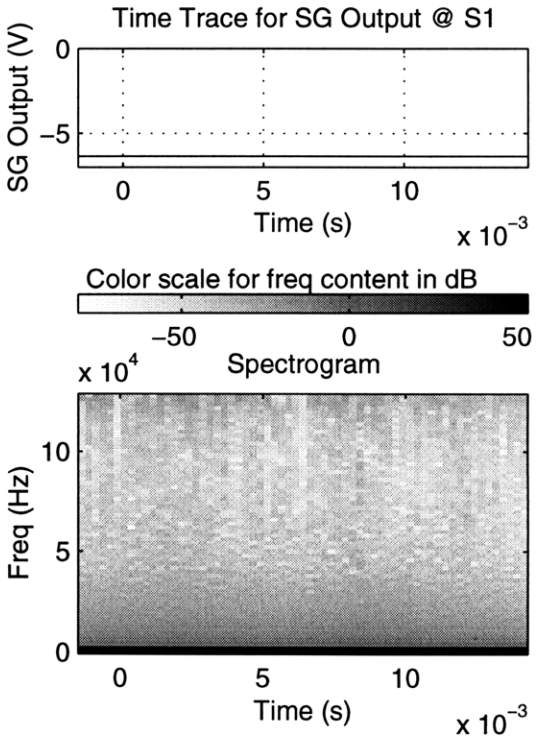

Radiation Test – October 3rd, 1997

Event #2

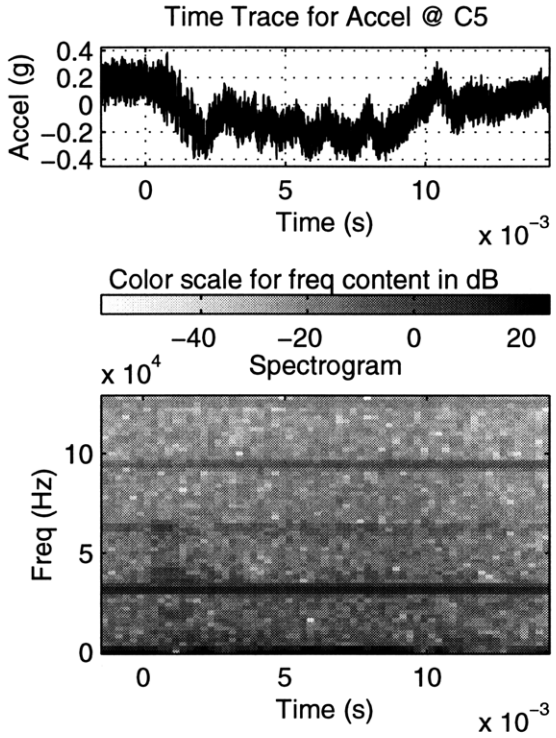

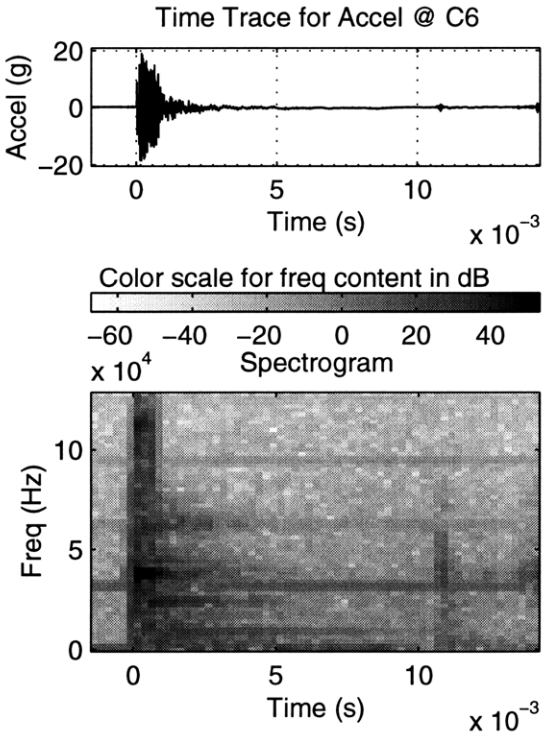

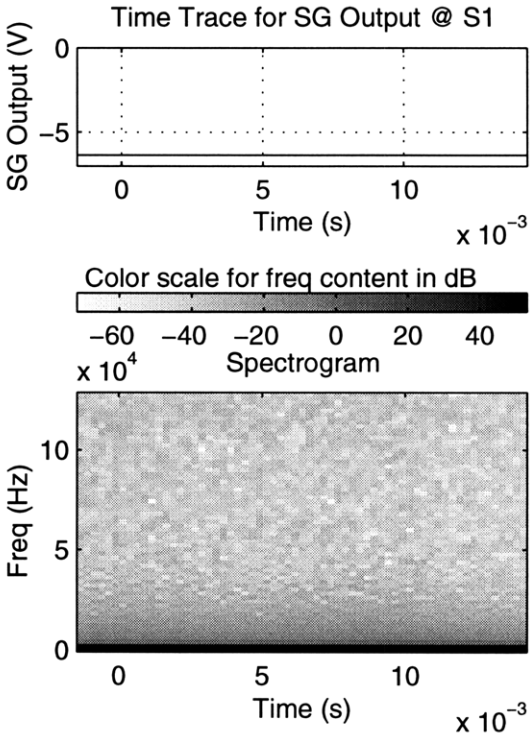

Radiation Test – October 8th, 1997

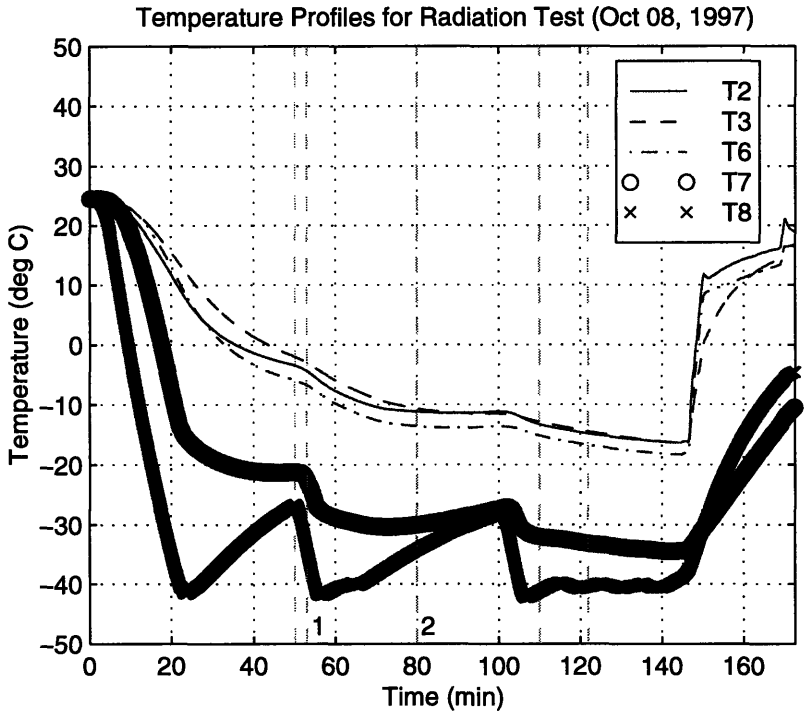

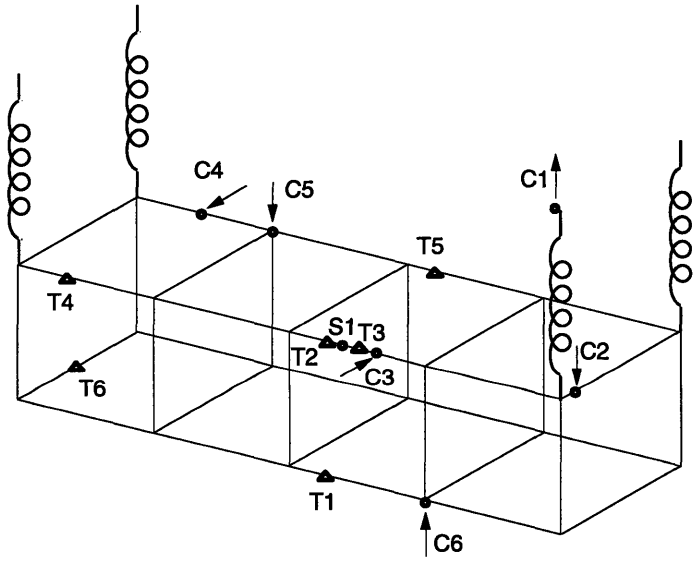

▲ T7 (on plate)

▲ T8 (on plate)

Test Procedure Notes: controlled radiation test using plate instead of shroud; 100kHz BW setting on 2nd data acquisition unit; AC coupling on strain gauge S1; 1st data acquisition unit did not trigger on events (channels C1, C2, C3 & C4 not available)

Radiation Test – October 8th, 1997

Event #1

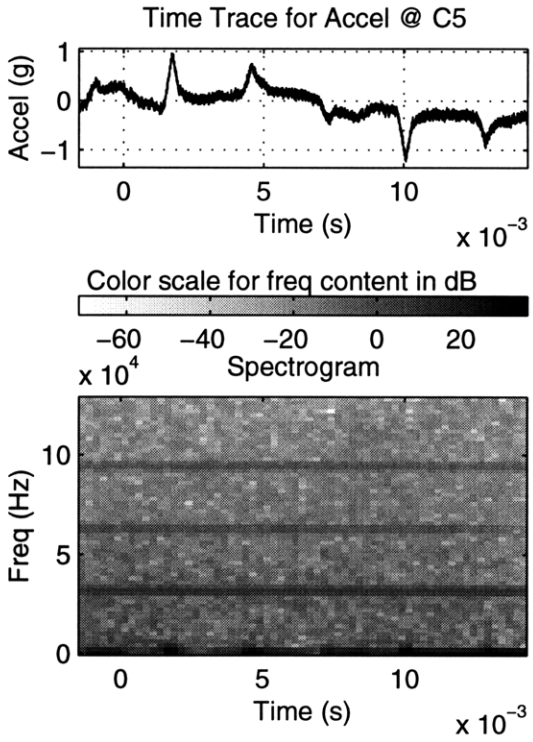

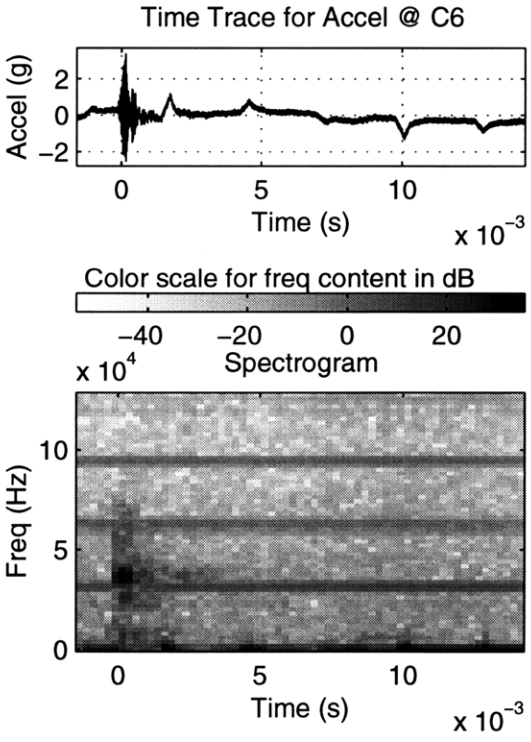

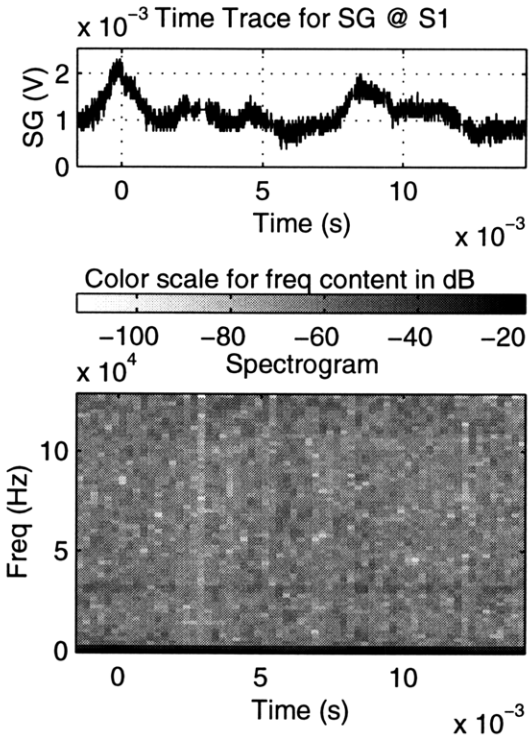

Radiation Test – October 8th, 1997

Event #2

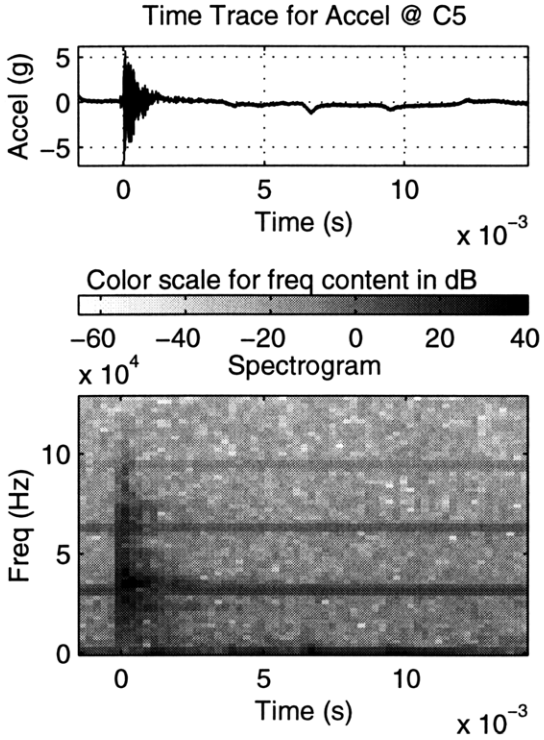

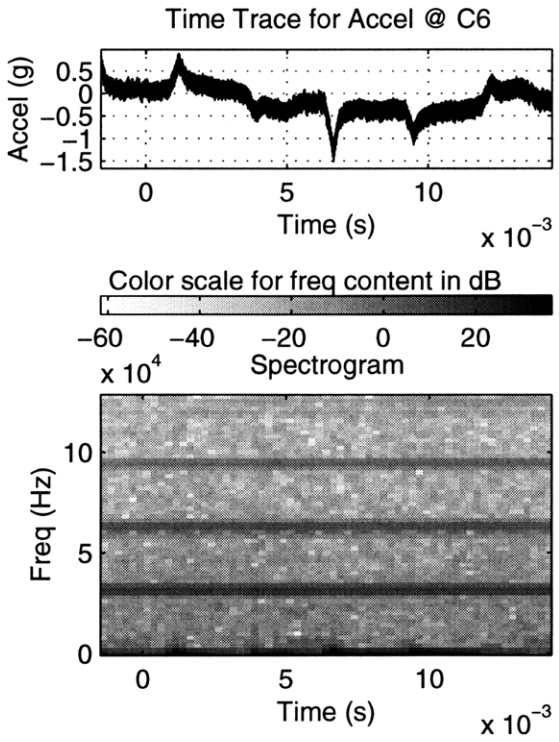

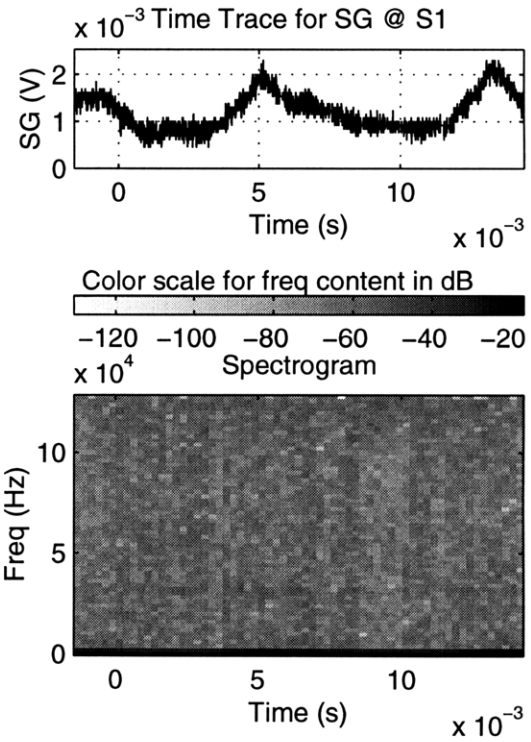

Radiation Test – November 25th, 1997

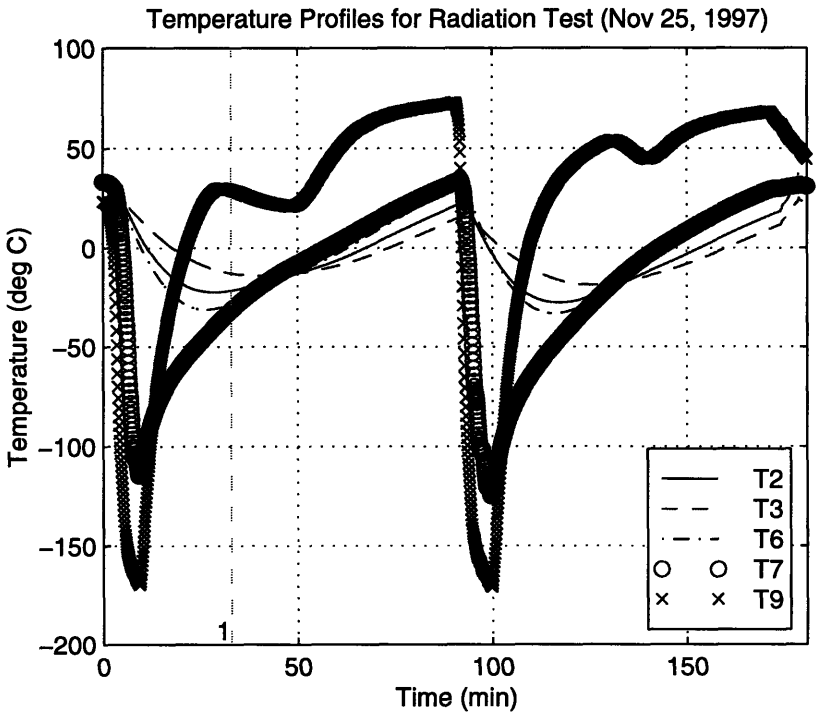

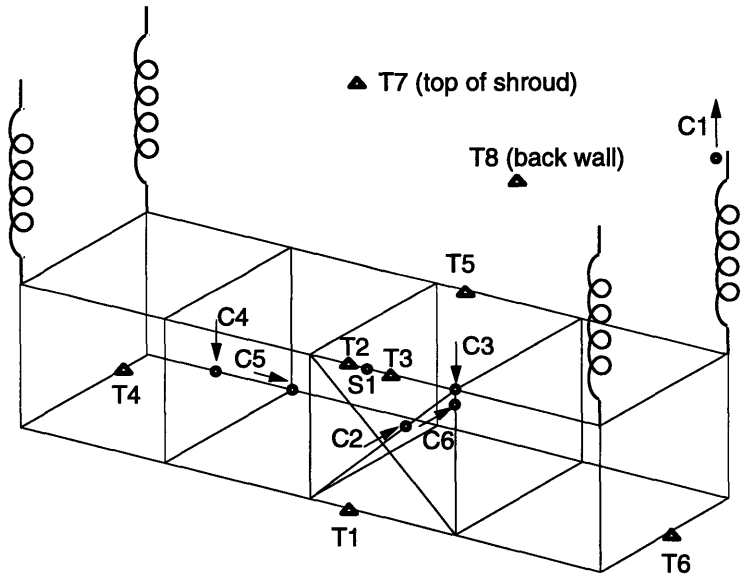

T9 (bottom of shroud)

Test Procedure Notes: 100 kHz BW setting on 1st data acquisition unit (channels C2, C3 &C6)

Radiation Test – November 25th, 1997

Event #1

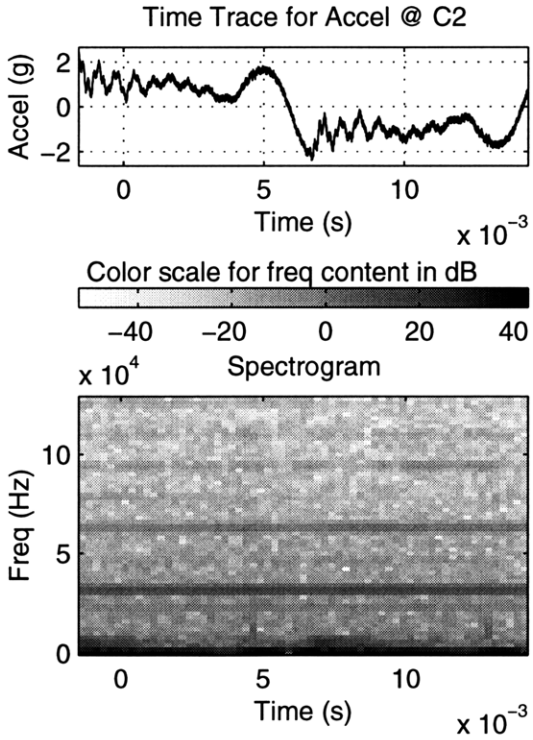

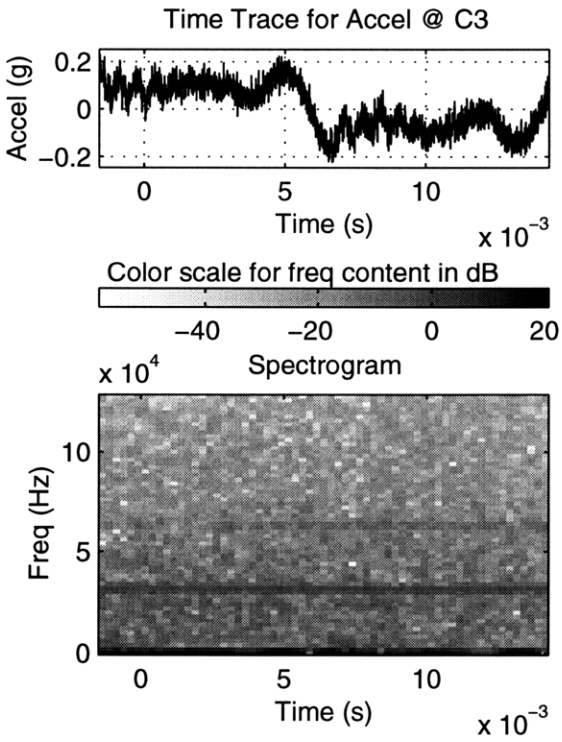

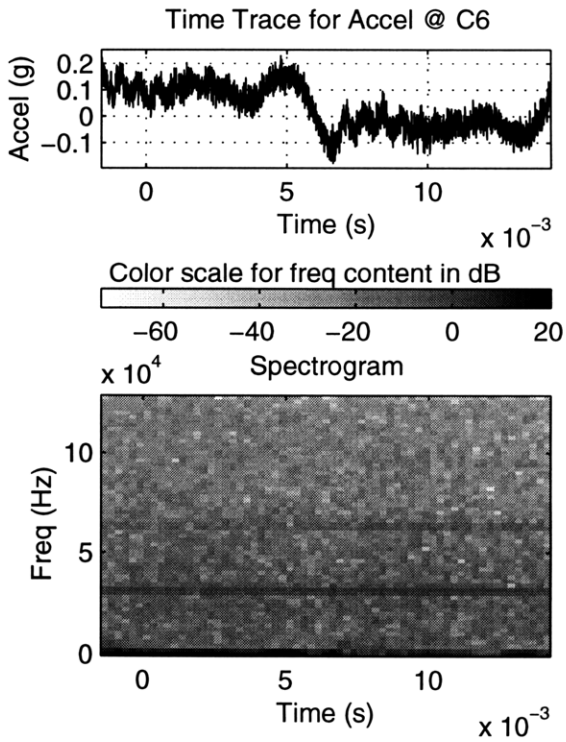

Radiation Test – November 25th, 1997

Event #1 (continued)